Water Droplet Impact Dynamics on Active and Passive Vibrating Surfaces

Patricia B. Weisensee[1,2], Jingcheng Ma[1], Junjiao Tian[1], William P. King[1], Nenad Miljkovic[1,3]

[1] Department of Mechanical Science and Engineering, University of Illinois at Urbana-Champaign, USA
[2] Department of Mechanical Engineering and Materials Science, Washington University in St. Louis, USA
[3] International Institute for Carbon Neutral Energy Research (WPI-I2CNER), Kyushu University, Japan

E-mail: p.weisensee@wustl.edu

Droplet impingement on vibrating surfaces is ubiquitous in nature and industrial applications, including impact on insect wings, plant leaves, or turbine blades. Droplet dynamics of water impact on stationary rigid superhydrophobic surfaces are well understood [1]. It has been shown previously that contact times t_c, i.e. the time between initial contact between droplet and substrate and lift-off, is independent of impact velocity [2]. Here, we show that substrate vibrations, both active (forced vibration) and passive (flexible substrate) can manipulate droplet dynamics and contact times. Using high-speed imaging, we studied the bouncing behavior of millimetric water droplets impinging superhydrophobic surfaces with impact speeds up to 2.2 m/s. During forced vibration, the rigid substrate was vibrating at frequencies of 60 – 320 Hz and amplitudes of 0.2 – 2.5 mm. We investigated the dependency of contact times on vibration frequency, amplitude, and impact phase. To study the effect of passive vibrations, we fabricated flexible superhydrophobic polymer substrates with stiffness ranging from 0.5 to 7630 N/m (rigid), and corresponding natural frequencies of 12 to 300 Hz. The impact force caused vibrating amplitudes up to 2.7 mm.

Substrate vibrations can strongly influence the droplet shape and contact time during recoil and lift-off. On a stationary rigid superhydrophobic surface, droplets spread, completely recoil and then lift off. On flexible surfaces, droplets can leave the surface in a pancake-like shape before fully recoiling due to a springboard effect. Upon impact, the droplet initiates, or intensifies, substrate vibration. Spreading on the flexible substrates is similar to that on a rigid surface. During recoil, however, the vibration of the flexible substrate accelerates the droplet upwards prior to it being able to completely recoil, and the contact time is reduced (Fig. 1).

We observed a similar lift-off behavior on some of the rigid vibrating surfaces. However, droplet dynamics and contact times on these rigid surfaces subject to forced vibration were much more diverse than on passive, flexible substrates. Depending on the phase, frequency, and amplitude of the vibration, we identified five different classes of droplet dynamics: Pancake bouncing, tulip splashing, droplet re-attachment, crown splashing, and jetting. Contact times can range from $t_c \approx 0.5 t_{c,th}$ (pancake bouncing) to $t_c \approx 1.6 t_{c,th}$ (re-attachment and jetting), where $t_{c,th}$ is the theoretical contact time on a stationary substrate. The droplet shape and thus contact time is a strong function of the impact phase. We determined a critical impact phase at which contact times transition rapidly from a minimum to the maximum (Fig. 2). Taking into account the probability of impact at a given phase we show that for low frequencies (< 80 Hz) average contact times increase, i.e. $t_c > t_{c,th}$, while contact times decrease for impact at higher vibration frequencies (> 100 Hz) (Fig. 3).

This study provides new insights into droplet impact physics on passive and active vibrating surfaces. We also develop guidelines for the rational design of surfaces to achieve controllable droplet wetting in applications utilizing vibration.

Acknowledgements. This work was supported by the National Science Foundation Engineering Research Center for Power Optimization of Electro Thermal Systems (POETS) with cooperative agreement EEC-1449548. N. Miljkovic gratefully acknowledges the funding support from the Office of Naval Research (ONR) with Dr. Mark Spector as the program manager (Grant No. N00014-16-1-2625). N. Miljkovic gratefully acknowledges the support of the International Institute for Carbon Neutral Energy Research (WPI-I2CNER), sponsored by the Japanese Ministry of Education, Culture, Sports, Science and Technology.

References

[1] Yarin, A. L. DROP IMPACT DYNAMICS: Splashing, Spreading, Receding, Bouncing…. *Annu. Rev. Fluid Mech.* **38**, 159–192 (2006).
[2] Richard, D., Clanet, C. & Quéré, D. Surface phenomena: Contact time of a bouncing drop. *Nature* **417**, 811–811 (2002).

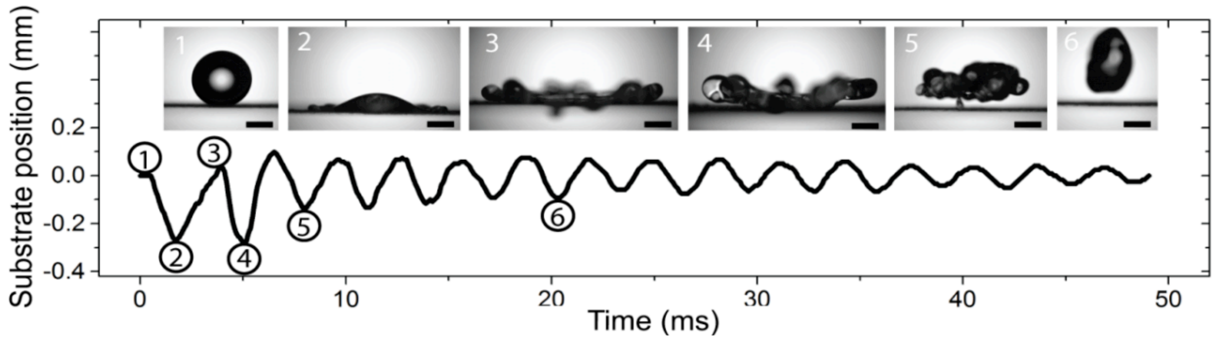

Fig. 1: Droplet impact on a flexible superhydrophobic substrate. Droplet impact causes the substrate to vibrate. The resulting springboard effect results in early droplet lift-off in a pancake shape and reduced contact time.

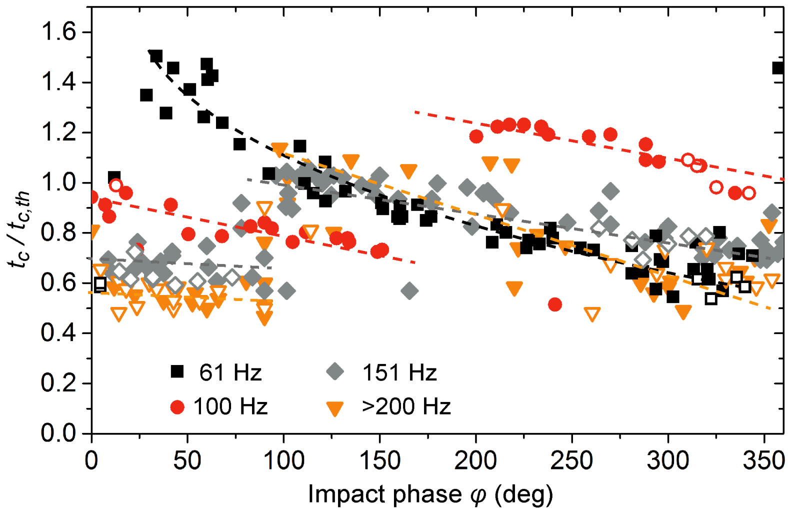

Fig. 2: Normalized contact times as a function of impact phase on vibrating rigid superhydrophobic surfaces. For each frequency, contact times suddenly increase at a certain impact phase and decrease thereafter.

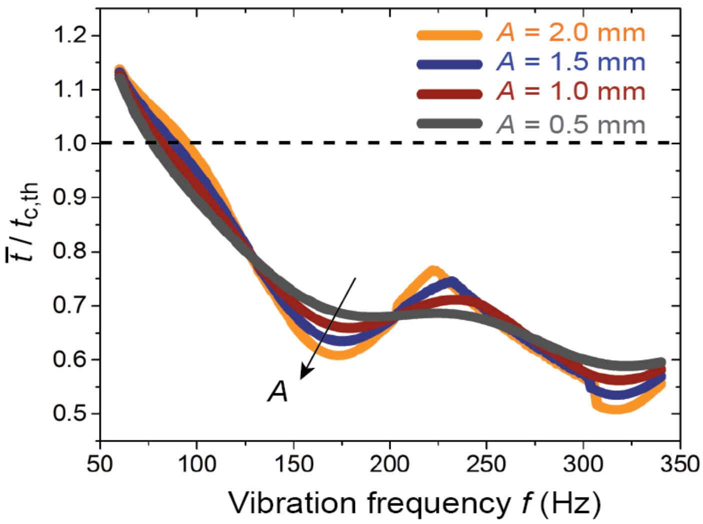

Fig. 3: Average normalized contact times for droplet impact on rigid vibrating rigid superhydrophobic surfaces. Contact times can be actively controlled via the substrate vibration frequency.

Thin-Film Evaporation of Capillary-Fed Copper Inverse Opals

Quang N. Pham[1], Bowen Shao[2], Mario Soler[3], Yoonjin Won[1,2]

[1]Department of Mechanical and Aerospace Engineering, UCI, Irvine, CA, USA
[2]Department of Chemical Engineering and Materials Science, UCI, Irvine, CA, USA
[3]Department of Chemical Engineering, UCI, Irvine, CA, USA

E-mail: won@uci.edu

Thermal dissipation from microelectronic packaging is increasingly challenging as heat flux of electronics continues to rise. The promising performance of evaporative cooling of small-area high-flux heat sources has recently garnered significant attention [1-3]. The passive cooling technique of evaporative heat transfer often utilizes a porous medium that wicks a working fluid to the hot spot by capillary action. In this process, evaporative heat transfer achieves effective thermal transport performances by utilizing the latent heat of the working fluid.

The porous media used in recent wicking and evaporation studies have included sintered particles [4,5], micropillars [6], carbon nanotubes [7], nanowires [8], and inverse opals [9,10]. These microstructures are often varied in dimensional characteristics failing in elucidating the structural effects on evaporative cooling. Inverse opals (IOs) possess crystalline arranged pores that are uniform in size and are relatively new in wicking applications. Inverse opals attain high level of porosity and surface area to volume ratio, making them ideal for two-phase thermal transport. Despite numerous advantages, the evaporative heat transfer of IOs is been underexplored.

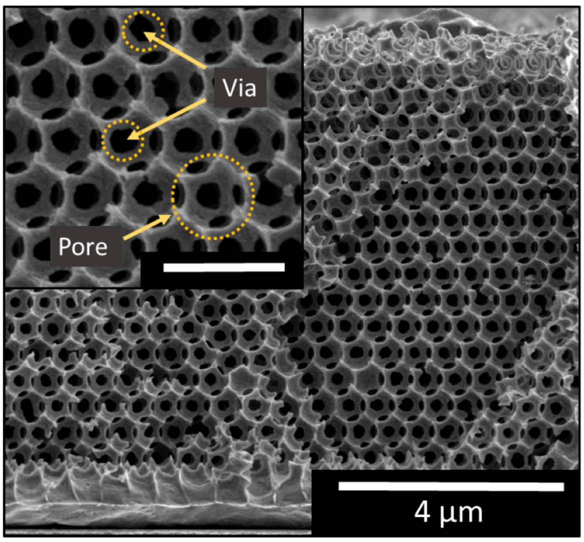

Figure 1. A cross-sectional SEM image of representative copper inverse opals. For this sample, 600 nm diameter pores are arranged in a crystalline order. The permeability of the inverse opal is determined by the via that interconnects adjacent pores. The scale bar of the inset is 2 µm.

In this work, we suggest using copper IOs as an advanced wicking medium [11]. We employ a templated-assisted electrodeposition to fabricate the copper IOs [12]. In the first step of the fabrication, sacrificial spheres are deposited into crystalline packing via self-assembly. Copper is then electroplated into the empty voids between the templated spheres. After dissolving the sacrificial spheres, a copper scaffold is revealed to show the inverted structure (Figure 1).

The wicking and evaporative characteristics are examined by vertically placing the copper IOs inside a sealed chamber for a controlled evaporation environment. The copper IO sample on a silicon substrate is slowly lowered until it comes in contact with the pool reservoir of isopropyl alcohol, which is used as the working fluid due to its low surface tension and desirable wettability on the copper surface. The liquid is immediately wicked up through the IOs. The rate of front propagation is monitored with a camera at 30 fps. The copper IO sample is then heated with joule heating by controlling the applied voltage and current with a DC power supply. As temperature slowly increases, the thin film of liquid evaporates, which is confirmed by observing the receding propagated front. The large meniscus contact region between the liquid reservoir and the sample sustains a constant liquid-feeding through the porous IOs. The surface temperature is confirmed using an attached thermocouple. High resolution thermal imaging from an infrared camera displays the changes of the two-dimensional temperature. By analyzing the differences in temperature, evaporative heat transfer coefficients as well as heat fluxes can be determined. The mass of the pool reservoir is weighed by an electronic balance over time, which is used to determine the mass flow rate of the working fluid that undergoes wicking and evaporation.

In order to determine the effects of structural characteristics of the copper IOs on the thermal and hydrodynamic transport, the pore size and interconnect via size (see Figure 1) will be systematically controlled using a template method and electroetching process, respectively. The modulation of the pore and via size significantly affects the permeability of the porous medium and

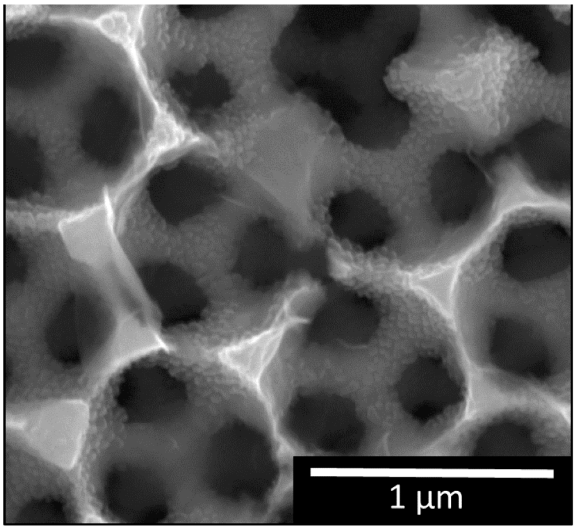

Figure 2. A top view SEM image of a copper inverse opal after electroetching process. After several electroetching cycles, increases in via size as well as formation of nanotextures on the surface of each pores are observed. The rough surface may contribute to improved wicking behavior.

thus, the effective transport rates. Characterization from scanning electron microscopy (SEM) will confirm the changes in the morphology of the copper IOs.

In conjunction with widening the interconnected via size, electroetching also creates nanotextures on the surface of the copper IOs (Figure 2). The roughened surface will have an influence on the wettability of the copper IOs, which can be examined by measuring the dynamic contact angle of the sample. With inkjet technology, picoliter sized droplets can be dispensed onto the nanotextured and porous IOs. Controlling the discharging frequency allows the advancing angles to be observed. As the droplet quickly evaporates, the contact angle decreases as a function of time as it reaches the receding angle. A high-speed camera operating at 100,000 fps is used to capture the evolutional changes of contact angle with time.

In summary, copper IOs are promising nanowicks in evaporative cooling devices due to its low-maintenance and self-pumping mechanism. Understanding the wicking performance of crystalline copper IOs under thermal loading can help elucidate its application and potential design in next-generation heat pipes and thermal ground planes.

Acknowledgement
This work was sponsored by the Samsung Advanced Institute of Technology.

References

[1] S. Adera, D. Antao, R. Raj, E.N. Wang. *International Journal of Heat and Mass Transfer*, (2016) **101**, 280-294.
[2] R. Ranjan, S.V. Garimella, J.Y. Murthy, K. Yazawa. *Nanoscale and Microscale Thermophysical Engineering*, (2011) **15**, 179-194.
[3] R. Xiao, S.C. Maroo, E.N. Wang. *Applied Phyiscs Letters*, (2013) **102**, 123103-123106.
[4] M.A. Hanlon, H.B. Ma. *8th AIAA/ASME Joint Thermophysics and Heat Transfer Conference*, (2002).
[5] X.L. Cao, P. Cheng, T.S. Zhao. *Journal of Thermophysics and Heat Transfer*, (2002) **16**, 547-552
[6] Y. Zhu, D.S. Antao, Z. Lu, S. Somasundaram, T. Zhang, E.N. Wang. *Langmuir*, (2016) **32**, 1920-1927.
[7] J.A. Weibel, S.S. Kim, T.S. Fisher, S.V. Garimella. *Nanoscale and Microscale Thermophysical Engineering*, (2012) **16**, 1-17.
[8] A. Rogacs, J.E. Steinbrenner, J.A. Rowlette, J.M. Weisee, X.L. Zheng, K.E. Goodson. *Journal of Colloid and Interface Science*, (2010) **349**, 354-360.
[9] C. Zhang, S. Lingammeni, M.T. Barako, J.W. Palko, M.A. Asheghi, K.E. Goodson. *15th IEEE ITHERM Conference*. (2016)1035-1038.
[10] J.W. Palko, C. Zhang, J.D. Wilbur, T.J. Dusseault, M. Asheghi, K.E. Goodson, J.G. Santiago. *Applied Phyiscs Letter*, (2015) **107**, 253903-253906.
[11] W. Liu, Y. Yang, M. Asheghi. *IEEE Transactions* (2006), 1171-1176.
[12] Q.N. Pham, P. P. Dubey, Y Won. *ASME Summer Heat Transfer Conference*. Washington, D.C., July 10-14

Drops Impacting Flexible Fibers with Variable Wetting Regimes

Salome Hussein[1], Dr. Geoff Willmott[1,2,3], Prof. Stuart Bradley[1], Matheu Broom[1,2]

[1]Department of Physics, University of Auckland, Auckland, New Zealand
[2] The MacDiarmid Institute for Advanced Materials and Nanotechnology, New Zealand
[3]School of Chemical Sciences, University of Auckland, Auckland, New Zealand

E-mail: salome.scott@auckland.ac.nz

Drop impacts are an increasingly popular subject for study, especially given the quality of modern high speed imaging techniques. Drops are of obvious practical importance as well, whether in the fine mists of industrial sprays, or falling as rain [7,12]. This project is motivated by the former, specifically, agricultural sprays. This area provides a myriad of opportunities to study interesting drop phenomena. In addition to using a variety of fluids between applications, there are often multiple crops of interest, and the different anatomy of individual crops provide their own challenges (e.g. blossoms require different handling than fruit, vines, or leaves) [11].

How water drops interact with plant surfaces is well-known, leading to the eponymous rose-petal or lotus effects, where drops can adhere or roll along the surface, without truly wetting that surface. In those instances, petals and leaves lend themselves well to simple experimental investigations because, relative to drop size, the impact surfaces are effectively flat. This is not the case for flower stigma or grape clusters, which have variable wetting morphologies and complex structural geometries. One must also consider multiple relevant time scales, and keep track of the forms of energy. There is elastic deformation of both the drop and structures, the formation of new surfaces and interfaces, and drag of a solid surface through a liquid if the drop carries through the structure.

The presented experiments utilize flexible fibers mounted as a cantilevered beam to simulate the reproductive anatomy of a blossom. Multiple studies have been conducted with drops impacting individual fibers, arrays of fibers, or cantilevered beams, as the applications of the phenomena range from textile treatment to piezoelectric energy harvesting [1-6]. Multiple experimental parameters are pertinent in this scenario, including the ratio of the fiber diameter to that of the drop, the kinetic energy of the drop, the impact parameter (the eccentricity of the drop's center with respect to the fiber's main axis) of the drop, the liquid properties of the drop, and the structural properties of the fiber. This study focuses on the role of the structural properties of the fiber, both its elasticity and its surface interactions with the liquid drop.

Drops were produced via flow through a hypodermic needle, then detaching and falling. Fibers were treated with polyurethane to increase the contact angle. The contact angle was determined using the method for contact angle on fibers developed in reference [8]. The Young's modulus using standard methods. Untreated fibers were segments of FEP microfluidic tubing, known to be hydrophobic. The experiments were filmed, from the front, side, and beneath, using a Photron Fastcam S5, and the videos were analysed using standard image processing techniques.

The experiments show that while a hydrophilic fiber will always retain some fluid post-impact, hydrophobic fibers only retain a significant volume of fluid if the drop is of a critical capture velocity as predicted by [1]. However, in those cases, because the entirety of the drop remains on the fiber, the efficiency of drop capturing is higher.

There is also a difference in the two cases in the oscillatory behavior of the fiber post-impact when a drop is not captured. Because the drop is in contact with and deforming a hydrophobic fiber for a longer time scale over the course of impact, the tip of the fiber is deflected farther initially. Furthermore, the amount of fluid left behind in the hydrophilic case results in higher damping of the fiber post impact.

Future work will involve the use of blossoms and industrial sprays to confirm that the described physical processes influence the effectiveness of chosen technology. If so, then available models will serve as a useful guide for selecting spray systems with the optimum drop characteristics for the application of interest.

Acknowledgements. This project was funded by The New Zealand Ministry of Business, Innovation, and Employment.

References

[1] Comtet, Jean, Bavand Keshavarz, and John WM Bush. "Drop impact and capture on a thin flexible fiber." *Soft matter* 12.1 (2016): 149-156.
[2] Dressaire, E., Sauret, A., Boulogne, F., & Stone, H. A. (2016). "Drop impact on a flexible fiber." *Soft matter*, *12*(1), 200-208.
[3] Kim, Sung-Gil, and Wonjung Kim. "Drop impact on a fiber." *Physics of Fluids* 28.4 (2016): 042001.
[4] Sauret, Alban, et al. "Drop morphologies on flexible fibers: influence of elastocapillary effects." *Soft Matter* 13.1 (2017): 134-140.
[5] Sauret, Alban, et al. "Wetting morphologies on an array of fibers of different radii." *Soft Matter* 11.20(2015): 4034-4040.
[6] Piroird, Keyvan, et al. "Drops impacting inclined fibers." *Journal of colloid and interface science* 334.1 (2009): 70-74.
[7] Yarin, A. L. "Drop impact dynamics: splashing, spreading, receding, bouncing…." *Annu. Rev. Fluid*

Mech. 38 (2006): 159-192.
[8] Schellbach, Sara L., Sergio N. Monteiro, and Jaroslaw W. Drelich. "A novel method for contact angle measurements on natural fibers." *Materials Letters* 164 (2016): 599-604.
[9] Sher, E., L. F. Haim, and I. Sher. "Off-centered impact of water droplets on a thin horizontal wire." International Journal of Multiphase Flow 54 (2013): 55-60.
[10] Liang, Gangtao, et al. "Rebound and spreading during a drop impact on wetted cylinders." *Experimental Thermal and Fluid Science* 52 (2014): 97-103.
[11] Ashgriz, Nasser, ed. *Handbook of atomization and sprays: theory and applications*. Springer Science & Business Media, 2011.
[12] Clift, Roland, John R. Grace, and Martin E. Weber. *Bubbles, drops, and particles*. Courier Corporation, 2005.
[13] Gart, Sean, et al. "Droplet impacting a cantilever: A leaf-raindrop system." *Physical Review Applied* 3.4 (2015): 044019.

INTERACTIONS BETWEEN THE EDGE OF AN IMPACTING DROPLET AND A MICROSCOPIC RIDGE

Geoff R. Willmott[1,2,3], Matheu Broom[1], Hossein Rashidian[4], Mathieu Sellier[4]

[1] Department of Physics, The University of Auckland, New Zealand
[2] School of Chemical Sciences, The University of Auckland, New Zealand
[3] The MacDiarmid Institute for Advanced Materials and Nanotechnology
[4] The University of Canterbury, 20 Kirkwood Ave, Christchurch, New Zealand

E-mail: g.willmott@auckland.ac.nz

Following a liquid drop impact on to a solid surface, the liquid typically forms a thin lamella which spreads over the surface [1, 2]. In this study, we focus on the interaction between the edge of the spreading laemlla and a micrometer-scale ridge on an otherwise flat surface. Research into water droplet impacts onto micropatterned solid surfaces is a growing area of interest [3, 4].

The lamella-ridge interaction is especially relevant in two areas that have recently been prominent in the literature. Firstly, researchers have noted the ability to reduce a droplet's contact time by direct impact on a thin hydrophobic ridge [5, 6]. In applications where the drop incidence is stochastic, droplets will more commonly impact the surface some distance away from a ridge, after which a spreading lamina will impact the ridge from the side.

The second area of specific relevance concerns the interplay between spreading dynamics and the Cassie and Wenzel states, which are more familiar from quasi-static wetting experiments. In the Cassie state, which is characteristic of superhydrophobic surfaces, the liquid is pinned on top of the surface microstructure, leaving air pockets adjacent to the surface. In the Wenzel state, the liquid completely wets the microstructure. Drop impact experiments have shown that pillar array microstructures can be penetrated over a limited area directly below the impact point, while the lamella edge spreads on top of the pillars [7-9].

In this study, we are using numerical simulations and high-speed photography experiments to elucidate the mechanism and conditions under which the spreading lamina surmounts a surface ridge. Three basic outcomes have been observed when the lamella comes into contact with the ridge (Fig. 1). Firstly, the advance of the lamella may be arrested before the drop reaches the far side of the ridge, an outcome known as pinning. Wetting, the second outcome, occurs when the drop advances and spreads over the surface beyond the ridge, while remaining intact. The third outcome is splashing, when smaller drops are generated with the lamella edge in contact with the ridge. In this work, we apply these classifications to the lamella when it is at maximum spread.

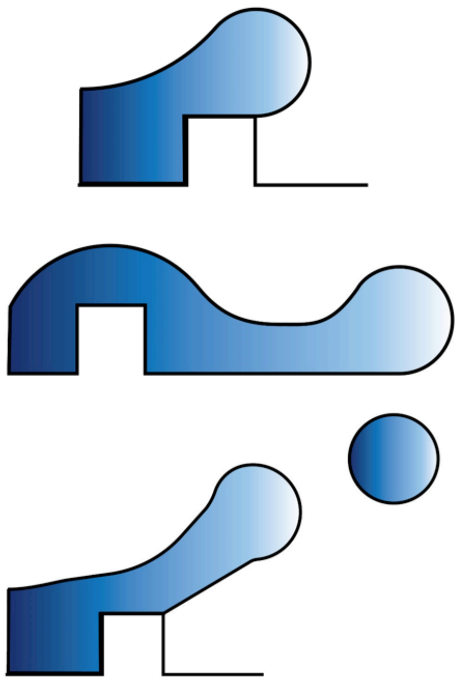

Figure 1: Schematic demonstration of lamella-ridge outcomes classified as pinning (upper), wetting (middle), and splashing (lower).

A Lattice-Boltzmann computational model was used to simulate impacts (Fig 2(a)). A key advantage to this approach is the ability to effectively simulate the air which escapes from underneath the drop as it comes into contact with the surface. In this initial work, a two dimensional model was used, so that the drop can be thought of as an impacting cylinder.

Experiments (Fig. 2(b)) have been carried out using a Photron Fastcam SA5 high-speed camera, with the water drop impact viewed from side-on. Ridges were created on PDMS substrates using soft lithography, with height and width in the range 40-100 μm. Drops were typically 2-3 mm in diameter, with impact Weber numbers ranging from approximately 50 to 250. Results show good agreement between the qualitative outcomes observed in experiments and simulations. (Figure 2).

The key parameters for analysis are the initial drop diameter (D_0), which is typically used to

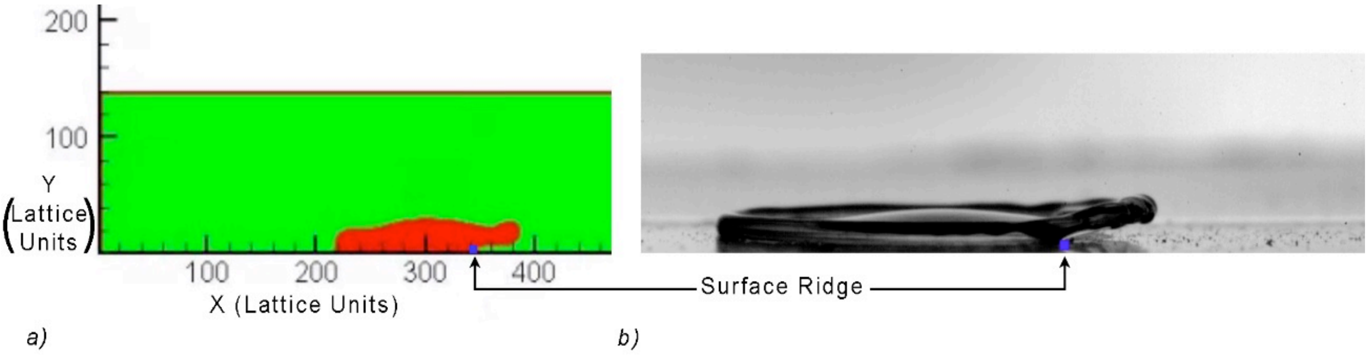

Figure 2: A spreading lamella comes into contact with a microscopic ridge, which causes it to lift off from the surface. (a) Lattice-Boltzmann simulation. (b) Image from a high-speed video captured at ~7000 frames per second.

non-dimensionalise length scales, the distance from the drop impact point to the near edge of the ridge (D_R), and the height and width of the rectangular ridge. Analysis is initially being carried out using simple energy conservation arguments – i.e by equating the increased surface energy of the drop at maximum spread with the kinetic energy at impact. Although significant energy is lost due to viscosity during spreading [10], this model correctly predicts the general shape of the pinning-wetting phase boundary as a function of Weber number and D_R / D_0. Moreover, the simplicity of the model means that it can be adapted to explore possible quantitative agreement between the two dimensional simulations and the experimental outcomes.

These initial results have shown that simple models can be developed to predict outcomes when a spreading lamella meets a surface ridge. Experiments are continuing with the aim of further elucidating the wetting-splashing phase boundary in particular. Further analyses are being developed to account for the viscous losses and the specific dynamics of the lamella as it comes into contact with the ridge. We also plan to extend the Lattice-Boltzmann modelling to three dimensions. The work could also be extended to other geometries, such as pillars or parts of pillar arrays, in order to understand how the drop 'leaps' from the penetrated microstructure to spreading on top of posts in an array.

References

[1] A.L. Yarin, Drop impact dynamics, Annu. Rev. Fluid Mech. 38 (2006) 159-192.
[2] C. Josserand, S.T. Thoroddsen, Drop impact on a solid surface, Annu. Rev. Fluid Mech. 48 (2016) 365-391.
[3] M. Marengo, C. Antonini, I.V. Roisman, C. Tropea, Drop collisions with simple and complex surfaces, Curr. Opin. .Coll. Interf. Sci. 16 (2011) 292-302.
[4] D. Khojasteh, M. Kazerooni, S. Salarian, R. Kamali, Droplet impact on superhydrophobic surfaces: A review of recent developments, J. Ind. Eng. Chem. 42 (2016) 1-14.
[5] J.C. Bird, R. Dhiman, H.-M. Kwon, K.K. Varanasi, Reducing the contact time of a bouncing drop, Nature 503 (2013) 385-389.
[6] A. Gauthier, S. Symon, C. Clanet, D. Quere, Water impacting on superhydrophobic macrotextures, Nature Communications 6 (2015) 8001.
[7] M. Reyssat, D. Richard, C. Clanet, D. Quere, Dynamical superhydrophobicity, Faraday Discussions 146 (2010) 1-15
[8] S. Robson, G.R. Willmott, Asymmetries in the spread of drops impacting on hydrophobic micropillar arrays, Soft Matter 12 (2016) 4853-4865.
[9] P. Tsai, M.H.W. Hendrix, R.R.M. Dijkstra, L. Shui, D. Lohse, Microscopic structure influencing macroscopic splash at high Weber number, Soft Matter 7 (2011) 11325-11333.
[10] S. Wildeman, C.W. Visser, C. Sun, D. Lohse, On the spreading of impacting drops, J. Fluid Mech. 805 (2016) 636-655.

Dropwise to filmwise condensation on transparent polycarbonate by surface texturing

Nicolas Pionnier[a], Elise Contraires [a], Stéphane Benayoun [a], Stéphane Valette [a].
[a] Université de Lyon, Ecole Centrale de Lyon, Laboratoire de Tribologie et Dynamique des Systèmes, UMR 5513,F-69131, Ecully, France

Keywords: Dropwise condensation, Filmwise condensation, Wettability, Polycarbonate, Texturation, Optical properties

1. Introduction

Polycarbonate is used in protection pieces such as diving mask visors. However, the presence of dew impairs surfaces' transparency by degrading light transmission. In order to improve visibility through these optical surfaces covered by dew, the knowledge of wettability properties is essential [1]. It is possible to modify interface wettability conditions by managing chemical and/or topographical properties [2, 3]. For anti-fogging treatments, the chemical approach is the most widespread in industries. However, it is expensive and has a limited life time. The topographical approach, studied in these works, has already been explored to optimize the condensers efficiency and thus favor water droplet formation [4]. Contrary to this kind of work, we search to limit the presence of droplets on a polycarbonate surface by creating a uniform liquid film. Consequently, we developed surface texturing methods and a dew control and observation apparatus.

2. Surfaces texturing

The polycarbonate surfaces are textured by micromachining. Two approaches can be highlighted: direct and indirect texturing. In the first case, the cutting tools modify surfaces by direct interaction. In the last case, a mold is textured and surfaces are reproduced by molding injection [5]. For industrial applications, indirect approach is more pertinent. Indeed, it does not generate additional step on the injection molding production line.

3. Dew tracking and observation setup

For controlled and repeatable observations [6], the samples are placed in a box controlled on temperature and relative humidity (FIGURE 1). The humidity is produced by mixing an approximately dry air and a water-saturated air. This method allows the box humidity to be set between 15 % and 60 % during condensation tests.

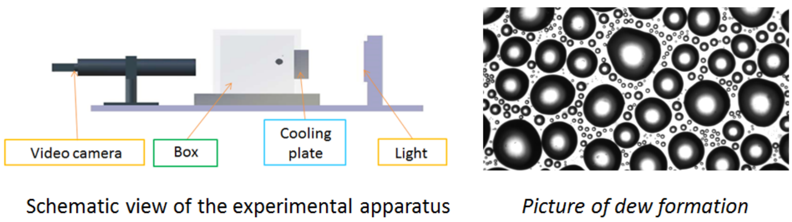

Figure 1: Drawing of the experimental apparatus and an experimental dew picture on non-textured polycarbonate surface.

To control the dew formation location, the samples are fitted on a cooled surface allowing its to reach a temperature lower than the dew point temperature (below this temperature water starts condensing).

The analysis of the condensation figures are realized with a video camera. A sequence of pictures taken at a normal incidence (FIGURE 1), is analyzed as a function of time to localize, to count and to measure the radii and the orientations of the droplets.

Corresponding author is Nicolas Pionnier, Stéphane Valette
Nicolas Pionnier: E-mail: nicolas.pionnier@doctorant.ec-lyon.fr, WWW: http://www.ltds.ec-lyon.fr, Telephone: +33 (0)4 72 18 62 48
Stéphane Valette: E-mail: stephane.valette@ec-lyon.fr, Telephone: +33 (0)4 72 18 64 38

4. Results

The analysis of the condensation figures on non-textured and textured polycarbonate will be presented. The texturation objective is to create filmwise condensation. An example showing condensation behavior on a surface textured with a cavity pattern is presented FIGURE 2. Different types of textured patterns were tested and a study of the optimum pattern parameters will be presented. Moreover, the condensation phenomenon of these textured surfaces will be described step by step.

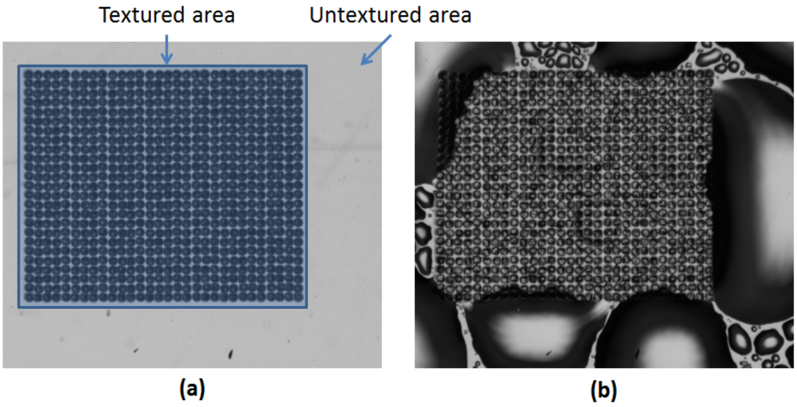

Figure 2: Pictures of polycarbonate surface textured with holes. (a) Before condensation (t=0 min). (b) During condensation test at t=2 h 20 min.

References

[1] B.J. Briscoe and K.P. Galvin. The effect of surface fog on the transmittance of light. *Solar Energy*, 46(4):191 – 197, 1991.

[2] P. Bizi-Bandoki, S. Benayoun, S. Valette, B. Beaugiraud, and E. Audouard. Modifications of roughness and wettability properties of metals induced by femtosecond laser treatment. *Appl. Surf. Sci.*, 257(12):5213–5218, 2011.

[3] V. Belaud, S. Valette, G. Stremsdoerfer, M. Bigerelle, and S. Benayoun. Wettability versus roughness: Multi-scales approach. *Tribology International*, 82, Part B:343 – 349, 2015.

[4] Konstantin O. Zamuruyev, Hamzeh K. Bardaweel, Christopher J. Carron, Nicholas J. Kenyon, Oliver Brand, Jean-Pierre Delplanque, and Cristina E. Davis. Continuous droplet removal upon dropwise condensation of humid air on a hydrophobic micropatterned surface. *Langmuir*, 30(33):10133–10142, 2014.

[5] Julie Vera, Anne-Catherine Brulez, Elise Contraires, Mathieu Larochette, Stéphane Valette, and Stéphane Benayoun. Influence of the polypropylene structure on the replication of nanostructures by injection molding. *Journal of Micromechanics and Microengineering*, 25(11):115027, 2015.

[6] Julian E. Castillo, Justin A. Weibel, and Suresh V. Garimella. The effect of relative humidity on dropwise condensation dynamics. *International Journal of Heat and Mass Transfer*, 80(0):759 – 766, 2015.

ELECTROWETTING-ASSISTED DROP CONDENSATION AND SHEDDING ON HYDROPHOBIC SURFACES

Davood Baratian, Ranabir Dey, Harmen Hoek, Dirk van den Ende, Frieder Mugele

Physics of Complex Fluids; MESA+ Institute for Nanotechnology; University of Twente; 7500 AE Enschede, The Netherlands

E-mail: f.mugele@utwente.nl

Dropwise condensation is know be more efficient in heat transfer than filmwise condensation. In case of dropwise condensation, efficient removal of drops from the condensor surface is crucial to maximize heat transfer. In this paper, we explore the use of electrowetting-functionalized surfaces to control the condensation of water vapor and to enhance the shedding of drops.

Using interdigitated electrodes submerged under a surface of Teflon AF, we show that the distribution of condensing drops can be actively controlled. Small drops are found to align preferentially along the edges of the electrodes, somewhat larger drops are found to become centered in between adjacent electrodes. These effects are can be explained semiquantitatively by considering the electrostatic energy landscape generated by the electrodes: balancing electrostatic forces with pinning forces due to finite contact angle hysteresis [2, 3] provides a reasonable description of the threshold for mobilizing drops.

Drop mobilization is frequently accompanied by coalescence. The abrupt increase in drop size upon coalescence in combination with the AC excitation using electrowetting enables efficient shedding of the drops from the surface in the presence of gravity. The drop characteristic size before shedding is found to be substantially smaller than on non-electrified control surfaces. This can be explained by the well-known electrowetting-induced reduction of the effective contact angle hysteresis in ambient air [3].

All these observations point towards a significant enhancement of the heat transfer as compared to conventional dropwise condensation.

Acknowledgements. Funding by the Dutch Science Foundation is acknowledged under grant 11380 in the VICI program.

References

[1] J.W. Rose, *Dropwise condensation theory and experiment: A review*. Proceedings of the Institution of Mechanical Engineers, Part A: Journal of Power and Energy, **216,** 115 (2002).
[2] R. de Ruiter, C. Semprebon, M. van Gorcum, M.H.G. Duits, M. Brinkmann, and F. Mugele. *Stability Limits of Capillary Bridges: How Contact Angle Hysteresis Affects Morphology Transitions of Liquid Microstructures*, Phys. Rev. Lett. **114**, 234501 (2015).
[3] D. J. C. M. 't Mannetje, C. U. Murade, D. van den Ende, and F. Mugele. *Electrically assisted drop sliding on inclined planes*, Appl. Phys. Lett. **98**, 014102 (2011).
[4] F. Li and F. Mugele, *How to make sticky surfaces slippery: Contact angle hysteresis in electrowetting with alternating voltage*, Appl. Phys. Lett. **92**, 244108 (2008).

Experiments on the breakup of drop-impact crowns by Marangoni holes

Abdulrahman B. Aljedaani[1], A. Jetly[1], S.T. Thoroddsen[1]

[1]Mechanical Engineering, Division of Physical Sciences and Engineering,
King Abdullah University of Science and Technology (KAUST), Thuwal, Saudi Arabia

E-mail: Abdulrahman.aljedaani@KAUST.edu.sa

We study the breakup of a high-viscosity drop impacting on a thin film of low-viscosity liquid, which also has lower surface tension, σ. The thin film effectively produces free slip of the drop liquid along the solid and makes it deform into a prominent crown shape, shown in Figure 1. The breakup of this crown is fundamentally different if the surface tension of the film is lower than that of the drop. Previous experiments [1,2] proposed that this crown-breakup resulted from a spray of fine droplets ejected from the thin film. These droplets hit the interior of the crown, forming spots with lower surface tension, driving the formation of a myriad of holes. Figure 1 compares the breakup when the surface tension of the film is lower in part (a) vs the film having the same surface tension as the drop in (b). The two sequences are qualitatively different, with multiple holes causing the breakup on the left vs edge- breakup on the right.

Herein we use high-speed video techniques to test the validity of this break-up mechanism using close-up imaging to identify individual spray droplets. The video footages show how the fine droplets emerge from the breakup of the thin sheet of film liquid. Subsequently these spray droplets hit the crown and promote the hole formation. The holes form in two steps. First, the divergence in the surface stress thins the crown locally; secondly, this thinner section ruptures. This is shown in the close-up top view in Figure 2, where individual drops are tracked and shown to form the holes. We therefore conclude that the breakup is indeed due to Marangoni instability.

To further investigate this, we have varied three main parameters: The viscosity of the drop μ_d, the surface tension of the thin film and thereby the strength of $\Delta\sigma$ and finally the thickness of the film on the solid surface δ. Throughout the impact experiments, the release height is kept constant at H = 5.4 m, leading to an impact velocity of U = 9.5 m/s on the thin liquid film. The drop falls through a 4 m long tube to minimize sideways drift owing to air motions during the long free-fall. The first images in the sequences in Figure 1, show that the drops are flattened by air-resistance, making the bottom radius of curvature much larger than their equivalent spherical shape, which would give $D \sim 5$ mm. We vary $\Delta\sigma$ from 0 to 42 dyn/cm by changing the ratio of isopropanol and water in the mixture used in the thin film which is deposited on the solid. We also test different glycerin/water mixtures in the drop to change μ_d from 500 to 1200 cP. Results are also obtained by varying the thin film layer thickness from 1 to 2 mm.

We use the close-up images, similar to those in Figure 2, to measure the growth-rate of the holes, for both the thinning and the rupture stages. We find a wide range for the growth-rates of the holes, with velocities in the range 1 – 5 m/s.

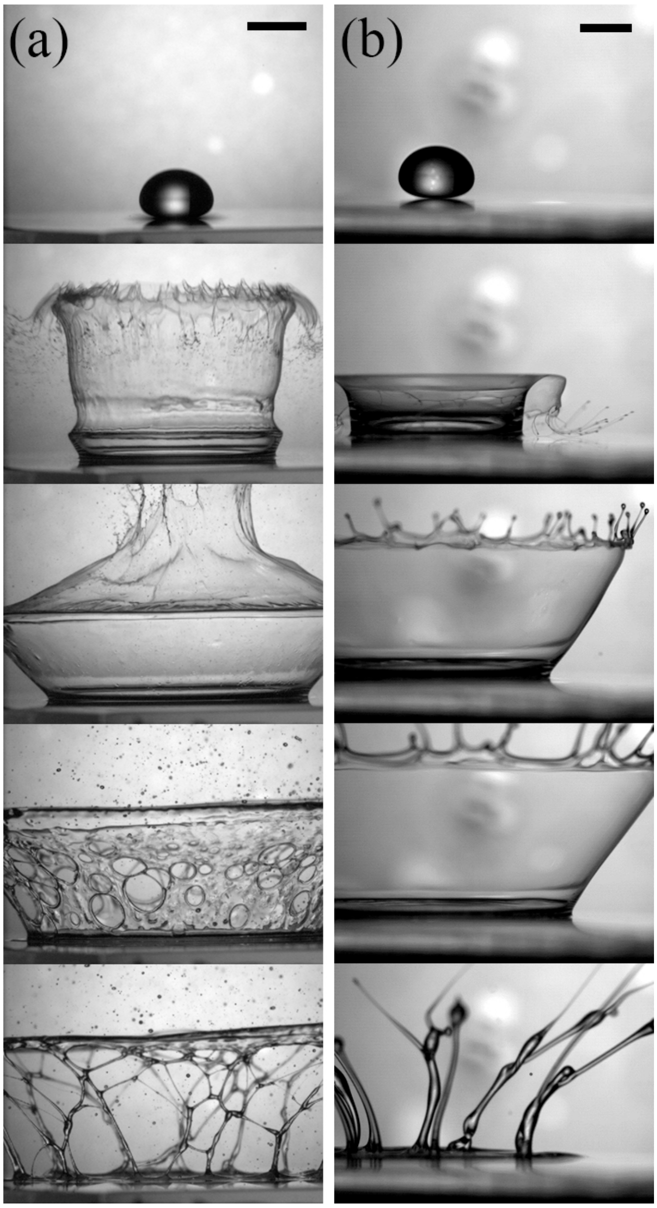

FIGURE 1. Comparison between crown breakup (a) when there is a difference in surface tension between the impact drop and the thin liquid film and (b) when the surface tension in the drop and thin film is the same. The scale bars are 5 mm long. The drops are both glycerin, but the film in (a) is isopropanol and in (b) is glycerin.

This depends on various parameters, such as the thickness of the crown sheets, which is difficult to ascertain in our measurements. This crown thickness depends on the trajectory and shape evolution of the crown, which in turn depends primarily on the drop viscosity and the film thickness on the solid.

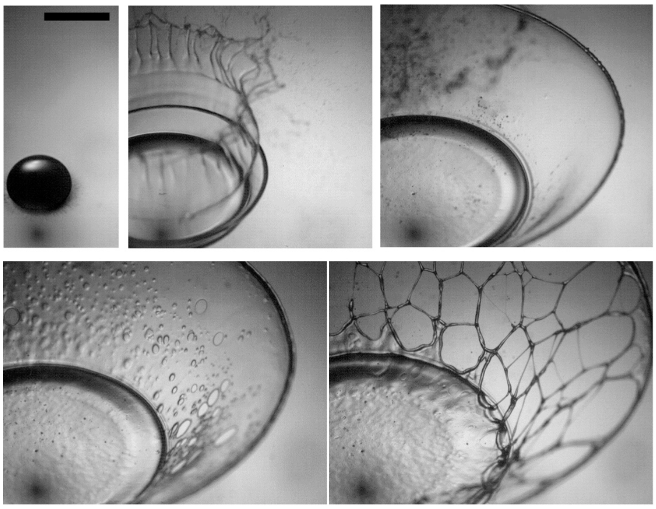

FIGURE 2. Top view sequence of a 500 cp glycerin/water drop impacting on a thin film of isopropanol, with a strong surface tension difference. The scale bar is 5 mm long.

In Figure 3 we have colored the drop with blue dye, to show clearly where the drop liquid has formed the crown and the thin sheet above it must have originated from the film on the substrate. The isopropanol film rises far above the drop crown and is pulled towards the centerline by the air-flow. Once the sheet ruptures, this air-flow also projects the fine spray droplets into the crown to hit the inside wall.

Acknowledgements. This research was funded by King Abdullah University of Science and Technology (KAUST).

References

[1] S. T. Thoroddsen, T. G. Etoh and K. Takehara, Crown breakup by Marangoni instability. *J. Fluid Mech.,* **557**, 63-72 (2006).
[2] S. T. Thoroddsen, T. G. Etoh and K. Takehara, Crown breakup by a thousand holes. *Phys. Fluids,* **18**, 091110 (2006).

FIGURE 3. The impact of a glycerin drop which has been colored with blue food dye. The thin sheet of isopropanol has risen above it and is starting to rupture. The scale bar is 5 mm long.

EVAPORATION OF LIQUID DROPLETS ON FLAT AND CURVED SOLID SUBSTRATES

Amirhossein Amini[1], G. M. Homsy[1]

[1]Department of Mechanical Engineering, University of Washington, Seattle, WA, USA

E-mail: aminia@uw.edu

We study the evaporation of a 2D symmetric, incompressible, Newtonian liquid droplet on both flat and curved heated substrates. We deploy the one-sided model [1] which, together with the lubrication approximation, results in an evolution equation for the local height of the droplet. Without making any pre-assumption for the shape of the drop, we formulate the problem for the two modes of evaporation: (i) pinned contact line and (ii) moving contact line with fixed contact angle. For each evaporation mode, we solve the problem numerically for both flat and curved solid substrates.

We first analyze the evolution equation for the case of flat solid substrates. For the pinned contact line case, we observe that after a time interval the contact angle, i.e. the angle between the solid and the interface at the contact line, dynamics become nonlinear and, interestingly, the local contact angle goes to zero in advance of total evaporation of the drop, which may signal depinning. For the moving contact line case, in which the singularity at the contact line is treated by a numerical slip model, we find that the droplet nearly keeps its initial circular shape and that the contact line recedes with constant speed.

We then analyze the problem for various periodic and quasi-periodic substrate profiles. For the case of a pinned contact line, we find the results to be very similar to the flat case. For the case of a moving contact line, we study the dynamics of the contact line and the apparent contact angle, i.e. the angle that the liquid appears to make with the solid surface when viewed at such a coarse resolution that the substrate appears flat (the angle between the horizon and the interface at the contact line). We find that the overall evaporation is faster compared to the flat substrates and the contact line exhibits an “apparent stick-slip” [2, 3] behavior, wherein it spends considerable time moving very slowly, giving the appearance of being pinned, followed by a shorter, high-speed region in which the speed of the contact line shows a spike.

For the simplest case of a periodic substrate, we find that the apparent contact angle is periodic in time. For doubly periodic substrates, we find that the apparent contact angle is again periodic and that the problem exhibits a phase-locking behavior. For multi-mode quasi-periodic substrates, we find the contact line behavior to be temporally complex and not only limited to an approximately step-like motion.

References

[1] Burelbach, J. P., Bankoff, S. G., & Davis, S. H. (1988). Nonlinear stability of evaporating/condensing liquid films. *Journal of Fluid Mechanics*, *195*, 463-494.
[2] Savva, N., & Kalliadasis, S. (2009). Two-dimensional droplet spreading over topographical substrates. *Physics of Fluids*, *21*(9), 092102.
[3] Espín, L., & Kumar, S. (2015). Droplet spreading and absorption on rough, permeable substrates. *Journal of Fluid Mechanics*, *784*, 465-486.

Reduced Symmetry of Impacting Water Droplets via Surface Patterning

Matheu Broom[1], Geoff R. Willmott[1,2,3]

[1] Department of Physics, The University of Auckland, New Zealand
[2] School of Chemical Sciences, The University of Auckland, New Zealand
[3] The MacDiarmid Institute for Advanced Materials and Nanotechnology

E-mail: m.broom@auckland.ac.nz

Superhydrophobicity, or extreme water repellency, is a subject that has been studied for nearly a century. Alongside the chemical nature of a material, surface roughness plays an important role in achieving superhydrophobicity. The role of surface texture was famously explored by Cassie-Baxter and Wenzel over 70 years ago [1, 2]. However, only recently has the role of roughness in superhydrophobicity been studied dynamically [3]. Given the advancements in high speed cameras, a wide range of dynamics can now be resolved. Understanding the dynamics of superhydrophobic wetting is important because the use of superhydrophobic materials in applications which control and repel water often relies on dynamic effects.

One key discovery in this field was the ability to produce asymmetries in the spreading rim of an impacting droplet. Liquid droplets impacting hard smooth surfaces at low Weber numbers tend to form symmetric (circular) spreading patterns. However on pillar array surfaces, ‘fingers’ can be formed in the outer spreading profile of the droplet (Fig. 1). Recent research suggests that the impacting droplet expels the underlying air held within the microstructured surface. This air flow follows preferred paths which could explain the direction of finger formation, usually on-axis relative to the surface pattern [4, 5]. We are interested in studying this ‘finger’ formation and the effect the surface array geometry has on the preferred direction.

This presentation will discuss a systematic study of droplet impacts on micropillar array patterns. Pillar designs consist of 20 μm diameter circular posts, spaced in regular square arrays with pitches ranging from 40 μm to 100 μm. With the aid of high speed video and video processing techniques, the dynamics of surface wetting are studied. Key features that we are studying include finger formation, jetting, bubble entrapment, asymmetric spreading and surface impregnation. Finger formation only occours above a critical Weber number. Another interesting thing to note is the central bubble region (Fig. 1).

Optically transparent polydimethylsiloxane (PDMS) surfaces are created via soft lithography. A Photron Fastcam SA5 is used in conjunction with an optical beam splitter to record droplet spread in plane. A Photron AX50 is sychronized to record droplet spread in side profile. Droplets are produced from a custom made 3D printed needle alignment system and illuminated via shadowgraph techniques. Custom Matlab software is used to perform background subtraction, binarizing, noise reduction and finally region properties. Using this method common variables can be calculated quickly, such as droplet diameter, velocity, and maximum spread.

Use of image stitching of microscope images and optical profilometry ensure samples are of high quality. Using image processing we can identify all of the objects on the surface. A bad sample is noted to have peaks above (bent pillar) and below (missing pillar) the expected pillar area (Fig. 2).

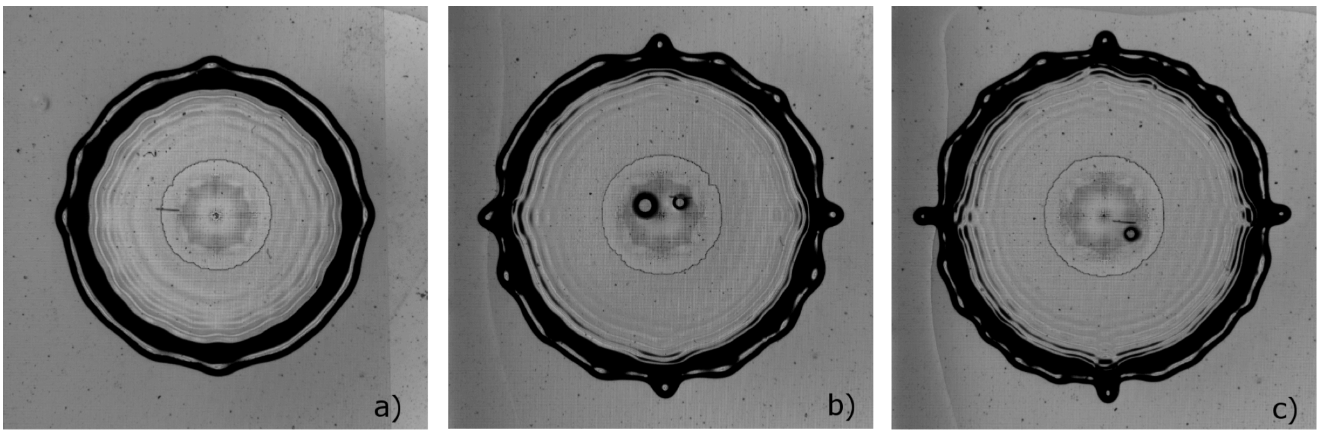

Figure 1. Images of droplet at maximum spread from impact experiments on a surface consisting of 20 μm circular pillars, pitch 40 μm and height 15 μm. The droplet diameter prior to impact is 2.8 mm. a) Weber number 100, slight protrusions from outer rim. b) Weber number 116, protrusions from outer rim begin to reach criteria for fingers. c) Weber number 132, clear fingers are seen along axis of underlying array.

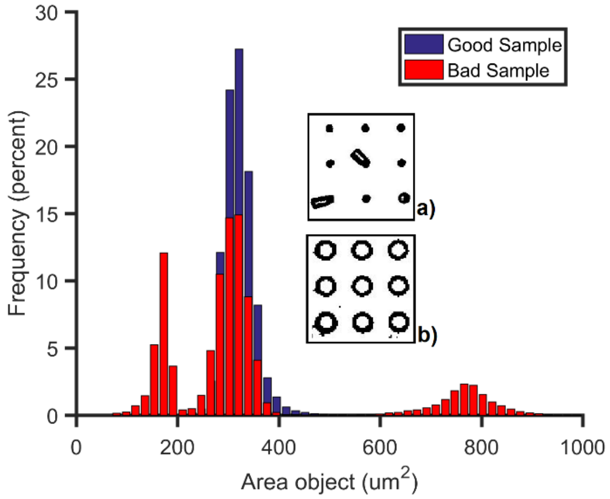

Figure 2. Frequency histogram of objects detected on the surface of a pillared sample. A bad sample, denoted in red, shows objects above and below the size of pillars, identifying missing and broken pillars as shown in inset a). Blue denotes a good sample, in which only objects of the expected size of the pillars are found, i.e. no broken or bent pillars, inset b).

Shown in Fig. 3 is a plot of the finger factor of identified fingers against their angular diverence from the underlaying array axis. The finger factor is a dimentionless number showing the ratio of the length of the finger extending from the rim to its width. A criteria for a finger is that the finger factor is greater then 1, so that the protusion extends from the rim a distance greater then its width.

As the Weber number increases, the finger factor increases as expected due to the increase in the maximum spread. However, contrary to previous studies, our results show that under certain conditions finger formation is preferred at a 45° angle to the principal axes of the array [4, 5].

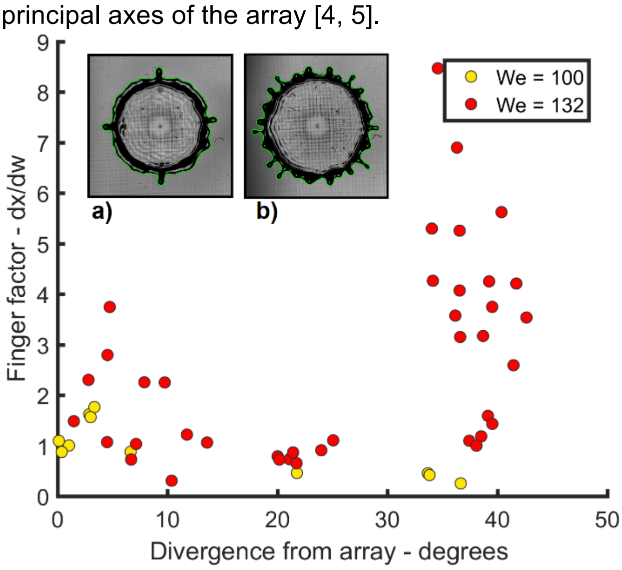

Figure 3. Finger factor vs divergence from array axis obtained from maximum spread images (insets) on a surface with 20 μm circular pillars, 60 μm pitch and 15 μm height. Yellow denotes a droplet with Weber number 100, where prominent fingers form along the axis i.e. at 0° to the array. Red denotes a droplet with Weber number 132, where all protrusions from the rim have a higher finger factor, i.e. thin and long. The most prominent fingers are concentrated at an angle to the array.

Ongoing analysis of the correlation between the array geometry and direction of fingers should lead to a library of design parameters for specific outcomes. Additionally, we can extract time evolution data to study to formation of these fingers in a dynamic way.

The topic of droplets impacting micropattern surfaces is extensive and we have many different avenues of future research. Previous studies have show the formation of jets, formed within the first few milliseconds of impact. It is believed that these jets could nucleate the formation of fingers at maximum spread. We are also interested in the dynamics of droplets retracting on these surfaces. Upon retraction the outer rim can become pinned to the surface pattern. As the retraction phase can greatly increase the contact time of a drop this investigation is key for optimum functional materials.

References

[1] Wenzel, R.N., Resistance of solid surfaces to wetting by water. Industrial & Engineering Chemistry, 1936. 28(8): p. 988-994.
[2] Cassie, A.B.D. and S. Baxter, Wettability of porous surfaces. Transactions of the Faraday Society, 1944. 40(0): p. 546-551.
[3] Khojasteh, D., et al., Droplet impact on superhydrophobic surfaces: A review of recent developments. Journal of Industrial and Engineering Chemistry, 2016, vol. 42, pp. 1-14, 10/25/ 2016.
[4] Robson, S. and G.R. Willmott, Asymmetries in the spread of drops impacting on hydrophobic micropillar arrays. Soft Matter, 2016. 12(21): p. 4853-4865.
[5] Tsai, P.C., et al., Microscopic structure influencing macroscopic splash at high Weber number. Soft Matter, 2011. 7(24): p. 11325-11333.

STABILIZATION OF DROPLETS BY NANOPARTICLES IN MICROFLUIDICS

Laura Chacon[1], Jean-Christophe Baret[1,2]

[1]CNRS, Univ. Bordeaux, CRPP, UPR 841, 33600 Pessac, France.
[2] Max Plank Institute for Dynamics and Self-organization,m Am Fassberg 17, D-37077 Goettingen, Germany

E-mail: jean-christophe.baret@u-bordeaux.fr

Pickering emulsions are liquid dispersions stabilized by solid particles. They have seen a surge in interest during the past two decades, owing to their enhanced stability against coalescence over surfactant-stabilized emulsions and due to a broad range of emerging applications [1], from the controlled release of substances for drug delivery [2,3], to the templating of new materials [4].
Recently, fluorinated Pickering emulsions have been combined to droplet-based microfluidics [5,6,7], which is a powerful technology for the miniaturization and automation of biochemical assays at high-throughput [5,6,8]. This technology allows the production and controlled manipulation of micron-size droplets carried by an immiscible phase within microchannels. The interface of droplets is stabilized by a surface-active agent, letting each isolated droplet to be considered as an independent microreactor.
To date, three main advantages make fluorinated Pickering emulsions attractive over surfactant-stabilized emulsions within droplet-based microfluidics: First, they have the property of reducing transport processes of small molecules between droplets [9]; Second, they provide a rigid layer at the interface to which adherent cells can bind [10]; Third, additional functional groups grafted at the nanoparticle interface provide functions such as molecular recognition increasing interface functionalities [10,11].
However, Pickering emulsions also introduce new challenges not encountered before with surfactant stabilized systems. For example, the non-specific adsorption of enzymes on the nanoparticle surface leads to a loss of enzymatic activity. PEG-functionalized nanoparticles have been recently proposed as a solution to this issue [12].
Another limiting factor of solid-stabilized emulsions is the adsorption dynamics of particles to the interface: Significantly higher timescales (~0.6 s) are required to stabilized droplets against coalescence [13], in contrast to surfactant stabilized emulsions (~0.035 s) [14]; translating into smaller throughputs for particle-stabilized droplets assays and thus, limiting a main advantage of droplet-based microfluidics technology.
The required stabilization time can be reduced by increasing the concentration of particles in the continuous phase to an excess, that is, in an amount that is significantly larger than it is required for the complete coverage and stabilization of the droplets. However, this leads to the undesired loss of particles, and it can also affect the flow properties of the emulsion through a thickening effect [15].
Nie *et al*, proposed an "Inside-Out" approach for Pickering emulsions fabrication: the particles are introduced in the droplets phase allowing to minimize the waste of particles [16]. However, this approach is not suitable for most of droplet-based microfluidic applications where the biochemical material inside droplets needs to be isolated. Furthermore, fluorinated silica nanoparticles cannot be effectively dispersed in the aqueous phase, which limits the application of the "inside-out" approach for this system.
In this study, we proposed a solid-stabilized droplet production method which plays with the confinement conditions that are manipulated in a microfluidic chip. The aim is to promote a faster particle adsorption to the interface and to minimize the waste of particles.
As shown in figure 1, the results between methods are compared by measuring stability after coalescence through stochastic collisions in coalescence chambers as described previously by Baret *et al* [14].

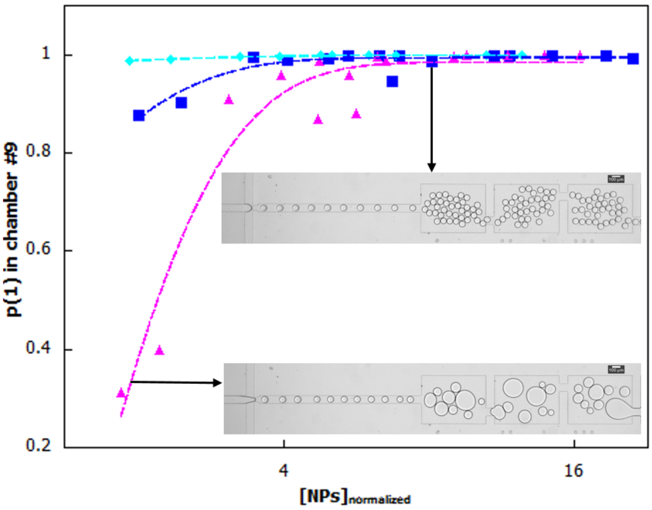

Figure 1. Droplets stability as a function of normalized particle concentration for three droplet-production methods: (- -◆- -) Confinement method #1 (- -■- -) Confinement method #2 (- -▲- -) Standard droplet production. (time scale ~0.015 s)

The stability parameter (*p(1)*), which is the proportion of unfused droplets over the total number of droplets is studied as a function of the particles concentration in the continuous phase normalized by the minimum number of particles required to form one hexagonally close packed layer of particles at the droplet interface.
Our results show that particle adsorption is significantly improved by confinement effects and provide an additional insight in the understanding of adsorption dynamics of particles to the aqueous/oil interface.

Acknowledgements. This project has received funding from European Research Council (ERC) Seventh Framework Programme (2007-2013) ERC Grant Agreement 306385-SOFt Interfaces and from the European Research Council (ERC) under the European Union's Horizon 2020 research and innovation programme (grant agreement No 727480), from the 'Région Aquitaine' and from the French Government 'Investments for the Future' Programme, University of Bordeaux Initiative of Excellence (IDEX Bordeaux) (Reference Agence Nationale de la Recherche (ANR)-10-IDEX-03-02).

References

[1] Ji Wu and Guang-Hui Ma. Recent studies of pickering emulsions: Particles make the difference. Small, 12(34):4633, 2016.
[2] Marie Wahlgren, Johan Engblom, Malin Sjoo, and Marilyn Rayner. The use of micro-and nanoparticles in the stabilisation of pickering-type emulsions for topical delivery. Current pharmaceutical biotechnology, 14(15):1222–1234, mar 2014.
[3] Marion Baillot, Ahmed Bentaleb, Eric Laurichesse, Véronique Schmitt, and Rénal Backov. Triggering the mechanical release of mineralized pickering emulsion-based capsules Langmuir, 32(16):3880–3889, 2016.
[4] Stéphane Arditty, Véronique Schmitt, Joanna Giermanska-Kahn, and Fernando Leal-Calderon. Materials based on solid-stabilized emulsions. Journal of Colloid and Interface Science, 275(2):659–664, jul 2004.
[5] Mira T. Guo, Assaf Rotem, John A. Heyman, and David A. Weitz. Droplet microfluidics for high-throughput biological assays. Lab on a Chip, 12:2146–2155, 2012.
[6] Ashleigh B Theberge, Fabienne Courtois, Yolanda Schaerli, Martin Fischlechner, Chris Abell, Florian Hollfelder, and Wilhelm T S Huck. Microdroplets in microfluidics: An evolving platform for discoveries in chemistry and biology. Angewandte Chemie International Edition, 49:5846– 5868, jun 2010.
[7] Philipp Gruner, Birte Riechers, Laura Andreina Chacon Orellana, Quentin Brosseau, Florine Maes, Thomas Beneyton, Deniz Pekin, and Jean-Christophe Baret. Stabilisers for water-influorinated-oil dispersions: Key properties for microfluidic applications. Current Opinion in Colloid & Interface Science, 20(3):183–191, 2015.
[8] J. J. Agresti, E. Antipov, A. R. Abate, K. Ahn, A. C. Rowat, J.-C. Baret, M. Marquez, A. M. Klibanov, A. D. Griffiths, and D. A. Weitz. Ultrahigh-throughput screening in dropbased microfluidics for directed evolution. Proceedings of the National Academy of Sciences, 107(9):4004–4009, feb 2010.
[9] Ming Pan, Liat Rosenfeld, Minkyu Kim, Manqi Xu, Edith Lin, Ratmir Derda, and Sindy K Y Tang. Fluorinated pickering emulsions impede interfacial transport and form rigid interface for the growth of anchorage-dependent cells. ACS applied materials & interfaces, 6(23):21446–53, 2014.
[10] Ilia Platzman, Jan Willi Janiesch, and Joachim Pius Spatz. Synthesis of nanostructured and biofunctionalized water-in-oil droplets as tools for homing T cells. Journal of the American Chemical Society, 135(9):3339–3342, 2013.
[11] Ming Pan, Minkyu Kim, Lucas Blauch, and Sindy K. Y.Tang. Surface-functionalizable amphiphilic nanoparticles for pickering emulsions with designer fluidfluid interfaces. RSC Adv., 6(46):39926–39932, 2016.
[12] Ming Pan, Fengjiao Lyu, and Sindy K. Y. Tang. Fluorinated Pickering Emulsions with Nonadsorbing Interfaces for Droplet-based Enzymatic Assays. Analytical Chemistry, 87(15):7938–7943, 2015.
[13] Craig Priest, Mathew D. Reid and Catherine P. Whitby. Formation and stability of nanoparticle-stabilised oil-in-water emulsions in a microfluidic chip. Journal of Colloid and Interface Science, 363(1):301-306, 2011.
[14] Baret, J.-C., Kleinschmidt, F., El Harrak, A. and Griffiths, A. D. Kinetic Aspects of Emulsion Stabilization by Surfactants: A Microfluidic Analysis. Langmuir 25, 6088–6093 (2009).
[15] Yves Chevalier and Marie-Alexandrine Bolzinger. Emulsions stabilized with solid nanoparticles: Pickering emulsions. Colloids and Surfaces A: Physicochemical and Engineering Aspects, 439:23– 34, 2013.
[16] Zhihong Nie, Jai II Park, Wei Li, Stefan A. F. Bon, and Eugenia Kumacheva. An 'Inside-Out' Microfluidic Approach to Monodisperse Emulsions Stabilized by Solid Particles. Journal of the American Chemical Society, 130 (49), 16508-16509.

CORRELATION FOR SESSILE DROP EVAPORATION

Peter Kelly-Zion[1], Christopher Pursell[2], Greg Wassom[1], Brenton Mandelkorn[1], Chris Nkinthorn[1]

[1]Department of Engineering Science, Trinity University, San Antonio, TX, USA
[2] Department of Chemistry, Trinity University, San Antonio, TX, USA

E-mail: plkelly@trinity.edu

To better understand how the evaporation of sessile drops and small puddles is controlled by the vapor phase transport mechanisms of mass diffusion and buoyancy-induced (natural) convection, the evaporation rates of eight liquids evaporating under a broad range of ambient conditions were correlated with physical and geometrical properties. The correlation provides a simple equation involving conventional parameters for diffusive and convective transport and is applicable to conditions for which vapor transport limits the rate of evaporation. Examination of the correlation equation provides valuable insight into how the roles of diffusive and convective transport change with physical and geometrical parameters; and the correlation is much easier to implement than a computational model based on the coupled conservation equations of mass, energy, and momentum for the two phases. In addition, the correlation provides a simple method for predicting evaporation rates and thus can be a valuable tool to help validate complex computational models and to aid in the analyses of applications involving sessile drop evaporation.

The correlation fits evaporation rate measurements with an RMS relative error of 6%. The experimental conditions were designed in order to yield large variations in the rates of diffusive and naturally convective transport of the vapor. The experimental conditions contain a factor of 16.7 variation in liquid volatility as indicated by the equilibrium vapor pressures, a factor of 52.2 variation in mass diffusivities, a factor of 3,557 variation in the density difference ratios (the driving force for natural convection), and a factor of 22 variation in drop radii. In terms of the Rayleigh number, the correlation fits data covering a range from 3 to 125,000. As a result, the correlation is applicable to a very broad range of conditions.

There are two mathematical forms that have been commonly used to correlate natural convection-driven evaporation. Both forms were developed for the evaporation of water. One form relates the Sherwood number (*Sh*), which is a dimensionless mass transfer coefficient for evaporation, to the Rayleigh number (*Ra*), which generally represents the relative effects of buoyancy and viscosity. A comprehensive review of published *Sh-Ra* correlations was conducted by Bower and Saylor [1]. The second popular correlation form is the Dalton model. This model relates the evaporation rate to the product of a set of velocity-dependent coefficients and the difference in partial vapor pressures of the evaporating liquid at the drop surface and in the ambient air, and the inverse of the latent heat of evaporation. A review of Dalton-type correlations was conducted by Jodat et al. [2], and they noted the inability of the Dalton based correlations to account for changes in the vapor density difference. Consequently, they proposed a modified Dalton model for natural convection. As discussed in [3] the *Sh-Ra* and the Dalton correlations were applied to a large set of evaporation rate data of hydrocarbons evaporating in air. While neither correlation performed satisfactorily, the *Sh-Ra* correlation performed much better than the Dalton correlation. As a consequence, our efforts to develop a more comprehensive correlation involved expanding and modifying the *Sh-Ra* correlation.

The new correlation fits measurements of two series of experiments which were designed to control the relative effects of vapor phase diffusion and buoyancy-induced convection. In all of the experiments, the drop was contained on a flat aluminum substrate and the drop was pinned by surface tension to a confined area in order to maintain a constant, controlled size. In one set of experiments, the rates of evaporation into air of eight hydrocarbons were measured for a broad range of drop radius from 1 to 22 mm. (The large drops are more aptly described as puddles.) This set of experiments was conducted at atmospheric pressure and is referred to as the Radius/Component (R/C) experiments. A second set of experiments was conducted for which the drop was placed in a sealed enclosure, which enabled the pressure and the ambient gas surrounding the drop to be controlled. The evaporation rates of two hydrocarbons, hexane and methanol, evaporating into four different gases at pressures from 1 to 6 atmospheres were measured. The gases were selected to provide a broad range of diffusivities and of differences between the vapor and gas densities. This second set of experiments is referred to as the Pressure/Gas (P/G) experiments.

The correlation was applied only to cases for which the molecular weight of the evaporating component was greater than or equal to the molecular weight of the ambient gas, and thus the correlation applies only to downward-directed natural convection and not upward convection as occurs when the vapor is lighter than the ambient gas. All of the experiments were conducted at room temperature, 23°C, in order to avoid currents in the ambient gas due to thermally-induced natural convection.

To successfully correlate the evaporation rate data, it is important both to include the important physical and geometric parameters and to use a function that can approximate the measured data. The R/C data had been correlated previously using a modified form of the *Sh*-*Ra* relationship [3]. However, this correlation does not adequately predict the evaporation rates over the expanded range of the P/G data. As a consequence, we refined our basic premise regarding the general form of the correlation function. The fundamental ideas which guided our development of the correlation are:

- Whereas there are many complex details that influence evaporation behavior, the net effect on the evaporation rate of a sessile drop can be predicted based on the drop radius, a small number of thermophysical properties, and the ambient temperature and pressure.
    - For conditions for which thermal energy transfer does not limit the evaporation process, the evaporation rate of a pure sessile drop is controlled by the vapor transport mechanisms of convection and diffusion.
- Convection and diffusion are coupled.
    - Diffusion spreads out the vapor distribution and thereby reduces the density difference ratio, which is the impetus for buoyancy-induced convection.
    - The term representing the strength of convection should be moderated by parameters for diffusion and vice-versa.
- The strength of convection is indicated by the Rayleigh number.
    - As the Rayleigh number tends to zero, suggesting a lack of convection, the correlation should reduce to a purely diffusive evaporation rate.
    - We allow the Rayleigh number to be split into its dimensionless components and allow each dimensionless component to influence the correlation independently. Thus while $Ra = GrPr = \left[\frac{(\rho_m - \rho_a)}{\rho_a}\right]\left[\frac{gR^3}{\nu^2}\right]\left[\frac{\nu}{\alpha}\right]$, each parameter in brackets is allowed to influence the correlation independently.
- To keep the correlation function simple, the diffusion-limited evaporation rate is modeled using the Weber's disk equation, which is the solution to the steady-state Laplace equation for a circular disk [4].
- The evaporation rate is equal to the sum of the diffusive and the convective vapor transports and so the correlation should be a sum of two terms, one which represents convection-influenced diffusion and the other which represents diffusion-influenced convection.

The effectiveness of the correlation is demonstrated by Fig. 1, which compares the results of the correlation to the Sherwood numbers based on the measured evaporation rates. The uncertainty in the measured values are represented by error bars. If the correlation perfectly fit the measured data, all of the points would fall on the dotted line. With a few exceptions the data do fall within the length of an error bar of the line.

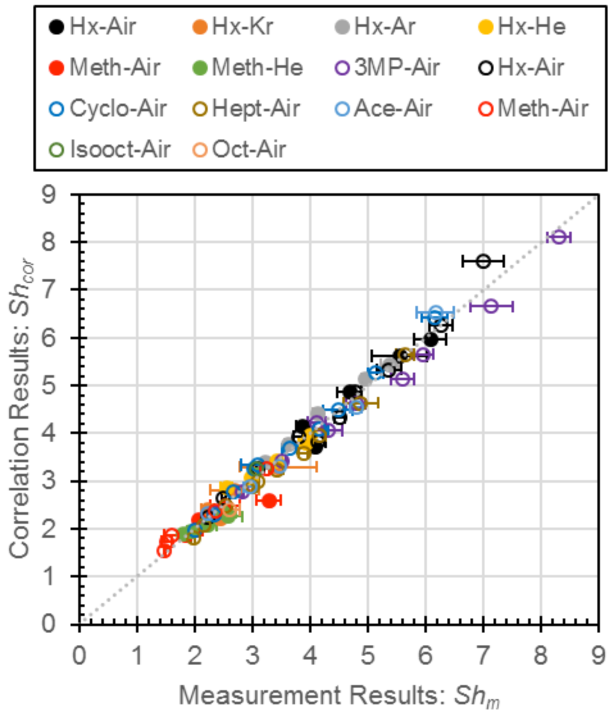

Figure 1. Plot comparing the dimensionless evaporation rates computed by the correlation, Sh_{cor}, versus the dimensionless measured evaporation rates, Sh_m. The solid symbols are data from the P/G experiments and the open symbols are data from the R/C experiments.

For low *Ra* values, the correlation suggests that evaporation is dominated by diffusion, as expected. As *Ra* increases, the correlation suggests that diffusive and convective transport contribute approximately equally to the overall evaporation rate.

Acknowledgements. Acknowledgement is made to the Donors of the American Chemical Society Petroleum Research Fund for support of this research.

References

[1] S.M. Bower, J.R. Saylor, A study of the Sherwood-Rayleigh relation for water undergoing natural convection-driven evaporation, Int J Heat Mass Transfer. (2009) **52**, 3055-3063.
[2] A. Jodat, M. Moghiman, M. Anbarsooz, Experimental comparison of the ability of Dalton based and similarity theory correlations to predict water evaporation rate in different convection regimes, Heat Mass Transfer. (2012) **48**, 1397-1406.
[3] P.L. Kelly-Zion, J. Batra, C.J. Pursell, Correlation for the convective and diffusive evaporation of a sessile drop. Int. J. Heat Mass Transfer. (2013) **64**, 278-285.
[4] J. Crank, The Mathematics of Diffusion, 2nd ed., Oxford University Press, New York, 1975.

SPREADING DYNAMICS OF EVAPORTING AND PERFECTLY WETTING LIQUIDS

S Dehaeck[1], A Y Rednikov[1], D Seveno[2], J De Coninck[3], P Colinet[1]

[1] TIPs (Transfers, Interfaces and Processes), Université Libre de Bruxelles,CP 165/67, Brussels, Belgium
[2] Department of Materials Engineering, KU Leuven, Heverlee, Belgium
[3] Laboratory of Surface and Interfacial Physics, Université de Mons, Mons, Belgium

E-mail: sam.dehaeck@ulb.ac.be

When a drop of liquid first contacts a solid substrate, the theoretical initial contact angle is 180° with the contact region being a single point. In most practical conditions, this is however not the equilibrium situation. What typically follows is an expansion of the contact zone and a lowering of the contact angle. As the contact angle reaches the static one defined by the evaporation-induced (for volatile liquids as here) and Young's contributions, the spreading dynamics slows down, reaching it only asymptotically. In the volatile case, evaporation will eventually lead to a recession of the contact line, during which the contact angle remains roughly constant.

The initial expansion stage is known as spreading and two major theories have been developed in the past to predict the contact line velocity and contact angle evolution over time: Hydrodynamic Theory (HT) (e.g. [1]) and Molecular-Kinetic Theory (MKT) (e.g. [2]). What both theories fundamentally differ upon is how the local contact angle is modified when it is in motion, i.e. the dependency of contact angle on contact line velocity. One of the goals here is to test both models on a low viscosity (0.7cSt), low surface tension liquid (16.2 mN/m) such as 3M™ Novec™ HFE-7500.

The experiments consist in gently depositing a drop of HFE-7500 on a clean glass wafer and tracking the contact line using Mach-Zehnder interferometry. The resulting images are analyzed with the algorithms detailed in [3, 4]. From these, we extract the drop height profiles over time and in particular the contact angle and location at all points of the three-phase line. From this location, an estimate for the contact line velocity is obtained. We need to stress here that both measurements are fully local, no global fitting of the perimeter with a circle nor of the height profile with a parabola was performed. As it was shown in [7], Marangoni effects can give rise to appreciable local curvatures near the contact line, and hence introduce significant errors in contact angle measurements when extracted from parabolic fittings. In the present context, such large local curvatures are deemed to occur due to the presence of a Cox-Voinov zone, with a logarithmic increase of the film slope, although the role of the Marangoni effect cannot be fully excluded either. Note that, due to the methodology employed for the interferometric image analysis, the measured contact angle is some kind of average over a small region near the contact line. The size of this region has not been fully quantified yet but is here expected to be of the order of some tens of microns.

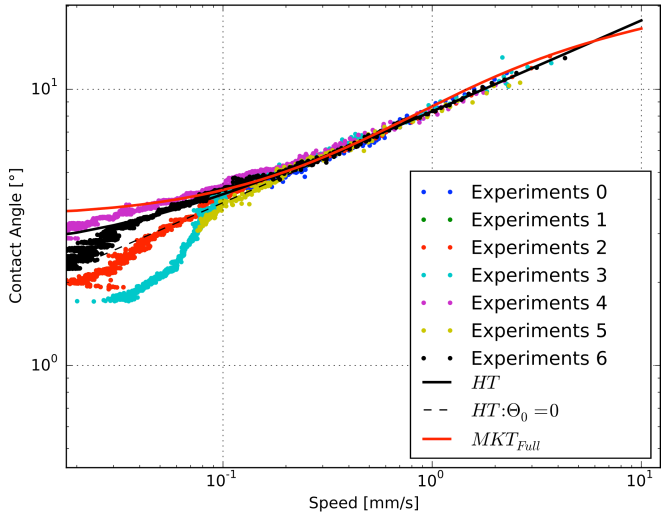

Figure 1: Contact angle versus contact line speed for a drop of HFE-7500 spreading on a glass substrate

In Figure 1, this measured contact angle is shown versus the contact line speed for different experiments, together with the fits for both theories. First, we notice that for speeds below 0.1mm/s a kind of transition behavior between the fast-spreading stage and the evaporation stage occurs. In this intermediate stage, the drop becomes non-axisymmetric leading to large discrepancies in the data. In the present study we discard this part and focus on the fast-spreading stage, for which we notice that all data collapse nicely and can be fitted with both theories equally well, although

HT seems to catch the large speed behavior better. Two fits are shown for HT, one with the static angle Θ_0 equal to zero and one where it was fitted to the data (for speeds above 0.1mm/s) resulting in Θ_0 = 2.5°. For MKT, the full formulation was applied and this yielded the best results for Θ_0 = 3.5°. This suggests that the evaporation-induced angle, which is indeed of this order ([7]), can be used as a replacement for the Young's one in the present context. This has already been shown to be the case for the Gibbs' criterion for pinning in [6]. Nevertheless, as the precision on the fitted static angles is quite small due to the large speeds in the fitted region, a fit with a zero contact angle is well within the uncertainty.

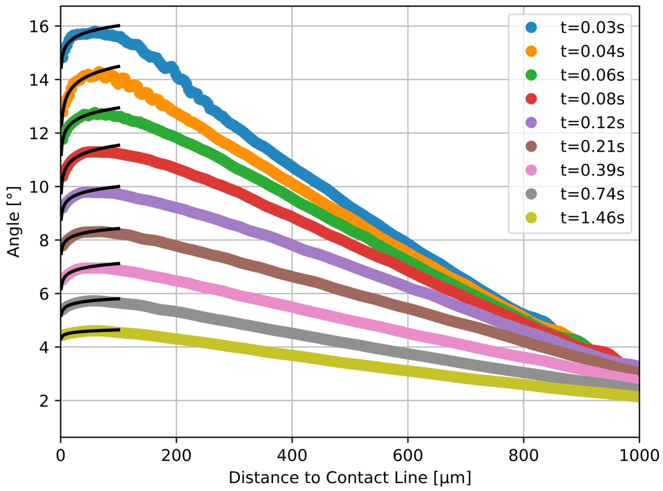

Figure 2: Local angle versus distance to the contact line at different times after deposition.

In Figure 2, a close-up of the local slope profile is shown versus the distance to the contact line. This profile clearly deviates from the classical static profile where the maximum angle would be obtained at the contact line itself. Here, the maximal angle is clearly seen at a distance of more or less 60µm from the contact line. This profile is strongly reminiscent of the profiles measured by [5], which can perhaps be associated to viscous bending of the droplet shape. Preliminary fits of these profiles with the HT law: $\Theta^3 = a \ln(x) + b$, yield the full lines in the figure. As can be seen, the correspondence is rather satisfactory. To the best of our knowledge, the evaporation channel has never been combined to MKT to describe droplet spreading. In this respect, note that appropriate care must be taken when interpreting this kind of experiments, especially for liquids with low viscosity.

In the present contribution, the spreading dynamics of HFE-7500 was investigated. Both Molecular Kinetic Theory and Hydrodynamic Theory are able to predict rather well the contact angle relaxation in a range from 15° to 4°. Evidence suggests that the evaporation-induced angle can simply replace the Young's one in the adopted formulation, but this is not conclusive for the moment. We also measured the presence of a possible viscous bending zone close to the contact line, as is theoretically predicted by Hydrodynamic Theory. In the future, a more thorough theoretical analysis of the measured profile will be performed.

Acknowledgements. The authors gratefully acknowledge financial support from the EVAPORATION and HEAT TRANSFER projects funded by the European Space Agency and by the Belgian Science Policy Office PRODEX Programme, and from the Interuniversity Attraction Poles Programme (IAP 7/38 MicroMAST) initiated by the Belgian Science Policy Office. PC thankfully acknowledges financial support from the Fonds de la Recherche Scientifique - FNRS. This work was also performed under the umbrella of COST Action MP1106.

References

[1] D. Bonn, J. Eggers, J. Indekeu, J. Meunier, E. Rolley. Wetting and spreading. *Rev. Mod. Phys.* **81** (2009) 739–805.

[2] M.J. de Ruijter, J. De Coninck, G. Oshanin. Droplet spreading: partial wetting regime revisited. *Langmuir* **15** (1999) 2209–2216.

[3] S. Dehaeck, P. Colinet. Improving speed and precision of local frequency analysis using gaussian ridge interpolation for wavelet and windowed Fourier ridge algorithms. *Optics and Lasers in Engineering* **77** (2016) 54–63.

[4] S. Dehaeck, Y. Tsoumpas, P. Colinet. Analyzing closed-fringe images using two-dimensional Fan wavelets. *Applied Optics* **54** (2015) 2939–2952.

[5] L.H. Tanner. The spreading of silicone oil drops on horizontal surfaces. *J. Phys. D: Appl. Phys.* **12** (1979) 1473–1484.

[6] Y. Tsoumpas, S. Dehaeck, M. Galvagno, A. Rednikov, H. Ottevaere, U. Thiele, P. Colinet. Nonequilibrium Gibbs criterion for completely wetting volatile liquids. *Langmuir* **30** (2014) 11847–11852.

[7] Y. Tsoumpas, S. Dehaeck, A. Rednikov, P. Colinet. Effect of Marangoni flows on the shape of thin sessile droplets evaporating into air. *Langmuir* **31** (2015) 13334–13340.

DROPLETS OF MOLEN STEEL VS CORE MELT DROPLETS: AN ESTIMATE OF THEIR CONTRIBUTION TO STEAM EXPLOSION TRIGGERING IN NUCLEAR REACTORS

Leonid A. Dombrovsky

Joint Institute for High Temperatures, NCHMT, Krasnokazarmennaya 17 A, 111116 Moscow, Russia
E-mail: ldombr@yandex.ru

Relative contributions of molten steel and core melt droplets to heat transfer from the droplets to ambient water at typical regimes of the droplet cooling and solidification are considered on the basis of transient heat transfer models for single droplets.

It is shown for the first time that fine fragmentation of steel droplets overheated significantly with respect to the steel solidification temperature makes these droplets more dangerous for the steam explosion triggering, and this effect cannot be neglected in nuclear safety analysis.

On the contrary, the solid crust on the surface of core melt droplets is formed before the first pressure drop in the steam envelope. As a result, the probability of fragmentation of these droplets is relatively small and there is no increase in the overall heat transfer due to the expected large total surface area of fine particles. [1-4].

The predicted behavior of uranium dioxide droplets is confirmed by the published data of laboratory experiments [5, 6]. It is interesting that experiments with alumina droplets indicate possible explosion because of predominant solidification of the central part of these droplets. This unusual behavior of semi-transparent droplets is explained by the optical effect of total internal reflection of thermal radiation at the droplet surface [7, 8]. This phenomenon is not observed for opaque core melt droplets.

In the safety analysis of nuclear reactors, it is recommended to revise the existing theoretical and computational models of steam explosion, paying more attention to the role of fine fragmentation of steel droplets.

Acknowledgements.
The present study was supported by the Russian Foundation for Basic Research (Grant No. 16-08-00157-a). The author is also grateful to Professor Truc-Nam Dinh for useful discussions during the author's visiting appointments at the Royal Institute of Technology (KTH, Stockholm, Sweden).

References

[1] T. Okkonen, B.R. Sehgal, Influence of melt freezing characteristics on steam explosion energetic, *Proc. ASME/JSME 4th International Conference on Nuclear Engineering (ICONE-4)*, 1996, v. 1B, 923-934.
[2] L.A. Dombrovsky, An estimate of stability of large solidifying droplets in fuel–coolant interaction, *International Journal of Heat and Mass Transfer*, (2007) (19-20) 3832-3836.
[3] L.A. Dombrovsky, T.N. Dinh, The effect of thermal radiation on the solidification dynamics of metal oxide melt droplets, *Nuclear Engineering and Design*, (2008) 238 (6) 1421-1429.
[4] L.A. Dombrovsky, Approximate model for break-up of solidifying melt particles due to thermal stresses in surface crust layer, *International Journal of Heat and Mass Transfer*, (2009) 52 (3) 582-587.
[5] I. Huhtiniemi, D. Magallon, H. Hohmann, Results of recent KROTOS FCI tests: alumina versus corium melts, Nuclear Engineering and Design, (1999) 189 (1–3) 379-389.
[6] I. Huhtiniemi, D. Magallon, Insight into steam explosions with corium melts in KROTOS, *Nuclear Engineering and Design*, (2001) 204 (1-3) 391-400.
[7] L.A. Dombrovsky, Thermal radiation from nonisothermal spherical particles of a semitransparent material, *International Journal of Heat and Mass Transfer*, (2000) 43 (9) 1661-1672.
[8] L.A. Dombrovsky, D. Baillis, Thermal Radiation in Disperse Systems: An Engineering Approach, Begell House, New York, 2010.

Pattern Formation In Drying Droplets Of CTAB Micellar Nanofluid

Biswajit Roy*[1], Sanat Karmakar[1], Abhra Giri[2] and Sujata Tarafdar[1]
[1] Condensed Matter Physics Research Centre, Physics Department, Jadavpur University, Kolkata 700032, India.
[2] Physics Department, St. Xavier's College, Kolkata 700016, India

*Corresponding author
Email: Roy.Biswajit.99@gmail.com , Mob: 9932681295

Drying droplets have become very important for the production of various evaporation induced nanostructures. Cetyltrimethylammonium bromide (CTAB) is known to play a vital role for building nanostructures using evaporation driven self assembly of nanomaterials formed in CTAB matrix [1]. We monitor the pattern formation from the drying droplet formed by CTAB-water system (Fig (a)). CTAB in water form a variety of liquid crystalline phases starting from spherical micelles at low concentration to a lamellar phase at high concentration [2]. The structure of these liquid crystalline phases can be tuned by the addition of salts, such as NaBr. Characteristics of liquid crystalline phases can easily be inferred using a polarizing optical microscope (POM). In this work we prepare an aqueous solution of CTAB in the presence of NaBr salt. Pattern formation in drying droplets on CTAB solution deposited on a glass substrate is studied using polarizing microscopy. When water evaporates from the droplets, ring like pattern appears as seen in Fig. (b) And at the final stage of drying dendritic aggregates are observed. We analyze the POM images obtained from the drying droplet using a Jones Matrix calculation. Interestingly, simulated image matches very well with that obtained from POM.

Acknowledgements: We acknowledge DST Govt. of India for funding this research.

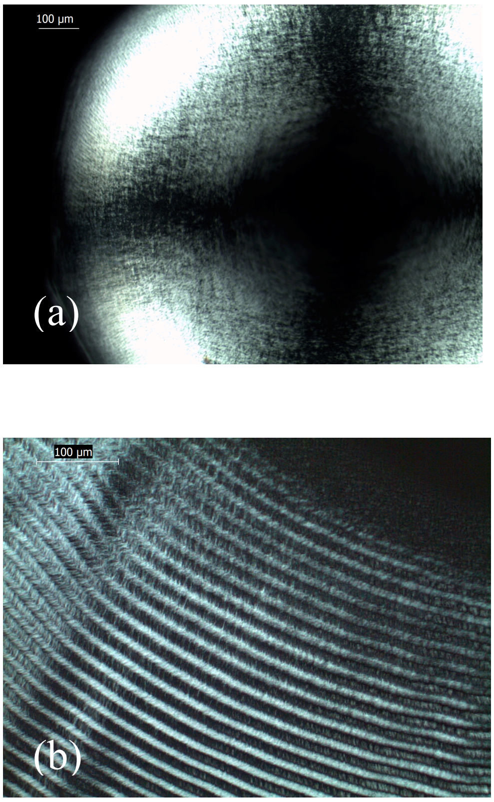

Fig(a) Drying droplet of CTAB+ Water(b) Drying droplet of CTAB+Water+NaBr

References

(1) Alfonso Martín, Carola Schopf, Andrea Pescaglini, Jin Jin Wang and Daniela Iacopino, Langmuir 2014, 30, 10206−10212.

(2) X. Auvray, C. Petipas,* R. Anthore,J. Phys. Chem. 1989, 93, 7458-7464.

ACCELERATION OF MACROSCOPIC CONTACT LINE OF A DROPLET SPREADING ON A SUBSTRATE INDUCED BY INTERACTION WITH A FIXED PARTICLE

Lizhong Mu[1,2], Daichi Kondo[3] , Motochika Inoue[3], Hiroki Himeda[4], Jumpei Fukushima[4]
Harunori N. Yoshikawa[5], Farzam Zoueshthiagh[6], Toshihiro Kaneko[1,7], Ichiro Ueno[1,7],

[1]Research Institute for Science and Technology, Tokyo University of Science, Japan
[2]School of Energy and Power Engineering, Dalian University of Technology, China.
[3]Division of Mechanical Engineering Graduate School of Science and Technology, Tokyo University of Science, Japan
, 2641 Yamazaki, Noda-shi, Chiba-ken 278-8510 Japan
[4]Department of Mechanical Engineering, Faculty of Science and Technology, Tokyo University of Science, Japan.
[5]Laboratoire J.-A. Dieudonné, UMR 7351 CNRS-Université de Nice Sofia Antipolis Parc Valrose, F-06108 Nice Cedex, France
[6]Universite de Lille 1-IEMN, CNRS8520, France
[7]Department of Mechanical Engineering, Faculty of Science and Technology, Tokyo University of Science, Japan

E-mail: muliz@dlut.edu.cn

Liquid propagation on structured surface has received broad interest due to the rich interfacial phenomena as well as wide applications in coating, cooling processes, dewetting, and self-cleaning. It is a broad consensus that the liquid droplet spreading on a smooth substrate obeys power-law time relation [1-3].

For a non-volatile liquid droplet spreading at macroscopic scales, the correlation between the dynamical contact angle θ_t and capillary number $Ca = \mu V_{CL}/\gamma$ was experimentally studied by Hoffman in a capillary, where μ is the viscosity of the liquid, V_{CL} is the velocity of the macroscopic contact line (M-CL), and γ is the surface tension [4]. Moreover, the spreading behavior of a droplet on a substrate with ultra-fine structures has also been presented. It has been reported that the obstacles within the solid surface can obviously pin the movement of the M-CL the initial stages of the spreading [5]. In another hand, a structured surface can enhance the droplet spreading [3, 6, 7]. In particularly, a uni-directional liquid propagation will be reduced by an asymmetric micro-structural surface [8-10]. However, there is few study which focused on the droplet spreading behavior induced by the interaction with a single micro obstacle on the substrate during the liquid propagation.

Here, the aim of this experimental study is to investigate the acceleration of the M-CL of a droplet spreading on a smooth substrate induced by interaction with a single particle.

In order to observe the motion of droplet spreading on the substrate, the interferometry was employed which was consisted of the laser (wavelength: 532 nm), spatial filter, collimator, polarizer, and a high-speed camera (Photron, Fastcam-Mini; resolution: 1028×728 pixels; frame rate: 250 frames per second) and an objective lens with 500× magnification. The test fluid is silicone oil with the kinematic viscosity of 2cSt, which volume $\Omega = 2.4 \pm 0.5$ μL. The perpendicular distance between the needle and the substrate was kept at 1.5 mm, and the horizontal distance between the needle tip and the particle was varied from 3.5 to 5.0 mm. Under these situation, Ca was smaller than 10^{-5}, and the particles are almost static. The process of cleaning the substrate was finished in a plasma cleaner (Harrick, PDC-32G) for 10 min.

Table 1 physical properties of particles used in this study.

		Geometry	Material	Size [μm]	Intrinsic contact angle
Regular shaped particle		Sphere	Gold nickel alloy coated acrylic particles	30, 40, 50	26 ± 5°
		Cylinder	SU-8 permanent epoxy negative photoresist	50± 5	19 ± 5°
		Triangle prism		50± 5	19 ± 5°
Irregular shaped particle		Irregular	Teflon	40± 10	40 ± 5°

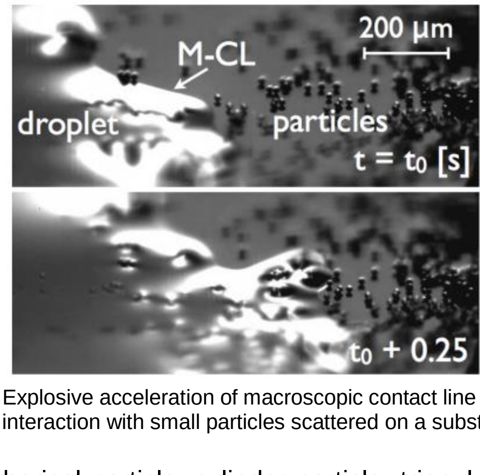

Figure 1 Explosive acceleration of macroscopic contact line of droplet via interaction with small particles scattered on a substrate

The spherical particle, cylinder particle, triangle prism, and irregular shaped particle were used in our experiments, which physical properties were shown in table 1. A typical example of interaction between the liquid and particles was illustrated in Figure1.

We found that: 1) At early stage of the droplet spreading, a droplet spreading on a smooth substrate obeying power law time dependence between the spreading radius and time with an inclination 1/10 which was described with Tanner's law, and then the inclination will changed into 1/8 prior to the interaction of the particle, which was reported by Lopez [2] and Cazabat and Stuart [3]. 2) When the M-CL makes contact with a single particle settled on the substrate, the movement of the M-CL near the particle is pinned. And then the M-CL is accelerated obviously. 3) After the interaction with particles, the M-CL's velocity is accelerated during a short time to attain the maximum V_{max}. In addition, the ratios of V_{max} to V_0 are around 10 ± 20%, where, velocity V_0, prior to the interaction of different particles.

In summary, for the silicone oil with the kinematic viscosity of 2cSt, we determined that the velocity of M-CL will be accelerated obviously by the interaction of the micro particle and the liquid. In one hand, for the fixed particles, the maximum of the velocity of M-CL was achieved is almost 10 times larger than the velocity prior to the interaction. In another hand, for the hydrophilic particles, the acceleration of M-CL was induced by regular cross-sectional particles and an irregular cross-sectional particles. This study provides new knowledge about the acceleration of the M-CL velocity of a droplet spreading on a smooth substrate induced by interaction with the particle and proposes a system to control the movement of the M-CL and droplet transportation using simple geometry without any energy input.

Acknowledgements. A part of this study was supported by the Tokyo University of Science (TUS) Fund for Strategic Research Areas. International collaboration is supported by Bilateral Joint Research Projects "SAKURA Program" by the Japan Society for the Promotion of Sciences (JSPS) and the Ministry of Foreign Affairs and International Development, France (MAEDI) for FY2015-2016. And thanks to Mr. Tetsuya Hibino, an ex-graduate student of TUS.

References

[1] L. H Tanner, The spreading of silicone oil drops on horizontal surfaces. Journal of Physics D: Applied Physics 12 (1979) 1473-1483.
[2] J. Lopez, C.A. Miller, E. Ruckenstein, Spreading kinetics of liquid drops on solids. Journal of Colloid and Interface Science 56 (1976) 460-468.
[3] A.M. Cazabat, M.C. Stuart, Dynamics of wetting: effects of surface roughness. The Journal of Physical Chemistry 90 (1986) 5845-5849.
[4] R.L. Hoffman, A study of the advancing interface. I. Interface shape in liquid-gas systems. Journal of colloid and interface science 50 (1975) 228-241.
[5] P. De Gennes, Wetting: statics and dynamics. Reviews of modern physics 57 (1985) 827-863.
[6] R. Xiao, N.E. Wang, Microscale liquid dynamics and the effect on macroscale propagation in pillar arrays. Langmuir 27 (2011) 10360-10364.
[7] R. Xiao, E. Ryan, E.N. Wang, Prediction and optimization of liquid propagatin in micropillar arrays. Langmuir 2010, 26, (19), 15070-15075.
[8] K. Chu, R. Xiao. E.N. Wang, Uni-directional liquid spreading on asymmetric nanostructured surfaces. Nature materials 9 (2010) 413-417.
[9] H. Chen, P. Zhang, L. Zhang, H. Liu, Y. Jiang, D. Zhang, Z. Han, L. Jiang, Continuous directional water transport on the peristome surface of Nepenthes alata. Nature 532 (2016) 85-89.
[10] X.M. Yang. Z.W. Zhong, E.Q. Li, Z.H. Wang, W. Xu. S.T. Thoroddsen, X.X. Zhang, Asymmetric liquid wetting and spreading on surfaces with slanted micro-pillar arrays. Soft Matter 9 (2013) 11113-11119.

Train of water droplets impacting porous stones: adsorption and film forming

Dominique Derome[1], Stefan Carl[1], Peter Vontobel[2], Jan Carmeliet[3]

[1]Laboratory for Multiscale Studies in Building Physics, Swiss Federal Laboratories for Materials Science and Technology, Empa, 8600 Dübendorf, Switzerland
[2]Laboratory for Neutron Scattering and Imaging, Paul Scherrer Institut (PSI), Villigen, Switzerland
[3]Chair of Building Physics, ETH Zürich, 8093 Zürich, Switzerland

E-mail: dominique.derome@empa.ch

Introduction

The phenomenon of drop impacting porous media is ubiquitous in nature and is associated with mechanisms found in various industrial applications. When a liquid droplet impacts a permeable surface, it spreads on the surface and is absorbed into the porous material due to capillary action. The spreading behavior of the impinging droplet on the surface is known to depend on the properties of the liquid, i.e. density, viscosity and surface tension, impact conditions such as drop size and impact velocity, and the surface wettability and roughness [1]. Also, absorption is governed both by the properties of the liquid and of the porous medium, i.e. porosity, pore size, wettability [2]. Once the deposited droplet is completely depleted from the surface, the liquid further redistributes within the porous medium due to capillary forces, while evaporation occurs at the surface [3]. In case of saturation of the porous medium, the remaining water lies at the surface in a pool, and, in the event of further impacts, a water film can build up. For a better understanding of the absorption process inside porous media, observing directly the liquid content redistribution in the porous medium is required. Absorption in porous media has been studied with several non-destructive techniques, namely X-ray, neutron and gamma-ray radiography, magnetic resonance imaging (MRI) and nuclear magnetic resonance, and destructive techniques.

In this study, we aim to capture the full absorption and film forming process of trains of impinging droplets on natural porous stones by using neutrons. Neutron radiography allows visualizing the moisture content distribution in porous stones. In track, we measure the mass of deposited water to validate the neutron measurements. The deposition and absorption process of trains of impinging droplets is continuously characterized during deposition, absorption, evaporation and redistribution, in terms of total mass in/above the stone and moisture distribution, in a time-resolved manner.

Methodology

Samples

Three stones with varying porosity and uptake characteristics are selected: two sandstones (Meule Bentheimer and one limestone (Savonnières), Figure 1. The porous stones are cut in cubes of 20 x 20 x 10 mm^3 for characterization and drop impact tests.

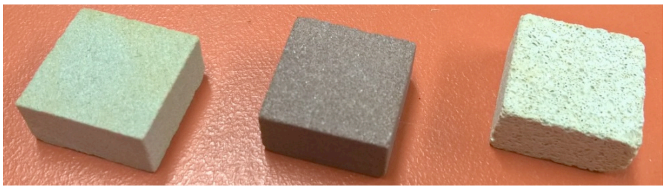

Figure 1. Photos of Bentheimer (left), Meule (center) and Savonnières samples.

Droplet generation

Water droplets are generated at the flat tip of a needle by pushing a syringe pump. The droplets have an initial diameter of 2 mm, reproducible with a relative error of 10%. When the droplet is released, it accelerates by gravity reaching an impact velocity of 0.5 m/s,1.0 m/s and 3.0 m/s, at rate of 4, 8 or 16 drops per minute.

Neutron radiography

The absorption process into the porous stone is captured by neutron radiography. Neutrons are attenuated by the hydrogen of water, but penetrate the porous stone. The experiment for the absorption of drop impact is performed at the NEUtron Transmission RAdiography (NEUTRA) beamline of the Paul Scherrer Institut, Villigen, Switzerland. The NEUTRA beamline is operated with neutrons within a thermal spectrum [4]. The necessary exposure time for each image is 3 seconds and the nominal spatial resolution of the neutron radiography is 47.2 μm/pixel. Figure 2 shows a schematic overview of the neutron beamline and the experimental setup for drop impact.

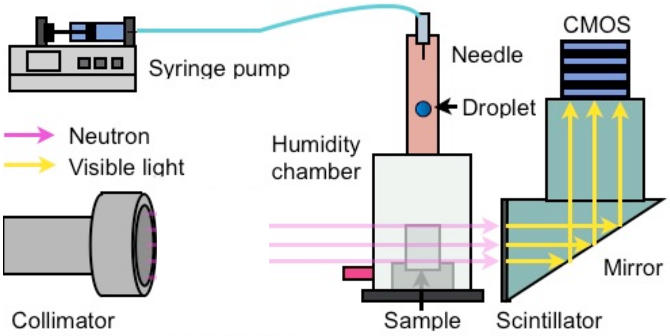

Figure 2. Schematic of NEUTRA beamline configuration

Using Beer-Lambert law, the variation of attenuation of the neutron beam yields the moisture content, further details on image analysis and post-processing can be found in [4]. Figure 3 shows the comparison between mass obtained from neutron images and deposition.

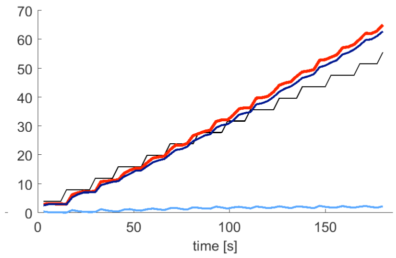

Figure 3. Validation by comparing total mass (mg) versus time comparing the total mass from neutron imaging (thick red) with actual water mass deposited (thin black). Total mass of water resting on the stone in blue, in the stone in dark blue.

Results

We present here only the results for Savonnières but results of all 3 stones are presented at the conference. In general, the uptake is faster for Savonnières with more water in the stone and less on the surface. Meule and Bentheimer undergo less moisture uptake in the same time and hence the surface water pool develops faster.

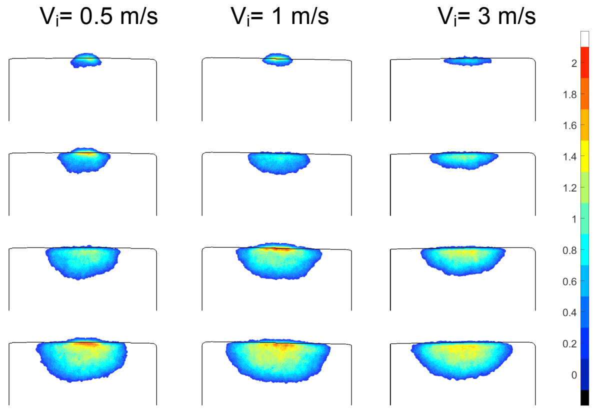

Figure 4. Moisture content (in thickness [mm] per pixel) for train of water droplets on Savonnières at the rate of 4 drops per minute for three impact velocities from top to bottom after 3, 33, 93 and 180 seconds.

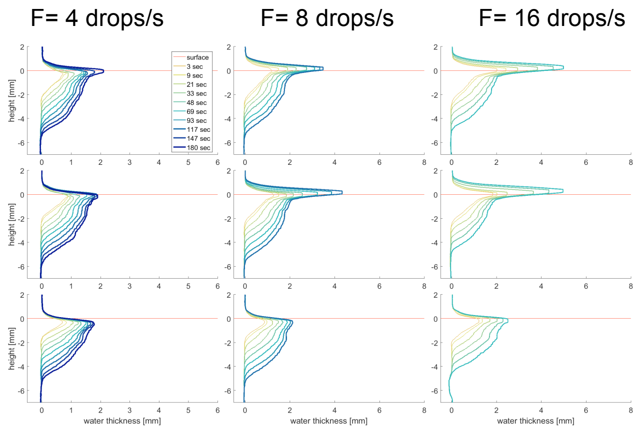

Figure 5. Vertical moisture content profiles for train of water droplets on Savonnières at the rate of 4, 8 and 16 drops per minute for three impact velocities from top to bottom of 0.5, 1 and 3 m/s. Pink line represents the stone surface.

In Figure 4, moisture content distribution is given after deposition of 1, 3, 7 and 13 droplets for three impact velocities. With time, water is transported in the stone further and further from the point of impact. In time water distribution has an elliptical shape that is quite independent from the impact velocities.

Figures 5 and 6 provide moisture content profiles versus time above and below the stone surface. Faster droplet rate leads to the development of water accumulation and thus water pool and film on the surface.

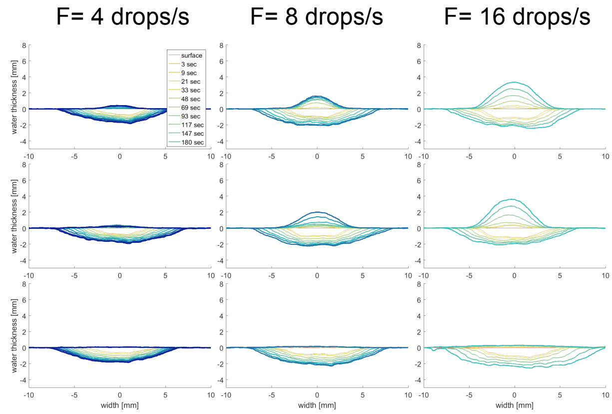

Figure 6. Horizontal moisture content profiles above and below the contact line for train of water droplets on Savonnières at the rate of 4, 8 and 16 drops per minute for three impact velocities from top to bottom of 0.5, 1 and 3 m/s.

Conclusion

This paper presents an experimental investigation of absorption and film forming during trains of liquid droplets impacting porous stones. Neutron radiography is used to quantify moisture absorption in three natural stones of varying porosity and moisture uptake characteristics. Film forming is found to be dependent on both transport properties and saturation degree of the stones. Moisture distribution within the porous stones, which are here all rather isotropic, is found to be dependent on impact velocity, and thus maximum spreading, for the first droplets of the train. Afterwards, the pooling of water yields similar moisture distribution.

Acknowledgements. We acknowledge the important contribution of the PhD work of Dr. Jaebong Lee to this paper. His PhD was made possible through Swiss National Science Foundation project no. 200021-135510. Guylaine Desmarais is acknowledged for the support in the preparation and running of the PSI Neutra experiment.

References

[1] J.B. Lee, D. Derome, J. Carmeliet. Drop impact on natural porous stones. J. Colloid and Interface Science, 469 (2016)147-156.
[2] J.B. Lee, D. Derome, J. Carmeliet. Absorption of impinging water droplet in porous stones. J. Colloid and Interface Science, 471(2016) 59-70.
[3] N.C. Reis, R.F. Griffiths, M.D. Mantle, L.F. Gladden. Investigation of the evaporation of embedded liquid droplets from porous surfaces using magnetic resonance imaging, Intern. J. of Heat and Mass Transfer, 46 (2003) 1279–1292.
[4] E.H. Lehmann. Recent improvements in the methodology of neutron imagin, Pramana, 71 (2008) 653–661.
[5] M. Sedighi Gilani, M. Griffa, D. Mannes, E, Lehmann, J. Carmeliet, D. Derome. Visualization and quantification of liquid water transport in softwood by means of neutron radiography, Intern. J. of Heat and Mass Transfer, 55 (2012) 6211-6221.

Train of water droplets impacting porous stones: adsorption and film forming

Dominique Derome[1], Stefan Carl[1], Peter Vontobel[2], Jan Carmeliet[3]

[1]Laboratory for Multiscale Studies in Building Physics, Swiss Federal Laboratories for Materials Science and Technology, Empa, 8600 Dübendorf, Switzerland
[2]Laboratory for Neutron Scattering and Imaging, Paul Scherrer Institut (PSI), Villigen, Switzerland
[3]Chair of Building Physics, ETH Zürich, 8093 Zürich, Switzerland

E-mail: dominique.derome@empa.ch

Introduction

The phenomenon of drop impacting porous media is ubiquitous in nature and is associated with mechanisms found in various industrial applications. When a liquid droplet impacts a permeable surface, it spreads on the surface and is absorbed into the porous material due to capillary action. The spreading behavior of the impinging droplet on the surface is known to depend on the properties of the liquid, i.e. density, viscosity and surface tension, impact conditions such as drop size and impact velocity, and the surface wettability and roughness [1]. Also, absorption is governed both by the properties of the liquid and of the porous medium, i.e. porosity, pore size, wettability [2]. Once the deposited droplet is completely depleted from the surface, the liquid further redistributes within the porous medium due to capillary forces, while evaporation occurs at the surface [3]. In case of saturation of the porous medium, the remaining water lies at the surface in a pool, and, in the event of further impacts, a water film can build up. For a better understanding of the absorption process inside porous media, observing directly the liquid content redistribution in the porous medium is required. Absorption in porous media has been studied with several non-destructive techniques, namely X-ray, neutron and gamma-ray radiography, magnetic resonance imaging (MRI) and nuclear magnetic resonance, and destructive techniques.

In this study, we aim to capture the full absorption and film forming process of trains of impinging droplets on natural porous stones by using neutrons. Neutron radiography allows visualizing the moisture content distribution in porous stones. In track, we measure the mass of deposited water to validate the neutron measurements. The deposition and absorption process of trains of impinging droplets is continuously characterized during deposition, absorption, evaporation and redistribution, in terms of total mass in/above the stone and moisture distribution, in a time-resolved manner.

Methodology

Samples

Three stones with varying porosity and uptake characteristics are selected: two sandstones (Meule Bentheimer and one limestone (Savonnières), Figure 1. The porous stones are cut in cubes of 20 x 20 x 10 mm^3 for characterization and drop impact tests.

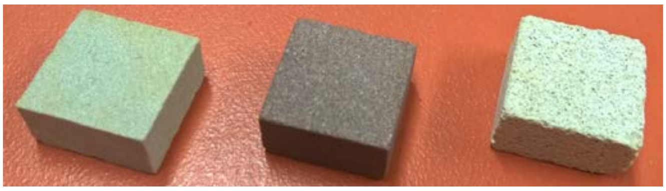

Figure 1. Photos of Bentheimer (left), Meule (center) and Savonnières samples.

Droplet generation

Water droplets are generated at the flat tip of a needle by pushing a syringe pump. The droplets have an initial diameter of 2 mm, reproducible with a relative error of 10%. When the droplet is released, it accelerates by gravity reaching an impact velocity of 0.5 m/s,1.0 m/s and 3.0 m/s, at rate of 4, 8 or 16 drops per minute.

Neutron radiography

The absorption process into the porous stone is captured by neutron radiography. Neutrons are attenuated by the hydrogen of water, but penetrate the porous stone. The experiment for the absorption of drop impact is performed at the NEUtron Transmission RAdiography (NEUTRA) beamline of the Paul Scherrer Institut, Villigen, Switzerland. The NEUTRA beamline is operated with neutrons within a thermal spectrum [4]. The necessary exposure time for each image is 3 seconds and the nominal spatial resolution of the neutron radiography is 47.2 μm/pixel. Figure 2 shows a schematic overview of the neutron beamline and the experimental setup for drop impact.

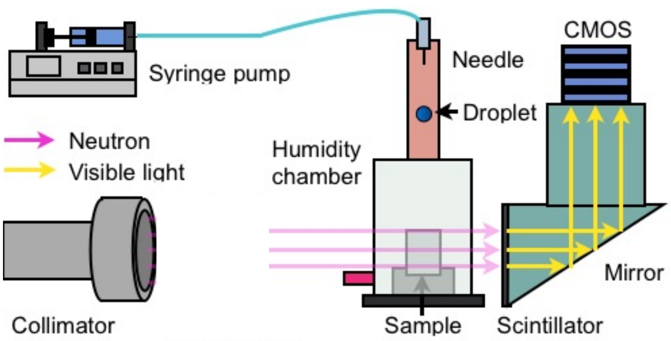

Figure 2. Schematic of NEUTRA beamline configuration

Using Beer-Lambert law, the variation of attenuation of the neutron beam yields the moisture content, further details on image analysis and post-processing can be found in [4]. Figure 3 shows the comparison between mass obtained from neutron images and deposition.

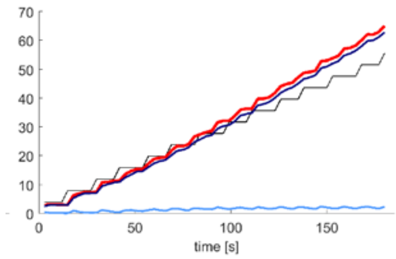

Figure 3. Validation by comparing total mass (mg) versus time comparing the total mass from neutron imaging (thick red) with actual water mass deposited (thin black). Total mass of water resting on the stone in blue, in the stone in dark blue.

Results

We present here only the results for Savonnières but results of all 3 stones are presented at the conference. In general, the uptake is faster for Savonnières with more water in the stone and less on the surface. Meule and Bentheimer undergo less moisture uptake in the same time and hence the surface water pool develops faster.

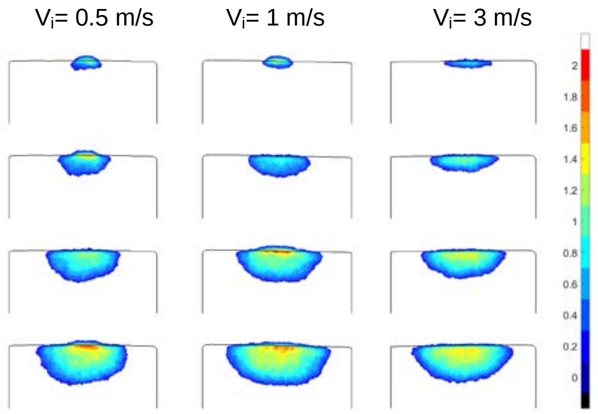

Figure 4. Moisture content (in thickness [mm] per pixel) for train of water droplets on Savonnières at the rate of 4 drops per minute for three impact velocities from top to bottom after 3, 33, 93 and 180 seconds.

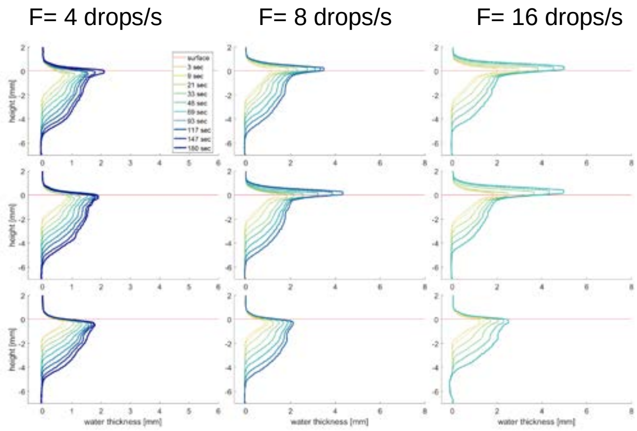

Figure 5. Vertical moisture content profiles for train of water droplets on Savonnières at the rate of 4, 8 and 16 drops per minute for three impact velocities from top to bottom of 0.5, 1 and 3 m/s. Pink line represents the stone surface.

In Figure 4, moisture content distribution is given after deposition of 1, 3, 7 and 13 droplets for three impact velocities. With time, water is transported in the stone further and further from the point of impact. In time water distribution has an elliptical shape that is quite independent from the impact velocities.

Figures 5 and 6 provide moisture content profiles versus time above and below the stone surface. Faster droplet rate leads to the development of water accumulation and thus water pool and film on the surface.

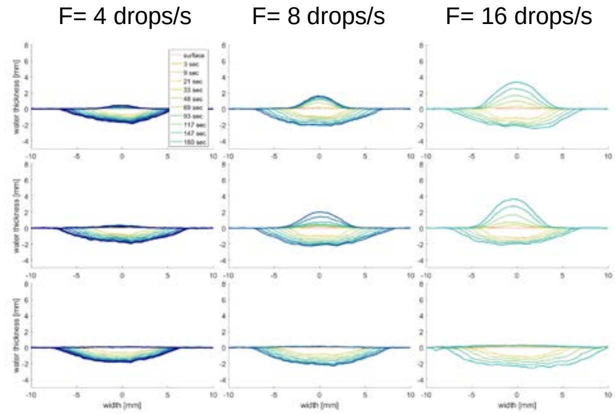

Figure 6. Horizontal moisture content profiles above and below the contact line for train of water droplets on Savonnières at the rate of 4, 8 and 16 drops per minute for three impact velocities from top to bottom of 0.5, 1 and 3 m/s.

Conclusion

This paper presents an experimental investigation of absorption and film forming during trains of liquid droplets impacting porous stones. Neutron radiography is used to quantify moisture absorption in three natural stones of varying porosity and moisture uptake characteristics. Film forming is found to be dependent on both transport properties and saturation degree of the stones. Moisture distribution within the porous stones, which are here all rather isotropic, is found to be dependent on impact velocity, and thus maximum spreading, for the first droplets of the train. Afterwards, the pooling of water yields similar moisture distribution.

Acknowledgements. We acknowledge the important contribution of the PhD work of Dr. Jaebong Lee to this paper. His PhD was made possible through Swiss National Science Foundation project no. 200021-135510. Guylaine Desmarais is acknowledged for the support in the preparation and running of the PSI Neutra experiment.

References

[1] J.B. Lee, D. Derome, J. Carmeliet. Drop impact on natural porous stones. J. Colloid and Interface Science, 469 (2016)147-156.
[2] J.B. Lee, D. Derome, J. Carmeliet. Absorption of impinging water droplet in porous stones. J. Colloid and Interface Science, 471(2016) 59-70.
[3] N.C. Reis, R.F. Griffiths, M.D. Mantle, L.F. Gladden. Investigation of the evaporation of embedded liquid droplets from porous surfaces using magnetic resonance imaging, Intern. J. of Heat and Mass Transfer, 46 (2003) 1279–1292.
[4] E.H. Lehmann. Recent improvements in the methodology of neutron imagin, Pramana, 71 (2008) 653–661.
[5] M. Sedighi Gilani, M. Griffa, D. Mannes, E, Lehmann, J. Carmeliet, D. Derome. Visualization and quantification of liquid water transport in softwood by means of neutron radiography, Intern. J. of Heat and Mass Transfer, 55 (2012) 6211-6221.

The air-film under an impacting ultra-viscous drop

S. T. Thoroddsen [1], K. Langley[1], E. Q. Li[1]

[1]Mechanical Engineering, Division of Physical Sciences and Engineering,
King Abdullah University of Science and Technology (KAUST), Thuwal, Saudi Arabia

E-mail: sigurdur.thoroddsen@KAUST.edu.sa

The impact of a drop on a solid surface is important in many manufacturing processes. Often it is undesirable to have bubbles entrapped under the impacting drop, for example during inkjet fabrication of electronic displays. It is therefore of interest to understand the dynamics and size of the resulting bubble sitting at the solid-liquid interface.

We use ultra-high-speed interferometry at up to 5 million fps to measure the air-layer profile under an impacting drop. Our focus is on the effect of increasing the drop viscosity on the air-layer dynamics. Earlier theoretical and experimental studies have primarily focused on low-viscosity drops, such as water, where only the viscosity of the air is important by providing a lubrication pressure to counteract the inertia of the liquid at the bottom of the drop [1-4]. This lubrication pressure in the air produces a dimple in the bottom of the drop, making the first contact of the drop, with the solid substrate, occur around a ring, which entraps the air-disc.

Figure 1 shows the typical optical setup, used in our interferometry experiments. The impact is on a microscope slide and is viewed from the bottom glass surface. We use the Kirana camera, which can take 180 frames at 200 ns inter-frame time. Each frame is illuminated with a separate red laser diode, with wavelength of 640 nm. The difference in air-layer thickness, between a dark and a bright fringe, is therefore 160 nm. It has been found that the shape of the drop influences the size of the air-disc and as our drops are larger than the capillary length, it is important to measure the bottom radius of curvature of the drop as it approaches the solid. We employ a second high-speed video camera (Phantom v710) to view the impact from the side, which allows us to measure this bottom radius for every impact.

In many of the experiments we have an unambiguous reference thickness, where the drop liquid touches the plate. In this case we can use the monochromatic red light and the B/W Kirana camera. However, for highly viscous drops the thickness where the first contacts occur is unclear, as is shown in the inset of the bottom panel of Figure 1. Therefore, we needed an independent measurement of the absolute thickness of the air film for some cases. This was accomplished by using two-color interferometry. A blue LED (peak wavelength 460 nm) in addition to the red laser provided illumination and a Phantom v710 color camera was used at 30 kfps to make these measurements. The red and blue channels can be considered as independent measurements of the air layer and comparing the air layer profile from each channel yields the absolute thickness of the film. The two profiles differ by less than 10 nm. Once the thickness where the film ruptures is identified. The monochromatic interferometry can be used at higher frame rates than allowed by the color setup to observe the formation of the central dimple.

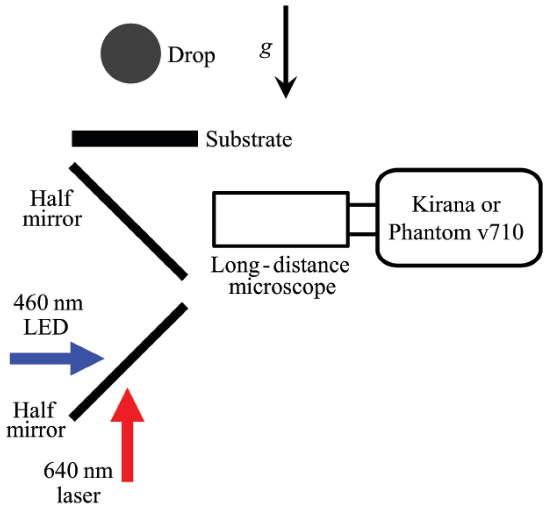

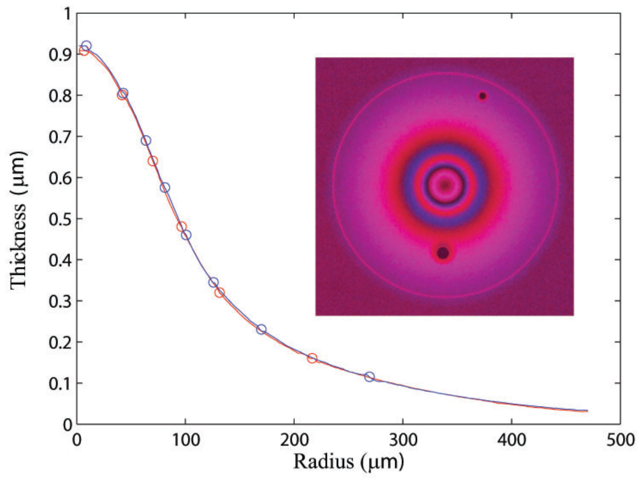

FIGURE 1. Top: Experimental setup for the high-speed interferometry. Bottom: The air-layer profile under the center of an impacting drop. Image taken with two-color illumination. Modified from [5].

Figure 2 shows the air-layer profile for drops impacting at V ~ 1 m/s for a range of viscosities from 10 cSt up to 1 million cSt. The viscosity of the drop affects the air disc in non-trivial ways. For a given velocity, the centerline height of the air-layer when the droplet makes contact decreases with increasing velocity. As the viscosity is increased, the radial extent of the air disc first increases and then decreases. These effects deviate from theory [3-4] and thus new scaling laws are required to predict the air disc size.

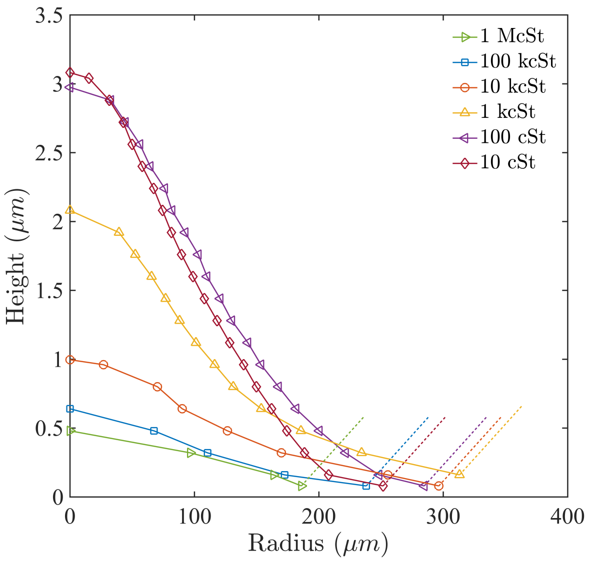

FIGURE 2. Air-layer profiles of silicone oil drops with an impact velocity of ~1 m/s for viscosities ranging from 10 cSt to 1 million cSt. The area under the curve is air and the drop is above the curve. Modified from [5].

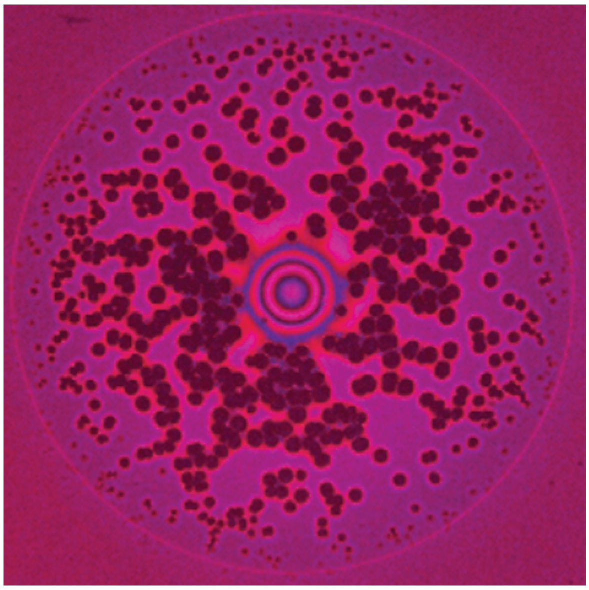

FIGURE 3. Interferometric view of a 10,000 cSt drop impacting at 2.8 m/s. The central dimple has closely spaced fringes while there is an extended very thin air-layer surrounding the dimple. The radius of the film is 590 µm and the bottom radius of the drop was 1.3 mm. Numerous ruptures of the air layer (dark spots) are seen throughout the film. Modified from [5].

After the initial formation of the central dimple in the bottom of the droplet, the viscosity of the droplet freezes the shape of the dimple and the drop spreads on an extended thin air layer. This gliding is fundamentally different than the film skating predicted by [3] for low viscosity drops, which is stabilized by surface tension versus viscosity.

As the drop glides on the air-layer, ruptures occur in random locations allowing the droplet to wet the substrate. Figure 3 shows an example of a 10,000 cSt drop impacting at 2.3 m/s. The central dimple is seen with closely spaced fringes. The air-film has extended to a radius of 590 µm at a thickness of 160 nm or less. There are numerous locations within the air film where the drop has contacted the substrate (seen as dark spots in the image).

The rate at which the localized contacts wet the substrate was measured. Surprisingly, the initial rates of wetting across all of the viscosities used were between 0.25 and 0.60 m/s. This extreme wetting behavior is several orders of magnitude faster than expected from current theories [6] for the highest viscosities. This initial wetting behavior seems to be independent of viscosity and thus we look to other possible causes such as rarified gas effects, van der Waals forces or the liquid draping onto the surface.

Detailed results, comparisons with the literature and further insights will be presented.

Acknowledgements. This research was funded by King Abdullah University of Science and Technology (KAUST).

References

[1] E. Q. Li and S. T. Thoroddsen, Time-resolved imaging of a compressible air disc under a drop impacting on a solid surface. *J. Fluid Mech.*, **780**, 636–648 (2015).
[2] E. Q. Li, I. U. Vakarelski and S. T. Thoroddsen, Probing the nanoscale: the first contact of an impacting drop. *J. Fluid Mech.*, **785**, R2 (2015).
[3] Mandre S., Mani M., Brenner M. P., Precursors to splashing of liquid droplets on a solid surface. *Phys. Rev. Lett.* **102**, 134502 (2009).
[4] Hicks, P. D. and Purvis, R., Air cushioning and bubble entrapment in three-dimensional droplet impacts. *J. Fluid Mech.* **649**, 135–163 (2010).
[5] K. Langley, E. Q. Li and S. T. Thoroddsen, Impact of ultra-viscous drops: air-film gliding and extreme wetting. *J. Fluid Mech.,* **813**, 647 (2017).
[6] Eddi, A., Winkels, K. G. and Snoeijer, J. H. Short time dynamics of viscous drop spreading. *Phys. Fluids* **25**, 013102 (2013).

Solutal Marangoni flow as the cause of ring stains from drying salty colloidal drops

Alvaro Marin[1*], Stefan Karpitschka[2], Diego Noguera-Marin[3], Massimiliano Rossi[1], Christian J. Kaehler[1]
Miguel A. Rodriguez-Valverde[3]
[1]Institute of Fluid Mechanics and Aerodynamics , Bundeswehr University Munich, Neubiberg, Germany
[2] Department of Bioengineering, Standford University, USA
[3] Biocolloid and Fluid Physics group, University of Granada, Granada, Spain

[*]Now at: Physics of Fluids group, University of Twente, The Netherlands
E-mail: a.marin@utwente.nl

Evaporating salty droplets are ubiquitous in nature, in our home and in the laboratory. However, the transport processes in such apparently simple systems differ strongly from ``sweet'' evaporating water droplets since the liquid flows completely in the inverse direction due to Marangoni stress at the surface. Such an effect has crucial consequences to the salt crystallization process and to the evaporation process itself. In this work we show unprecedented measurements that, not only confirm clearly the details of the inverted flow patterns, but also permit us to calculate the surface tension gradients responsible for the reversal. Contrary to what has been often reported in the literature, such a reversal does not prevent the coffee-stain effect, but particles accumulate and get trapped at the liquid-air interface driven by the surface flow. We therefore demonstrate that the accumulation of particles at the contact line in coffee-stains is not related with the direction of the flow.

Evaporating sessile droplets have been intensively studied in recent years, especially after the seminal work of Deegan et al.[1] In most practical applications, the droplet does not only contain a pure solvent and solid particles, but it could contain many other components. If such components are surface-active, the transport processes inside the droplet can be drastically affected. That is the case of bi-component droplets [2–4] or surfactant solutions [5, 6].

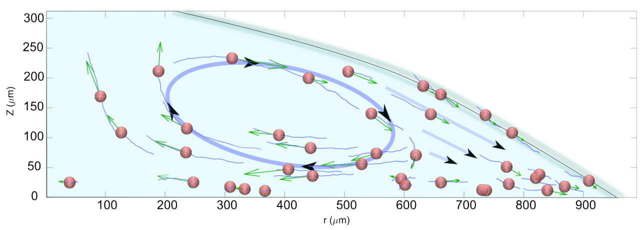

Figure 1. Experimental particle trajectories and velocity components clearly revealing the inverted convective circulation inside a water droplet containing 100 mM NaCl.

The effect of non-volatile soluble solutes like salt is paramount since most solutions of biological interest include different salts to match the ion concentration and pH of those in the human body. Salty droplets are also of particularly high interest for the pharmaceutical industry, where the formation of crystals with controlled properties is crucial. Salt solutions in contact with metallic surfaces provoque corrosion, and although ubiquitous, its mechanism is still poorly understood [8]. Interestingly, when the liquid partially wets the substrate, crystallization and growth of the deposit patterns typically nucleate at the contact line [10]. The internal flow is also known to affect the solute distribution, as recently reported by Soulie et al. [8], who also identified that the peripheral salt enrichment could lead to Marangoni flows inside the droplet. The existence of a different flow profile inside an evaporating droplet brings immediately the question: Will the stain left behind still show a ring shape?

In this paper we show experimental and numerical evidence of the existence of solute-induced Marangoni flows in evaporating salt solution droplets and demonstrate the existence of a new type of ring-shaped stain driven by Marangoni flow and not by a bulk-driven capillary flow as shown by Deegan et al. [1]. To show this unambiguously we first measure the

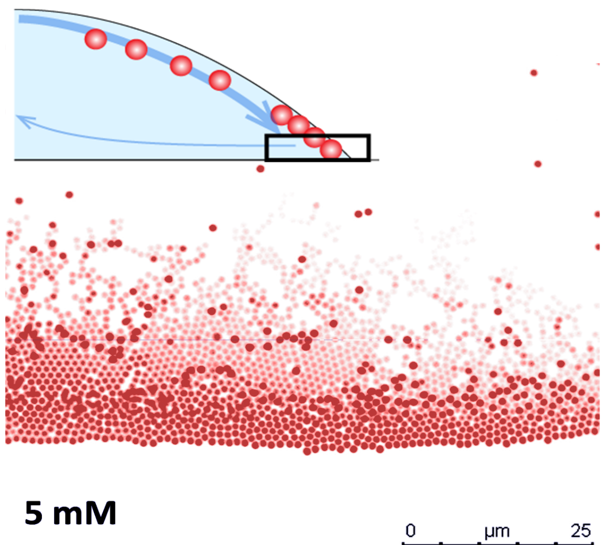

Figure 2. Confocal microscopy images of 1-μm-diameter polystyrene colloids aggregating at the droplet's contact line in the last stages of an evaporating water droplet containing 5 mM NaCl. Note the particles being aggregated along the droplets interface

full three-dimensional flow inside the evaporating salty droplet using 3D particle tracking velocimetry [7] (Figure 1), secondly we use confocal imaging to quantify the growth of the particle deposits for different salt concentrations (Figure 2). Finally, we compare the experimental results with numerical simulations that capture the solvent evaporation, the evaporation-induced liquid flow and the quasi-equilibrium liquid-gas interface (Figure 3).

In conclusion, we will show experimentally and numerically that a solutal Marangoni flow is responsable for the ring-shaped stain in evaporating droplets containing solutes with “anti-surfactant” effect [11]. This is not only the case of sodium chloride, but similar results have been observed for sodium iodide. The same flow inversion has been observed in evaporating Ouzo droplets [12], in which the enrichment of water provoques a positive surface tension gradient towards the contact line and therefore

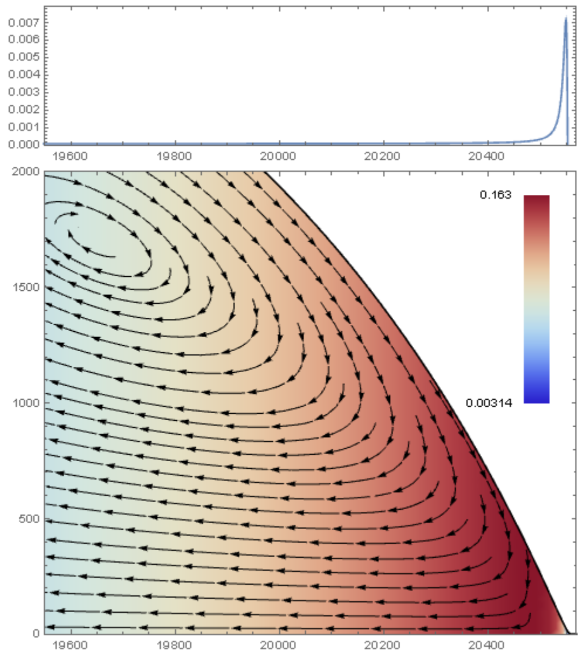

Figure 3. Numerical simulations showing (top) the salt concentration in arbitrary units as a distance from the contact line and (bottom) the streamlines generated by the solutal Marangoni effect. Confirming the trend observed in the experiments.

the inverted flow profile. This effect must have a crucial role in the formation of salt crystals, and probably also in their eventual migration towards the center of the droplet [10].

Acknowledgements. AM acknowledges financial support by the German Research Foundation grant KA 1808/17-1. MARV and MCV acknowledges financial support by the MINECO grant MAT2014-60615-R and Junta de Andalucia grant P12-FQM-1443.

References

[1] R. Deegan, O. Bakajin, T. Dupont, G. Huber, S. R. Nagel, and T. Witten, Nature (1997).
[2] S. Karpitschka and H. Riegler, Langmuir 26, 11823 (2010).
[3] S. Karpitschka and H. Riegler, Physical review letters 109, 066103 (2012).
[4] N. J. Cira, A. Benusiglio, and M. Prakash, Nature 519, 446 (2015).
[5] A. Marin, R. Liepelt, M. Rossi, and C. J. Kähler, Soft Matter 12, 1593 (2016).
[6] W. Sempels, R. De Dier, H. Mizuno, J. Hofkens, and J. Vermant, Nature communications 4, 1757 (2013).
[7] M. Rossi and C. J. Kaehler, Exp Fluids 55, 1809 (2014).
[8] V. Soulie, S. Karpitschka, F. Lequien, P. Prene, T. Zemb, H. Moehwald, and H. Riegler, Phys. Chem. Chem. Phys. 17, 22296 (2015).
[10] N. Shahidzadeh, M. F. L. Schut, J. Desarnaud, M. Prat, and D. Bonn, Scientific Reports , 1 (2015).
[11] J. J. A. Conn, B. R. Duffy, D. Pritchard, S. K. Wilson, P. J. Halling, and K. Sefiane, Phys. Rev. E 93, 043121 (2016).
[12] H. Tan, C. Diddens, P. Lv, J. G. M. Kuerten, X. Zhang, and D. Lohse, Proceedings of the National Academy of Sciences 113, 8642 (2016).

Droplet breakup in multiple emulsions under application of shear stress

Laura Luhede[1], Udo Fritsching[1]

[1]Department of Mechanical Process Engineering, FB 4, University of Bremen, Germany

E-mail: l.luhede@iwt.uni-bremen.de

Multiple emulsions are complex multiphase structures that are of significant interest in pharmazeutical, food, and cosmetic industry. They allow the encapsulation of active molecules in the internal dispersed phase. This gives potential applications as drug carrier systems, or the masking of flavours and encapsulation of vitamins in food industry. Also, the protection of sensitive media is of high intrest. In contrast to a conventional two-component emulsion like water in oil (WO) or oil in water (OW), the multiple emulsion system consists of bothe OW and WO emulsions simultaneously. Thus, a potential sensitive medium is protected by an additional layer, drugs are encapsulated and the release can be controlled. The disadvantage is that this type of emulsion is highly unstabe as it consists of two thermodynamically unstable interfaces. Multiple emulsions are sensitive to shear stress which can lead to ruption and thus the release of its content.

Conventional emulsification processes for multiple emulsions are a high shear method for the internal emulsion as high energy is required to generate small droplets. Classic emulsification methods as colloid mills, high pressure homogenization or ultra sound can be used.
For the outer emulsion low stress is required as shear forces cause internal streaming in the droplets. Thus the collision frequency is increased which results in higher coalescence rates. Also the droplets are elongated which increases the interface available for encapsulated droplets to escape [1]. Classical methods used are stirring at low rpm and membranes.

The use of membranes allows a shear sensitive method to produce multiple emulsions. Especially for the outer emulsion this process allows the production of high qualitiy emulsions as narrow drop size distributions and high encapsulation efficiencies can be achieved This is of interest for various applications using shear sensitive media like bacteria.
Additional advantages is the low energy cost compared to conventional emulsification methods and the ability to use shear sensitive media if required.

For most applications of multiple emulsions a controlled release is required. Especially for pharmazeutical purposes it is essential that drugs are not released before arriving at the destined area. Therefore the study of multiple emulsion stability is of great importance.
Schuch et al. [2] investigate the effect of inner dispersed phase concentration on the multiple emulsion breakup. They visually show the drop deformation and found that shearing has no influence on inner drop collisions. The deformation and relaxation time of droplets was not influenced by the internal emulsion's dispersed phase concentration.
Our assumption is that the internal emulsion stability influences the encapsulation efficiency of the double emulsion. Therefore WO emulsions with different surfactants and surfactant concentrations are created. Lower surfactant concentrations make coalescence phenomena more likely. Also, the surfactant concentration between the water-oil interface of the inner emulsion has an influence on the oil-water interface of the outer emulsion. The surfactant concentration of the outer emulsion remains constant. Thus, only effects appearing due to concentration changes in the inner emulsion are included in the analysis. With PGPR and Span 80 two different WO surfactants are used to see if the surfactant type has an additional effect on the emulsion stability.

For our experiments we used Tween 80 (Sigma Aldrich) as OW surfactant, and Span 80 (Sigma Aldrich) and PGPR (aliacura) to stabilize the internal WO emulsion. The oil phase was middle chain triglyceride (MCT) (Endima) and the watery phase bi-destilled water. 0.5 m% NaCl (Sigma Aldrich) was added as a marker to the internal water phase to determine the encapsulation efficiency.
The ratio of oil to water was 2:1 for the WO emulsion and 2:1 water to WO emulsion for the double emulsion. The surfactant concentration was varied from 1 .. 10 m% of the continuous oil phase.
Double emulsions were prepared by membrane emulsification and were compared to emulsions created via ultra-turrax and stirring. The membranes used were obtained by ROBU and had a porosity of P3, P4 and P5. The functionalization to create the WO emulsion was done as described by Kroll et al. [3] using a 0.1 M HDTMS (Sigma Aldrich) solution.

Viscosity and drop size distribution of the WO emulsion are measured before performing the second emulsification step.

After the second emulsification step shear stress is applied to the multiple emulsion. The emulsion is sheared in a range from 1 .. 1500 s^{-1} using a double gap with samples taken at defined intervalls.The gap size is 100 µm. To analyse drop rupture, the drop size distribution is measured. pH and conductivity measurements show if release of the internal phase occurs.

Results show that the drop size distribution is affected by the shear stress applied. Low shear rates have almost no influence on the drop size. Shear rates of 200 s^{-1} or higher show a decrease in the big drop sizes.

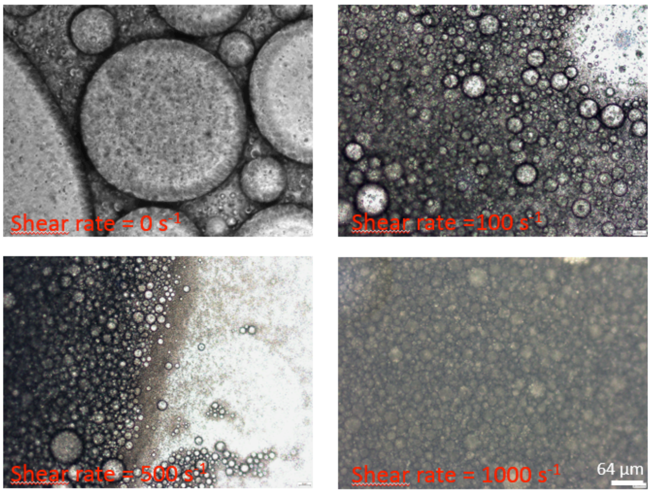

Figure 1 Multiple emulsions after being stressed by different shear rates

Figure 1 shows images of multiple emulsion drops after being sheard at different rates. At first a polydisperse emulsion can be seen, with the encapsulated drops. After shearing the drop size decreases rapidly. When anlyzing the drop size using diffraction spectrometry, it can be observed the mean drop size is decreasing slightly until 500 s^{-1} before the d_{50} shifts significantly to bigger drop sizes (Figure 2).The main driving force for this shift is coalescence. Due to the shearing the droplets are streteched and their surface is enlarged. The surfactant concentration is lower on this new generated surface. Coalescence can occur in these parts, which can be seen in the drop size distribution, which gets significantly broader. With less surfactant in the system, coalescence becomes more likly. Thus the effect is higher for lower surfactant concentration.

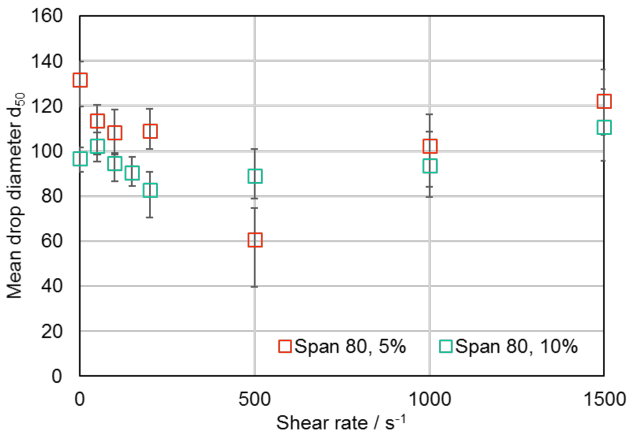

Figure 2 Mean drop size of multiple emulsions after shearing

This is in contrast to the microscopy images showing a basically broken emulsion even at low shear rates of 100 s^{-1}. The reason for the high d_{50} is due to the ratio of the few large drops compared to the broken smaller ones. The drop size distribution gets broader with the shear rate. The broken emulsion can also be seen in the encapsulation efficiencywhich is affected strongly by the shear stress.

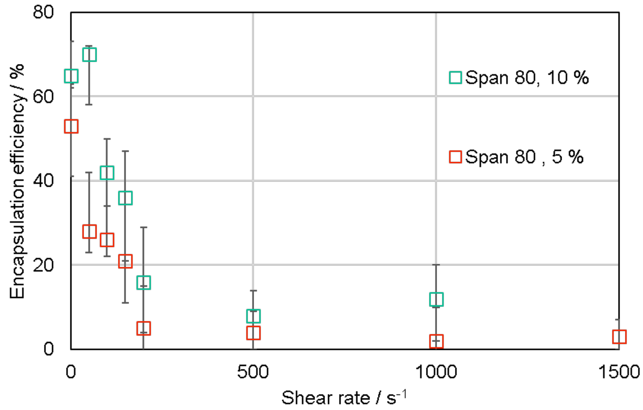

Figure 3 The encapsulation efficiency decreases faster with lower surfactant concentration

Figure 3 shows that the encapsulation efficiency decreases strong at rates > 100 s^{-1}. This corresponds with the microscopy images in Figure 1. The increase in surface area with lower surfactant load gives more ways for drop release. The internal phase is thus able to escape faster

In conculsion we can show that the stability of the internal phase has an influence on the overall multiple emulsion. A high quality internal phase makes the outer phase more resilent to shear stress. Thus the encapsulation efficiency stays higher even at increased shear rates.

Acknowledgements. Funded by DFG Graduate School 1860 Mimenima.
Thanks to Benjamin Besser for providing the functionalization of the membranes.

References

[1] S. Vandergraaf, C. Schroen, and R. Boom, Preparation of double emulsions by membrane emulsification - a review, *J. Memb. Sci.*, vol. 251, no. 1–2, , (2005). 7–15.

[2] A. Schuch, L. G. Leal, and H. P. Schuchmann, Production of W/O/W double emulsions. Part I: Visual observation of deformation and breakup of double emulsion drops and coalescence of the inner droplets, *Colloids Surfaces A Physicochem. Eng. Asp.*, vol. 461, (2014) 336–343.

[3] S. Kroll, C. Soltmann, D. Koch, P. Kegler, A. Kunzmann, and K. Rezwan, Colored ceramic foams with tailored pore size and surface functionalization used as spawning plates for fish breeding, *Ceram. Int.*, vol. 40, no. 10, (2014) 15763–15773.

LEVITATING CLUSTERS OF DROPLETS OVER THE LOCALLY HEATED COLD WATER: A MODIFIED LABORATORY INSTALLATION AND NEW EXPERIMENTAL RESULTS

Alexander A. Fedorets[1], Leonid A. Dombrovsky[1,2], Pavel I. Ryumin[1]

[1] Tyumen State University, Semakov 10, Tyumen, 625003, Russia
[2]Joint Institute for High Temperatures, NCHMT, Krasnokazarmennaya 17 A, 111116 Moscow, Russia
E-mail: ldombr@yandex.ru (presenting author)

A wide range of possible temperatures of levitating water droplets is expected to be interesting for the upcoming laboratory studies of biochemical processes in the droplets. The previously obtained temperature of droplets levitating above the locally heated water of room temperature appeared to be too high for some biochemical experiments [1-5].

It was not obvious that one can generate much colder droplets. Fortunately, this problem is solved experimentally in the present study with the use of a strong cooling of both water layer and ambient air.

The modified laboratory installation which include a separate volume of cooled air just above the central part of cold water layer is designed for the first time to work at quite different temperature conditions.

It is shown that even moderate local heating of water surface is the most important factor to produce sufficiently large self-assembled levitating clusters of water droplets which are similar to those observed at normal temperature conditions.

The effect of ambient temperature on both the formation and the parameters of droplet clusters is studied in some details.

The paper is illustrated by close-up photographs and video.

Acknowledgements

The authors are grateful to the Russian Foundation for Basic Research (Grant No. 15-08-00248-a) for the financial support of the present study. This work was conducted in the frame of the Russian State assignment (project №3.8191.2017/БЧ).

References

[1] A.A. Fedorets, Droplet cluster, *Journal of Experimental and Theoretical Physics Letters*, (2004) 79 (8) 372-374.

[2] E.A. Arinstein, A.A. Fedorets, Mechanism of energy dissipation in a droplet cluster, *Journal of Experimental and Theoretical Physics Letters*, (2010) 92 (10) 658-661.

[2] A.A. Fedorets, L.A. Dombrovsky, A.M. Smirnov, The use of infrared self-emission measurements to retrieve surface temperature of levitating water droplets, *Infrared Physics and Technology*, (2015) 69, 238-243.

[3] A.A. Fedorets, L.A. Dombrovsky, and D.N. Medvedev, Effect of infrared irradiation on suppression of condensation growth of water droplets in levitating clusters, *Journal of Experimental and Theoretical Physics Letters*, (2015) 102 (7) 452-454.

[4] L.A. Dombrovsky, A.A. Fedorets, D.N. Medvedev, The use of infrared irradiation to stabilize levitating clusters of water droplets, *Infrared Physics and Technology*, (2016) 124-132.

[5] A.A. Fedorets, L.A. Dombrovsky, Generation of levitating droplet clusters above the locally heated water surface: A thermal analysis of modified installation, *International Journal of Heat and Mass Transfer*, (2017) 104, 1268-1274.

3rd International Conference on Droplets
University of California Los Angeles, USA, July 24th to 26th, 2017

Wetting Behaviors of the Bijel-derived Hierarchical Nanostructures

Jonggyu Lee[1], Kyle McDevitt[2], Ali Mohraz[2], Yoonjin Won[1,2]

[1]Department of Mechanical and Aerospace Engineering, UCI, Irvine, CA, USA
[2]Department of Chemical Engineering and Materials Science, UCI, Irvine, CA, USA

E-mail: jonggyul@uci.edu

Phase change heat transfer has been a topic of significant scientific and technological interest as it can serve as an efficient cooling method for high heat flux applications. The key advantage in two-phase systems is the utilization of latent heat during phase change [1]. In particular, heat transfer during boiling regimes is considered as one of the most promising approaches to address thermal issues in various applications. To pursuit of the efficient boiling, various types of porous materials have been suggested [2] [3]. Fundamental challenges for effective boiling heat transfer are to increase potential cavities to facilitate efficient bubble nucleation and departure and to provide effective liquid and vapor paths. These challenges can be addressed by integrating bi-level porous materials. Therefore, it is imperative (1) to create new class of bi-level porous materials and (2) to better understand how the complex geometry of bi-level porous materials can affect the boiling physics. In order to minimize the complexity of the physical phenomena due to the complex geometry of porous materials, it is the key feature to precisely control the detailed pore morphology [4]. Bi-level porous structures with well-defined pore morphology will help to systematically understand the role of hierarchical porosity with a desired efficiency of phase change heat transfer.

In this study, we demonstrate the hierarchically porous constructs using self-assembled soft materials called bicontinuous interfacially jammed emulsion gels (bijels). This fabrication method enables to create a unique array of hierarchically porous metallic structures in which uniform and continuous pores on two independently tunable length scales [5]. Therefore, such hierarchically porous structures can simultaneously provide (1) a continuous path of microchannels for fluid transport with minimal flow resistance (1st order pores), (2) the required nanoporosity to help preserve the trapped vapor during subcooling to assist the bubble nucleation with a high frequency (2st order pores), and (3) sufficient specific surface area for thermal transports between solid and liquid phases.

For the first step of the fabrication, an initial formation of bijel starts with interpenetrating domains of two dissimilar fluids such as water and 2,6-lutidine system.

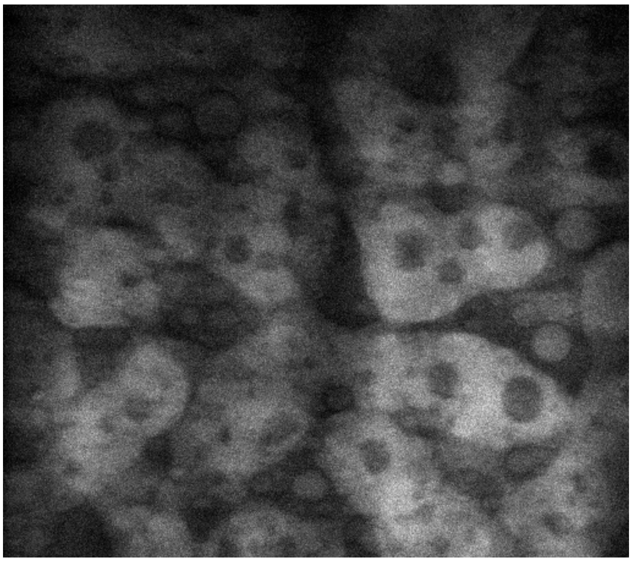

Figure 1. Confocal microscopy image of bijel structure showing the mixture of water and 2,6-Lutidine interfaces stabilized by silica nanoparticles.

Bijels form through arrested spinodal decomposition at the critical mixing point of two solutions. In this process, two solutions are separated by a monolayer of silica particles with diameter of 500 nm at the interfaces as shown in Figure 1. The silica particles provide enough mechanical stabilities for the following monomer exchange. In this step, polyethyleneglycol-diacrylate (PEGDA) is used to selectively dissolve the sacrifical polymer template into one fluid phase. Ater the monomer exchange step, silica nanoparticles are etched using hydrogen fluoride (HF) solution. The resulting bijel template will serve as a host for metallic structure construction. For this, scaffold is immersed into $PdCl_2$ and $SnCl_2$ solution for overnight to allow the solution to penetrate into the scaffold or attaching catalyst to provide nucleation site of metal deposition. An electroless deposition method deposits metal to the non-conductive bijel template forming biporous metal structure. After the metal deposition, the samples are calcinated inside the furnace on nitrogen atmosphere to remove the polymer matrix. The post-processing will be followed to coat the metallic structure's surface with low-surface energy solution.

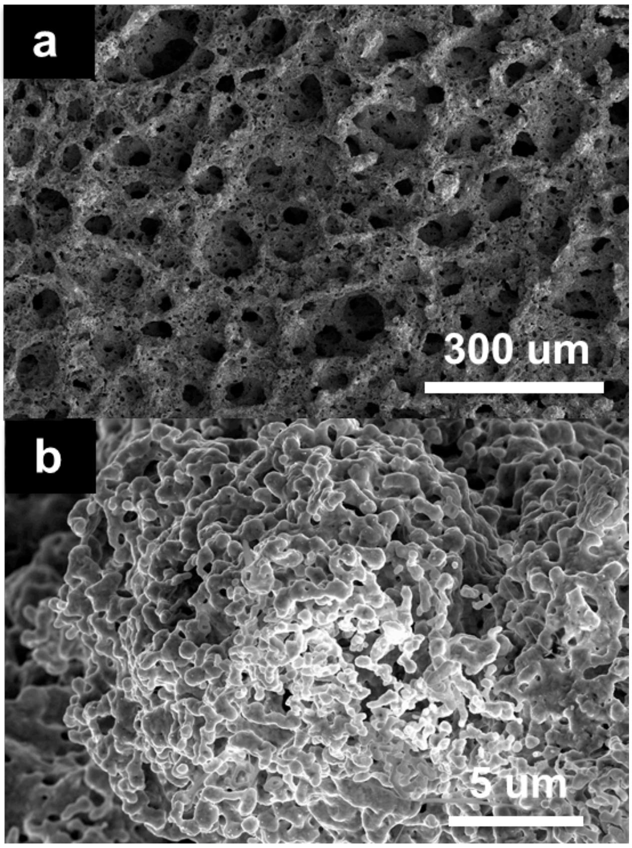

Figure 2. Scanning electron microscope images of bijel-derived hierarchical nickel structures. These structures provide bi-level pores consisting of (a) 1st order micropores with 30 μm diameter, and (b) 2nd order nanopores with 200 nm diameter.

A new class of bijel materials are suggested to provide bi-level porous characteristics in boiling regimes. In bijel structures, the 1st order pores (d_1) might play an important role to transport liquid to the bubble nucleation sites. Here, d_1 can be controlled by changing the silica nanoparticle concentration of the emulsion solution which is the mixure of water, 2,6-lutidine, and silica nanoparticles. In this process, the active surface area will be inversely proportional to d_1. In addition, the 2nd order pores have critical impacts on the bubble nucleations due to roughness enhancement. In the manufacturing process, d_2 is suggested to be controlled by crosslinking density of polymer matrix. The amount of monomer exchange changes the crosslinking density, which affects the amount of metal deposition inside the bijel scaffold. Figure 2 shows an example of bijel-derived hierarchical nickel fabricated in this study where d_1=30 μm and d_2=200 nm.

Then, we will investigate the wetting and corresponding hydrodynamic transport physics of bijel-based metallic structures as a function of the morphological parameters (i.e. pore sizes). In order to confirm the wettability of the porous structures, a sessile drop technique is used. The size of the deionized water droplet dispensed through the capillary tip is controlled by the injection pressure, ranging from 20-50 nl. The measured contact angles are confirmed by using environmental scanning electron microscope (ESEM) images. Using ESEM, the evaporation and condensation of droplets can be explored as well [6].

In summary, we suggest bijel-based bicontinuous materials to enhance boiling heat transfer by means of bi-level pore morphlogy. Such bijel structures are designed to provide efficient paths for liquid and vapor, active cavities, and large surface area. In this study, we will study the fabricaiton method of bijel-based materials and wetting behaviors of thses materials. This study using a new class of materials with precise control will help to design efficient boiling materials and understand the boiling mechanism.

Acknowledgements. This work was sponsored by the National Science Foundation (NSF), (CBET-TTP 1643347, Dr. Jose Lage, the Program Director, Thermal Transport Processes).

References

[1] H. O'Hanley, C. Coyle, J. Buongiorno, T. McKrell, L.-W. Hu, M. Rubner, R. Cohen, Separate effects of surface roughness, wettability, and porosity on the boiling critical heat flux, Applied Physics Letters, 103 (2013) 024102.
[2] S. Bhavnani, V. Narayanan, W. Qu, M. Jensen, S. Kandlikar, J. Kim, J. Thome, Boiling Augmentation with Micro/Nanostructured Surfaces: Current Status and Research Outlook, Nanoscale and Microscale Thermophysical Engineering, 18 (2014) 197-222.
[3] R. Jafari, M. Farzaneh, Fabrication of superhydrophobic nanostructured surface on aluminum alloy, Applied Physics A, 102 (2010) 195-199.
[4] T. Darmanin, E. Taffin de Givenchy, S. Amigoni, F. Guittard, Superhydrophobic surfaces by electrochemical processes, Adv Mater, 25 (2013) 1378-1394.
[5] M.N. Lee, A. Mohraz, Hierarchically porous silver monoliths from colloidal bicontinuous interfacially jammed emulsion gels, J Am Chem Soc, 133 (2011) 6945-6947.
[6] M. Nosonovsky, B. Bhushan, Biomimetic superhydrophobic surfaces: multiscale approach, Nano Lett, 7 (2007) 2633-2637.

MODELING OF COLLOIDS SELF-ASSEMBLY IN DRYING PICOLITER DROPLET DEPOSITED TO SOLVATOPHOBIC SUBSTRATE

P. Lebedev-Stepanov

Photochemistry Center RAS (FRC Crystallography & Photonics RAS) Novatorov St., 7a/1, Moscow, 119421;
National Research Nuclear University "MEPhI" Kashirskoe Shosse St., 31, Moscow, 115409, Russia.

E-mail: petrls@yandex.ru

Evaporating sessile droplet of aqueous solution deposited on sovatophobic (for example, hydrophobic) surface is an urgent object both for theoretical modeling (evaporation dynamics, microfluidics inside the drop, particle dynamics in evaporating drop, etc) and applied researches (printing technologies, nanoparticle ensemble self-assembly processes, hydrophobic coatings, etc).

There are three basic problems to estimate the colloidal particles self-assembly in evaporating droplets: 1) solute evaporation from the droplet surface to surrounding air (outer problem), 2) hydrodynamic flows in droplet volume (inner problem), 3) particle dynamics into drioplet with account of interparticle interactions, particle-surfaces interactions, particle-flow interactions, solvation effects [1,2].

Although self-assembly investigation in evaporating droplet of colloidal solution on smooth surfaces with quite acute contact angles has been widely studied recently for liquids of different properties including binary solute mixtures [3-8], nanoparticles ensemble self-assembly processes in droplet deposited on hydrophobic and superhydrophobic surfaces has not received much attention up to date.

.

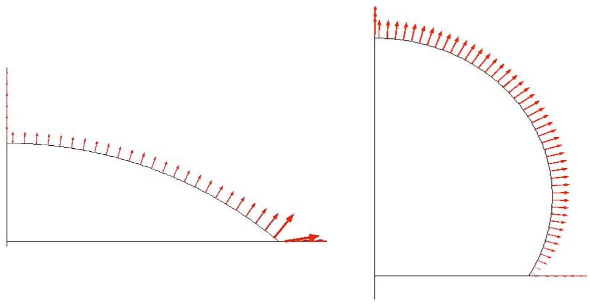

Figure 1: Evaporative flux density (evaporation rate) on a surface of sessile droplet with acute wetting angle (left) and with obtuse angle (right); the pictures were estimated by Comsol.

The wetting angle of 'hydrophobic' droplet has a value in interval from about 90^o to about 180^o. In this case, evaporation flow density has no the integrable singularity at contact line, unlike a drop with an acute angle (Fig.1).

Deegan (2000), Popov (2005), Hu and Larson (2002, 2005) have elaborated the useable models of evaporation of sessile drop of single liquid based on Maxwell diffusion model.

This model has a good approbation for calculation of the evaporation flow for the wetting angle interval from 0^o to 90^o. In framework of this model, the evaporation flow density on the droplet surface is given by

$$J(r) = J_0(\phi)\left(1-\frac{r^2}{R_d^2}\right)^{-\lambda(\phi)}, \quad \lambda(\phi) = \frac{1}{2}-\frac{\phi}{\pi}. \qquad (1)$$

where ϕ is a contact angle; R_d is a droplet radius (Fig. 2).

Computer modeling the self-assembly of an ensemble of nanoparticles in drying droplet requires the using of quick analytic approximation solutions for the evaporation flow, so that a good example of which are the Hu-Larson's [5] solution given by Eq.1. But, up to date, such a solution for droplet on solvatophobic substrate is absent.

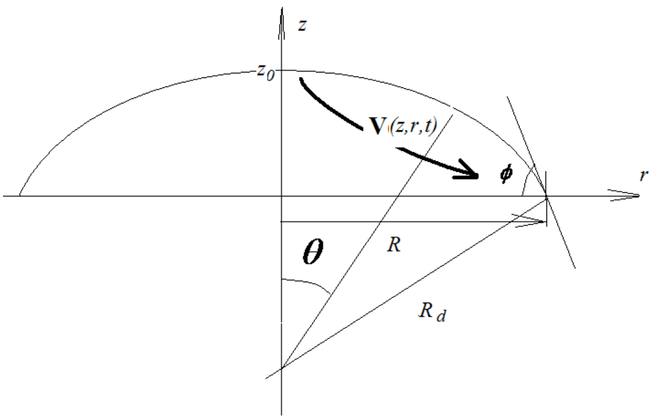

Figure 2: Geometry of liquid capillary-sized droplet on a flat substrate.

According to the generally accepted opinion, Popov's model with integral formula for the evaporation flux [7] can be used for whole interval of contact angles from about 0^o to 180^o. However, such a diffusion-only model has significant deviations from experiment for droplets on superhydrophobic surfaces with negligible contact angle hysteresis [9].

The similar situation takes place for inner problem (hydrodynamic flows into droplet). Lubrication approximation analisys given by Oron [9], Deegan et al

[4] can be applied only for the flow field produced by droplet evaporation under the additional approximation of a flat droplet (small contact angles). Deegan et al. have used the lubrication approximation to calculate the hydrodynamic flow into a droplet with acute angle and pinned contact line.

Hu and Larson have developed such a semianalytical approximation in their model of hydrodynamic flows in drying drop. The kinematic boundary condition with a phase change is

$$(\mathbf{n},\mathbf{V}) = [n_r, n_z][0,\dot{Z}] + \frac{(\mathbf{n},\mathbf{J})}{\rho}, \qquad (2)$$

where (**n**,**J**) is the evaporation flux along the direction normal to the free surface, where **n** is a unit vector along the normal direction, and n_r and n_z are the r and z components of the unit normal vector **n**, respectively.

In our work [1], the boundary conditions of a more general form for the rate of flow on the top of drop surface were proposed:

$$V_z(\theta,t) = \frac{J(\theta,t)}{\rho}\cos\theta - \frac{dZ(\theta,t)}{dt}, \qquad (3)$$

$$V_r(\theta,t) = \frac{J(\theta,t)}{\rho}\sin\theta - \frac{dR(\theta,t)}{dt}, \qquad (4)$$

where ρ is a mass density of a liquid, $\frac{dZ(\theta,t)}{dt}$ and $\frac{dR(\theta,t)}{dt}$ are z- and r-components of velocity of the geometrical point on a drop surface. Such a shift takes place due to the evolution of the form and size of the evaporated drop with account of the contact line movement (Fig.3).

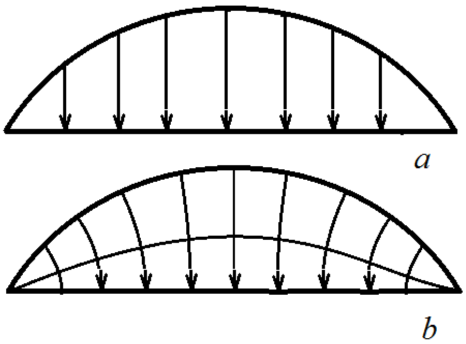

Figure 3: Pictures showing the trajectories of displacement of the points on surface of drying droplets with acute contact angle during evaporation with a pinned contact line: **a**) lubrication theory (wrong); **b**) our model [1,2].

These boundary conditions were successfully used to simulate the self-assembly of nanoparticles in sessile droplets with contact angles having the value smaller than right angle. However, applicability of Eqs. (3-4) for hydrophobic droplets still has not been investigated.

The boundary conditions for general case which includes the obtuse contact angles are still absent in scientific publications.

This report includes the analysis the application of existing droplet evaporation models, the boundary conditions for the hydrodynamic flows on the drop surface (Fig.4), as well as the nanoparticle dynamics in the hydrophobic droplet, and the dry pattern formation processes modeling.

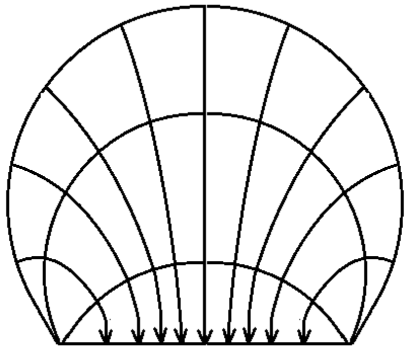

Figure 4: Trajectories of displacement of the points on surface of drying droplets with obtuse contact angle during evaporation with a pinned contact line according to our new model.

The necessity to develop the existing models of evaporation and boundary conditions for hydrophobic sessie droplets is shown. For the first time, self-assembly model in drying droplets on hydrophobic substrate is described and estimated.

Acknowledgements. This work was financially supported by the Russian Foundation for Basic Research, project no. 15-03-08050 and by the Competitiveness Program of National Research Nuclear University “MEPhI”.

References

[1] P. Lebedev-Stepanov, K. Vlasov. Simulation of self-assembly in an evaporating droplet of colloidal solution by dissipative particle dynamics. Colloids and Surfaces A : Physicochem. Eng. Aspects. 432 (2013) 132-138.
[2] Lebedev-Stepanov P. Introduction to self-organization and self-assembly of ensembles of nanoparticles (in Russian). Monograph. NRNU MEPhI: Moscow, 2015. 304 p.
[3] R.G. Picknett, R. Bexon. The evaporation of sessile or pendant drops in still air. J. Colloid Interface Sci. 61 (1977). 336−350.
[4] R.D. Deegan, O. Bakajin, T.F. Dupont, G. Huber, S.R. Nagel, T.A. Witten. Contact line deposits in an evaporating drop. Phys. Rev. E 62(2000). 756-765.
[5] H. Hu, R.G. Larson. Evaporation of a Sessile Droplet on a Substrate. J. Phys. Chem. B. 106 (2002). 1334-1344.
[6] H. Hu, R.G. Larson. Analysis of the Microfluid Flow in an Evaporating Sessile Droplet. Langmuir. 21(2005). 3963-3971.
[7] Yu.O. Popov. Evaporative deposition patterns: Spatial dimensions of the deposit. Phys. Rev. E. 71(2005) 036313.
[8] E.L. Talbot, H.N. Yow, L. Yang, A. Berson, S.R. Biggs., C.D. Bain. Printing Small Dots from Large Drops. ACS Appl. Mater. Interfaces. Vol. 7 (2015). 3782–3790.
[9] S. Dash, S.V. Garimella. Droplet Evaporation Dynamics on a Superhydrophobic Surface with Negligible Hysteresis. Langmuir.. 29 (2013)10785−10795.
[10] A. Oron, S.H. Davis, S.G. Bankoff. Long-scale evolution of thin liquid films. Reviews of Modern Physics. 69 (1997). 931-980.

CAPILLARY OSCILLATION AND BREAKUP OF DROPLET COALESCENCE: IDENTIFYING REGIME AND TRANSITION

Le Qin PENG, Zheng Yuan LUO, Gang YAN, Bo Feng BAI*

State Key Laboratory of Multiphase Flow in Power Engineering, Xi'an Jiaotong University, Shaanxi, 710049, China

E-mail: bfbai@mail.xjtu.edu.cn

When two identical droplet come into contact with each other, they typically coalesce into a larger one for minimizing the free surface energy. Notably, the hydrodynamic behaviors during the process after coalescence, including rapid expanding of liquid bridge formed between two droplets, are of great scientific interest because of the richness of the underlying physics, such as free surface flow[1-4], Rayleigh-Plateau instability[5-7], and singularity dynamic[8], all of which are also essential to appropriately manipulate droplet coalescence in various application[9-11]. The capillary driven expansion of the neck generates capillary waves from the released surface energy. The wave carry momentum and propagate axisymmetrically along the droplet surfaces, thereby be blocked by the connecting solid surface, e.g. needle, simultaneously, stretch outward from the opposite poles to form protrusions, which are sometimes pinched off to form satellites. Chen et al.[9] observed three regimes after pinched droplet coalescence, with on satellite droplet formation. Thoroddsen et al.[7, 12, 13] provided models for predicting the satellite size generated from the capillary wave induced by drop coalescence, and the pinch-off limitation.

In this work, we have systematically studied the oscillation process of liquid bridge after the coalescence of a pendent and sessile droplet pinched on the needles. As shown in Figure 1(a), the coalescence of the distilled water droplets in atmosphere were controlled inside a stainless steel cell with sight glass. Two droplets were formed at the flat extremities of facing vertical coaxial needles by injecting liquid from corresponding syringe pump. The injection rate of micropump (Harvard PHD ULTRA) was set from 0.01ml/min to 0.2ml/min for obtaining various approaching speed. A sessile droplet was first generated on the lower needle extremity by controlling the volumetric flowrate Q_v and running time of pump. Then a pendent droplet grew on the upper needle extremity. The dynamic process of millimeter-sized droplets after generation, including the process from coalescence to oscillation, and sometimes broken, is directly recorded by a high-speed camera (Photron MINI UX100 with 1280 × 480 resolution) cooperated with long distance microscope lens (KEYENVE VH-Z50) from the side, at the frame rate of 10000 fps. A LED parallel light source (power 3W, spot diameter 20mm) was used to provide back-lit illumination. The side-view image of a pendent and a sessile droplet pinched on the needle before coalescence is shown in Figure 1(b). This allows the study of a liquid bridge of volume V attached to the edges of two facing solid disks of diameter D (corresponding radius R) separated by a distance H. Droplet volume, centroid coordinates (x_c, y_c) and curvature radius r_1, r_2 were determined via image analysis using Matlab software.

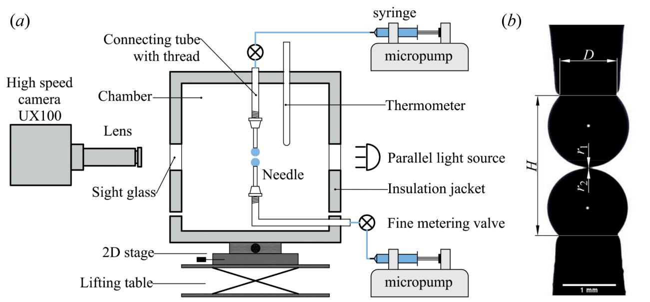

Figure.1 (a) Schematic of the experimental set-up. (b) The side-view of two initial droplets before merging. The distance between needles H, width of droplet contacting with needle D and curvature radius of two droplets r1, r2.

Results and discussion

Three different coalescence regimes are observed during the entire droplet coalescence process, including pinch-off in two necks during first necking stage (*type I*) (Figure 2a), pinch-off in one neck during second necking stage (*type II*) (Figure 2b), and stable liquid bridge with no pinch-off (*type III*) (Figure 2c).

Note that, these results indicate that gravity turns to be increasingly pronounced in morphologies development of coalescences after the initial expansion of the liquid bridge, especially in the final pinch-off process. Therefore, we represent these regimes using the Bond number (Bo=$\rho g R^2 \gamma^{-1}$, which compares gravity to the surface tension forces), and the Weber number (We=$\rho u^2 R \gamma^{-1}$, which compares inertial to surface tension forces).

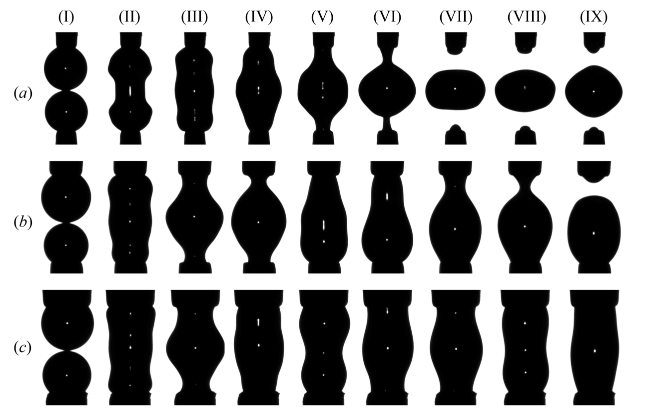

Figure.2 Evolutions of the liquid bridges after coalescence of

the two distilled water droplets. (I) Initial arrangement; (II)-(IX) Oscillation of liquid bridge formed by coalescence of droplets. Three typical regimes: (a) satellite droplet generated from pinch-off in two necks during first necking stage (volumetric flow rate: 0.01ml/min, outer diameter: 0.55mm, time interval: 60ms); (b) pinch-off in one neck during second necking stage (0.05ml/min, 0.9mm, 150ms); (c) stable liquid bridge with on pinch-off (0.01ml/min, 1.34mm, 150ms).

We use Matlab software to obtain the contour of the gas-liquid interface on each image, and plot W, normalized by W_{max}, as a function of time in Figure 3(b). This damping behavior of nondimensional W is clearly illustrated by the blue dotted line and exhibits a single dominant period intuitively. Using the damped oscillation sine function to fit. Then, the dependence of the oscillation parameters (A, γ, T) on the pinned needle and approaching speed.

$$w(t) = w_0 + Ae^{-\delta t}\sin\left(2\pi\frac{t}{T}+\phi\right) \qquad (1)$$

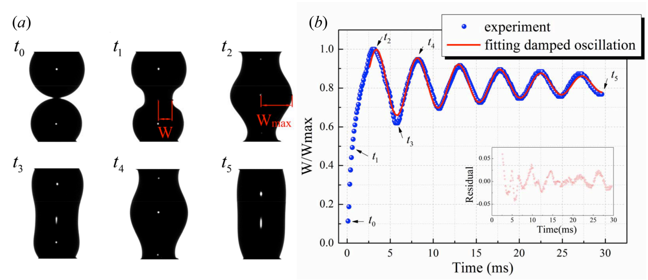

Figure.3 (a) Typical moments of coalescence process of DI water droplets pinched on the needles, corresponding to the marked time in (b). At t_0 = 0 ms, the droplets are just contact; At t_1 = 0.5 ms, the liquid bridge expanding, corresponding half of width is marked as W; At t_2 = 2.9 ms, W reaches its maximum value W_{max} for the first time; Then it decreases until t_3 = 6.3 ms; At t_4 = 8.1 ms, W reaches the peak once again. After several damped oscillation periods, the liquid bridge closes to a static state at the final recording time t_5= 29.6 ms. (b) Normalized width in the middle of the bridge W/W_{max} versus time; blue dotted line represents the experimental results obtain from sequence images; red line is the fitting curve by damped sine function. Inset: the residual of W/W_{max} with fitting.

Furthermore, we analyze the oscillation behavior of liquid bridge in the middle position at various volumetric flowrates and needle diameters. The damped behaviors are significantly influenced by the contact condition with the needle tips, conversely, less influenced by the approaching speed.

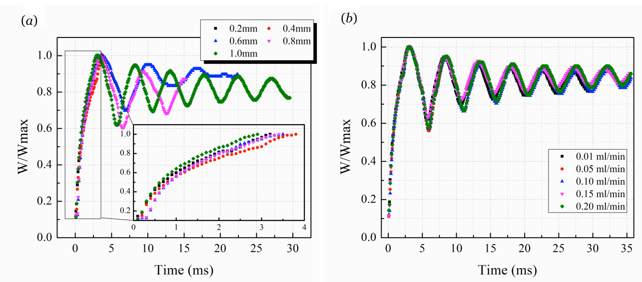

Figure.4 Normalized width in the middle of the bridge W/W_{max} versus time t. (a) width oscillation of liquid bridge pinned on inner diameters 0.2, 0.4, 0.6, 0.8, 1.0 mm (using inner diameter for convenience; outer diameters used as analytical size) at the same approaching speed; (b) oscillation of bridge at 0.01, 0.05, 0.1, 0.15 and 0.2 ml/min volumetric flowrate and 0.2 mm diameter needle.

We will further study these three regimes and transition, especially the pinch-off and damped oscillation from aspect of wave instability.

Acknowledgements. This work was supported by the China National Funds for Distinguished Young Scientists (Grant No. 51425603).

References

[1] J. Billingham and A. C. King, *J Fluid Mech*, (2005) 533.
[2] J. Billingham, *SIAM Journal on Applied Mathematics*, (2006) **66**(6), 1949-1977.
[3] H. N. Oguz and A. Prosperetti, *J Fluid Mech*, (2006) **203**, 149.
[4] J. Lu, S. Fang, and C. M. Corvalan, *Phys Rev E*, (2016) **93**(2), 023111.
[5] F. Blanchette and T. P. Bigioni, *J Fluid Mech*, (2009) **620**, 333.
[6] H. Aryafar and H. P. Kavehpour, *Physical Review E*, (2008) **78**(3).
[7] F. H. Zhang, M. J. Thoraval, S. T. Thoroddsen, and P. Taborek, *J Fluid Mech*, (2015) **782**, 209-239.
[8] B. W. Zeff, B. Kleber, J. Fineberg, and D. P. Lathrop, *Nature*, (2000) **403**(6768), 401-404.
[9] Y. Chen, C. Shen, and G. P. Peterson, *Industrial & Engineering Chemistry Research*, (2015) **54**(37), 9257-9262.
[10] X. Li, H. Ren, W. Wu, H. Li, L. Wang, Y. He, J. Wang, and Y. Zhou, *Scientific reports*, (2015) **5**, 15190.
[11] T. Li, W. Wu, and H. Li, Phys. Chem. Chem. Phys., (2016) **18**(39), 27500-27506.
[12] F. H. Zhang, E. Q. Li, and S. T. Thoroddsen, *Phys Rev Lett*, (2009) **102**(10), 104502.
[13] H. Ding, E. Q. Li, F. H. Zhang, Y. Sui, P. D. M. Spelt, and S. T. Thoroddsen, *J Fluid Mech*, (2012) **697**, 92-114.

DRYING DYNAMICS OF A CHARGED COLLOIDAL DISPERSION IN A CONFINED DROP

Charles Loussert, Anne Bouchaudy, Jean-Baptiste Salmon

Lab LOF, CNRS UMR 5258 – Univ. Bordeaux – IPB – Rhodia,
178 Av. Dr Schweitzer, F-33608 Pessac, France

E-mail: charles.loussert-ex@solvay.com

We perform a thorough investigation of the drying dynamics of a charged colloidal dispersion drop in a confined geometry [4].

We develop an original methodology based on Raman microspectroscopy to measure spatially resolved colloids concentration profiles during the drying of the drop. These measurements lead to estimates of the collective diffusion coefficient of the dispersion over a wide range of concentration. The collective diffusion coefficient is one order of magnitude higher than the Stokes-Einstein estimate, showing the importance of the electrostatic interactions for the relaxation of concentration gradients.

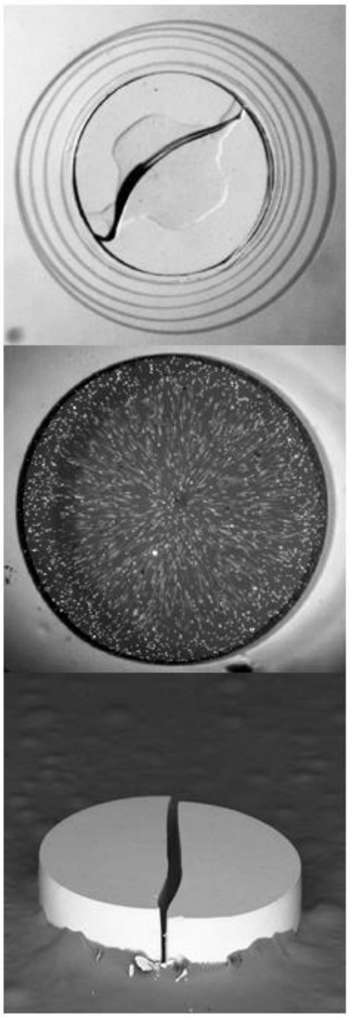

At the same time, we also perform fluorescence imaging of tracers embedded within the dispersion during the drying of the drop, which reveals two distinct regimes. At early stages, concentration gradients along the drop lead to buoyancy-induced flows. Strikingly, these flows do not influence the colloidal concentration gradients that generate them, as the mass transport remains dominated by diffusion.

At longer time scales, the tracer trajectories reveal the formation of a gel that dries quasi homogeneously. For such a gel, we show using linear poroelastic modeling that the drying dynamics is still described by the same transport equations as for the liquid dispersion.

However, the collective diffusion coefficient follows a modified generalized Stokes-Einstein relation, as also demonstrated in the context of unidirectional consolidation by Style and Peppin [Style and Peppin, Crust formation in drying colloidal suspensions, Proc. R. Soc. A 467, 174 (2011)].

[1] L. Daubersies and J.-B. Salmon, *Phys. Rev . E* **84**, 031406 (2011)
[2] B. Selva, L. Daubersies, and J.-B. Salmon, *Phys. Rev . Letters* **108**, 198303 (2012)
[3] L. Daubersies, J. Leng, and J.-B. Salmon, *Soft Matter* **8**, 5923 (2012)
[4] C. Loussert, A. Bouchaudy, and J.-B. Salmon, *Phys. Rev. Fluids* **1**, 084201 (2016)

Characterization of the main instability mechanisms in sessile droplet evaporation

Marc Medale[1], Sergey Semenov[2], David Brutin[1]

[1] Aix-Marseille Université, CNRS, IUSTI UMR 7343, Technopôle de Chateau-Gombert, 13013 Marseille, France
[2] Aix-Marseille Université, CNRS, MADIREL UMR 7246, Campus de Saint Jérôme, 13013 Marseille, France

E-mail: marc.medale@univ-amu.fr

While the involved physical phenomena are nowadays properly understood, sessile droplet evaporation remains an active research area since several experiments are not comprehensively explained. Indeed, recent experimental works have provided very interesting dynamics [1-5], whose characteristics strongly depend on control parameters, such as substrate temperature, ambient pressure and the various thermo-physical properties of substrate, droplet liquid and surrounding gas. There is no general agreement in the scientific community about the root-causes of the observed behavior. Are they hydro-thermal waves, Rayleigh-Bénard-Marangoni instabilities, or even something else?

One of the means to unmistakably answer this question would consist in conducting a stability analysis of the fully coupled and transient fluid flow, heat and mass transfer problem [6]. However, to do so, one must first overcome two major difficulties. The first one concerns the computation of the transient base state, whose complexity arises from the strong non-linearities associated with the three competing driving mechanisms: i) Stefan flow draining liquid towards the interface and more specifically to the triple line when the latter is pinned; ii) buoyancy in the liquid and vapor inducing thermo-solutal convection; iii) surface tension gradient along the liquid-gas interface inducing thermo-soluto-capilary convection. The second level of complexity to perform a relevant stability analysis consists in the intrinsic unsteadiness of the sessile drop evaporation process, in which several time scales co-exist.

For particular evaporation configurations, the dynamics of perturbations lies in a much shorter time scale than the total evaporation time, so in this case one can separate perturbations from the base state in a frozen time approach. This enabled us to find that the prevalent perturbations of the base state mainly come from the liquid droplet in which they trigger tridimensional flow structures. Therefore, we have then conducted 3D computations restricted to the droplet and its substrate with a one-sided model, in which heat and mass transfer across the liquid-gas interface is modeled in a semi-analytical way. These unsteady computations are performed during the first stage of the evaporation process in which the triple line is pinned to the substrate, so that the droplet diameter is kept constant, meanwhile the contact angle continuously decreases over time. The obtained results are in good agreement against several experiments performed either under terrestrial conditions or reduced gravity (parabolic flights), cf. figure 1.

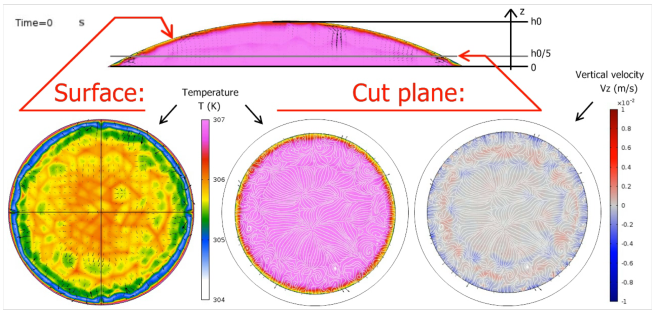

Figure 1 – 3D unsteady computations: thermal and velocity fields over the droplet surface and in a cut plane.

These one-sided model computations helped us to understand one of the potential instability scenarios. At the beginning, a torus roll appears in the wedge close to the pinned triple line and drives eventually an inner roll by viscous stress depending on the droplet aspect ratio (height/radius). As their intensity increases over time they split into thermo-capillary cells owing to Rayleigh-Bénard-Marangoni instability. Then, the number of cells evolves in time owing to the fact that the plane wavelength of these cells is closely related to their depth. As in the first stage of droplet evaporation the triple line is pinned the wetting angle consequently decreases, so does the liquid height, changing correspondingly the thermal Bond number (ratio of Rayleigh to Marangoni numbers). As the number of thermo-convective cells changes over time, hydro-thermal waves take place to redistribute the internal energy in the droplet. In the second stage of evaporation the droplet diameter continuously decreases, so does its perimeter, while the wetting angle stays roughly constant. Therefore the height of peripheral cells remains also constant; consequently their number has to decrease in order to match the droplet perimeter. Here again, hydro-thermal waves enter the game to redistribute the internal energy in the droplet.

The dark side of this approach is that computing times are still prohibitive to perform any parametric study this way. Therefore we have conducted a dimensional analysis to account for the main physical components of the problem. As usual, one assumes perturbations been able to destabilize the base state provided their energy reaches a certain amount of the total energy of the system, made-up of the liquid droplet and its surrounding gas (air + liquid vapor). To approximate these energy levels, prevalent terms have to be evaluated. In terrestrial conditions the two prevalent driving terms are buoyancy (thermal and solutal) together with surface tension gradients (thermo and soluto-capillary forces). The first one can be quantified thanks to thermal and solutal Rayleigh numbers, meanwhile the second one can be quantified by thermal and solutal Marangoni numbers. On the other hand, the energy involved in the evaporation process is related to the vapor flux throughout the droplet interface times the latent heat of vaporization. Therefore, a linear combination of all these terms enables to quantify the total energy involved in the evaporation process. Computing the latter in various experiments where instabilities have been either observed or not (cf. figure 2), enabled us to empirically determine a threshold of instability occurrence.

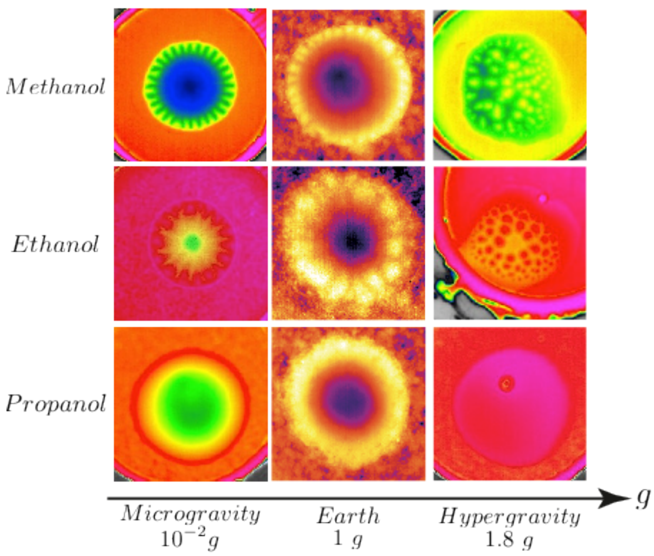

Figure 2 – Top view images from infra-red camera of sessile drop evaporation revealing somehow their internal flow patterns (same thermal conditions but different fluids and gravity levels).

This semi-empirical analysis enables us to discern instances of instability depending on experimental sets of parameters. However, some further work has to be performed to improve the described model in order to become predictable.

Acknowledgements. The authors acknowledge the French spatial agency (CNES) for funding support: parabolic flight experiments and second author's post-doc.

References

[1] K. Sefiane, A. Steinchen, R. Moffat. On hydrothermal waves observed during evaporation of sessile droplets. *Colloids&Surfaces A*, 365 (2010) 95–108.

[2] D. Brutin, B. Sobac, F. Rigollet, C. Le Niliot. Infrared visualization of thermal motion inside a sessile drop deposited onto a heated surface. *Exp. Therm. Fluid Sci.*, 35 (2011) 521–530.

[3] B. Sobac, D. Brutin. Thermocapillary instabilities in an evaporating drop deposited onto a heated substrate. *Phys. Fluids*, 24 (2012) 032103.

[4] F. Carle, B. Sobac, D. Brutin. Hydrothermal waves on ethanol droplets evaporating under terrestrial and reduced gravity levels. *J. Fluid Mech.*, 712 (2012) 614–623.

[5] G. Karapetsas, O.K. Matar, P. Valluri, K. Sefiane. Convective Rolls and Hydrothermal Waves in Evaporating Sessile Drops. *Langmuir*, 28 (2012) 11433–11439.

[6] H.A. Dijkstra, F.W. Wubs, A.K. Cliffe, E. Doedel, I.F. Dragomirescu, B. Eckhardt, A.Y. Gelfgat, A.L. Hazel, V. Lucarini, A.G. Salinger, E.T. Phipps, J. Sanchez-Umbria, H. Schuttelaars, L.S. Tuckerman, U. Thiele. Numerical Bifurcation Methods and their Application to Fluid Dynamics: Analysis beyond Simulation. *Commun. Comput. Phys.*, 15 (2014) 1–45.

GEL DROPS AND BEADS UNDER EXTREME DEFORMATIONS

Srishti Arora[1], Christian Ligoure[1], Laurence Ramos[1]

[1] Laboratoire Charles Coulomb, CNRS, Université de Montpellier, F-34095, Montpellier CEDEX 05, France
E-mail: laurence.ramos@umontpellier.fr

Impact experiments are conducted to investigate the behavior of gels under very large deformations. We focus on the dynamics of thin sheets freely expanding in air, which are produced by impacting a drop or a bead onto a small solid target or onto a cushion of liquid nitrogen, in order to suppress any dissipation process. To disentangle the role of capillary, viscous and elastic forces in the dynamics of the sheets, a large variety of materials is investigated, whose rheological characteristics are tuned over many orders of magnitude: viscous liquids, and permanent and transient gels. The reversible gels are self-assembled viscoelastic Maxwell fluids characterized by an elastic modulus, G_0, a relaxation time, τ, and a zero-shear viscosity, $\eta_0=G_0\tau$. The permanent gels are cross-linked polymer networks with an elastic modulus as low as 10 Pa.

For transient gels, when τ is shorter than the typical lifetime of the sheet (~ 10ms), we show that the dynamics of the sheet is similar to that of Newtonian viscous liquids with equal zero-shear viscosity. In that case, the maximal expansion of the sheet, d_{max}, decreases with η_0 and can be quantitatively accounted for by a model based on energy conservation arguments taking into account the viscous dissipation on the small solid target. On the other hand, when τ is longer than the typical lifetime of the sheet, the behavior drastically differs. The sheet expansion is strongly enhanced as compared to that of viscous samples with comparable zero-shear viscosity, but is heterogeneous with the occurrence of cracks, revealing the elastic nature of the viscoelastic fluid. By contrast, the sheets produced by the impact of ultrasoft solid beads composed of permanent gels can expand significantly but never break (fig. 1).

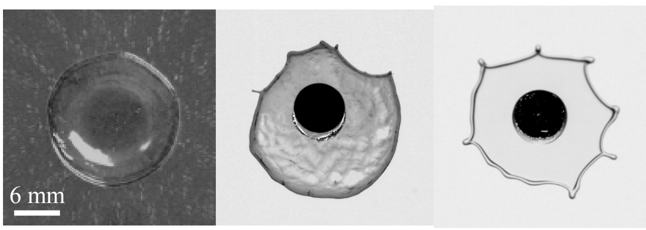

Fig. 1*: Images of a soft elastic drop (left), a viscoelastic gel drop (middle) and a viscous drop (right) impacting a solid surface covered with liquid nitrogen (left) and a small solid target (middle and right). Images are taken at the sheet maximal expansion. The scale is the same for the three images.*

Furthermore, we demonstrate that the surface tension of the drops and soft beads of gel must be taken into account in order to successfully model their expansion.

We define the maximum spread factor λ as d_{max} over d_0 (with d_0 the initial size of the drop or bead). Hence, once surface tension, elasticity, and viscous dissipation are quantitatively taken into account, we experimentally show a universal evolution of λ with the impact velocity normalized by the velocity of generalized elastic and capillary deformations. Figure 2 demonstrates that liquids (with surface tension in the range [28-72] mN/m), Newtonian fluids (with viscosity in the range [2-700] mPa.s, solids (with elastic modulus in the range [10-700] Pa) and viscoelastic gels (with G_0 in the range [2-20] Pa) all collapse onto a single mastercurve with λ proportional to the normalized velocity, as predicted by our model.

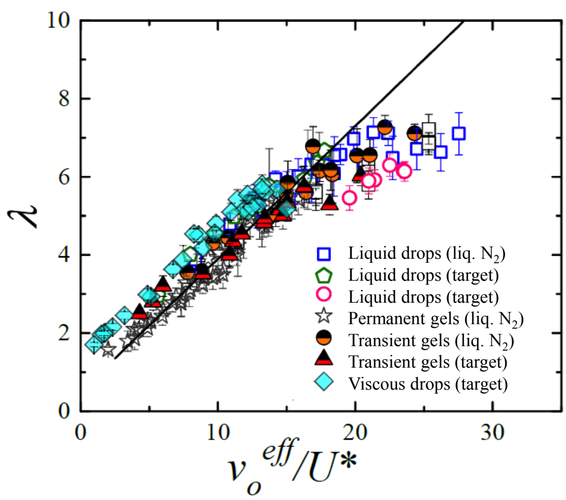

Fig. 2*: Maximal spreading factor (maximal expansion of the sheet normalized by initial drop/bead size) as a function of a normalized impact velocity that takes into account the viscous dissipation on the solid target divided by a velocity of generalized elastic and capillary deformations.*

Overall, we have quantitatively rationalized the spreading dynamics of impacting drops and beads for viscous, viscoelastic and elastic materials by taking into account surface tension, elastic deformation and viscous dissipation.

Acknowledgements. This work was supported by the EU (Marie Sklodowska-Curie ITN Supolen, Grant No. 607937).

References

[1] S. Arora, C. Ligoure, L. Ramos. Interplay between viscosity and elasticity in freely expanding liquid sheets. *Phys. Rev. Fluids* 1 (2016) 083302.
[2] S. Arora, L. Ramos, C. Ligoure. Submitted for a publication.

Microstructure Adjustment of Single Metal Droplets Generated via Drop-on-Demand Droplet Generator

Saeedeh Imani Moqadam, Nils Ellendt, Lutz Mädler

Foundation Institute of Materials Science (IWT), Department of Production Engineering, University of Bremen, Germany

E-mail: s.imani@iwt.uni-bremen.de

Introduction

Production of uniform micron sized droplets from molten materials is needed in many engineering applications such as placing solder balls on chips in electronics industries or rapid prototyping technologies similar to inkjet printing [1,2]. Pneumatic drop-on-demand (DOD) droplet generators are very promising and reliable for such applications as they can generate individual droplets while providing control over droplet size. Cooling single molten metal droplets is a well-defined reproducible process and a suitable method of producing uniform sized droplets. It is a well-suited process in which the microstructure of the metallic particles can be adjusted.

In the process of producing particles via droplet-on-demand generators, sudden short pulses of pressurized gas, created via a solenoid valve that opens and closes rapidly, are applied to the molten metal liquid in the crucible [3]. The melts are ejected from the nozzle and detach in the form of single droplets. Droplet-on-demand generators are cheap and convenient to use since there is no moving part in contact with the molten alloy and therefore there is no inherent restriction on the operating temperature [4].

In this study, metallic micro particles with various particle diameters are produced using a pneumatic droplet-on-demand generator. The resulting microstructure, physical and chemical properties are determined after defined cooling of the droplets. Correlation for the heat transfer of the falling molten droplet is provided. As there are no correlations of heat transfer coefficients validated in the desired high temperature range for molten alloys, we are focusing on evaluating how well the experimental results fit conventional models. In order to provide a comparison of results for different materials, single metal droplets of Cu-6%Sn and Al-4.5%Cu of various diameters were generated using a Drop-on-demand droplet generator.

Experiments

Our experimental setup for the micro metal droplet generation, mainly including a pneumatic droplet-on-demand generator is illustrated in Figure 1. The droplet-on-demand generator which is designed to produce spherical uniform metal droplets on demand comprises a solenoid valve, a graphite/ceramic crucible, and an induction heating furnace. The system is connected to a Nitrogen/Helium/Argon source both for purging and providing the pressure needed to force out and detach the single droplets. During the process, a function generator controls the solenoid valve to transfer pressure pulses to the molten liquid in the crucible. The detached droplets are subsequently cooled during the free fall and then quenched in water at a defined falling distance. Owing to the fact that the process parameters vary for different alloys and depend on the material properties, in-situ characterization and determination of the droplet size was performed throughout the experiments and the microstructures of the particles were determined.

Al-Cu and Cu-Sn alloys are widely used in industrial processes. In this study, single droplets of Cu-6%Sn and Al-4.5%Cu were produced. Setting the falling distance, melt te-

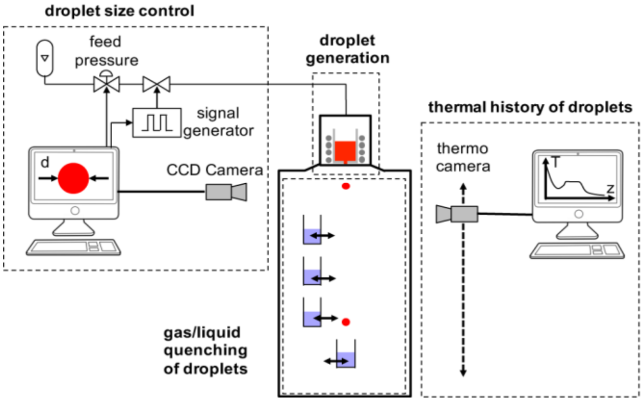

Fig.1. Schematic of experimental setup

-mperature and quenchant media, the particles were consequently cooled. The temperature of the droplet generator and molten metal were constantly observed during the process. The test chamber was continuously purged with nitrogen until the oxygen content of the system was below 30 ppm. A summary of the process conditions is shown in Table 1.

Table 1. Summary of process conditions of the droplet generation via DOD

Material	Al-4.5%Cu	Cu-6%Sn
Melt temperature(°C)	800	1200
Quenching atmosphere	Nitrogen	Nitrogen
Quenching distance(m)	0.82	0.82
Quenchant	water	water

Modeling

The thermal energy for a hot single metal droplet moving in a cooler fluid is transferred via forced convection and radiation while there is also heat conduction within the particle [5]. In order to model the cooling rate and solidification, the droplet motion and heat transfer were taken into account. In previous studies for modeling such droplets, a low temperature gradient was used to calculate the heat transfer coefficient in molten metal droplets. However, high temperature gradients (1000 K or more) should be considered due to high temperature difference between the ambient gas and the droplets. To model the heat transfer around the single droplets at elevated temperatures and the boundary layer, an axially symmetric 2D steady state conjugate heat transfer model was developed embracing the effect of large temperature gradient on the drag and convective heat transfer of the spheres. A correction to the Schiller-Naumann-Correlation [6] is introduced for non-isothermal conditions. The equations are solved via the commercial solver “Comsol Multiphysics 5.2” with a parametric fully-coupled solver. Finally, the experimental results are used to validate the model and the comparison of the heat transfer for the two selected alloys is made and the results are analyzed.

Analyses

Dendrite arm spacing is related to solidification time and cooling rate based on previous studies and available correlations [7,8]. In order to characterize the solidification structure of metals and alloys, determining the primary and secondary dendrite arm spacing (SDAS) is of high importance. The synthesized spherical micro samples are embedded, grinded, polished and etched hierarchically in order to determine their microstructure and consequently, the SDAS. Based on the correlation and experimental measurement of SDAS, the cooling rate of the spheres are determined. Furthermore, using the proposed model, the cooling rate of the falling molten droplets is calculated. The results of the model and experiments are in good agreement.

Acknowledgements. This research is supported financially by German Research Foundation (DFG) as the subproject U01 ‘Generation of spherical microscopic samples with single droplet solidification’ of the Collaborative Research Center (SFB) 1232 and the support is gratefully acknowledged.

References

[1] Liu Q, Orme M. High precision solder droplet printing technology and the state-of-the-art. Journal of materials processing technology. 2001 Sep 24;115(3):271-83.
[2] Gao F, Sonin AA. Precise deposition of molten microdrops: the physics of digital microfabrication. In Proceedings of the Royal Society of London A: Mathematical, Physical and Engineering Sciences 1994 Mar 8 (Vol. 444, No. 1922, pp. 533-554). The Royal Society.
[3] Chandra S, Jivraj R, inventors. Apparatus and method for generating droplets. United States patent US 6,446,878. 2002 Sep 10.
[4] Cheng SX, Li T, Chandra S. Producing molten metal droplets with a pneumatic droplet-on-demand generator. journal of materials processing technology. 2005 Feb 10;159(3):295-302.
[5] Wiskel JB, Henein H, Maire E. Solidification study of aluminum alloys using impulse atomization: Part I: Heat transfer analysis of an atomized droplet. Canadian metallurgical quarterly. 2002 Jan 1;41(1):97-110.
[6] L. Schiller, A. Naumann, A drag coefficient correlation, Vdi Zeitung, 1935; 77: 318
[7] Jones H. The status of rapid solidification of alloys in research and application. Journal of Materials Science. 1984 Apr 1;19(4):1043-76
[8] Choi, J. (1987). Einfluss der Erstarrungsgeschwindigkeit auf Gefüge und Eigenschaften technischer Kupferlegierungen. Max-Planck-Institut für Metallforschung

LUBRICATION PRESSURE GENERATED INSIDE AN AIR FILM BETWEEN A LEVITATING DROPLET AND A MOVING WALL

Erina SAWAGUCHI[1], Kai HAMA[1], Masafumi SAITO[1], Yoshiyuki TAGAWA[1†]

[1]Department of Mechanical Systems Engineering, Tokyo University of Agriculture and Technology, Tokyo, JPN

[†]E-mail: tagawayo@cc.tuat.ac.jp

When a droplet is deposited onto a moving wall, the droplet can steadily levitate. There is an air film between the levitating droplet and the moving wall. It is thought that lubrication pressure generated inside the air film dominantly sustains the droplet. However, experimental validation based on three-dimensional measurements has not been conducted although previous study[1] had conducted two-dimensional numerical simulations.

Our purpose is to calculate lubrication pressure distribution generated inside the air film between the levitating droplet and the moving wall in experiments. For calculation of lubrication pressure, we first verify the assumption that lubrication theory can be applied to the air film by using numerical simulation since Reynolds number in our experiment is around 2. We then calculate lubrication pressure, and assess global and local force balances on the levitating droplet. First, integrated value of lubrication pressure is compared with the levitating droplet's weight. Second, lubrication pressure is compared with the pressure due to surface tension and hydrostatic pressure. Based on these two balances, we experimentally clarify that lubrication pressure dominantly sustains the levitating droplet.

We first discuss whether lubrication theory is applied to the air film under the levitating droplet. Navier-Stokes equation of steady incompressible flow is

$$(\boldsymbol{u} \cdot \nabla)\boldsymbol{u} = -\frac{1}{\rho}\nabla p + \frac{\mu}{\rho}\nabla^2 \boldsymbol{u}, \tag{1}$$

where $\boldsymbol{u}$=(u, v, w), p(x, y), ρ, and μ respectively stand for velocity vector, lubrication pressure, density of air, and viscosity coefficient of air. A coordinate system of the levitating droplet is shown in Fig. 1(a). We set x-axis to the direction along wall movement, y-axis to the direction in front of paper and z-axis to the vertical direction to wall. The origin is located at the position where the center of droplet is projected onto the wall.

When Reynolds number is sufficiently smaller than 1, that is to say, when inertia term is sufficiently smaller than viscosity term, inertia term can be neglected. Thus, Eq. (1) is rewritten as

$$-\nabla p + \mu \nabla^2 \boldsymbol{u} = 0. \tag{2}$$

In addition, when the air film thickness h(x, y) is much smaller than the length scale along mainstream, we can assume velocity w vertical to the wall to be 0. Consequently, we set up simultaneous equations of Eq. (2) and equation of continuity, and then obtain Reynolds equation[3] as

$$\frac{\partial}{\partial x}\left(\frac{h^3}{\mu}\frac{\partial p}{\partial x}\right) + \frac{\partial}{\partial y}\left(\frac{h^3}{\mu}\frac{\partial p}{\partial y}\right) = 6U\frac{\partial h}{\partial x}, \tag{3}$$

where U denotes wall velocity. Eq. (3) is the governing equation of the air film in applying lubrication theory.

We show a schematic view of our experimental setup in Fig. 1(b)[2]. A hollow glass cylinder rotates on its axis in the horizontal direction with constant circumferential velocity U=1.57 m/s. A droplet is deposited onto the inner wall of the cylinder, resulting in its steady levitation. The three-dimensional shape of the air film between the droplet and the wall is measured by using interferometric method. Monochromatic incident light with wavelength 630 nm through coaxial zoom lens reflects off the droplet's bottom and the wall respectively, which makes interference fringes. We obtain an image of the fringes with a high-speed camera (FASTCAM SA-X, Photron), and reconstruct three-dimensional shape of the air film (shown in Fig. 2)[2]. In our experiment, we use the droplet of silicone oil (surface tension σ=20.9 mN/m, density ρ_s=960 kg/m^3, and viscosity ν=100 cSt) with diameter 3.16 mm.

In this paper, we conduct numerical simulation in order to consider whether lubrication theory can be applied to the air film under the levitating droplet. We compute pressure distributions generated inside the air film with two kinds of governing equations: (i) general Navier-Stokes equation (Eq. (1)) and equation of continuity, (ii) Navier-Stokes equation neglecting inertia term (Eq. (2)) and equation of continuity. We investigate the effects of inertia term by comparing two pressure distributions, and that of velocity w vertical direction to the wall to wall velocity U. Consequently, we consider whether lubrication theory can be applied to the air film. We use COMSOL Multiphysics, which is the simulation software using the finite elemental methods. We assume that the gas-liquid interface is a solid wall with a no-slip condition because the measured air film shape is steady and the velocity of the droplet's surface is negligible with respect to the wall velocity. The velocity of the moving wall is U along x-axis and the pressure outside experimental calculation area is atmospheric pressure p_0 (shown in Fig. 1(a)).

After confirming the assumption that lubrication theory can be applied to the air film, we experimentally calculate lubrication pressure by applying lubrication theory (Eq. (3)). In order to solve Eq. (3), we conduct iterated calculation by central finite difference method in MATLAB. Now, we use the air film shape shown in Fig. 2(a) for our experimental calculation. Then, we verify two kinds of balances about lubrication pressure generated inside the air film. First, we compare the lift force L acting globally on the levitating droplet with the droplet's weight W. Lift L and weight W are calculated by following equations:

$$L = \iint p\,dx\,dy, \tag{4}$$

$$W = mg\cos\theta, \tag{5}$$

where m, g and θ respectively stand for mass of the droplet, gravitational acceleration and the angle between the direction normal to the wall and that of gravity (shown in Fig. 1(a)). Second, we verify a local balance of lubrication pressure at gas-liquid interface. It is thought lubrication pressure balances with surface tension and hydrostatic pressure[1]. Therefore, we can write the equation of balance at the droplet's bottom,

$$2\sigma(\kappa_0 - \kappa) + \Delta\rho g[(z_0 - z)\cos\theta + (x_0 - x)\sin\theta] = p, \tag{6}$$

where $\Delta\rho$, κ and κ_0 respectively stand for density difference between air and the droplet, curvature at the gas-liquid interface and curvature at the point (x_0, y_0, z_0). Now, there is the point (x_0, y_0, z_0) on blue line in Fig. 2(a), and x_0=-d_t/2, y_0=0, z_0=h(x_0, y_0) where d_t denotes diameter of experimental calculation area. We calculate sum pressure p_s of surface tension and hydrostatic pressure, and then compare it with lubrication pressure.

Fig. 3(a) and (b) respectively show pressure distribution computed by governing equations (i) and (ii). Fig. 4(a) shows lubrication pressure p calculated by applying lubrication theory (Eq. (3)). All pressure distributions have positive pressure in a whole area except the part of downstream side. Both peak values of positive and negative pressure agree within 4 % between two pressure distributions, and integrated values of pressure distributions also agree within 6 %. In addition, velocity w vertical to the wall has much small value within 2 % of wall velocity U in the flow field with governing equations (i). Therefore, pressure is not affected by inertia term in Navier-Stokes equation and velocity w. In short, lubrication theory can be applied to the air film between the levitating droplet and the moving wall.

We then assess local and global force balances on the levitating droplet experimentally. First, we calculate the lift force L by Eq. (4) and the droplet's weight W by Eq. (5). Consequently, we obtain quantitative agreement between L=(1.06±0.05)×10^{-4} N and W=(1.11±0.02)×10^{-4} N. Second, Fig. 4(b) shows the sum pressure p_s of surface tension and hydrostatic pressure (left side of Eq. (6)). Both pressures by lubrication theory (Eq. (2)) and by Eq. (6) have positive pressure in a whole range of experimental calculation area except area near the downstream rim. Two pressure distributions indicate reasonable agreement although the peak values of negative pressure are different due to the limit of interferometric method. Therefore, we verify that lubrication pressure locally balances with surface tension and hydrostatic pressure at the droplet's bottom.

In summary, we have confirmed that lubrication pressure can be applied to the air film by using numerical simulation, and then calculated lubrication pressure generated inside the air film between the levitating droplet and the moving wall. Then, we have verified two kinds of force balances. First, we obtain quantitative agreement between the lift force integrating lubrication pressure and the droplet's weight. Second, we experimentally verify that lubrication pressure locally balances with surface tension and hydrostatic pressure. In conclusion, to the best of the authors' knowledge, for the first time, we experimentally verify that lubrication pressure dominantly sustains the levitating droplet.

References

[1] H. Lhuissier, Y. Tagawa, T. Tran, C. Sun. Levitation of a drop over a moving surface. *J. Fluid Mech.*, Vol. 733 (2013), **R4**.

[2] M. Saito, Y. Tagawa. Lift force acting on a levitating drop over a moving surface. *Transactions of the JSME* (in Japanese), **81**, No. 825, p.15-00059 (2015).

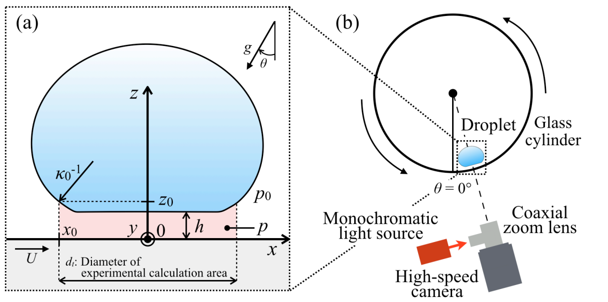

Fig. 1: (a) Coordinate system of the levitating droplet. (b) Schematic view of our experimental setup.

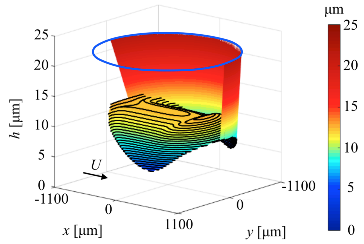

Fig. 2: Measured air film shape. A front part of the air film is not displayed.

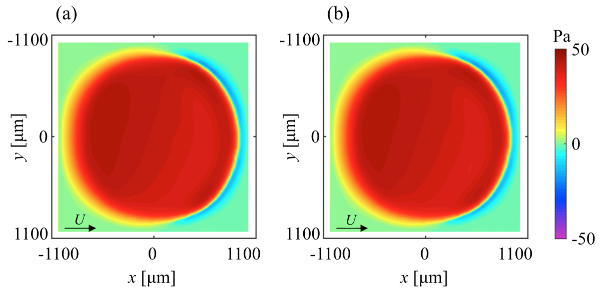

Fig. 3: Pressure distribution computed respectively (a) by governing equations (i) and (b) by (ii).

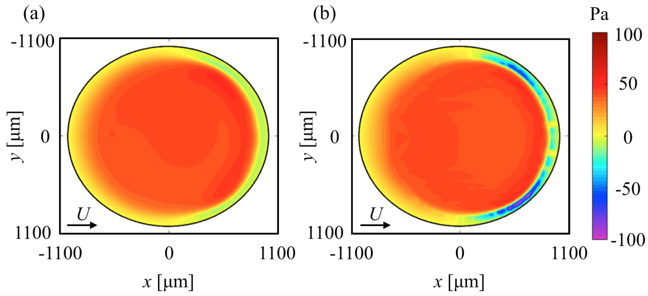

Fig. 4: (a) Lubrication pressure p calculated by applying lubrication theory (Eq. (3)) and (b) the sum pressure p_s of surface tension and hydrostatic pressure by Eq. (6).

Oscillation mode transition in sessile droplets induced by evaporation

Apratim Sanyal[1], Saptarshi Basu[1]

[1]Department of Mechanical Engineering, IISc, Bangalore, KA, INDIA

E-mail: sanyal6ap@gmail.com

In the present work we have devised an innovative yet simple methodology of exciting multiple oscillation modes in a single droplet without varying the driving frequency *f*. This is achieved simply by allowing the droplet to evaporate [1,2]. Different modes of oscillations are excited each at different instances in the evaporation process. The substrates chosen are PDMS (10:1) coated glass slides which are attached to the platform of an electrodynamic shaker. The fluid used is de-ionised water. The deployed droplet volume, equatorial radius and contact angle are 5.4±0.4 μl, 110±1° , and 1.2±0.02 mm respectively. A transparent enclosure is mounted atop the platform covering the droplets from any external convection. The frequencies chosen are *f*=400 to 800Hz in steps of 100Hz. The oscillated droplet shapes are imaged using Photron FASTCAM Mini UX100 camera and a zoom lens. The amplitude of the shaker is kept within 12±1.5 microns in each run. The ambient temperature and relative humidity is maintained at 25±0.5°C and 42.5±2.5%.

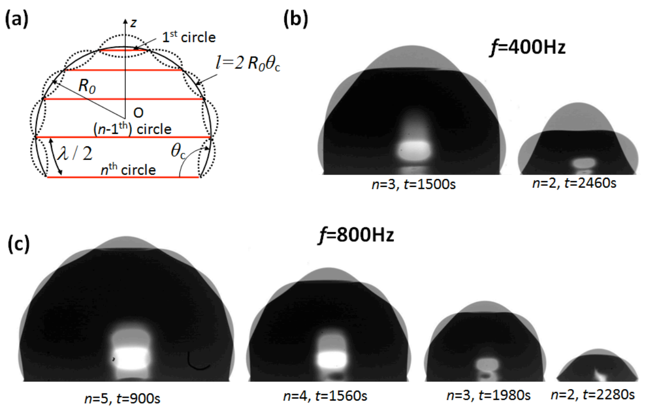

Fig 1 (a) Schematic showing interface oscillations and relevant dimensions. (b) Resonance of different modes at *f*=400Hz (c) Resonance of different modes at *f*=800Hz.

A previously proposed method has been adopted to describe the oscillation modes [3]. Fig 1 (a) shows a schematic with oscillating droplet shapes (dotted lines) against a hypothetical spherical dome shape (solid line). This hypothetical shape represents the stationary interface. The entire configuration is assumed axisymmetric along the axis z. R_0 and θ_c are the spherical radius and static contact angle of this hypothetical shape. The interface oscillations form a standing wave. The nodes of the wave along constant values of z form nodal circles (red lines). It is seen in the present work that the contact line is non-oscillating. Thus it is also a nodal circle. According to the adopted approach the mode order *n* of oscillation is given by the number of such circles. The amplitude at the apex is Δh. Resonance of a mode is detected by local maxima in Δh.

We consider the dispersion relation for capillary waves [4] -

$$f = \alpha\left(\frac{2\pi\gamma}{\rho\lambda^3}\right)^{\frac{1}{2}} \tag{1}$$

ρ=1000 Kg/m^3 and γ=0.072 N/m are the density and surface tension of water, λ is the wavelength of the standing interface wave and α is a correction factor [4]. The interface length l can be expressed at resonance of mode *n* as -

$$\left(n-\frac{1}{2}\right)\lambda = l = 2R_0\theta_c \tag{2}$$

From (1) and (2) we can derive an expression for the resonance frequency f_n of mode *n* as [1] -

$$f_n^{\,2} = \frac{\alpha^2\pi^2\gamma}{12}\left(n-\frac{1}{2}\right)^3\frac{g(\theta_c)}{m} \tag{3}$$

The droplet mass is

$$m = \rho\pi R_0^{\,3}\left(\cos^3\theta_c - 3\cos\theta_c + 2\right)\big/3$$ and

$$g(\theta_c) = \left(\cos^3\theta_c - 3\cos\theta_c + 2\right)\big/\theta_c^{\,3}.$$

Conventional mode resonance detection in droplets involve tuning the driving frequency *f* to match f_n for desired *n*. We have proposed an alternate method where there is no need to tune *f* [1]. Droplets oscillating at constant *f* self tune to resonances of various modes *n* when allowed to evaporate. Evaporation reduces the mass *m* and static contact angle θ_c. From (3) it can be said that for a particular value of *n*, f_n will keep on increasing with evaporation. So *f* will automatically match with f_n for each *n* at different instances in evaporation. Since f_n is increasing the modes excited will be in descending order. As an example for a droplet oscillating at *f*=800Hz, mode *n*=5 will be excited first, then *n*=4 and so on till *n*=2 (lowest allowable mode). This is clearly shown in the high speed images in Fig 1 (b) and (c).

To quantify this evaporation driven natural tuning of mode resonances we have proposed a parameter based on (3) [1]. The variations of *m* and θ_c can be combined into a single parameter Ω -

$$\Omega = \frac{f^2 m}{\gamma g\left(\theta_c\right)} \quad (4)$$

In other words evaporation brings about variation in Ω to excite mode resonances in a single oscillating droplet. Plotting $\Delta h/R_0$ against Ω represents an evaporation driven spectrum shown in Fig 2 [1].

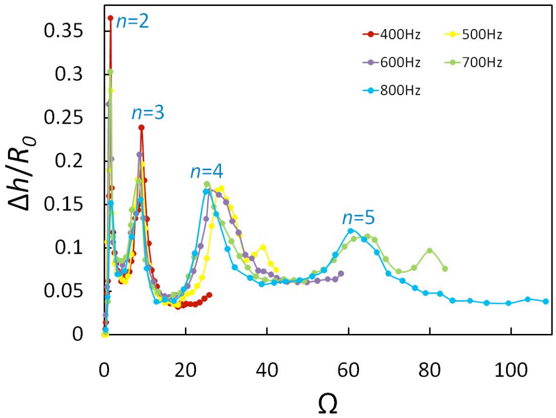

Fig 2. Resonance spectrum based on Ω [1].

Note that Ω decreases with *t* so time progresses in the negative direction of the horizontal axis in Fig 2. From the merging of the resonance peaks at different values of *f* we see that the adopted theory for 1D capillary waves works fairly accurately for the present case.

A physical explanation for the mode transition is as follows [1]. From (1) we see that *λ* should not vary with evaporation. So as the interface length *l* reduces, and the distance between nodal circles i.e. *λ*/2 is kept constant, all the nodal circles (except the contact line) have to shift downwards. Now in Fig 1a the circles are numbered from the top to bottom. So as the nodal circles shift, the $(n\text{-}1)^{\text{th}}$ circle approaches the contact line (n^{th} circle) and subsequently merges with it. Thus the mode order is reduced from *n* to *n*-1 resulting in mode transition.

Acknowledgements. This work is supported by Department of Science and Technology, Government of India.

References

[1] A. Sanyal, S. Basu. *Langmuir*, (2016) **32** (19), 4784-4791.
[2] A. Sanyal, S. Basu. *Chemical Engineering Science*, (2017) **163**, 179-188.
[3] X. Noblin, A. Buguin, F Brochard-Wyart. *The European Physical Journal E*, (2004) **14** (4), 395-404.
[4] J.S. Sharp. *Soft Matter*, (2012) **8** (4), 399-407.

EFFECT OF POLYMER-COATED GOLD NANOPARTICLE SURFACTANTS ON PAIRWISE DROP COALESCENCE

Carolina Vannozzi

Department of Chemical Engineering, UCSB, Santa Barbara, CA, USA

E-mail: carolina.vannozzi@gmail.com

Polymer-coated gold nanoparticles (PGNPs) can substitute block-copolymer (BCs) compatibilizers in immiscible polymer blends. However, the interfacial gold cores may enhance the thin film disjoining pressure (Π^{part}), leading to a drainage time (*td*) reduction. This could explain previous four-roll mill experiments [1] of two drops stabilized by PGNPs, undergoing flow-induced coalescence in extensional flow, that showed a puzzling 70% reduction of *td*, compared to drops stabilized by BCs, despite PGNPs being more surface active. Since Π^{part} was unknown, its effect could not be assessed [1].

Here, we quantify the effect of Π^{part} on *td* through scaling and simulations, by treating PGNPs as surfactants and employing our newly derived analytical expression for Π^{part}, function of the nanoparticle concentration and size [2]. We also compare it to the effects of the surface Peclet number, related to PGNP interfacial diffusivity (D_s), and the Marangoni number.

Flow-induced coalescence was very sensitive to all three parameters. 3nm gold core particles reduced *td* by 60% for touching cores, increasing significantly the coalescence probability of sub-micrometric drops, but this reduction softened considerably with decreasing particle concentration.

To obtain the same experimental reduction, enhanced Π^{part} had to be present together with D_s higher than its Stokes-Einstein estimate, suggesting its break-down similar to bulk [3].

Acknowledgement

CNSI supercomputer facility at UCSB where the simulations were performed.

References

[1] M. Borrell, L.G. Leal. *Langmuir*, (2007) **23**, 12497-12502.
[2] C. Vannozzi. *Soft Matter*, (2012) **8**, 5214.
[3] A. Tuteja, M. E. Mackay, S. Narayanan, S. Asokan, M. S. Wong. *Nanoletters* (2007).

Oleoplaning droplet on lubricated surfaces

Dan Daniel[1], Jaakko V.I. Timonen[1,2], Ruoping Li[3], Seneca J. Velling[3], and Joanna Aizenberg[1,3,4*]

[1]John A. Paulson School of Engineering and Applied Sciences, Harvard University, Cambridge, MA 02138, USA
[2] Department of Applied Physics, Aalto University School of Science, Espoo, FI-02138, Finland
[3] Wyss Institute for Biologically Inspired Engineering, Harvard University, Cambridge, MA 02138, USA
[4]Department of Chemistry and Chemical Biology, Harvard University, Cambridge, MA 02138, USA
E-mail: jaiz@seas.harvard.edu

Recently, there has been much interest in using lubricated surfaces to achieve extreme liquid-repellency. On such surfaces, a foreign droplet immiscible with the underlying lubricant layer slides off at a small tilt angle < 5° [1,2]. This behavior was hypothesized to arise from the absence of droplet-solid contact due to a thin intercalated lubricant film beneath the droplet, but this has not been confirmed unambiguously [3,4]. Here, using dual-wavelength, confocal reflection interference contrast microscopy, we are able to visualize the intercalated lubricant film with nanometric resolution (Fig. 1). Under static conditions, three lubrication states are observed: a stable continuous (nanometric) film, partially dewetted film and fully displaced film. We attribute the wetting/dewetting behavior to a combination of interfacial tensions effects and long-ranged van der Waals' interactions. On the other hand, under dynamic conditions, we observe a transition to a micron-thick lubricant film, whose thickness is velocity-dependent and obeys the Landau-Levich-Derjaguin law (Fig. 2). This dynamic lubrication state can be stable, even if the film is unstable under static conditions. In this oleoplaning state – akin to tires hydroplaning on a wet road – we measure minimal dissipative forces (down to 0.1 μN for 1 μl droplet using a cantilever sensor) and show that they originate from viscous dissipation and not from contact line pinning. The techniques and new mechanistic insights presented in this study will inform future work on the fundamentals of wetting for lubricated surfaces and enable their rational design.

Acknowledgements. The work was supported partially by the ONR MURI Award No. N00014-12-1-0875 and by the Advanced Research Projects Agency-Energy (ARPA-E), U.S. Department of Energy, under Award Number DE-AR0000326. J.V.I.T. was supported by the European Commission through the Seventh Framework Programme (FP7) project DynaSLIPS (project number 626954). We acknowledge the use of the facilities at the Harvard Center for Nanoscale Systems supported by the NSF under Award No. ECS-0335765 and at the Harvard Materials Research Science and Engineering Center (MRSEC) under Award No. DMR-1420570.

References

[1] T.-S. Wong, S. H. Kang, S. K. Tang, E. J. Smythe, B. D. Hatton, A. Grinthal, and J. Aizenberg, *Nature*, (2011) **477**, 443-447

[2] A. Lafuma and D. Quéré, *EPL*, (2011) **96**, 56001

[3] J. D. Smith, R. Dhiman, S. Anand, E. Reza-Garduno, R. E. Cohen, G. H. McKinley, and K. K. Varanasi, *Soft Matter*, (2013) **9**, 1772

[4] F. Schellenberger, J. Xie, N. Encinas, A. Hardy, M. Klapp er, P. Papadopoulos, H.-J. Butt, and D. Vollmer, *Soft Matter* (2015) 11, 7617

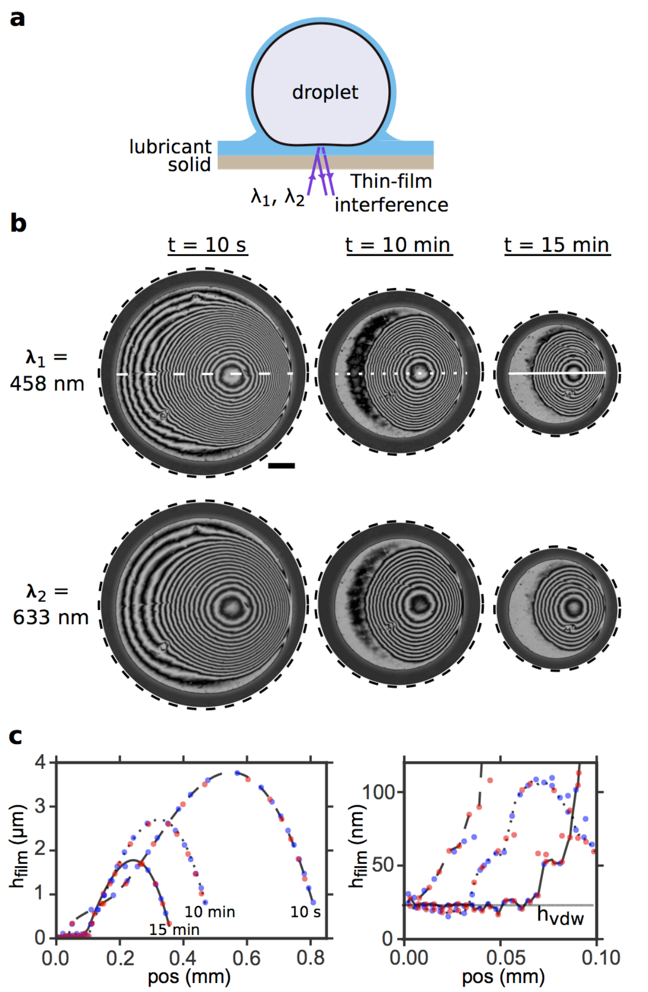

Fig 1. Visualization of the lubricant film profile using dual-wavelength, confocal RICM.

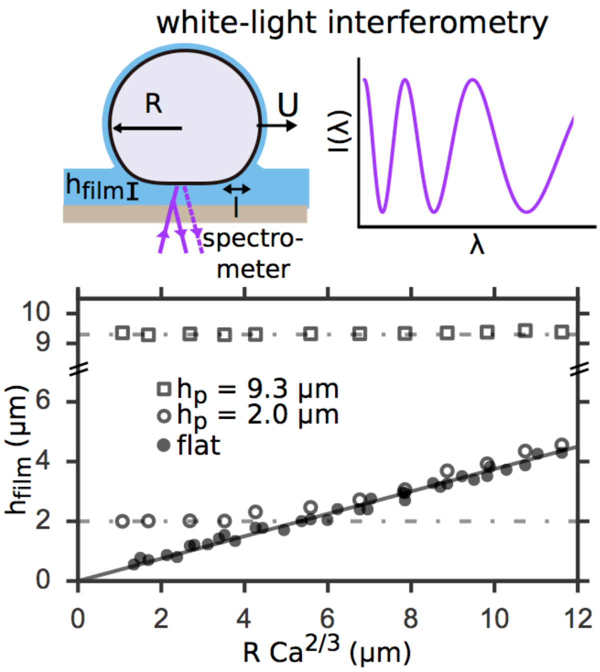

Fig. 2. Micron-thick lubricant film is stabilized under motion and follows the Landau-Levich-Derjaguin law.

Enhancing drainage and thinning of a liquid film between a bubble and a solid using surface waves

Amihai Horesh[1], Matvey Morozov[1], Ofer Manor[1]

[1]Department of Chemical Engineering, Technion, Haifa, Israel

E-mail: manoro@technion.ac.il

The drainage of liquid films determines the fate of an abundant number of natural phenomena and engineering applications, from the stability of suspensions and emulsions and the efficiency of particulate separation and coating procedures to the stability of tear films and the adhesion of bacteria to solids. Here we explore the physics of drainage of a micron thick liquid film trapped between a solid and a micro-bubble while it is exposed to a propagating MHz-frequency Rayleigh surface acoustic wave (SAW).

The most interesting observation we report is related to the rate of drainage. In the absence of the SAW, the intermediate liquid film between the bubble and the solid drains due to capillary stresses for a period of one to twelve hours (according with the viscosity of the draining liquid in our experiments). In the presence of the SAW, the drainage of the film is reduced to minutes. The viscous penetration of the wave into the liquid generates an acoustic flow that breaks the symmetry of the liquid film. The film deforms in a manner akin to a kinematic wave until capillary stresses, resisting this motion, impose a self-similar film geometry, supporting fast drainage of liquid out of the film.

We explored this intriguing phenomenon using both experiment and theory. We designed the experimental system shown in figure 1, where we utilized previous findings on the geometry of long bubbles moving in rectangular tubes. By abruptly arresting the motion of a bubble in a microfluidic channel we imposed a model system for the drainage of the intermediate film between the bubble and the solid surface of the channel. In particular, this procedure allows for reducing the dimensionality of the drainage. The micron thick film between the bubble and the solid was then exposed to a front of a SAW, propagating in the solid substrate of the channel and along the draining path. This event is illustrated in figures 2 and 3. We monitored the spatiotemporal variations in the thickness of the intermediate film between the bubble and the substrate using the diffraction of monochromatic light.

A corresponding theory is in good agreement with experiment, highlighting the struggle between acoustic and capillary mechanisms in the microenvironment explored. In particular, both theory and experiment predict the time of drainage support a power low with the ratio between the acoustic and capillary stresses in the liquid film.

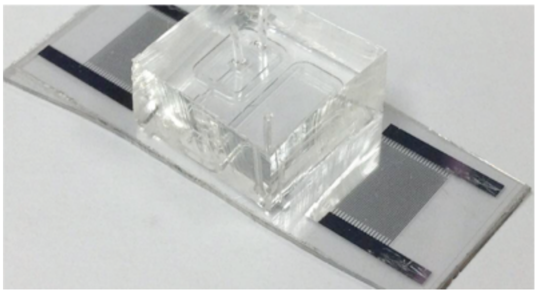

Figure 1: SAW microfluidic platform for undertaking the experiments where a micro-bubble near a solid surface is exposed to MHz surface acoustic waves.

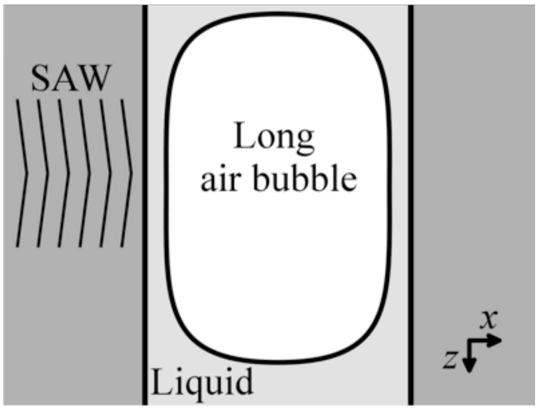

Figure 2: A view from above of the bubble in the channel while a surface acoustic wave is propagating in the substrate.

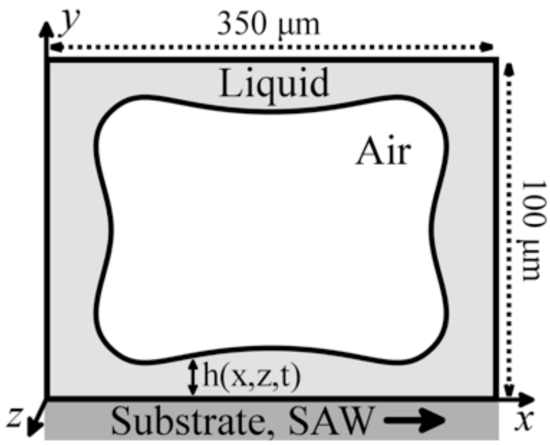

Figure 3: A cross section view of the bubble in a channel of a rectangular circumference, while a surface acoustic wave is propagating in the substrate below.

Acknowledgements: This research we supported by the Israel Science Foundation (ISF)

An Evaporation Ouzo Drop on a Superamphiphobic Surface[1]

Huanshu Tan[1], Christian Diddens[2], Michel Versluis[1], Hans-Jürgen Butt[3], Detlef Lohse[1,4], Xuehua Zhang[5,1]

[1] Physics of Fluids group, Department of Science and Technology, Mesa+ Institute, and J. M. Burgers Centre for Fluid Dynamics, University of Twente, P.O. Box 217, 7500 AE Enschede, The Netherlands
[2] Department of Mechanical Engineering, Eindhoven University of Technology, P.O. Box 513, 5600 MB Eindhoven, The Netherlands.
[3] Max Planck Institute for Polymer Research, 55128 Mainz, Germany
[4] Max Planck Institute for Dynamics and Self-Organization, 37077 Göttingen, Germany
[5] Soft Matter & Interfaces Group, School of Engineering, RMIT University, Melbourne, VIC 3001, Australia

E-mail: h.tan@utwente.nl; d.lohse@utwente.nl; xuehua.zhang@rmit.edu.au

Evaporation of multi-component drops is crucial to various technologies and has numerous potential applications because of its ubiquity in nature. We use an ouzo drop as a model for a ternary liquid mixture and investigate its evaporation process on surface. The Greek drink Ouzo (or the French Pastis or the Turkish Raki) is a miscible solution and primarily consists of water, ethanol and anise oil. When the water concentration is increased by adding water or by reducing ethanol, the solution becomes opaque due to the "ouzo effect", i.e. the spontaneous nucleation of oil microdroplets [2].

Recently, we discovered how the preferential evaporation of ethanol triggers the "ouzo effect" in an evaporating ouzo drop [3]. Four life phases can be distinguished during the drying. As a remarkable phenomenon, we found that the evaporation-triggered nucleation starts at the rim of the ouzo drops, which is attributed to the flat drop geometry, namely the singularity at the rim.

In the current work, we performed evaporation experiments on a superamphiphobic, which is both superhydrophobic and superoleophobic, to achieve low wettability for the ouzo drops. In this case, the ouzo drops initially hold a large static contact angle (larger than 150^{o}). Thus the singularity at the three phase contact line is absent. Codetermined by the evaporation flux distribution and volatility difference between water and ethanol, the evaporation-triggered Ouzo effect preferentially occurs at the apex of the drop. Our numerical simulations also reproduce this observation. During the evaporation process, two distinct slopes characterize the volume decrease of the ouzo drop. The initial steep slope is dominantly caused by the evaporation of ethanol, followed by the slower evaporation of water. At later stages, thanks to Marangoni forces, a new remarkable phenomenon appears: part of the nucleated oil microdroplets form an oil shell wrapping up the ouzo drop, instead of forming a persistent oil ring at the contact line. Theoretically, based on Popov's diffusion model for quasi-steady natural evaporation of pure liquid drops [4], we also propose an approximate diffusion model for the drying characteristics of ouzo drops with more than one component. The generalized diffusion model predicts the evaporation of the drops in agreement with experiment and numerical simulation results.

This work highlights the influence of substrate on the evaporation process of ouzo drops. A better understanding of the dynamics of an evaporating ouzo drop may provide valuable information for the investigation of the evaporation process of multi-component mixture drops.

Evaporating ouzo droplets on superamphiphobic surface. The diameter of the droplets is around 1.5 mm.

Acknowledgements. We thank Alvaro Marin, Pengyu Lv, Hans Kuerten, Gabriele Schäfer, Florian Geyer and Sanghyuk Wooh for their support to this work. We also acknowledge the China Scholarship Council (CSC, file No. 201406890017), Océ-A Canon Company, the Dutch Technology Foundation STW, and the Dutch Organization for Research (NWO), the Ministry of Economic Affairs, and the Netherlands Center for Multiscale Catalytic Energy Conversion (MCEC) and the Max Planck Center Twente for Complex Fluid Dynamics for financial support.

References

[1] H. Tan, C. Diddens, M. Versluis, H. Butt, D. Lohse and X. Zhang, Soft Matter, 2017, DOI: 10.1039/C6SM02860H.
[2] S. A. Vitale, and J. L. Katz, *Langmuir*, (2003) **19**, 4105-4110.
[3] H. Tan, C. Diddens, P. Lv, J. G. M. Kuerten, X. Zhang and D. Lohse, *PNAS*, (2016) **113**, 8642–8647.
[4] Y. O. Popov, *Phys. Rev. E*, (2005) **71**, 036313.

Measured Vapor Distributions Above Sessile Drops and Implications for Vapor Transport

Peter Kelly-Zion[1], Christopher Pursell[2], Hoa Nguyen[3], Michael Batista[3], Greg Wassom[1], Taylor Piske[1]

[1]Department of Engineering Science, Trinity University, San Antonio, TX, USA
[2] Department of Chemistry, Trinity University, San Antonio, TX, USA
[3] Department of Mathematics, Trinity University, San Antonio, TX, USA

E-mail: plkelly@trinity.edu

The vapor distributions surrounding sessile drops of hexane, 3-methylpentane (3MP) and methanol were measured using infrared spectroscopy and computed tomography. The measurement technique is based on the procedure described in reference [1]. Knowledge of the vapor distribution enables analyses of the relative effects of diffusion and natural convection on the evaporation rate. When the molecular weight of the vapor is heavier than that of the background gas, natural convection tends to compress the height of the vapor distribution and extend it radially. Consequently, a condition with strong convection is marked by a relatively flat and wide vapor distribution compared to that of a strictly diffusive vapor transport condition, which has an approximately hemispherical shape. Thus, the measured vapor distribution provides a qualitative indication of the relative strengths of convection and diffusion. Quantitative information about the rate of diffusion are computed from the concentration gradient and, by comparing that rate to the overall evaporation rate, inferences about the convective flow may be made.

The drop evaporation occurred in air at room temperature conditions. Hexane and 3-methylpentane were chosen for this study because their evaporation rates are substantially influenced by natural convection [2-4]. Hexane and 3MP both have moderately high equilibrium vapor pressures and molecular weights that are substantially greater than that of air. Thus the density of their vapor-air mixtures near the surface of the drop is substantially higher than the ambient gas density, and this density difference instigates the convective flow.

Methanol, which is expected to have predominately diffusive vapor transport, was chosen to provide contrast to the strong convective transport of hexane and 3MP. The molecular weight of methanol is nearly equal to the molecular weight of air and so there is expected to be very little difference between the density of the vapor-air mixture at the surface of the drop and the density of the ambient gas; and consequently little if any natural convection occurring. Furthermore, since the diffusion coefficient for methanol is more than twice the value for hexane and 3MP, and the equilibrium vapor pressure is comparable (just a little lower) to that of hexane, it is expected that the rate of diffusive transport for methanol vapor is much higher than that for hexane or 3MP vapor.

The measured vapor distributions for hexane and methanol are presented in Fig. 1. The distributions are presented in a vertical plane passing through the center of the drop. Axisymmetry was assumed in the computed tomography process used to generate the distributions. In all cases, the sessile drop had a contact line radius of 6.5 mm. The distribution for 3MP is very similar to the distribution for hexane and is not shown.

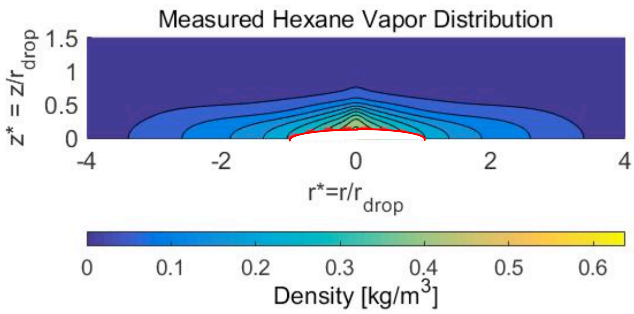

(a)

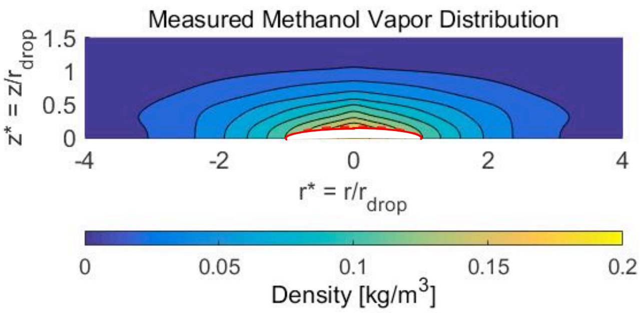

(b)

Figure 1. Measured vapor distributions surrounding a hexane drop (a) and a methanol drop (b). The white region outlined in red indicates the sessile drop. The colormaps indicate vapor density and range from 0 (dark blue) to the saturated density (bright yellow), which are different for the two drops.

The shape of the hexane vapor distribution is relatively flat and shows the influence of a natural convective flow that is down and radially outward from the drop. This behavior agrees with observations from schlieren movies of the vapor flow [1,4]. In comparison to the hexane (and 3MP) distributions, the methanol vapor distribution extends further up and appears more like the hemispherical distribution that is expected when vapor transport is by diffusion alone. Still, considering that the molecular weight of methanol (32 g/mol) is nearly equal to that of air (29 g/mol), it was expected that the distribution would have a more hemispherical shape.

With knowledge of the vapor distribution, the gradient may be computed in order to evaluate the diffusive flux. The diffusive flux was integrated along the surface of a control volume surrounding the drop to obtain the net rate of diffusion out of the control volume. Figure 2 shows a cylindrical control volume surrounding a methanol drop and the diffusive flux along the surface of the control volume. The white arrows indicate the magnitude of the diffusive flux (length) and the direction. Only the component normal to the surface was employed to compute the total diffusive rate from the control volume. For a steady-state condition the evaporation rate is equal to the sum of the vapor transport by diffusion and convection and therefore by comparing the diffusion rate to the evaporation rate the strength of convection may be inferred. Furthermore, by varying the dimensions of the control volume, regions where convection and diffusion are high may be determined.

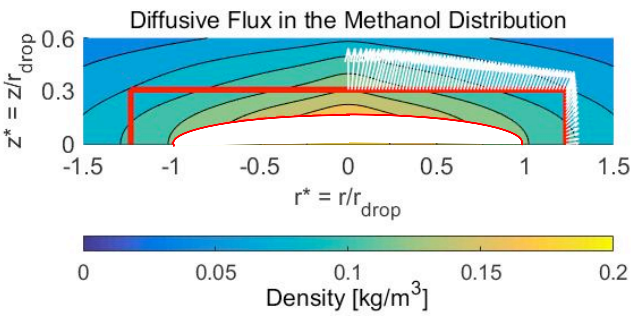

Figure 2. Diffusive flux along the surface of a control volume surrounding a methanol drop. For clarity, the flux is shown on half of the control volume.

Figure 3 shows the diffusion rate as a function of control volume height and radius. Included in the figures are dashed lines indicating the evaporation rates computed from the steady-state Laplace equation for diffusion-limited evaporation. As may be seen, the diffusion rates computed from the vapor measurements are much different than what is computed by the Laplace equation. In order to account for the measured evaporation rates (not shown in Fig. 3), convection must be occurring. The results shown in Fig. 3 are consistent with a downward and radially outward convective flow, even for methanol, though the methanol convection appears much weaker than the convection occurring in the hexane and 3MP distributions.

Acknowledgements. Acknowledgement is made to the Donors of the American Chemical Society Petroleum Research Fund for support of this research as well as to past students who have contributed to this work, especially Zach Tuten.

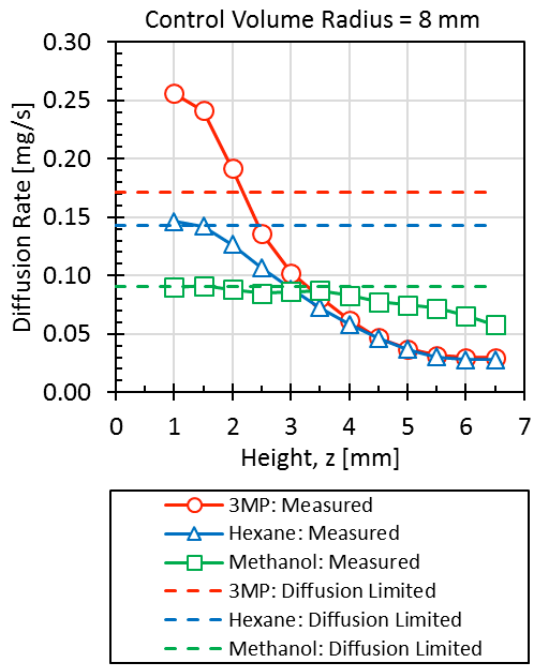

(a)

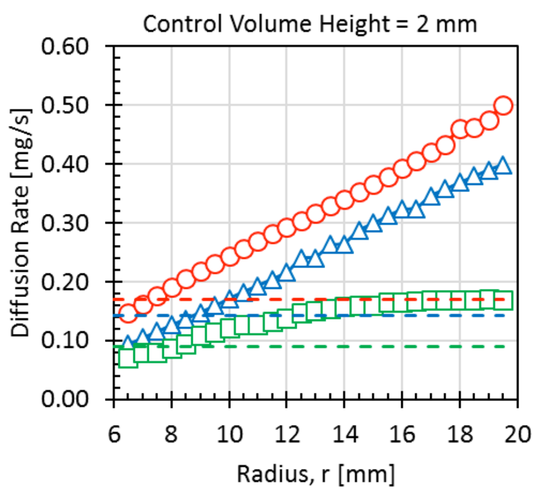

(b)

Figure 3. Variation of the rate of diffusion as a function of control volume dimensions. Fig. 3a presents the variation as a function of control volume height and Fig. 3b presents the variation as a function of radius.

References

[1] P.L. Kelly-Zion, C.J. Pursell, N. Hasbamrer, B. Cardozo, K. Gaughan, K. Nickels, Vapor distribution above an evaporating sessile drop. Int. J. Heat Mass Transfer. 65 (2013) 165-172.
[2] P.L. Kelly-Zion, J. Batra, C.J. Pursell, Correlation for the convective and diffusive evaporation of a sessile drop. Int. J. Heat Mass Transfer. 64 (2013) 278-285.
[3] P.L. Kelly-Zion, C.J. Pursell, S. Vaidya, J. Batra, Evaporation of sessile drops under combined diffusion and natural convection. Colloids Surf. , A. 381 (2011) 31-36.
[4] P.L. Kelly-Zion, C.J. Pursell, R.S. Booth, A.N. Van Tilburg, Evaporation rates of pure hydrocarbon liquids under the influences of natural convection and diffusion. Int. J. Heat Mass Transfer. 52 (2009) 3305-3313.

Drying of agrochemical droplets on a model surface: co-localization of adjuvant and active ingredient

Axa Piñeiro Romero[a], Dennis Selse[b], Turgut Battal[b] and Colin D. Bain[a]

[a] Durham University, Department of Chemistry, Stockton Road, Durham, DH1 3LE, U. K.
[b] Akzo Nobel Surface Chemistry AB, Hamnvägen 2, 444 85 Stenungsund, Sweden

E-mail: a.a.pineiro-romero@durham.ac.uk

Surfactants are widely used in agrochemical applications as adjuvants to facilitate the action of another substance, the active ingredient (AI). Surfactants also provide other benefits such as spray drift reduction, surface wettability and formulation adhesion enhancement. One of the main reasons for using surfactants in agrochemical spray applications is to increase the trans-cuticle transport of systemic pesticides and plant nutrients. A challenge for the agrochemical sector is to produce agrochemicals sustainably and to minimize any adverse impact on the environment. An important part of this challenge is to increase the bioavailability of active ingredients (AIs) so as to reduce (perhaps dramatically) the quantity of AIs that need to be sprayed on crops.

For systemic pesticides, the surfaces of leaves provide an almost impenetrable barrier to AIs so 'adjuvants' are added to crop sprays to enhance the passage of the AI through the cuticle of the leaf. It is believed that to be effective, the AI and the adjuvant have to end up in the same place on the leaf surface when a droplet of spray dries on the leaf, though firm evidence is lacking [1]. We present results on the deposition of a fungicide, tebuconazole, onto a model hydrophobic surface formed by treatment of a silicon wafer with a chlorodimethyloctylsilane. The water contact angle on this surface is ~90°. A suspension of tebuconazole was prepared with three different adjuvants: one nonionic, one cationic and one amphoteric. Printed droplets had a volume of 1.5±0.1 nL and were dried in air. A high-speed camera was used to follow the drying of the droplets.

Scanning Electron Microscopy (Hitachi SU-70 FEG) was used to study the morphology of the final deposit. The distribution of surfactant and active ingredient was studied by energy-dispersive X-ray spectroscopy attached to the SEM, which provides an elemental map of the sample, and by Raman imaging (modified Renishaw Raman microscope) that provides a chemical map. The Raman spectrum in Figure 2 shows sharp peaks from crystalline tebuconazole above 2900 cm^{-1} overlapping a broader peak from the surfacant at wavenumbers below 3000 cm^{-1}. A tunable filter was used to create chemical images of the surface.

In the presence of AI and surfactant, the droplets typically pin at the contact line as they dry and exhibit convective transport towards the contact line leading to the formation of a ring stain of varying width. Figure 1 shows an SEM image of a typical deposit formed from tebuconazole together with a nonionic surfactant, showing that most of the tebuconazole crystals are associated with a 'pool' of surfactant.

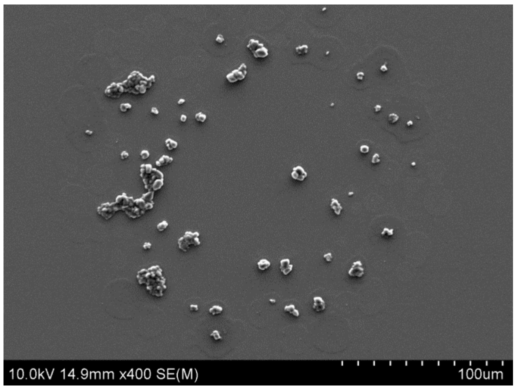

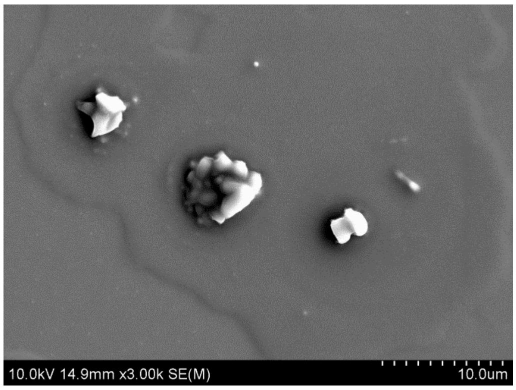

Figure 1: SEM image of a whole deposit of a non-ionic surfactant at a concentration of 1 g/L with active ingredient (upper). A zoomed-in image (lower).

The Raman images in Figure 2 confirm that the surfactant is associated with the AI.

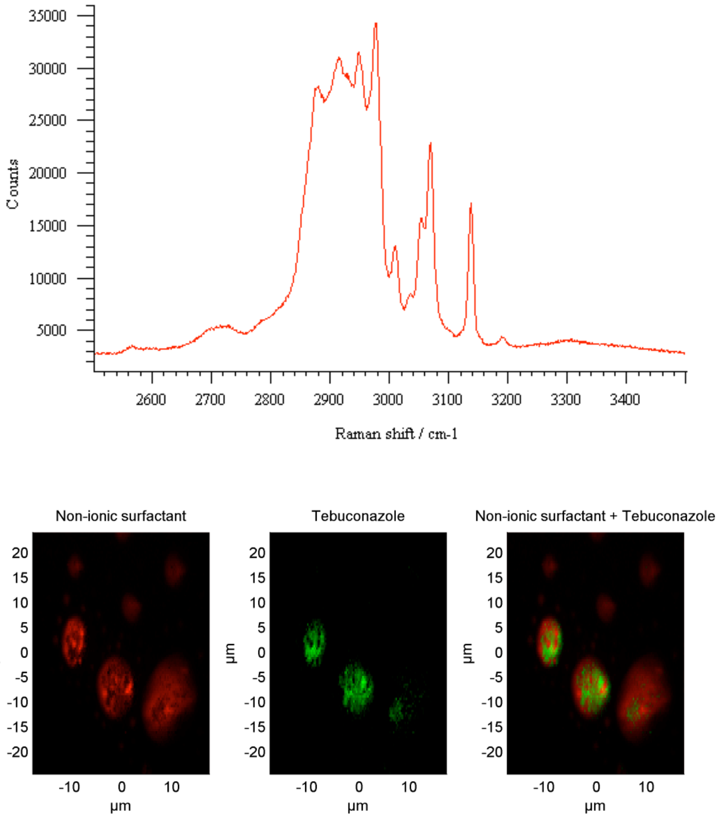

Figure 2: Raman spectrum (upper figure) obtained from the area shown in the right hand image in Fig. 1 and a chemical map of the same area (lower figure): red = surfacant; green = tebuconazole. Right-hand image is an overlay of the left and centre images.

Reference

[1] Faers MA at al. Pest Manag. Sci. 64:820-833 (2008)

Evaporation of Picolitre Droplets on Patterned Substrates

Beth Kazmierski[1], Lisong Yang[1], Emma Talbot[1], Li Wei Tan[2], Dan Walker[2], Colin D. Bain[1]

[1] Department of Chemistry, Durham University, Science Site, South Road, Durham, DH1 3JP, United Kingdom
[2] Merck Chemicals, Chilworth Technical Site, University Parkway, Chilworth, Southampton, SO16 7QD, United Kingdom

E-mail: b.k.kazmierski@durham.ac.uk and c.d.bain@durham.ac.uk

It is well known that droplets containing solutes or suspensions of particles do not dry on flat substrates to give even deposits. Enhanced evaporation at the contact line and capillary flows within the drops often lead to ring-like deposits, commonly referred to as the coffee-ring effect[1,2]. There are a number of reports in the literature of ways of mitigating rind stains but they are usually specific to certain applications or processes[3-6].

The majority of the published literature on droplet drying involves either isolated drops in the vapour phase or sessile drops on flat substrates. Unconstrained drops on flat substrates adopt the shape of a spherical cap, so giving the drying problem azimuthal symmetry. In many applications however, one wants to define exactly where the drop ends up on the substrate or to separate one region of fluid from another using physical or chemical barriers. The presence of barriers breaks the symmetry of the drying problem and modifies evaporation patters across the drop and boundary conditions at the contact line, both of which modify capillary flows in the drying droplet. As a consequence, fixing strategies which give even deposits on flat substrates may not be applicable to patterned substrates. In order to create fixing strategies for patterned substrates we must first understand what is causing the deposit to be uneven in the first place.

In this work we have imaged the drying of picolitre droplets of organic solvents contained within square wells defined by banks of polymer resist in order to develop an understanding of the drying processes in constrained geometries. Interferometry has been used to observe the profile of drops during drying. Interferometry measurements have revealed that the major cause of uneven deposits when printing onto patterned substrates is the capillary suction caused by negative curvature of the drop once the level of fluid drops below the tops of the walls defining the wells, if the drying drop is pinned at the wall tops. For fast evaporating drops we observed the formation of a raised region in the centre of the well towards the end of drying. There is evidence for thermal Marangoni effects in fast-drying solvents and for solutal Marangoni effects in binary mixtures.

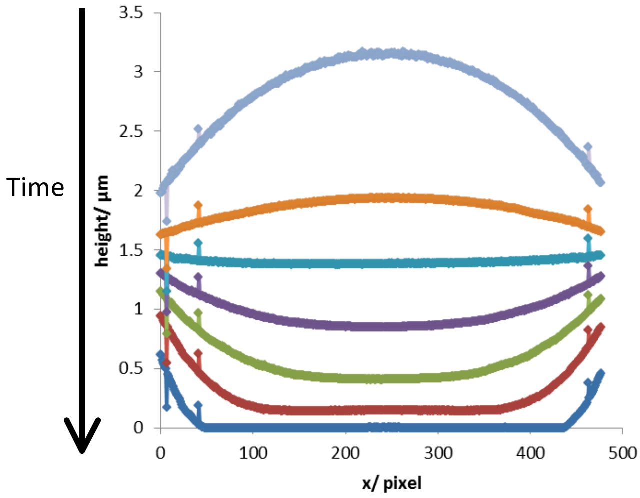

Figure 1: *Plot showing the film profile progression during drying for a drop of dimethyl anisole.*

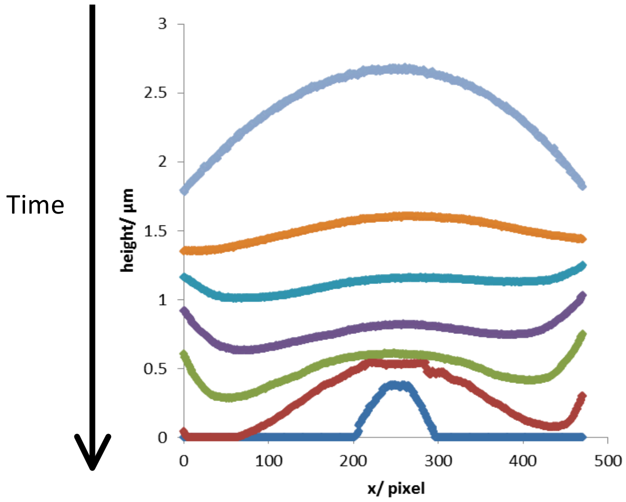

Figure 2: *Plot showing the film profile progression during drying for a drop of dimethyl anisole.*

Acknowledgements.
The authors acknowledge the EPSRC and Merck Chemicals for the funding for this project which has been run as an iCase studentship.

References

[1] Deegan, R. D.; Bakajin, O.; Dupont, T. F.; Huber, G.; Nagel, S. R.; Witten, T. A. *Nature* **1997**, *389*, 827.
[2] Deegan, R. D.; Bakajin, O.; Dupont, T. F.; Huber, G.; Nagel, S. R.; Witten, T. A. *Physical Review E* **2000**, *62*, 756.
[3] Talbot, E. L.; Yang, L.; Berson, A.; Bain, C. D. *ACS Applied Materials & Interfaces* **2014**, *6*, 9572.
[4] Talbot, E. L.; Yow, H. N; Yang, L.; Berson, A.; Biggs, S. R. Bain, C. D. *ACS Applied Materials & Interfaces* **2015**, *7*, 3782-3790.
[5] Park, J.; Moon, J. *Langmuir* **2006**, 22, 3506
[6] Dugyala, V. R.; Basavaraj, M. G. *Langmuir* **2014**, 30, 8680– 8686

INFLUENCE OF THE IMPACT ENERGY ON THE PATTERN OF BLOOD DRIP STAINS

Fiona Smith[1], Céline Nicloux[2], David Brutin[1]

[1] Aix-Marseille University, IUSTI UMR 7343, 13013 Marseille, France
[2] Institut de Recherche Criminel de la Gendarmerie Nationale, 95300 Pontoise, France

E-mails: Fiona.smith@univ-amu.fr; david.brutin@univ-amu.fr

The maximum spreading diameter of complex fluids droplets has been extensively studied but with much debate. This research focuses therefore on a new aspect, the bulging outer rim observed on the final dried pattern of blood droplets. Correlation is made between the inner diameter, the maximum spreading diameter and the impact energy. This shows how the drying mechanism of a blood drip stain is influenced by the impact energy, which induces a redistribution of red blood cells inside the droplet. An empirical relation is established between the final dried pattern of a passive bloodstain and its impact energy, yielding a possible forensic application. Indeed, being able to relate accurately the energy of the drop with its final pattern would give a clue to investigators, as currently no such simple and accurate tool exists.

A lack of adequate scientific validity in some of forensic methods has been pointed out (K. G. de Bruin, 2011). In order to prevent wrong convictions due to doubtful interpretation of forensic evidence, some governments are currently strengthening and promoting a more rigorous approach to forensic science. In this respect, the study of bloodstains is divided into three categories, passive, altered or projected blood spatters. We focus here only on passive traces by examining links between the final pattern and the nature of an impact of a drop dripping naturally. Indeed, the effect of gravity on a blood mass induces the mass to release droplets which will next travel through the air while retaining a spherical shape due to surface tension. The drop then impacts a surface at an angle of 90°, a circular stain is induced. The present work is devoted to cases of blood droplets dripping only due to gravity, without any initial velocity. Initial kinetic energy would modify the final impact energy, and it would then not be possible to recalculate the initial height of fall.

To test different impact energies, we used sixteen different heights of fall ranging from 0.6 cm to 152 cm and two needle diameters, a first one of 25G (0.5080 mm in diameter) and a second one of 18G (1.219 mm in diameter). For each case we repeated the experiment twice. The substrate used was wood flooring since it is a substrate encountered very often on crime scenes. The droplets were released into a humidity of 30 +/- 5 % on average and were then left to dry in a glovebox (Jacomex T-Box, V=350L) at a constant humidity of 30 +/- 2%. To record the impacts of droplets, we used a high-speed camera (Fastcam-ultima 1024). To measure the volume of the droplet, the initial diameter of the droplet, its speed at the time of the impact, and its maximum spreading diameter we used the software imageJ to analyze the pictures recorded with the high-speed camera. After drying, one droplet for each different case was then scanned with a confocal microscope (STIL - Micromesure 2, with two different optical sensors: 4000m CCS prima n2 and 150m CCS prima) in order to obtain the 3D profile of the dried droplets. Scans lasted on average 5 hours. A final picture of the dried droplet was then taken with a camera (Canon EOS 7D digital camera, resolution: 5184 x 3456 pixels).

The aim of the research is to find the relationship between the final observed pattern and its velocity, U, at the time of the impact. To do so, we choose to first validate our data with two already existing spreading models for droplets. The approach of N. Laan et al. (2014) presented in figure 3 relates capillary, viscosity and inertia forces according to J. Eggers et al. (2010) approach. In order to do so we quantitatively relate the maximum spreading diameter to the impact velocity which takes into account that energy conservation is the only physical principle required to explain droplet spreading behavior. This model uses
the following Pade's approximation:

$$\left(\frac{D_{max}}{D_0}\right)Re^{-1/5} = \frac{P^{1/2}}{A + P^{1/2}},$$

with another impact parameter $P = We.Re^{-2/5}$ and the fitting constant A = 1.24. The approach describes the correlation that exists between the maximum diameter of the spreading droplets and the velocity for a non-porous substrate. However, in order to find the impact velocity from the final pattern, it is necessary to determine the original volume of the droplet. Moreover, this model is not applicable at low Reynolds and Weber numbers as can be seen in Fig. 1.

After drying we observed that on the final pattern of dried droplets, a circular bulge was visible around its rim. Additionally, these visual observations reveal that the width of the bulging outer rim, corresponding to the distance between the inside diameter and the maximum spreading diameter of the droplet, varies depending on the impact energy. This bulging outer rim seen on the final pattern is the biological deposit that forms during drying due to the internal flow driving the RBCs to the periphery of the droplet, which corroborates our previous assumption that the internal flow is modified by the impact velocity. The 3D prole visualization of the dried bloodstain was used to characterize the peaks marking the rim dimensions in a radial cross section.

Thus we were able to record the internal diameter of each droplet by averaging its measurement in different radial cross-sections, and comparing it to photographic analysis.

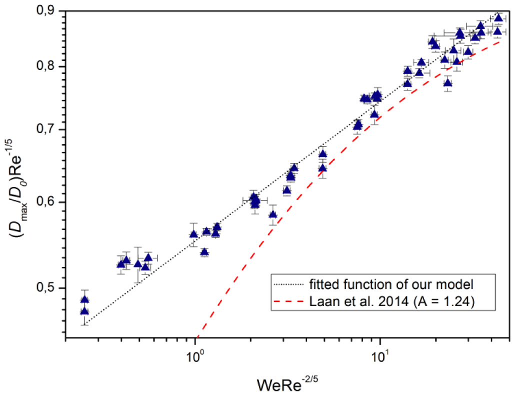

Fig. 1. Rescaled maximum spreading ratio as a function of $WeRe^{-2/5}$ according to solution proposed by Laan et al. for maximum spreading diameters of droplets on solid substrates.

We expressed both diameters as spreading ratios, $\beta_1 = D_1/D_0$, and $\beta_2 = D_2/D_0$, with D_0 being the initial diameter of the droplet, as function of the impact velocity U as shown in figure 2a.

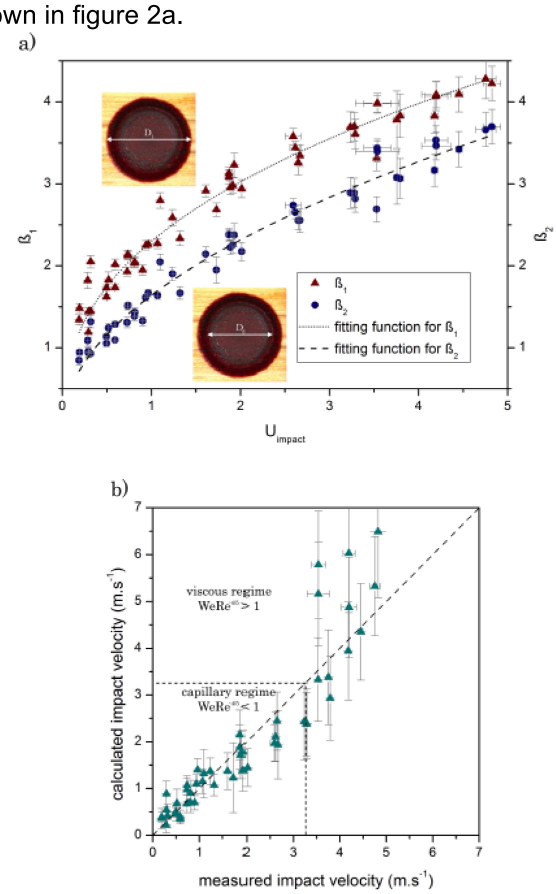

Figure 5. a) Maximum spreading ratio as a function of U in red, and its fitted function. Internal spreading diameter as a function of U in blue, and its fitted function. b) Calculated impact velocity using final versus measured impact velocity.

The first approximation function in Fig. 2 which relates β_1 to U is given by:

$$\beta_1 = aU^b,$$

with a = 2.34 and b = 0.374. This is obtained by means of a least-square fit (R^2 = 0.960). The second approximation function relating β_2 to U is:

$$\beta_2 = cU^d,$$

with c = 1.66 m and d = 0.487, also obtained by means of a least-square fit (R^2 = 0.966). We assume that these evaluated constants are substrate-dependent and correspond to the wooden flooring used during our experiment. The internal natural convection of the drop is thus widely influenced by the impact energy at the time of the impact. Indeed, the impact velocity of the droplet changes its internal mechanical properties. Thus this accumulation of biological elements at the edge of the droplet leading to the bulge formation gives us a new feature that can be exploited to find information on the initial state of the falling droplets. To do so we can calculate the initial velocity U from both fitted functions 3.2 and 3.3 by correlating them together such as the obtained expression for the velocity is:

$$U = (\frac{D_1}{D_2}\frac{c}{a})^{1/(b-d)}$$

As demonstrated, there is a correlation between the width of the bulging outer rim and the impact energy, which is observed when measuring D_2 and D_1. The drying pattern of a deposited blood drip stains is already well explained as well as the maximum spreading ratio of dripping blood drops. However, this new parameter enables us to understand how the observed final pattern is influenced by the kinetic energy of a blood droplet at the time of the impact and how can it be exploited in forensic applications. Indeed, by measuring the internal diameter of a dried droplet after impact, we have quantified their influence of the impact velocity on the internal ow of a drying blood droplet. This kinetic energy provokes the RBCs distribution to be more evenly spread inside the droplet, as an increase of the internal diameter ratio is measured respectively with an increase invelocity.

Acknowledgements. We would like to thank the volunteers who gave their blood and the nurse who sampled this blood. This work received a _nancial grant from the French Agence Nationale de la Recherche in the frame of the project ANR-13-BS09-0026. Also, this work has been carried out in the framework of the Labex MEC (ANR-10-LABX-0092) and of the A*MIDEX project (ANR- 11-IDEX-0001-02), funded by the Investissements d'Avenir French Government program managed by the French National Research Agency (ANR).

References

K. G. de Bruin, R. D. Stoel, J. C. M. Limborgh 2011 Improving the point of origin determination in bloodstain pattern analysis. Journal of Forensic Sciences 56 (6), 1476-1482.
N. Laan, K. G. de Bruin, D. Bartolo C. Josserand & Bonn, D. 2014 Maximum diameter of impacting liquid droplets. Phys. Rev. Applied 2, 044018.
J. Eggers, M. A. Fontelos, C. Josserand & Zaleski, S. 2010 Drop dynamics after impact on a solid wall: Theory and simulations. Phys. Fluids 22 (062101).

How drops start sliding over solid surfaces

Nan Gao[1,2], Florian Geyer[1], Dominik W. Pilat[1], Sanghyuk Wooh[1], Doris Vollmer[1], Hans-Jürgen Butt[1], Rüdiger Berger[1]

[1] Max Planck Institute for Polymer Research, Ackermannweg 10, 55128 Mainz, Germany

[2] Future Industries Institute, University of South Australia, Adelaide, Australia

E-mail: butt@mpip-mainz.mpg.de

It has been known for more than 200 years that the maximum static friction force between two solid surfaces is usually greater than the kinetic friction force. In contrast to solid–solid friction, there is a lack of understanding of liquid–solid friction, i.e. the forces that impede the lateral motion of a liquid drop on a solid surface. We demonstrate that the lateral adhesion force between a liquid drop and a solid can be divided into a static and a kinetic regime. This striking analogy with solid–solid friction is a generic phenomenon that holds for liquids of different polarities and surface tensions on smooth, rough and structured surfaces.

Talk preferred

Hyaluronic acid at fluid interfaces

María Olalla Olea Romacho, Julia Maldonado-Valderrama, Miguel Cabrerizo-Vílchez, María José Gálvez-Ruiz.

[1]Departmento de Física Apliacada. Universidad de Granada. 18071. Granada. Spain

E-mail: mcabre@ugr.es

Liquid lipid nanocapsules (LLNs) are colloidal systems consisting of a liquid lipid core surrounded by an amphiphilic protective shell [1]. LLNs constitute a new generation of nanoparticles with a higher degree of biocompatibility and versatility, especially when they are prepared with natural materials that possess the biocompatibility, biodegradability, and non-toxicity required for use in humans. In the desing of the LLNs and in order to its stabilization, the protective shell is projected to be formed by hyaluronic acid in combination with another bioactive molecules. Hyaluronic acid is a natural compound that can be potentially used for targeted delivery of drugs on the tumour cell through its selective binding to an specific receptor, CD44 [2]. However, the interfacial properties of hyaluronic acid have not been studied in detail to date. In this work we show a detailed interfacial characterization of hyalurinc acid adsorbed layers at fluid interfaces. The objective is to understand the interfacial phenomena underlying degradation and stability of LLN with the aim of optimizing the preparation and performance of these nanocarriers to use *via* oral.

Acknowledgements. This work has been sponsored by RYC-2012-10556, MAT2015-62644-C2-1-R, MAT2014-60615R.

References

[1] J.A. Molina-Bolívar, F. Galisteo-González, Olive-oil nanocapsules stabilized byHSA: influence of processing variables on particle properties, J. Nanopart. Res. (2015) **17**, 1–13.
[2] K. Y. Choi, G. Saravanakumar, J. H. Park, K. Park, Colloids and Surfaces B: Biointerfaces (2012) **99** 82–94.

COFFEE-RING EFFECT REVISITED

Vahid Vandadi[1], Saeed Jafari Kang[1], James D. Felske[2], Hassan Masoud[1]

[1]Department of Mechanical Engineering, University of Nevada, Reno, Nevada 89557, USA
[2]Department of Mechanical and Aerospace Engineering, State University of New York, Buffalo, New York 14260, USA

E-mail: hmasoud@unr.edu

Understanding why a spilled drop of coffee leaves behind a ringlike stain after it dries out [1] might have been a matter of academic curiosity at first. However, soon, it was found that the lessons learned from studying the so-called 'coffee-ring' effect and phenomena related to it have important implications in ink-jet printing ordered structures via the evaporative self-assembly technique (see Ref. [2] and references therein). This has motivated many researchers to investigate mechanisms underlying the deposition of nonvolatile solutes in evaporating sessile drops [3-44]. A review of recent studies can be found in [45]. the interfacial adsorption and transport of particles as a one-dimensional advection-generation process in toroidal coordinates (see Fig. 1b). We show, perhaps surprisingly, that, if the solutes are initially distributed uniformly within the drop (the usual case), then their bulk concentration remains uniform during evaporation. Physically, their capture by the interface is counterbalanced by the reduction in drop volume due to evaporation. Therefore, the consideration of interfacial transport alone is sufficient for determining where on the substrate the particles will finally reside.

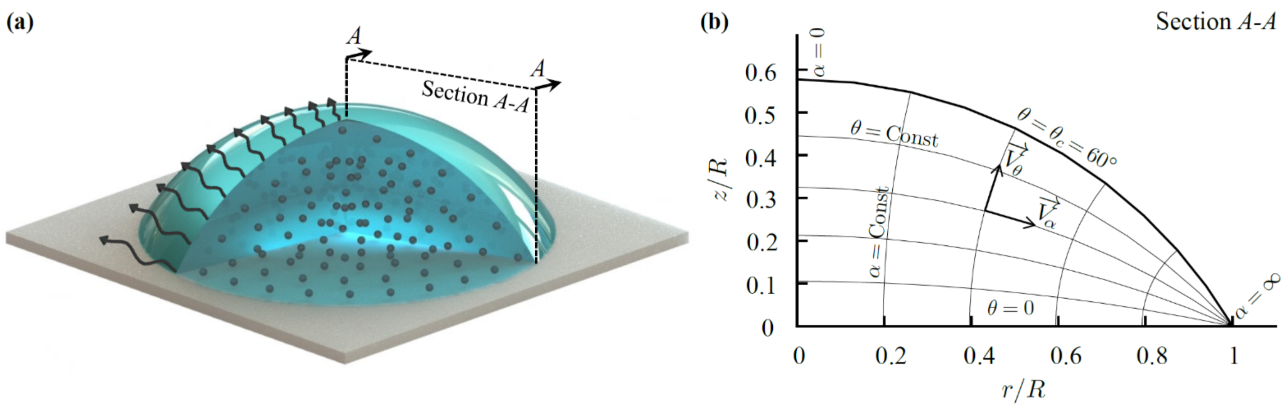

Figure 1. (a) An evaporating sessile droplet containing a dilute suspension of nonvolatile particles. (b) The lines of constant α and θ and positive direction of velocity components in a (left-handed) toroidal coordinate system that fits the boundaries of the drop on the meridian plane *A-A*.

The majority of investigations to date have assumed (or concluded) that the particle deposition is a consequence of the evaporation-induced bulk flow transporting particles either directly to the substrate or to a pinned contact line. By contrast, fewer studies have considered that the bulk flow carries particles to an inevitable intersection with the liquid-gas interface (see, e.g., Refs. [3, 4, 12, 20, 28, 32, 33, 36, 42]. Here, we demonstrate that this inevitable intersection results from the coupling of the receding of the interface with the bulk internal flow. We also reexamine the particle deposition during the drying of a colloidal sessile droplet (see Fig. 1a) by explicitly taking into account the intersection of nonvolatile suspended particles with the liquid-gas interface.

We propose that upon arriving at the interface the particles move with the velocity of the surface, wherein the tangential component of the fluid flow carries them towards the contact line. This assumption splits the transport of solutes into interfacial and bulk. We model

We numerically solve the transport equation for the evolution of particle concentration at the interface. Indeed, we find that the results predict ringlike deposition patterns and they quantitatively agree with available experimental data. These findings raise the possibility of an alternative mechanism for the coffee-ring effect in which the free surface plays an active role in the particle deposition.

References

[1] R. D. Deegan, O. Bakajin, T. F. Dupont, G. Huber, S. R. Nagel, and T. A. Witten, Nature (London) 389, 827 (1997).
[2] W. Han and Z. Lin, Angew. Chem., Int. Ed. 51, 1534 (2012).
[3] R. D. Deegan, O. Bakajin, T. F. Dupont, G. Huber, S. R. Nagel, and T. A. Witten, Phys. Rev. E 62, 756 (2000).
[4] R. D. Deegan, Phys. Rev. E 61, 475 (2000).
[5] B. J. Fischer, Langmuir 18, 60 (2002).
[6] L. Shmuylovich, A. Q. Shen, and H. A. Stone,

Langmuir 18, 3441 (2002).
[7] L. Pauchard and C. Allain, Phys. Rev. E 68, 0528019 (2003).
[8] Y. O. Popov, Phys. Rev. E 71, 036313 (2005).
[9] T. Heim, S. Preuss, B. Gerstmayer, A. Bosio, and R. Blossey, J. Phys.: Condens. Matter 17, S703 (2005).
[10] Z. Lin and S. Granick, J. Am. Chem. Soc. 127, 2816 (2005).
[11] H. Hu and R. G. Larson, J. Phys. Chem. B 110, 7090 (2006).
[12] T. P. Bigioni, X.-M. Lin, T. T. Nguyen, E. I. Corwin, T. A. Witten, and H. M. Jaeger, Nat. Mater. 5, 265 (2006).
[13] I. I. Smalyukh, O. V. Zribi, J. C. Butler, O. D. Lavrentovich, and G. C. L. Wong, Phys. Rev. Lett. 96, 177801 (2006).
[14] A. L. Yarin, J. B. Szczech, C. M. Megaridis, J. Zhang, and D. R. Gamota, J. Colloid Interface Sci. 294, 343 (2006).
[15] M. Schnall-Levin, E. Lauga, and M. P. Brenner, Langmuir 22, 4547 (2006).
[16] E. Widjaja and M. T. Harris, AIChE J. 54, 2250 (2008).
[17] R. Bhardwaj, X. Fang, and D. Attinger, New J. Phys. 11, 075020 (2009).
[18] R. Bhardwaj, X. Fang, P. Somasundaran, and D. Attinger, Langmuir 26, 7833 (2010).
[19] A. S. Joshi and Y. Sun, Phys. Rev. E 82, 041401 (2010).
[20] P. J. Yunker, T. Still, M. A. Lohr, and A. G. Yodh, Nature (London) 476, 308 (2011).
[21] Á. G. Marín, H. Gelderblom, D. Lohse, and J. H. Snoeijer, Phys. Rev. Lett. 107, 085502 (2011).
[22] T. Still, P. J. Yunker, and A. G. Yodh, Langmuir 28, 4984 (2012).
[23] M. A. Hampton, T. A. Nguyen, A. V. Nguyen, Z. P. Xu, L. Huang, and V. Rudolph, J. Colloid Interface Sci. 377, 456 (2012).
[24] R. G. Larson, Angew. Chem. Int. Ed. 51, 2546 (2012).
[25] S. Das, P. R. Waghmare, M. Fan, N. S. K. Gunda, S. S. Roy, and S. K. Mitra, RSC Adv. 2, 8390 (2012).
[26] S. Das, S. Chakraborty, and S. K. Mitra, Phys. Rev. E 85, 046311 (2012).
[27] M. Majumder, C. S. Rendall, J. A. Eukel, J. Y. Wang, N. Behabtu, C. L. Pint, T.-Y. Liu, A. W. Orbaek, F. Mirri, J. Nam, et al., J. Phys. Chem. B 116, 6536 (2012).
[28] P. J. Yunker, M. A. Lohr, T. Still, A. Borodin, D. J. Durian, and A. G. Yodh, Phys. Rev. Lett. 110, 035501 (2013).
[29] W. Sempels, R. De Dier, H. Mizuno, J. Hofkens, and J. Vermant, Nat. Commun. 4, 1757 (2013).
[30] T. A. H. Nguyen, M. A. Hampton, and A. V. Nguyen, J. Phys. Chem. C 117, 4707 (2013).
[31] W. Chen, J. Koplik, and I. Kretzschmar, Phys. Rev. E 87, 052404 (2013).
[32] T. Breinlinger and T. Kraft, Powder Technol. 256, 279 (2014).
[33] M. Anyfantakis and D. Baigl, Angew. Chem., Int. Ed. 53, 14077 (2014).
[34] A. W. Wray, D. T. Papageorgiou, R. V. Craster, K. Seane, and O. K. Matar, Langmuir 30, 5849 (2014).
[35] N. R. Devlin, K. Loehr, and M. T. Harris, AIChE J. 61, 3547 (2015).
[36] M. Anyfantakis, Z. Geng, M. Morel, S. Rudiuk, and D. Baigl, Langmuir 31, 4113 (2015).
[37] F. Boulogne, F. Ingremeau, J. Dervaux, L. Limat, and H. A. Stone, EPL (Europhys. Lett.) 112, 48004 (2015).
[38] H. Y. Erbil, Adv. Colloid Interface Sci. 222, 275 (2015).
[39] X. Du and R. Deegan, J. Fluid Mech. 775, R3 (2015).
[40] M. Pack, H. Hu, D.-O. Kim, X. Yang, and Y. Sun, Langmuir 31, 7953 (2015).
[41] Y. Y. Tarasevich, I. V. Vodolazskaya, and L. V. Sakharova, Eur. Phys. J. E 39, 1 (2016).
[42] Y. Li, Q. Yang, M. Li, and Y. Song, Sci. Rep. 6, 24628 (2016).
[43] G. Karapetsas, K. Chandra Sahu, and O. K. Matar, Langmuir 32, 6871 (2016).
[44] H. Kim, F. Boulogne, E. Um, I. Jacobi, E. Button, and H. A. Stone, Phys. Rev. Lett. 116, 124501 (2016).
[45] R. G. Larson, AIChE J. 60, 1538 (2014).

OBSERVATIONS OF THREE DIMENSIONAL FLOW INSIDE AN EVAPORATING DROP

G. Corkidi[1], F. Montoya[1], S. Piedra[2], A. Bribiesca[3], P. Hernández-Herrera[3], E. Ramos[4]

[1]Biotechnology Institute, Universidad Nacional Autónoma de México, Cuernavaca, Mor., Mexico
[2] National Center for Aeronautical Technology, Querétaro de Santiago, Qro., Mexico
[3]Center for Research in Sciences, UAEM, Cuernavaca, Mor., Mexico
[4]Renewable Energy Institute, Universidad Nacional Autónoma de México, Cuernavaca, Mor., Mexico

E-mail: erm@ier.unam.mx

We present an experimental and numerical study of the flow inside an evaporating sessile drop of water. The drop volume analyzed ranges from 0.3 to 1 microliters and the range of footprint radii is from 0.5 to 1 mm. The observations of the velocity field are obtained with an experimental device designed to monitor the motion of tracers at a number of horizontal planes located at different heights [1]. We used one micrometer diameter latex spheres covered with fluorescein as tracers. With image analysis techniques, the transit of individual tracers to adjacent planes can also be captured. The collections of data are further post processed to reconstruct the full three dimensional, three component velocity fields. In this sense, a time-dependent, tomographic information of the velocity field inside the drop is recorded. A finite-volume numerical method coupled with a front tracking strategy is used to solve the mass, and momentum conservation equations. The boundary conditions at the evaporating upper surface of the drop are imposed according to a diffusive transport of vapor in the surrounding atmosphere. The evaporation model used follows that proposed in reference [2]. The results from the numerical simulation include the velocity and temperature fields. Details of the numerical code can be found in reference [3].

Given the initial volume and the surface tension forces in the water-air interface, the shape of the drop after deposition is a spherical cap with a contact angle of approximately 40º and a maximum height of 250 micrometers. The time for full evaporation is approximately 120 s. Figure 1 shows the position of particles in a water drop at an early stage of the evaporation process, together with samples of the path followed by individual particles (thin white lines). The thick vertical arrow indicates the axis of symmetry of the drop and the particles at the free surface delineate its initial shape. A particle path is constructed by adding together the displacements of a particle at two subsequent times. It is pertinent to emphasize that the particle paths are built with images obtained at subsequent times. The general flow in the horizontal planes is mostly radial and the average velocity increases in the region close to the substrate. A descending flow was found near the center of the droplet, with the maximum velocities of 3 micrometers per second in the regions close to the axis of symmetry. Inspection of the flow in the vertical planes indicates that the flow is axially symmetric and thus projecting the velocity fields around the symmetry axis gives a picture of the general flow.

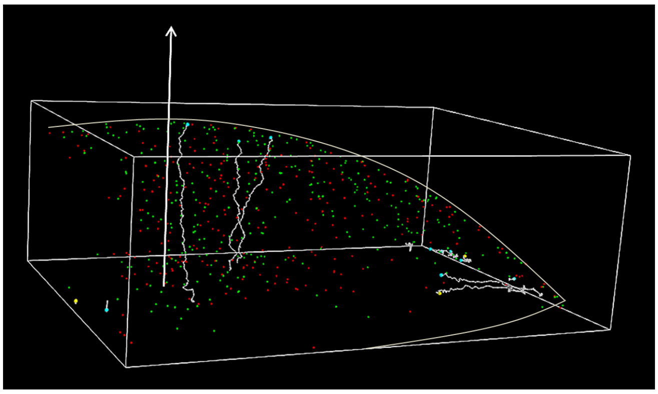

Figure 1. Experimentally recorded position of particles with sample trajectories. The general direction of motion of the red dots is towards the center of the droplet while the green ones to the contact line. The initial position of the particles that follow the trajectories indicated with white lines is denoted with a blue dot. The diameter of the footprint of the drop is 1.1 mm and the information corresponds to data taken 10 sec. after deposition.

Figure 2 shows the average velocity field obtained with projections of the whole volume of the droplet, at a short time after deposition. The general flow in the core of the droplet is horizontal and toward the free surface. We have observed that there is a small region similar to a boundary layer near the surface where the particles move toward the axis of symmetry. This feature is not shown in Figure 2.

A sample of the numerical simulations of the flow under the physical and geometrical conditions similar to the experimental observations is shown in Figure 3. In the numerical model a time dependent, three dimensional problem is considered and the flow is solved inside and outside of the drop. As can be appreciated, the numerically calculated motion in a two dimensional vertical plane inside the drop displays a descending trend near the axis of symmetry and radially in the region close to the substrate. These features are in qualitative agreement with the experimental observations.

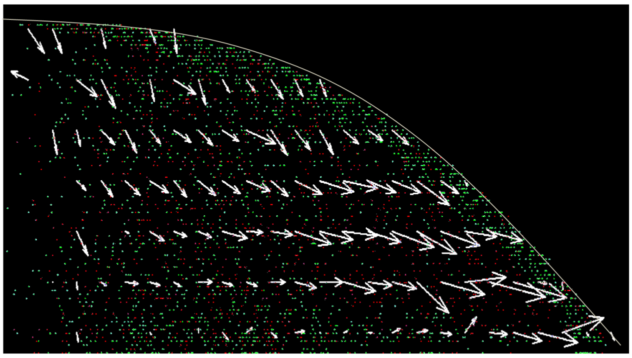

Figure 2. Experimentally observed velocity field in half a vertical plane obtained with projections of the whole volume of the droplet . Physical and geometrical properties of the drop are the same as those of Figure 1. Also, the color of the particles indicates the general motion of the particles with the same color code as in Figure 1.

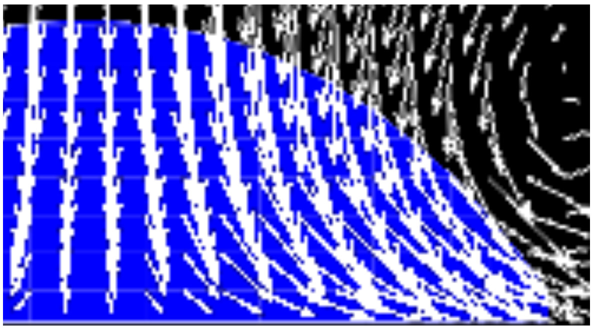

Figure 3. Two dimensional section of the numerically calculated velocity field.

The technique reported provides observational evidence of the dynamics of the suspended particles and is expected to be useful under a variety of physical conditions that include suspended particles of different geometries, non isothermal flows or flows with hydrothermal waves on the free surface of the drop. This in turn will contribute to understand the processes that drag suspended particles near the substrate and the formation the pattern of the deposits.

References

[1] G. Corkidi, B. Taboada, C. D. Wood, A. Guerrero and A. Darszon. Tracking sperm in three-dimensions Biochem. and Biophys. Res. Comm. **373** No 1, 125-129 (2008)
[2] Deegan R., Bakajin O., Dupont T.F., Huber G. Nagel S.R. and Witten T.A. Contact line deposits in an evaporating drop. Phys. Rev E. **62** No 1, 756 – 765 (2000)
[3] S. Piedra, Numerical Study of Bubble Dynamics Ph.D Thesis UNiversidad Nacional Autonoma de Mexico (2015)

The Effect of Nanoparticle Surface Charge on Evaporative Deposition patterns on Mica and age-conditioned Mica

Joan E. Curry*, Shelby Hoglund, Aubrey McKinney, and Phillip Yang

Department of Soil, Water and Environmental Science, University of Arizona, Tucson, AZ

E-mail: jecurry@email.arizona.edu

It is well known that colloidal particle deposition on surfaces depends on a number of variables. In this work we explore the effect of nanoparticle composition on particle patterns through the simple process of evaporative deposition. We investigate patterns produced by CeO_2, Al_2O_3, fumed silica and colloidal silica nanoparticle solutions on freshly cleaved mica and age-conditioned mica. The silica particles are negatively charged while the CeO_2 is closer to neutral and the alumina particles are positively charged. The residue patterns are strongly correlated with the type of particle. Spoke-like patterns are formed with colloidal silica, the well-known honeycomb patterns emerge for the ceria and fumed silica solutions and the alumina solution gives a more homogeneous deposition pattern. Additionally, deposition patterns from surfactant stabilized graphene nanoparticle suspensions are being investigated.

DIGITAL MICROFLUIDICS STARTER KIT

Jia Li* and Chang-Jin "CJ" Kim

Department of Mechanical Engineering, UCLA, Los Angeles, CA, USA
*E-mail: killeyzib@gmail.com

Digital microfluidics by electrowetting-on-dielectric (EWOD) is a simple and compact lab-on-a-chip platform expected to miniaturize and automate many traditional chemical and biological workflow processes. It enables handling of liquids in droplets in open 2D space rather than in confined channels using electric signals rather than pumps and valves. Small droplets can be introduced from a liquid reservoir into the EWOD digital microfluidics and transported, split, and merged independently and simultaneously, following electronic instructions. Over the last several years, several biological and medical companies began to integrate their assays into digital microfluidics, making combination product. Illumina, Inc. integrated its DNA library prep kit with digital microfluidic system and introduced a combination product (Neoprep) into market in 2015 [1]. GenMark Diagnostics [2] has developed ePlex system by integrating infectious disease testing panel with digital microfluidics. In 2017 Baebies, Inc. received FDA clearance for its lysosomal storage disease newborn screening platform [3], which uses digital microfluidics technology for its sample preparation. Nanopore has developed a digital microfluidics sample preparation module VolTRAX™ for its portable sequencer [4]. Sofiebio is developing digital microfluidics platforms for synthesizing radioactive drugs. Digital microfluidics has become a backbone for various new biomedical products during the last 2 years and is expected to continue for the years to come.

When the potential is well utilized, we expect not just several labs and companies but thousands of companies and research labs will benefit from the EWOD digital microfluidics. Unfortunately, currently even for major companies who let electrical engineers build digital microfluidic control system and hire staff or make business arrangement to fabricate the digital microfluidic chips, it still takes years to establish the technology. As described in Figure 1, only a very small portion of the people who can benefit from the EWOD digital microfluidic technology actually use or plan to use the technology.

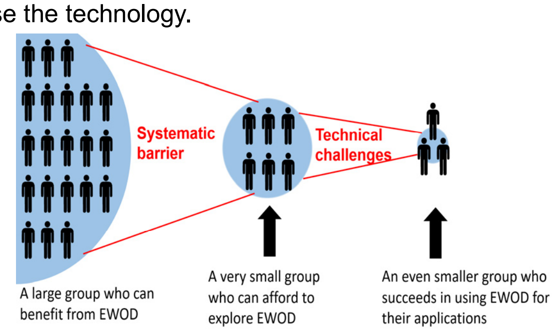

Figure 1: Current situation in EWOD digital microfluidics R&D

Our motivation to put an effort to developing a digital microfluidics starter kit is to lower the barrier of utilizing digital microfluidics for researchers. The starter kit currently includes (1) control module, (2) universal chip socket, and (3) GUI. Similar approach has been adopted by Nanopore technology, who introduced "VolTRAX Introduction Programme" to researchers. Their system includes a portable control system and digital microfluidic chips, which integrate heating, cooling and magnetic. However, VolTRAX's system is physically fixed, leaving little room for the users to reconfigure. The lack of flexibility is problematic for researchers who makes their own digital microfluidic chips. We are designing our digital microfluidic system in the spirit that researchers can reconfigure the system to accept various chips, add-on modules and assays fitting their own needs.

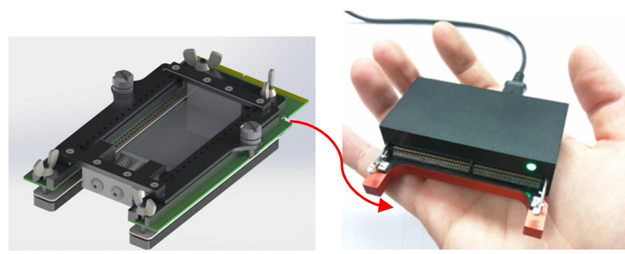

Figure 2: The universal chip socket with the control module

We have developed several control modules over the years [5]. Figure 2 shows our latest control module with the universal chip socket. The system is in dimension of 2.87'' × 2.25" ×0.7", small enough to be integrated into larger systems while it can also work independently as a standalone system. The system controls 256 independent channels of high voltage signals ranging between 0-300 V and 0-10 kHz in rectangular waveform. The whole system is designed to be low cost to serve the mass.

The universal chip socket (shown in Figure 2 left) contains 256 Pogo pins that are direct mapping of the 256 channels in the control module. The socket can be attached/detached to the control module at ease. A 4'' wafer can be put into the socket directly without dicing. The socket also includes a mechanism which aligns the contact pads on the wafer with the pogo pins. To maximize the flexibility, the socket can adjust the gap between top plate and bottom substrate for the digital microfluidic chips.

The control module communicates with PC through USB cable which is also the sole power source for the control module. We developed GUI compatible with both Windows and Mac OS GUI (shown in Figure 3). In the GUI, we guide users through the 4 steps: (1)

layout, (2) mapping, (3) programming, and (4) command. “Layout” step enables users drag and place electrode pattern onto a canvas reflecting the actual electrode pad layout on their digital microfluidic chip. In “mapping” step, user maps channels of control module to the electrode pattern. In ”programming” step, user pre-defines actuation sequence of the electrode pattern as programs. In “command” section, user executes actuation sequence, and the control module will actuate electrode pads according to the programs. All the layout and program can be saved into file and shared among users.

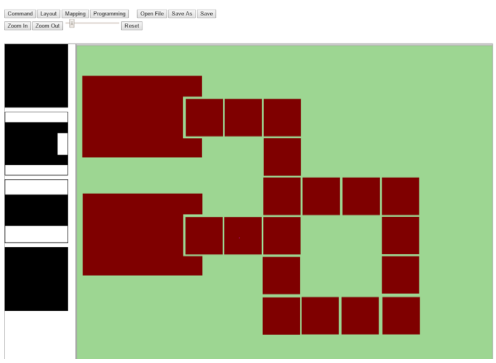

Figure 3: Screen shot of GUI

The control module, universal socket and GUI comprises the digital microfluidics starter kit. The starter kit was not designed to be a final product; rather it was designed to be a leverage that boosts more companies and research labs to take advantage of the digital microfluidics. After getting familiar with the starter kit and taking advantage of it during R&D, companies can build their own system as a product (shown in Figure 4).

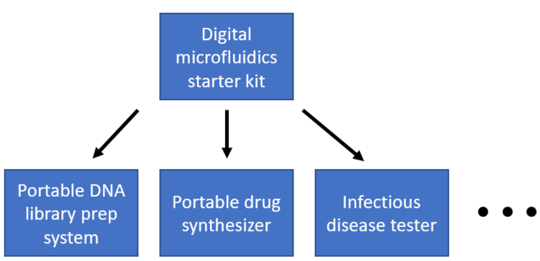

Figure 4: Digital microfluidic starter kit as a leverage to boost more spetialized systems

In coming years, we expect to see a surge of demand for reliable digital microfluidic chips as more and more specialized systems are developed and commercialized. The barrier of digital microfluidics is likely against digital microfluidic chips rather than control system for major companies and research labs. Although our starter kit currently does not provide digital microfluidic chips and only applicable for those who can make their own digital microfluidics, we are planning to add digital microfluidic chips in the system eventually.

[1]https://www.illumina.com/company/news-center/press-releases/press-release-details.html?newsid=2018793
[2]https://www.genmarkdx.com/solutions/systems/eplex-system/
[3] http://baebies.com/products/seeker/
[4] https://nanoporetech.com/products/voltrax
[5] J. Li and C.-J. Kim, Proc. Int. Conf. Miniaturized Systems for Chemistry and Life Sciences (microTAS), Gyeongju, Korea, Oct. 2015, pp. 1199-1201.

USING EWOD DEVICE FOR THE MOVEMENT AND DYNAMIC CULTURE OF MOUSE EMBRYOS

Yao-Hsien Huang[1], Yi-Wen Wang[2], Hong-Yuan Huang[2] and Da-Jeng Yao[1]
1 Institute of NanoEngineering and MicroSystems, NTHU, Hsinchu, Taiwan.
2 Department of Obstetrics and Gynecology, Lin-Kou Medical Center, Chang Gung Memorial Hospital.

Email:sean00132032@gmail.com; Tel.:+886985685032

The Bio-MEMS research had become an attraction in recent years. Electrowetting-on-dielectric (EWOD), one of microfluidic systems, has been used for in vitro fertilization culture (IVF), shown the feasibility of EWOD chip in biomedical science application [1].

The experiment is similar to our previous work [2], but reduce the number of fertilized embryos in the HTF (Human Tubal Fluid) droplets. This method can reduce the interaction of embryo-embryo secretions, improving the reliability of the experiment.

In our study, the application of EWOD in reproductive medicine is making use of EWOD chip as a dynamic culture platform for fertilized embryos. Since the embryos are moving in a spiral manner in this process, our digital microchannels are designed as a ring-shaped to imitate the fallopian tube, as shown in figure 1. Figure 2 shows the development of embryos from two cell to blastocyst stage. The most critical period is the blastocyst stage, which is the best embryo implantation period. Because the implantation in the blastocyst stage has a higher pregnancy rate. The morula is also the embryo implantation period, so we recorded the morula and blastocyst stage embryos.

In our experiment, we manipulated the HTF droplets with electro-wetting force in an oil bath environment to imitate the dynamic movement of the embryos inside the mother. The experiments contained three groups, the traditional droplet culture method is taken as the experimental control group, the second one is the static culture group on chip without any movement, and the third one is dynamic culture group driven by electric wetting force on the chip. In the static culture group, the fertilized embryos were injected into equilibrated culture medium and placed them in the oil on the EWOD chip. In the dynamic culture group, the fertilized embryos were injected into equilibrated culture medium droplet, and the culture medium droplet was moved every 5 minutes for two hours to imitate the dynamic process of the fertilized embryos moving from the fallopian tube to the uterus, as shown in figure 3.

The chip is fabricated as follows shown on figure 4.The photolithography process was used for defining the pattern of electrodes. After that, 450 nm thickness of Si_xN_y was deposited by PECVD. Then, SOG was spin-coated on the dielectric and baked at 200℃ for 30 mins, and Teflon was coated on the chip and baked at 95 ℃ for 2 hrs. Finally, PDMS ring was bonded on the chip as a spacer.

Figure 5 shows the development rate of the embryos on petri dish (control group) and EWOD chip (static group and dynamic group). The embryos development rates are 69.4% (N=36) , 54.2% (N=40) and 62.5% (N=40) for petri dish, static culture and dynamic culture, respectively. The results show the development rate of the static group are lower than the other two groups, but the development rate of dynamic culture group is close to the petri dish (control group), a little lower than the control group, which indicates that the electro-wetting force is harmless to the embryos. This result prove the biocompatibility of EWOD and the potential of EWOD chip for delivering biological cells and cells culture.

Word Count: 518

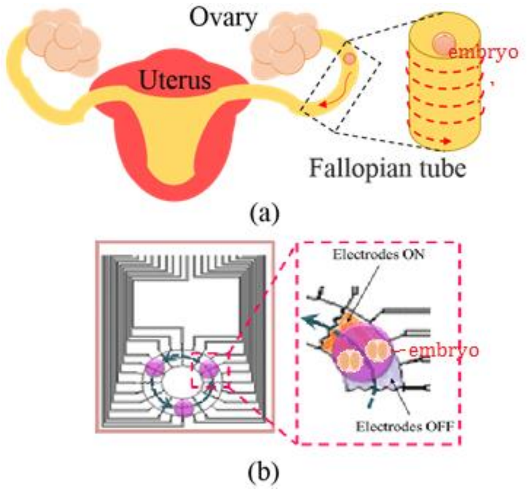

Figure 1: (a) The fallopian tube. The embryos are moving in a spiral manner in the fallopian tube. (b) A ring-shaped microchannel. Using ring-shaped microchannel (2-Dimension) to imitate the spiral movement of embryos in the fallopian tube.

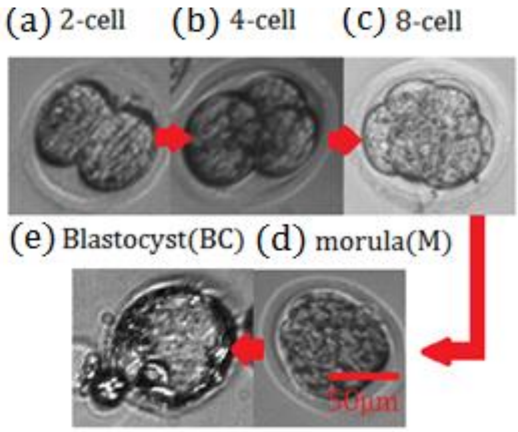

Figure 2: (a) 2-cell stage (b) 4-cell stage (c) 8-cell stage (d) Morula stage (e) Blastocyst stage. The morula and blastocyst stage are the implantation period.

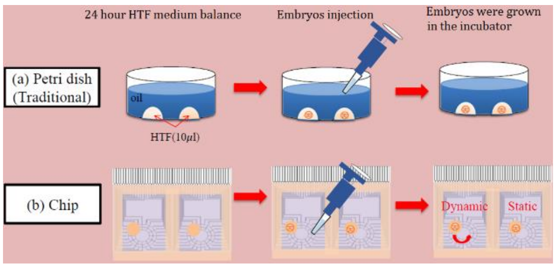

Figure 3: (a) Petri dish culture. (b) Using EWOD chip for embryos culture. The embryos of dynamic and static group were injected into the medium on a chip, the medium of dynamic group were actuated.

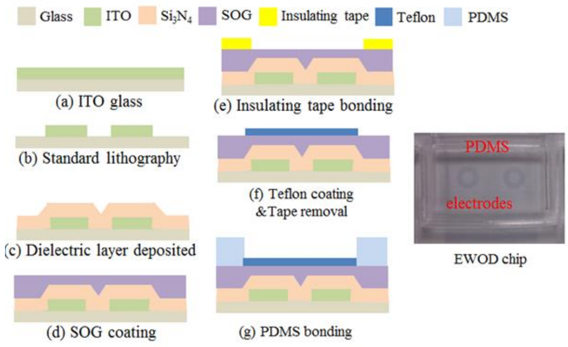

Figure 4: EWOD chip fabrication. (a) An ITO glass. (b) Photolithography process. (c) 450 nm Si_xN_y was deposited by PECVD. (d) SOG was spin-coated on the dielectric layer. (e) Insulating tape bonding. (f) Teflon was spin-coated on the SOG layer. (g) Bonding PDMS ring as the spacer.

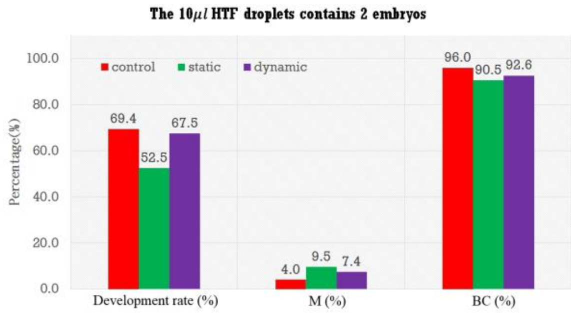

Figure 5: The development of the embryo on EWOD chip and petri dish. The red line, green line, purple line are development rates for petri dish, EWOD for static culture and EWOD for dynamic culture, respectively.

REFERENCES:

[1] L. Y. Chung, H. H. Shen, Y. H. Chung, C. C. Chen, C. H. Hsu, H. Y. Huang, et al., "In vitro dynamic fertilization by using EWOD device," in 2015 28th IEEE International Conference on Micro Electro Mechanical Systems (MEMS), 2015, pp. 519-522.

[2] H. Y. Huang, H. H. Shen, L. Y. Chung, Y. H. Chung, C. C. Chen, C. H. Hsu, et al., "Fertilization of Mouse Gametes in Vitro Using a Digital Microfluidic System," IEEE Transactions on NanoBioscience, vol. 14, pp. 857-863, 2015.

A molecular coating reduces contact angle hysteresis by hiding nanodefects

Eugene Choi[1], Romain Lhermerout[1], Kristina Davitt[1]

[1]Laboratorie de Physique Statistique, Ecole Normale Supérieure
UPMC Univ Paris 6, Univ. Paris-Diderot, CNRS, 24 rue Lhomond 75005 Paris, France

E-mail: echoi@lps.ens.fr, kristina.davitt@lps.ens.fr

Drops on typical surfaces exhibit contact angle hysteresis due to heterogeneities present on the solid surface that pin the contact line. A surface is often considered to have *low* hysteresis when it is less than a few degrees. Delmas et al. showed that structural defects as small as 1 nm can produce a contact angle hysteresis [1], demonstrating the difficulty of producing a pristine surface with no contact angle hysteresis.

In a recent study, we showed that short chains of polydimethylsiloxane (PDMS, polymerization index 126) irreversibly adsorbed on silicon can reduce the contact angle hysteresis to 0.1° or below. We observed that this occurs for liquids that are good solvents of PDMS and postulated that in this case the polymer layer is swollen, yielding a liquid-like surface capable of self-smoothing and hiding defects on the underlying solid [2].

In this study, we investigate the role of such a swollen layer when structural defects are present on the underlying surface. To do this, we prepare samples coated with PDMS or with Octadecyltrichlorosilane (OTS). OTS forms a self-assembled monolayer and does not swell in the presence of liquid, therefore serving as a control surface. Defects of known size, shape and density are prepared by high-temperature sintering of silica nanobeads. The contact angle hysteresis on these surfaces is measured in an optimized dip-coating setup, yielding a precision of about 0.1°**.**

Figure (1) shows the normalized hysteresis measured using decane or perfluorodecalin as the wetting liquid. They are, respectively, good and bad solvents for PDMS. Here the hysteresis is defined as $H = \gamma (\cos\theta_R - \cos\theta_A)$, where γ is the surface tension of the liquid and the advancing and receding angles θ_A and θ_R have been measured at a contact line velocity of 10 μm/s. We first note that the contact angle hysteresis depends linearly on the defect density for all cases we encountered, indicating that our defects are independent. Therefore, the slope of the lines shown in Fig (1) give the energy dissipated over one defect. In the case of a poor solvent, PDMS does not swell and the two surfaces yield very similar slopes. On the other hand, for a good solvent, the dissipated energy is roughly 300 k_BT for OTS and only 30 k_BT for PDMS. We attribute this difference to the smoothing of the defect when it is covered by a liquid-like layer (see inset in Fig.1). In particular, the maximum slope of the defect is reduced, which reduces the pinning force.

In this study we show how a molecular coating only a few nanometers thick can indeed hide defects on a solid and produce an extraordinarily low hysteresis. We also explore the influence of defect shape and size on this effect, and compare our measurements to the scaling expected for strong, non-interacting defects [3].

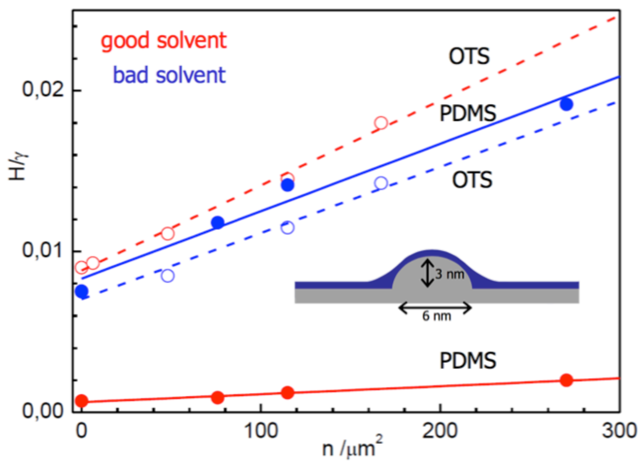

Figure (1): Contact angle hysteresis as a function of defect density measured on PDMS-coated surfaces (closed circles) and OTS-coated surfaces (open circles) with a good (red) and a poor (blue) solvent of PDMS. The hysteresis is small: for reference, the full scale in this figure corresponds to roughly 1.5 degrees. Inset: schematic illustration of a defect and the modification of its topography by a liquid-like layer.

Acknowledgements. We acknowledge funding from ANR REALWET.

References

[1] M. Delmas, M. Monthioux, T. Ondarçuhu. Contact angle hysteresis at the nanometer scale. *PRL*, **106** (2011) 136102.
[2] R. Lhermerout, H. Perrin, E. Rolley, B. Andreotti, K. Davitt. A moving contact line as a rheometer for nanometric interfacial layers. *Nature Communications* (2016) 7:12545.
[3] J.F. Joanny, P.G. de Gennes. A model for contact angle hysteresis. *J. Chem. Phys.* **81** (1984) 552-562.

VOLUME IMPACT ON MORPHOLOGIES OF DROPLETS DEPOSITED ON LINEAR GROOVES

U. SOUPREMANIEN[1], B. CHANDESRIS[1]

[1]Université Grenoble Alpes, CEA/LITEN/DTNM/LRME, 17 avenue des Martyrs 38054 Grenoble, France
e-mail: ulrich.soupremanien@cea.fr

Linear grooves offer a way to guide droplets passively in a predefined direction. This structure modifies droplet morphology and generates elongated droplets. The understanding of the droplet volume impact on droplets distortion (length/width) is an important aspect that need to be better studied, as linear grooves act as energy barriers that pinned the droplets' contact line to the grooves' edges[1, 2]. This distortion is strongly increased with substrate wettability.

Experiments were conducted on silicon substrates. Trapezoidal linear grooves were obtained using reactive ion etching technique. The structures[3] had similar grooves width (~10µm) spaced by ~10µm. Only the grooves heights (h_g) were modified between samples. Three structuration's heights have been tested: 0, 247 and 1183 nm. Thin layers (~100nm) of OMCTSO were deposited using PECVD technique on the structured silicon. Wettability was modified by adding dioxygen gas during the OMCTSO deposition. Three droplet volumes were evaluated: 1.5µl, 2µl and 3 µl. Parallel, perpendicular contact angles, length, width (Figure 1) and height of the droplets were determined using a DSA 10 Krüss measuring system.

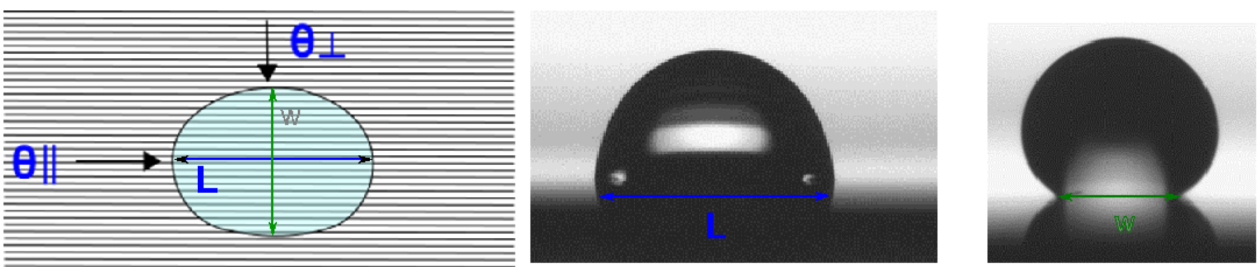

Figure 1: Perpendicular, parallel contact angles length and width of a droplet deposited on linear grooves

Droplet lengths were similar for smooth and patterned surfaces for contact angles perpendicular to the grooves (θ⊥) above ~93° whatever the droplet volume. When the contact angle was decreased, the droplet length increased rapidly on the structured surfaces and with droplets volume also. Droplets widths differ strongly and their values were lower compared to the ones deposited on smooth surfaces. Droplet distortion became lower when droplet volume was increased and the energy barriers impact was assumed to be weaker.

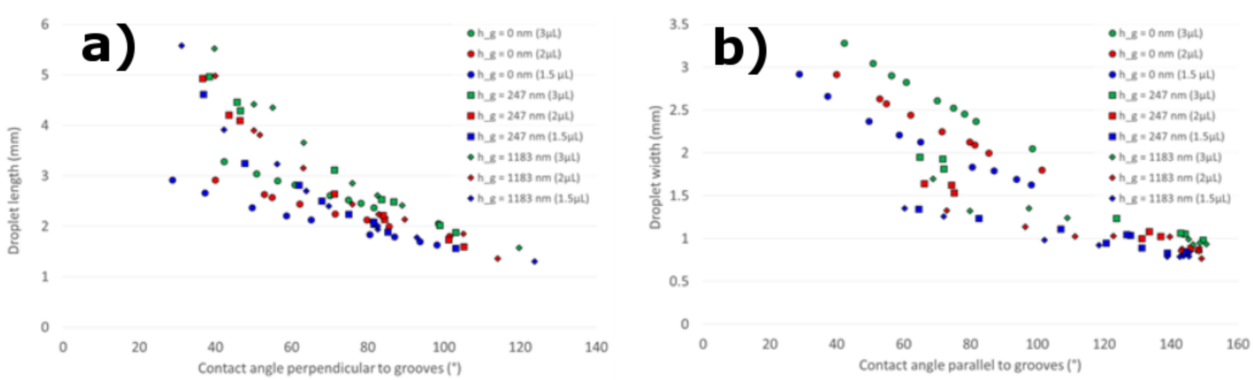

Figure 2: Droplet a) length evolution versus perpendicular contact angle b) width variation versus parallel contact angle

Contact angles in direction parallel to the groove (θ//) were above 140° when θ⊥ was larger to ~85° for h_g = 247 nm or larger than ~70° for h_g = 1183 nm whatever the droplet volume (Figure 3).

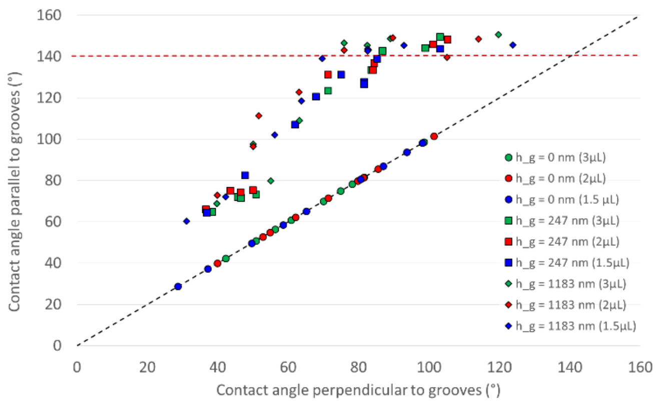

Figure 3: θ// versus θ⊥ for different grooves height

Droplet height is one of the parameter that drives droplet velocities[4, 5]. For small droplet volumes (1.5µL), the difference in height was small for structured surface compared to smooth surface. This difference was increased for larger volumes of droplets (Figure 4).

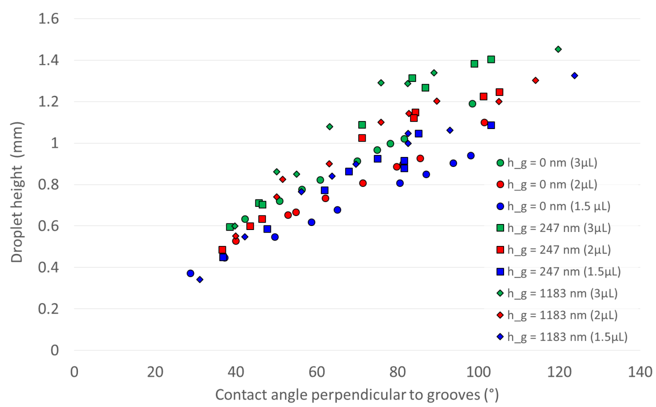

Figure 4: Droplet height variation with wettability and grooves height

The choice of droplet volume would play an important role on displacement of droplets subjected to surfaces with wettability gradient.

References

1. Li, W.; Amirfazli, A. A thermodynamic approach for determining the contact angle hysteresis for superhydrophobic surfaces. *Journal of Colloid and Interface Science* **2005,** *292* (1), 195-201.
2. Wu, D. W.; Chen, Q.-D.; Yao, J.; Guan, Y.-C.; Wang, J.-N.; Niu, L.-G.; Fang, H.-H.; Sun, H.-B. A simple strategy to realize biomimetic surfaces with controlled anisotropic wetting. *Applied Physics Letters* **2010,** *96*.
3. Chandesris, B.; Soupremanien, U.; Dunoyer, N. Uphill motion of droplets on tilted and vertical grooved substrates induced by a wettability gradient. *Colloids and Surfaces A: Physicochemical and Engineering Aspects* **2013,** *434*, 126-135.
4. Moumen, N.; Subramanian, R. S.; McLaughlin, J. B. Experiments on the Motion of Drops on a Horizontal Solid Surface Due to a Wettability Gradient. *Langmuir* **2006,** *22*, 2682--2690.
5. Brochard, F. Motions of Droplets on Solid Surfaces Induced by Chemical or Thermal Gradients. *Langmuir* **1988,** *5*, 432--438.

Simulations of Droplet Impacts on Hydrophobic Moving Walls

Hosein Heidarifatasmi[1], Ozgur Ertunc[1]

[1]Department of Mechanical Engineering, Ozyegin University, Istanbul, Turkey

E-mail: hosein.heidarifatasmi@ozu.edu.tr

Numerical simulations of water drop impact onto hydrophobic surfaces (Wax, Teflon) are carried out through usage of Eulerian multiphase model. Volume of fluid (VOF) model is used to capture the deformation of the water drop interface. Importance of contact angle modeling approach and flow regime are shown by taking static contact angle (SCA)/dynamic contact angle (DCA) approaches and laminar/turbulent flow regimes. Two and three dimensional simulations are conducted. Validation of the numerical scheme is done by obtaining good agreement between simulated results and experimental results of [1]. Internal flow of the liquid during the process of impact is analyzed, particularly for the case of partial rebound. Energy profiles are sketched for each case to provide insight on the dynamics of impact whether the surface is moving or stationary.

The presence of drop impacts on moving surfaces in ink-jet printing, material jetting, spray coating, moving spray cooling and internal combustion engines shows the importance of such impacts in variety of industrial processes. In this regard there exist some experimental based research done by [2]–[5]. Outcomes of drop impacts on a hydrophobic moving wall (Teflon) were classified as partial rebound, deposition and split deposition as a function of normal and tangential Weber numbers(Fig. 1)[4]. The normal Weber is defined by the droplet's normal impact velocity and the tangential one is defined by the surface velocity.

Two and three dimensional simulations of droplet impacts on solid surfaces have been done in a commercial CFD package software. Effect of contact angle modeling approach was investigated in 2D axisymmetric simulations. It was observed that this effect can cause a forceful change in the outcome of the drop impact rom total rebound to deposition which can be noticed by looking into the vortices inside the droplet at the receding stage. In three dimensional simulations, vortex structures in liquid close to the wall and moving contact line, were observed which they reduce the speed of the retarding contact line and hence decreasing the contact angle and preventing the whole drop to detach from the surface for water drop impact on stationary wax surface (taken as our validation case, see Fig. 2). Graphs of internal flow structure of our validation case (Fig.2) together with the energy profiles of that impact (Fig.3) were showing that when the drop reaches to the maximum spreading diameter (at $t = 3.14\ ms, t^* = Vt/D = 2.96$) and , kinetic energy of the fluid is low, because vortices are active inside the drop hence making viscous dissipation more alive. Looking into energy analysis curve of the validation case right at the region of non-moving CL and receding time, it works as a reducing mechanism for kinetic energy of the drop (see Fig. 3). This creates a phase lag between the time at which maximum of the interfacial energy happens and the minimum of kinetic energy. Looking to the cases for moving surfaces, we observed this phase lag decreases as tangential Weber number of the impact increases. In case of deposition on Teflon surface these two times are matching almost with each other. And more increase in inertia would result minimum of kinetic energy lagging behind the maximum of interfacial energy. In split deposition case, the role of bubble entrainment in the first splitting was observed (see Fig. 5) while later because of high tangential velocity the trail of the spreading drop ruptures. The physical and numerical models used in this work was sufficiently good to resolve the observed phenomena when water droplets hits to moving smooth hydrophobic surfaces[4].

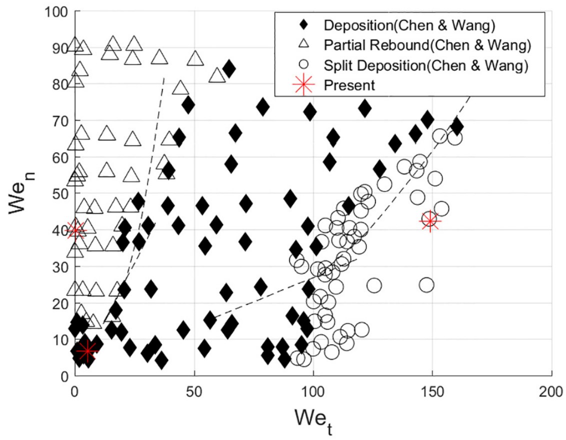

Figure 1 - Outcomes of water drop impact on a hydrophobic (Teflon) moving wall along with selected computational data points. Graph is regenerated from [4].

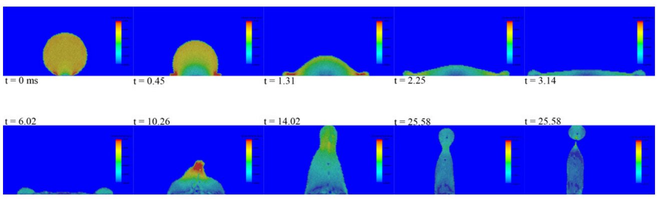

Figure 2 - Internal flow structure of the reference case. Prevention of total rebound in presence of vortex structures near to wall can be noticed specially at later stages of impact.

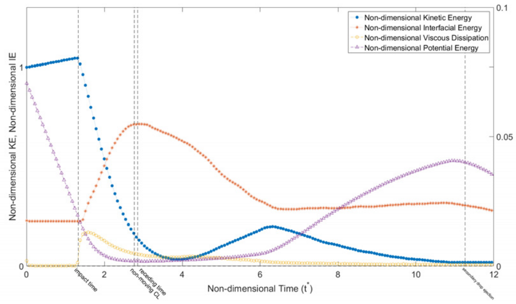

Figure 3 - Energy profiles extracted from the impact of a water drop on a smooth Wax surface. Normal We number in this case is 52 (static wall, validation case, $t^* = Vt/D$)

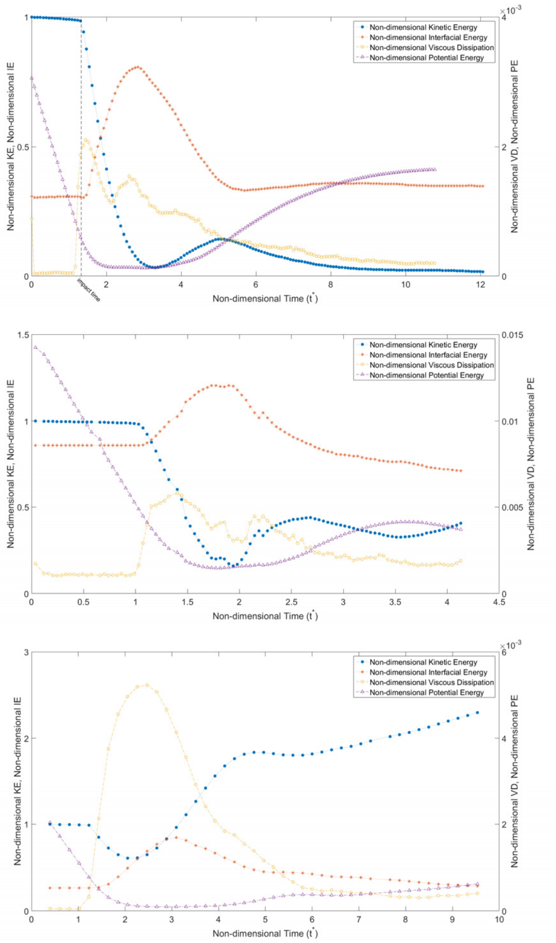

Figure 4 - Energy profiles of water drop impacts on moving Teflon surface. From top to bottom the cases are partial rebound, deposition and split deposition respectively. Impact conditions are given in Fig. 1.

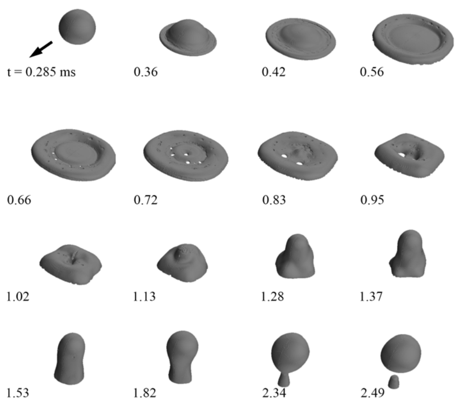

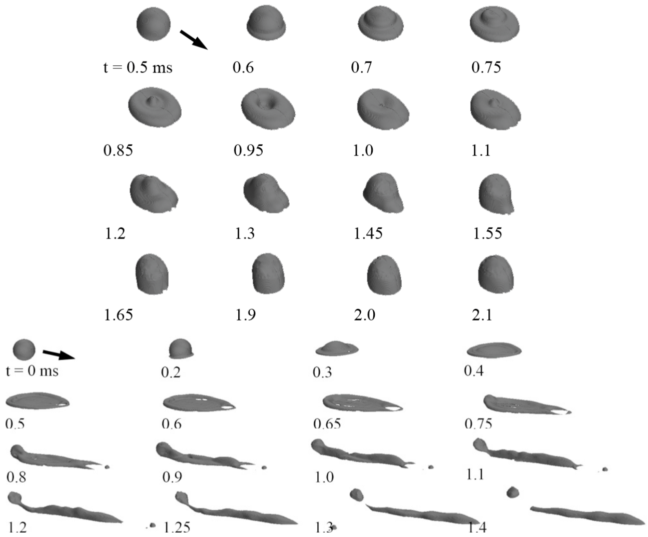

Figure 5 - Time evolution of water drop impacts on moving Teflon surface. From top to bottom the cases are partial rebound, deposition and split deposition respectively. Impact conditions are given in Fig. 1. Arrows denote the surface motion direction.

Acknowledgements. The authors would like to gratefully acknowledge TUBITAK for providing financial support to 114M423 research project. Also, special thanks to IBM Shared University Research (SUR) program and Asst. Prof. Dr. Ismail Ari for providing computational resources to carry out numerical simulations.

References

[1] R. Rioboo, M. Marengo, and C. Tropea, “Time evolution of liquid drop impact onto solid, dry surfaces,” *Exp. Fluids*, vol. 33, no. 1, pp. 112–124, Jul. 2002.

[2] S. Fathi, P. Dickens, and F. Fouchal, “Regimes of droplet train impact on a moving surface in an additive manufacturing process,” *J. Mater. Process. Technol.*, vol. 210, pp. 550–559, 2010.

[3] J. C. Bird, S. S. H. Tsai, and H. a Stone, “Inclined to splash: triggering and inhibiting a splash with tangential velocity,” *New J. Phys.*, vol. 11, no. 6, p. 63017, Jun. 2009.

[4] R. H. Chen and H. W. Wang, “Effects of tangential speed on low-normal-speed liquid drop impact on a non-wettable solid surface,” *Exp. Fluids*, vol. 39, pp. 754–760, 2005.

[5] T. S. Zen, F. C. Chou, and J. L. Ma, “Ethanol drop impact on an inclined moving surface,” *Int. Commun. Heat Mass Transf.*, vol. 37, no. 8, pp. 1025–1030, 2010.

Droplet Impact on Moving Superhydrophobic Surfaces

Gökhan Kayansalçik[1], Özgür Ertunç[1]
[1]Department of Mechanical Engineering, Ozyegin University, Istanbul, Turkey

E-mail: gokhan.kayansalcik@ozu.edu.tr

Droplet impingement phenomenon has many technical applications such as surface coating, ink-jet printing, rapid spray cooling of hot surfaces, internal combustion engines and so on and so forth. There are numerous publications about the impact of droplets on static surfaces. However, there are few studies on the droplet dynamics upon impact on to moving surfaces [1-4]. In the present study, behavior of droplets on the moving superhydrophobic surfaces ($\theta_{rough=}$ 159.9° ± 5.6, θ_{smooth}=166.7±2.9) have been studied experimentally. In the experiments, droplets which have different diameter and velocity have been generated and impacted on the surfaces. Also, surface roughness and the tangential velocity of the surface have been changed. Droplet motion was recorded by a high-speed camera and from the observations regime maps of droplet behavior have been constructed as a function of normal and tangential Weber numbers. In addition to density and surface tension of the fluid and droplet diameter, normal velocity which is the velocity of droplet and tangential velocity which is the velocity of surface are used to calculate normal and tangential Weber numbers.

It was seen that when a droplet hits to a superhydrophobic surface, various types of rebound occur depending on the normal and tangential Weber number and the surface roughness (Figures 1 & 2).

If droplet impacts to a smooth superhydrophobic surface;

- At low tangential and normal Weber numbers, droplet rebounds from the surface. However, increase in the normal Weber number, droplet hits to the surface and it creates an upward jet and some portion split vertically while rebounding.
- If the tangential Weber number is increased, droplets which have either low or high normal Weber number rebound. In other words, the tangential velocity of the surface suppresses the vertical split.
- At the very tangential Weber numbers, droplet split from leading edge while the rest rebounds.

Vertical split with splashing and rebound with trailing edge split were rarely observed as shown in Figure 1.

When the surface roughness is increased;

- At low tangential Weber numbers, droplets which has low normal Weber number rebound from the surface similar to the smooth surface, but when the normal Weber number of the droplets are increased, droplet rebounds with splitting from both sides and splashing occurs.
- However, if the tangential Weber number is increased, outcome changes into rebound with both sides split and splashing even at the low normal Weber numbers. Similar results can be seen at high normal Weber number cases.

In addition to the smooth and rough surfaces, one more superhydrophobic surface which is moderately roughly is being prepared to understand the effect of the roughness to the droplet behavior completely. Data on the surface topology obtained through optical measurements will also be provided.

Acknowledgements
The study was supported by the Scientific and Technological Research Council of Turkey (TÜBİTAK), Project No: **114M423.**
Prof. Dr. Mehmet Arık for lending the high speed camera to us for visualization.
Assoc. Prof. Dr. Bahar Başım for valuable comments on the surface preparation.

References

[1] Bird, J. C., Tsai, S. S. H., & Stone, H. a. (2009). Inclined to splash: triggering and inhibiting a splash with tangential velocity. New Journal of Physics, 11(6), 063017.
[2] Chen, R. H., & Wang, H. W. (2005). Effects of tangential speed on low-normal-speed liquid drop impact on a non-wettable solid surface. Experiments in Fluids, 39, 754–760.
[3] Mundo, C., Sommerfeld, M., & Tropea, C. (1995a). Droplet-wall collisions: Experimental studies of the deformation and breakup process. Int. J. Multiph. Flow, 21(2), 151–173.
[4] Mundo, C., Sommerfeld, M., & Tropea, C. (1995b). Droplet-wall collisions: Experimental studies of the deformation and breakup process. International Journal of Multiphase Flow, 21(2), 151–173.

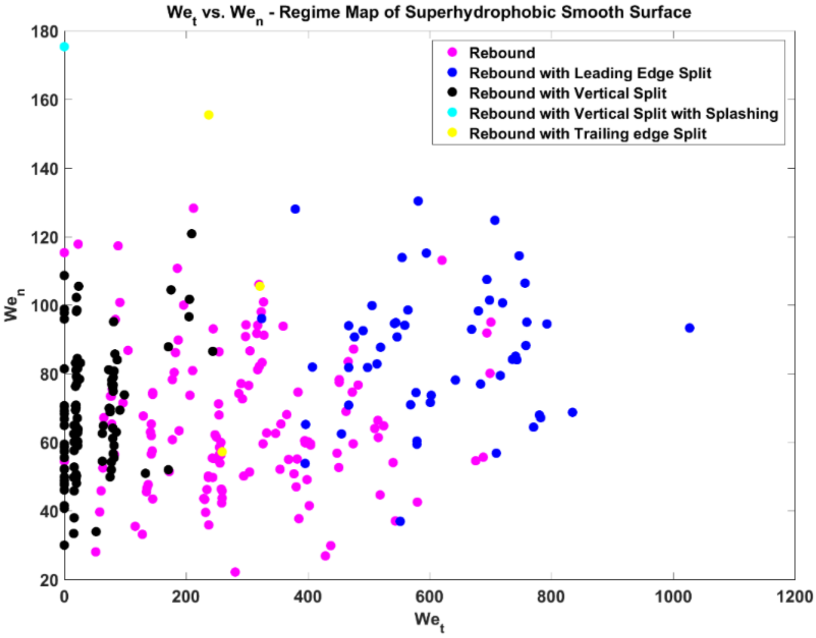

Figure 1: Droplet Regime Map for the Superhydrophobic Smooth Surface

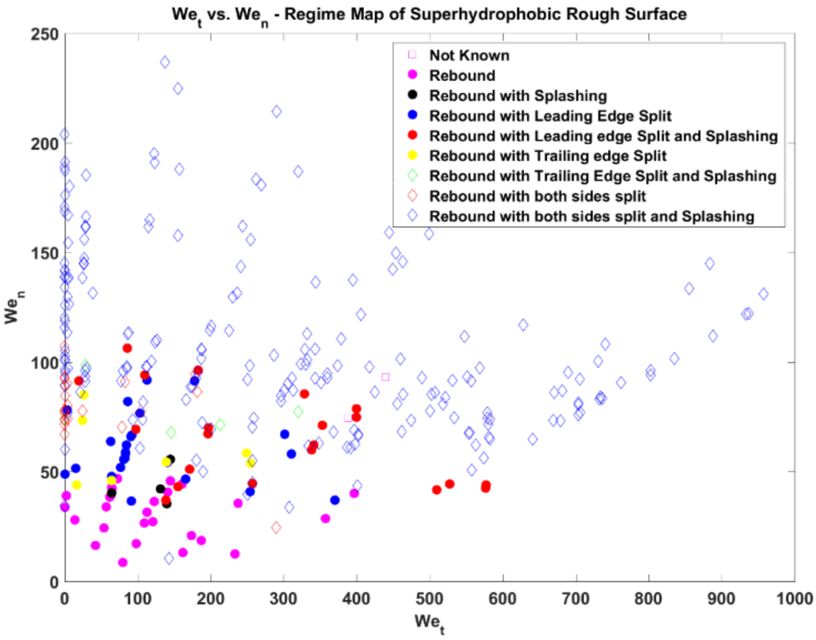

Figure 2: Droplet Regime Map for the Superhydrophobic Rough Surface

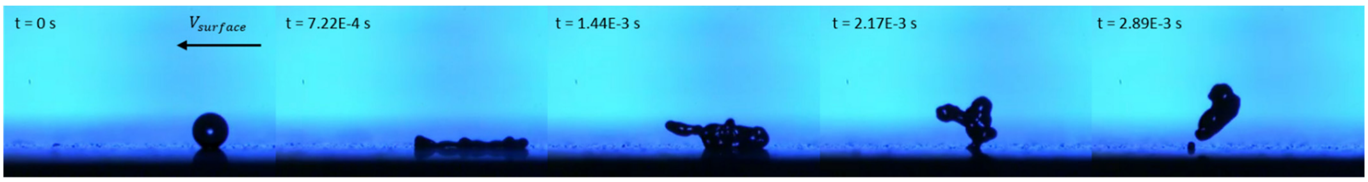

Figure 3: Droplet Behavior at Smooth Surface We_n= 93.91 and We_t=359.55 (Rebound)

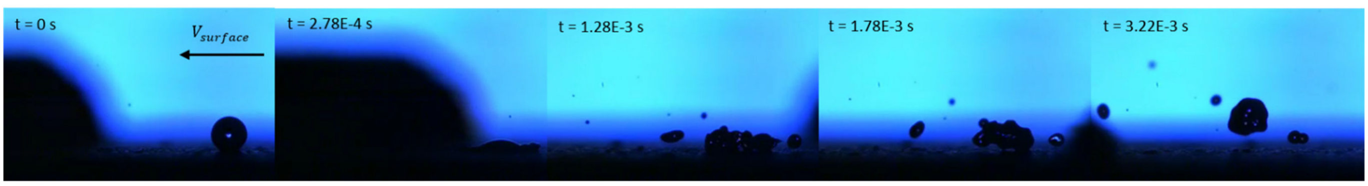

Figure 4: Droplet Behavior at Rough Surface We_n = 94.77 and We_t= 359.72 (Rebound with both sides split and Splashing)

AN EXPERIMETNAL INVESTIGATION ON THE DORP/INTERFACE COALESCENCE WITH SURFACTANTS

Teng Dong[1], Weheliye Hashi Weheliye[1],Panagiota Angeli[1]

[1] ThAMeS Multiphase Group, Department of Chemical Engineering, UCL, London,UK

E-mail: p.angeli@ucl.ac.uk

When a droplet approaches through an immiscible liquid to the interface of its identical liquid, it will merge with the homophase after the rupture of the thin film. In some conditions, the droplet cannot merge fully with the bulk liquid at one stage but leaves a secondary droplet on the interface. This phenomenon is called *partial coalescence*. Partial coalescence can repeat itself many times until the droplet is fully mixed with the bulk. This work aims to investigate the drop coalescence (both partial and total coalescence) with a flat organic/aqueous interface when surfactants are present.

The experiments were conducted in a transparent acrylic tank with 50mm square section width and 150mm height. The aqueous phase was placed up to 50mm from the bottom and the organic phase was placed on the top with the same height. Droplets of aqueous liquids were generated by injecting the liquid into the organic phase through nozzles with different inner diameters (0.5mm, 1mm, 2mm). The nozzles were fixed at approximately 20 mm above the aqueous/organic interface to minimise any variation on the droplet impact locations. Shadowgraphy was first used to observe the drop interface behaviour during coalescence. The observation area was illuminated by a backlight fixed at the back of the vessel, while the whole process was captured by a high-speed camera. The aqueous phase was water-glycerol mixtures with different mass fractions including ζ=0, ζ=25%, ζ=35%, ζ=42.5%. The organic phase was a 5 cst silicon oil. For the surfactant tests, different amounts of Span 80 were introduced into the oil with mass ratios, φ, of surfactant to oil equal to 0, 2×10^{-5}, 5×10^{-5}, 1×10^{-4}.

The velocity fields inside the droplet were investigated with Particle Image Velocimetry (PIV). A laser plane with 1mm thickness was generated by a continuous laser in the middle of the coalescence cell. For the PIV tests of total coalescence, the organic phase was Exxsol D80 oil and the aqueous phase was a glycerol solution. The concentration of glycerol is set at ζ=80% w/w to match the refractive index of Exxsol D80 oil (r=1.443 at room temperature) and avoid any light distortions. The organic phase for partial coalescence was a 0.65cst silicone oil and the aqueous phase was a 33% glycerol solution with r=1.372 at room temperature. For both partial and total coalescence tests, the droplets were seeded with 1 μm Rhodamine tracer particles. For the surfactant tests, different amounts of Span 80 were introduced into the oil phase.

The boundary between partial and total coalescence was first presented through an Oh-Bo base phase map for both non-surfactant and surfactant systems. For small Bo a critical Oh for partial coalescence was found. The critical Oh reduced when surfactant was introduced into the oil. Correspondingly, the partial coalescence area shrunk. The drop ratios ξ at each stage of the partial coalescence cascade were plotted in a three-regime figure (Chen et al., 2006). In the gravity regime, the drop ratio ξ remained about 0.17-0.30 and was only slightly affected by the surfactants. The value of the drop ratio reduced when surfactants were present in the inertio-capillary regime. For φ=0, the drop ratio could remain 0.50 for a wide range of Oh but it decreased to 0.22 when φ was increased to 1×10^{-4}. Th epresence of surfactants also reduced the range of the inertio-capillary regime. According to Martin and Blanchette (2015) the decrease of the drop ratio was attributed to the uneven distribution of surfactants along the drop surface during coalescence.

The velocity fields were then measured with PIV for total coalescence. It was found that the surfactant promoted the deformation of the interface before the rupture of the film. After the rupture, the drop surface experienced an oscillation for low surfactant concentrations below $\varphi=1\times10^{-4}$, while the drop surface smoothly approached to the finally flat interface for high surfactant concentration. For all the surfactant concentrations investigated, a pair of counter-rotating vortices was observed at the bottom of the droplet which then moved upwards and spread in the droplet. However, the presence of surfactants reduced the magnitude of the vortices (Weheliye et al., 2017).

Velocity fields were also studied in the partial coalescence regime. For φ=0, a daughter droplet was observed on the interface after coalescence, while total coalescence occurred when φ was increased to 1.31×10^{-6}. In partial coalescence the vertical downward motion of the liquid in the drop after the film rupture creates a low pressure area in the meniscus which leads to pinch off and the generation of a daughter droplet. For $\varphi=1.31\times10^{-6}$, the rupture points were shifted away from the centre. The evolution of vortices for coalescence are discussed for different surfactant conecntrations.

Acknowledgements.
This project was funded by the UK Engineering and Physical Sciences Research Council (EPSRC) Programm Grant MEMPHIS. The authors would like to acknowledge the EPSRC Instrument Pool for the loan of the high-speed camera. Teng Dong would like to thank the Chinese Scholarship Council (CSC) for providing his studentship.

References

[1]. CHEN, X., MANDRE, S. & FENG, J. J. 2006. Partial coalescence between a drop and a liquid-liquid interface. *Physics of Fluids,* 18**,** 051705.
[2]. MARTIN, D. W. & BLANCHETTE, F. 2015. Simulations of surfactant effects on the dynamics of coalescing drops and bubbles. *Physics of Fluids (1994-present),* 27**,** 012103.
[3]. WEHELIYE, W. H., DONG, T. & ANGELI, P. 2017. On the effect of surfactants on drop coalescence at liquid/liquid interfaces. *Chemical Engineering Science,* 161**,** 215-227.

DYNAMICS OF PARTICLE-LADEN LIQUID SHEETS

Alban Sauret, Anthony Troger, Pierre Jop

SVI, UMR 125 CNRS/Saint-Gobain, 93303 Aubervilliers, France
E-mail: alban.sauret@gmail.com

Introduction. Suspensions of solid non-brownian particles in a liquid are encountered in various geophysical, industrial or biological systems. Whereas most of the past studies have characterized the transport of particles in bulk flow or the rheology of suspensions [1, 2], situations in which the thickness of the liquid layer becomes comparable to the particle size are less understood. In this situation, the particles are able to deform the liquid interface, which leads to complex interactions with the interfaces and between the particles.

The presence of particles in liquid film of comparable size can be especially important for its stability as it has been shown to modify the pinch-off of viscous fluid during drop formation [3, 4]. Typically, the detachment becomes accelerated and depends on the particle volume fraction and size. This uncommon situation cannot be explained with a classical Newtonian fluid approach or classical rheology of diluted suspensions. Indeed, the presence of particles perturbs locally the thinning of the filament. It then leads to the acceleration of the droplet formation compared to the detachment observed for a pure fluid. However, the pinch-off is due to a 1D flow and more complex situations remain poorly understood. In particular, the influence of particles in self-suspended liquid films, which constitutes a 2D situation, could lead to a modification of its stability [5].

In this study, we consider experimentally a classical model system in which a drop impacts at the center of a flat target of size comparable to the drop diameter [6]. Upon impact the liquid flattens into a self-suspended liquid sheet that expands radially. Such experiments have been performed with Newtonian and non-Newtonian fluids to characterize the radial expansion of the liquid sheet and its fragmentation into droplets [7, 8].

Experimental Methods. The generation of the transient liquid sheet is based on a method adapted from the original experiments of Rozhkov *et al.* [6]. In our experimental set-up, shown in Fig. 1, a drop impacts the flat cross-section of a solid cylindrical target of diameter d_t = 6 mm. The drop of diameter d_0 = 3.9 impact the trarget with a velocity u_0. The drop then spreads into a liquid sheet. We record the spreading of the sheet from the top using a high speed camera with a macro lens.
The suspensions are prepared with spherical polystyrene PS particles (Dynoseeds) of density $\rho \simeq 1058$ kg m^{-3} dispersed in a mixture of 25%wt glycerol/water solution such that the particles are neutrally buoyant. We use particles of diameter d = 140 µm that are larger than the mean thickness of the liquid sheet.

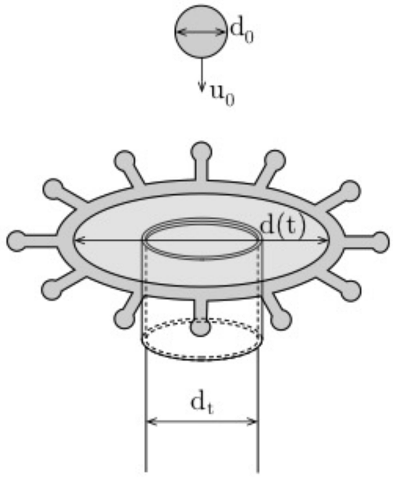

Figure 1. Schematic of the experimental set-up: a drop of diameter d_0 impacts the cylindrical target (diameter d_t) at a velocity u_0, leading to the formation of a transient liquid sheet of diameter d(t)=2 R(t)

Phenomenology. Two experiments, without and with particles, are shown in Fig. 2 and illustrate the dynamics of the liquid sheet from the impact of the drop on the target at t = 0 ms to the retraction and the atomization into droplets after about 10 ms. We observe that the geometry of the liquid sheet during the spreading satisfies to the cylindrical symmetry of the geometry: a thin liquid sheet sur- rounded by a rim extends horizontally, suspended in air until it reaches the maximum diameter that results from a balance between the inertial and capillary effects. As shown on this figure, the value of the maximum diameter depends on the presence or absence of particles but also on the size of the drop and the impactor as well as the impact speed. Once the liquid sheet reaches its maximum diameter, the film retracts under the effect of capillary forces and destabilizes, losing its cylindrical symmetry. We also note that during most of the process, especially during the recessing phase, droplets are generated.

Spreading. We have systematically studied the effect of the 140 µm diameter particles on the spreading dynamic of the liquid sheet (Fig. 3). The particles are larger than the liquid sheet thickness and are therefore subject to capillary force. We observe that, although the evolution is similar in all cases, there is a strong decrease of the maximum spreading diameter, even at low concentrations. A first assumption can be made to explain these observations: the increase in viscosity due to the addition of particles leads to the change of dynamics.

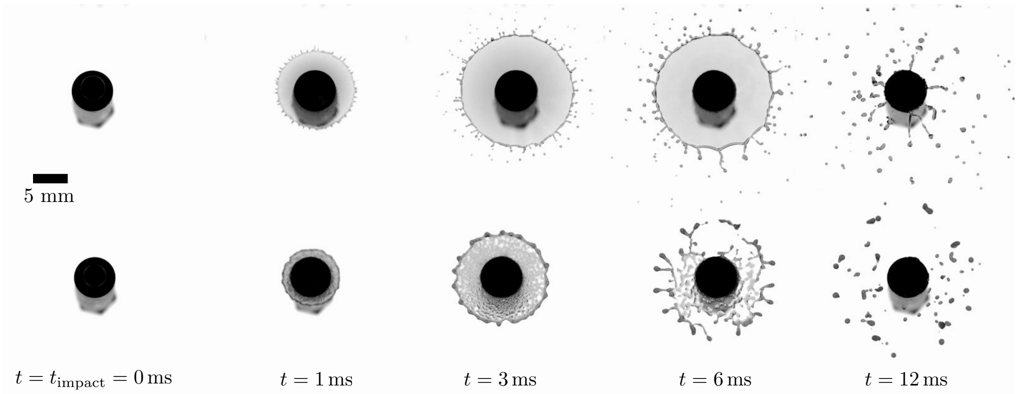

Figure 2. Successive pictures showing the time-evolution of a liquid sheet for the liquid (top pictures) and a suspension with ϕ=0.35 (bottom)

To quantify this influence, we performed similar experiments using water/glycerol mixture that have an effective dynamic viscosity identical to the suspensions. The time-evolution of this Newtonian liquid sheet illustrate that the increase in viscosity induced by the particles cannot account for the differences observed. Indeed, for water/glycerol concentrations corresponding to suspensions with ϕ<20%, no difference is observed. Therefore, the modification of the spreading dynamics is an intrinsic local effect of the particles. Qualitatively, the presence of particles larger than the thickness of the sheet creates a deformation of the interface that limits its expansion and dynamics [9].

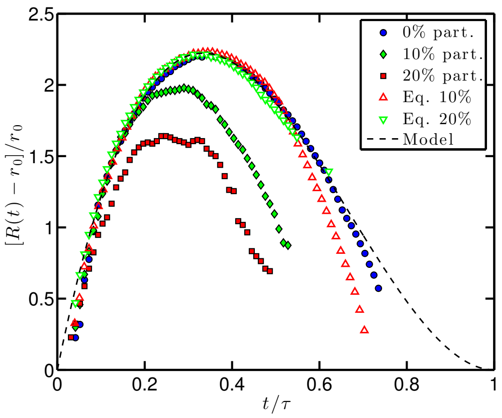

Figure 3. Evolution of the rescaled radius of the liquid sheet as a function of the dimensionless time t/τ for the pure liquid and various suspensions. The measurements performed with Newtonian liquids of same viscosities than the 10% and 20% suspensions are also reported. The dotted is the model developed in [7] for a Newtonian liquid.

We have also measured the resulting droplet size distributions for increasing particles concentration. It shows that the distributions share a similar trend even if they tend to be larger and shift to larger radii as the concentration in particles increases. We also notice that the larger the concentration is, the less numerous are the droplets emitted at each impact and these droplets tend to have a large diameter.

Conclusion. In this study, we have experimentally studied the formation and atomization of a particle-laden liquid sheet formed upon impact of a drop on a small target. The presence of spherical, neutrally buoyant, non-colloidal particles introduces various effects that make the dynamics of the liquid sheet different from that of a pure liquid. Our experimental results have first illustrated the influence of the particles on the spreading of the liquid film. We have also investigated the destabilization of the liquid sheet and its atomization in droplets with and without particles. Our results suggest that the particles do not alter the physical mechanism of droplet generation, but they modify the mean radius of the drops generated.

Acknowledgements. The authors acknowledge the support from the ANR (project ProLIFIC ANR-16- CE30-0009) and partial support from a CNRS PICS grant n°07242.

References

[1] E. Guazzelli & J. F. Morris, A physical introduction to suspension dynamics (Cambridge University Press, 2011) 256 pp
[2] M. M. Denn & J. F. Morris, Annu. Rev. Chem. Biomol. Eng. 5, 203-228 (2014)
[3] R.J.Furbank & J.F.Morris, Phys. Fluids 16 (5),1777-1790 (2004)
[4] C. Bonnoit, T. Bertrand, E. Clément & A. Lindner, Phys. Fluids 24(4), 043304 (2012)
[5] F. O. Addo-Yobo, M. J. Pitt & H. A. Obiri, AIChE J. 57(8), 2007-2024 (2011)
[6] A. Rozhkov, B. Prunet-Foch & M. Vignes-Adler, Proc. Roy. Soc. A 460(2049), 2681-2704 (2004)
[7] E. Villermaux & B. Bossa, J. Fluid Mech. 668, 412-435 (2011)
[8] B. Keshavarz, E. C. Houze, J. R. Moore, M. R. Koerner, & G. H. McKinley, Phys. Rev. Lett. 117(15), 154502 (2016)
[9] L. A. Lubbers, Q. Xu, S. Wilken, W. W. Zhang & H. M. Jaeger, Phys. Rev. Lett. 113(4), 044502 (2014)

ENTRAINMENT OF DROPLETS OF AMBIENT LIQUID IN PINCHING-OFF PROCESS OF VAPOR BUBBLE INJECTED TO SUBCOOLED POOL

Ichiro Ueno*, Yusuke Koiwa, Toshihiro Kaneko

Department of Mechanical Engineering, Faculty of Science & Technology, Tokyo University of Science, Chiba, Japan

*E-mail: ich@rs.tus.ac.jp

In this study, we investigated the pinching-off process of vapor bubbles exposed to subcooled liquid in a Hele–Shaw cell by carrying out experiments. We injected water vapor, generated by a vapor generator, through the orifice into a narrow gap region between two glass plates that were submerged in a subcooled pool of distilled water. From this series of experiments, we determined the interaction between a single vapor bubble and subcooled liquid in a quasi-two-dimensional system. Vapor bubbles passing the Hele–Shaw cell were captured by high-speed imaging (Fig. 1).

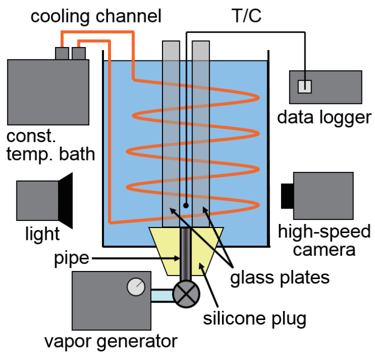

Fig. 1 Experimental apparatus

Ambient liquid around the neck of the vapor bubble was entrained into the vapor bubble after its detachment from the vapor column. A myriad of droplets were formed and scattered upwards inside the vapor bubble in the case where the degree of subcooling exceeded 30 K. These droplets collided with the interface from on the inside of the vapor bubble to generate fine disturbances. We show that the volume of the droplets scattered inside the vapor bubble increases as time elapses, that is, these droplets become condensation nuclei and accelerate the condensation of the vapor bubble. The entrainment of ambient liquid into the vapor bubble is substantially enhanced with the degree of subcooling, resulting in abrupt condensation of the vapor bubble.

We limited our scope to the injection rate of the vapor that is low enough in order to prevent disturbances because of the high shear on the vapor column interface (Fig. 2). This helps us to maintain a rather smooth surface of the vapor bubble during the growth in the cell. The vapor injected into the Hele–Shaw cell grows and then detaches to form a vapor bubble after leaving the residual vapor column near the orifice. We obtained the following results by varying the degree of subcooling from 20 to 70 K under atmospheric pressure. During the detaching process, surrounding liquid is sucked into the necking part of the vapor column, and penetrates the preceding bubble for any degree of subcooling. We reproduced the penetrating behavior for degree of subcooling ΔT_{sub} = 20 K, as indicated by Kamei and Hirata [1].

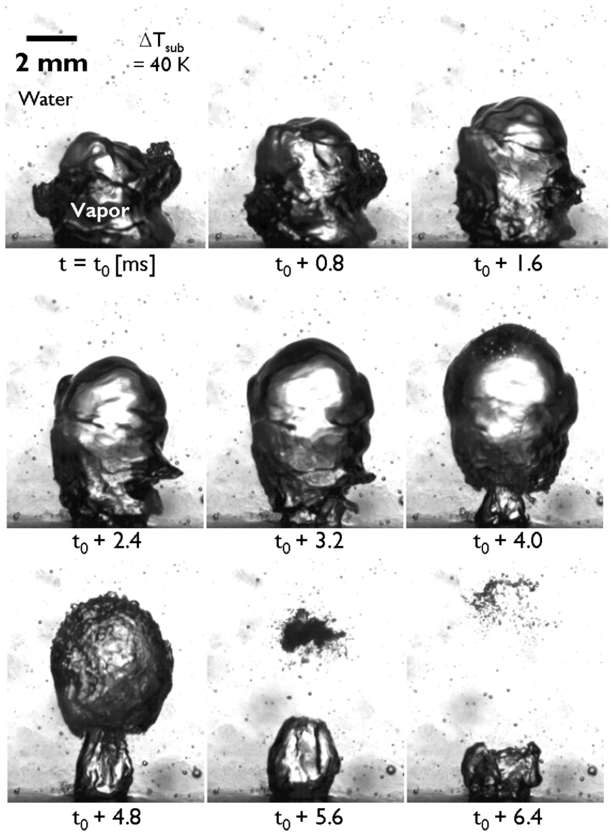

Fig. 2 Typical example of growing and condensing processes of the injected vapor bubble through the orifice into the pool of 40 K in the degree of subcooling [2]. Scale bar in the first frame corresponds to 2.0 mm. Shutter speed is of 1/72080 s.

For $\Delta T_{sub} \geq$ 30 K, the penetrated liquid breaks apart to form a myriad of tiny droplets that scatter inside the vapor bubble. These scattering droplets collide with the vapor bubble interface to produce fine disturbances, as reported by Ueno et al. [2]. A downward microjet is formed at the same time in the following vapor column after the preceding bubble detaches. This jet draws the subcooled liquid to the orifice and the substrate, and the supply of fresh subcooled liquid results in the removal of the heated liquid from the neighbor of the orifice and maintains the low temperature of the liquid around the orifice.

The scattered droplets produced during the detaching process grow in size as they travel inside the preceding vapor bubble to play a significant role as the condensation nuclei. This droplet formation and their growth trigger the abrupt condensation of the vapor bubble for $\Delta T_{sub} \geq 30$ K. We proposed the liquid–vapor contact-ratio within the preceding vapor bubble to discuss the condensation process using a rough evaluation of the contribution of the penetrated liquid and scattered droplets. The correlation between the abrupt condensation to collapse and the ratio is illustrated as a function of the degree of subcooling.

Acknowledgements. Parts of this study were financially supported by the 45th Research Grant in Natural Sciences received from the Mitsubishi Foundation (2014−2015), and by Grants in Aid for Research on Boilers and Pressure Vessels by the Japan Boiler Association (JFY2016). Image of the microbubble emission boiling was provided from Ms. Kazuna Horiuchi, a graduate school student belonging to the present authors' group. The author IU acknowledges the Tokyo University of Science (TUS) Fund for Strategic Research Areas.

References

[1] S. Kamei, M. Hirata, Condensaiton phenomena of single vapor bubble into subcooled water: 1st report, flow visualization, Trans. Japan Society for Mechanical Engineers B (in Japanese) 53 (486) (1987) 464–469.
[2] I. Ueno, J. Ando, Y. Koiwa, T. Saiki, T. Kaneko, Interfacial instability of a condensing vapor bubble in a subcooled liquid, European Physical Journal Special Topics 224 (2015) 415–424.

The Origin of Droplets' Retention on Superhydrophobic Surfaces

Youhua Jiang, Zongqi Guo, and Chang-Hwan Choi

Department of Mechanical Engineering, Stevens Institute of Technology, Hoboken, New Jersey 07030, USA

The controllable droplets' mobility on superhydrophobic surfaces is of great significance in many engineering applications including self-cleaning and anti-icing surfaces, targeted coating, ink-jet printing, microfluidic devices, and biological and chemical detection. However, the origin of the retention of droplets on superhydrophobic surfaces, which is generally attributed to the surface morphology and material hydrophobicity, still remains vague despite recent extensive studies. In this work, we propose a theory to quantitatively correlate the bulk droplet retentive force to surface solid structures along the droplet boundary, particularly based on the change of droplet energy induced by the exchange of solid-gas and solid-liquid interfaces, and the deformation of liquid-gas interfaces. By visualizing the contact line evolution on surface structures, we develop a universal model, which can describe droplet retention on superhydrophobic surfaces as a function of the structure size, contact line length, and intrinsic retention of the surface material. This model successfully predicts the droplet retentive force on superhydrophobic surfaces, verified by experiments. Its universality is also verified by comparing the predicted and measured values on superhydrophobic surfaces with different morphological types (pillar *vs* pore), a wide range of solid fractions (from 0.03 to 0.99), and various intrinsic retentions (different surface materials/coatings). Particularly, transparent superhydrophobic surfaces with the different morphological types and systematically varying dimensions are fabricated and employed for experiments. Evolutions of droplet boundaries when droplets advance and recede are visualized and the densities of contact lines are quantified by

using a reflection interference contrast microscopy method. According to this visualization, we categorize the key factors inducing the droplet retention as, (1) the energy required to exchange the solid-liquid and solid-gas interfaces, (2) the energy expended to deform the liquid-gas interfaces, and (3) the frictional energy consumed when the contact line slides on solid surfaces. By following this basis, the exchange of solid-liquid and solid-gas interfaces and the frictional energy consumption can be quantified by the visualization of contact lines. The deformation of liquid-gas interface can also be estimated on the basis of energy minimization. This model is further applied to predict the droplet retentive forces on superhydrophobic surfaces with the data reported by other researches, showing great agreement with their measured results. This study offers explanations of droplets' pinning on natural textured surfaces and provides guidelines to engineer synthetic structured surfaces serving customized applications, such as targeted coating, ink-jet printing, microfluidic devices, biological and chemical detection.

Droplets 2017
UCLA, Los Angeles, CA, USA
July 24-26, 2017

WETTING TRANSITION FROM OCTAGON TO SQUARE SHAPE OF WATER-ETHANOL BINARY DROPLETS ON MICRO-PYRAMID SUBSTRATE

H.C. Feng, J.H. Ren, and Fei Duan*

School of Mechanical and Aerospace Engineering, Nanyang Technological University, 639798, Singapore

* feiduan@ntu.edu.sg

ABSTRACT

Controlling droplet wetting and evaporation on patterned substrates are of importance in the abroad applications of biology, self-cleaning, printing, thermal management, etc. It has attracted more attention from the researchers. Hitherto, most strategies about the case of droplet drying on patterned substrates for the manipulation of droplet shapes and dynamics are related to the surface properties, such as altering the shape, size and density of artificial structures, chemical heterogeneity, and hydrophobicity of the substrates. However, the effect of solution for sessile droplets on the wettability and the corresponding evaporation modes on patterned substrates has not been well reported.

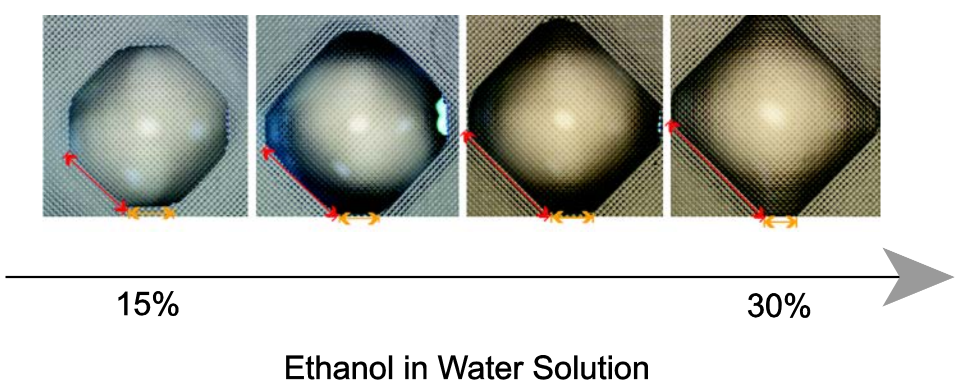

Figure 1: Droplet initial wetting on the substrate with micro-pyramid cavities with an increase of the mass concentration of ethanol in water.

In the study, the water-ethanol binary mixture fluids are prepared by mixing nanofiltered deionized water of the resistivity and ethanol, the wetting and evaporation are investigated as the droplets were put on the micro-pyramid substrate made from nanoimprinting. The droplet evaporation is simultaneously visualized from a top view by the optical microscope and two side views by the high-speed cameras. The evaporation dynamics and shape manipulation of water-ethanol mixture droplets are observed on the patterned substrates through varying ethanol concentration in water-based solution. The increasing ethanol concentration recovered the droplet wetting area from an octagon to a square.

The initial wetting side ratio increased with an increase of ethanol concentration till the droplet cannot be formed. Different from the pure water droplets on the patterned substrate exhibiting three stages over the lifetime, i.e., the constant contact line (CCL) stage, the constant contact angle (CCA) stage, and the final mixture stage. The water-ethanol binary droplets experienced one more mixed stage between the CCL and CCA stages due to the different depinning times along the two line-of sights. Droplets depinned earlier at a higher ethanol concentration. The micro-pyramid cavities on the substrate contributed to the nonlinear behavior between the volume with a power of two thirds as a function of evaporation time. The present study might provide us a possibility to control the droplet wetting area and evaporation on the patterned surfaces by simply varying the solution in droplets.

DYNAMICS OF LIQUID INTERFACE FOLLOWING DROPLET COLLISION

Jun-ya Kohno

Department of Chemistry, Faculty of Science, Gakushuin University, Tokyo, Japan

E-mail: jun-ya.kohno@gakushuin.ac.jp

Reactions induced by mixing two solutions play a central role in chemistry. Most of synthetic reactions proceed by mixing one organic and/or aqueous solution to another. In order to investigate the kinetics of the reactions induced by mixing two solutions, one has to wait until the solution turns to be a homogenous solution after the mixing. It makes difficult to obtain the kinetics of rapid chemical reactions. We approach to the rapid reactions by employing a collision of liquid droplets. We have so far investigated a droplet-collision dynamics of ethanol (EtOH) and water [1,2] and a chemical reaction between phenolphthalein and NaOH [3].

On the other hand, the liquid droplets facilitates light-emission spectroscopies, such as Raman or fluorescence spectroscopies, because the emitted light enhances in intensity within the droplet owing to a resonance of the light trapped within the droplet. We have obtained a Raman spectrum envelope free from the resonance condition by scanning the incident laser wavelength [4] and obtained the molecular distribution in the colliding droplets [2]. A fluorescence spectroscopy has been applied to observe the rapid chemical reaction induced by the droplet collision [5].

In the present study, we report a dynamics of metastable interface, whcih emerges in the course of the collision of miscible two droplets. The interface dynamics is observed by a simple image observation as well as by Raman spectroscopy of the colliding drolpets of bisulfate and alkaline which result in sulfate. And we found that the interface moves toward the side of droplet with less surface tension.

The apparatus employed in this study is shown in Figure 1. Liquid droplets were produced by a set of piezo-driven nozzles. A white light-emitting diode was employed as a strobe light in order to collect a droplet-collision image. We employed a second harmonic of a Q-switched Nd:YAG laser for excitation of the Raman scattering. The emitting light passed through a long-pass filter which removed the most of the Rayleigh scattering, and divided into two components: The transmitted light was allowed to focus onto a CCD camera to observe the image of the emitting light, and the reflected light was guided to an in-house constructed CCD spectrometer to observe the spectrum. The image and the corresponding spectrum were simultaneously recorded for each laser shot.

Figure 2 shows a collision sequence of water and 1 M Na_2SO_4 aqueous solution droplets of sizes 71 μm (left) and 78 μm (right), respectively. The images are shown in a center-of-mass frame with the collision velocity parallel to the horizontal axis of the images. As seen in Figure 1, a contact region is generated as a disk between the two droplets after 10 μs from the collision, and the disk grows into an oblate shape (30 μs). The merged droplets then undergo an oblate-prolate-oblate oscillation. Note that the longitudinally or horizontally elongated shape in the images corresponds to an oblate or a prolate shape, respectively.

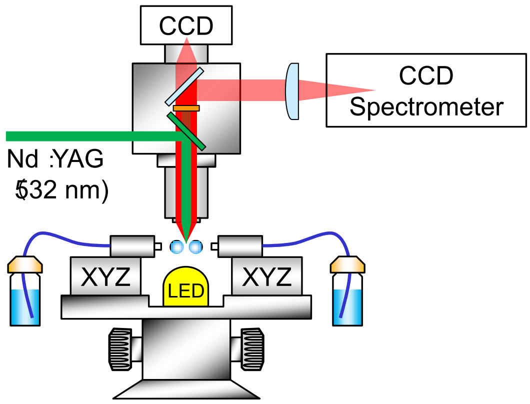

Figure 1 Schematic view of droplet-collision apparatus.

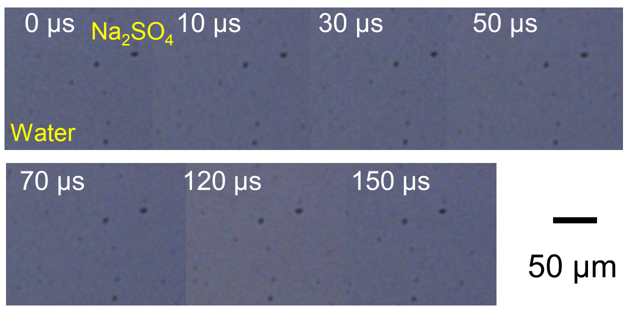

Figure 2 Collision sequence of water (left) and 1 M Na_2SO_4 aqueous solution (right) droplets.

Figure 3 shows colliding droplets of 1 M Na_2SO_4 and ethanol aqueous solutions at the collision times of 80 and 200 μs. The ethanol concentrations are 0, 0.8, and 1.6 % for panels a, b, and c, respectively. A clear interface is observed in each image, which moves toward the ethanol-solution side with increase in the collision time. The interface is observed only for the prolate-shaped droplets. By comparison of panels a – c, on the other hand, one can see that the velocity of the interface movement enlarges by the increase of the ethanol concentration.

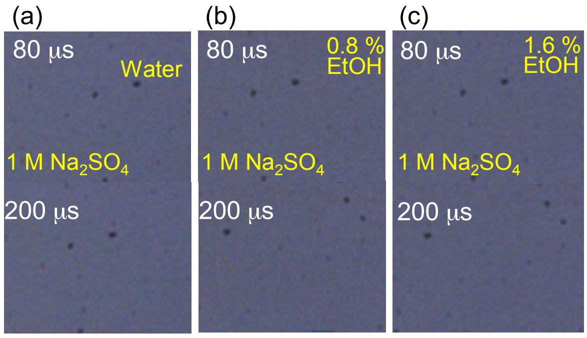

Figure 3 Colliding droplets of 1 M Na_2SO_4 and ethanol aqueous solutions at the collision times of 80 and 200 µs.

The interface movement is likely to result from a spread of a droplet with less surface tension on the other one. Figure 4 depicts the oscillation with a probable liquid flow inside the colliding droplet. As shown with arrows in Figure 4, the liquid inside the droplets flows from the edge to the interface of the droplet when the droplet transforms from oblate to prolate. This flow induces shear at the interface of the colliding droplet, because the central part of the colliding droplet resist the deformation. This results in the interface movement. This shear flow at the interface is not significant when the droplet transforms from prolate to oblate, because the inside flow from the center to the edge is free from the resistance of the droplet itself.

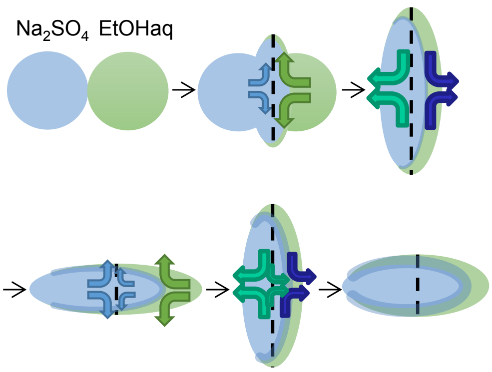

Figure 4 Droplet-collision model.

The interface in the oblate droplet, which is not observable in the image, is measured by a Raman spectroscopy. Figure 5 shows the spectra and corresponding images of the Raman scattered light emitted from colliding droplets of 1 M H_2SO_4 and (2 M NH_3 + EtOH) aqueous solutions. The collision time is 270 µs, when the colliding droplet is the oblate. The Raman spectra consist of HSO_4^- and SO_4^{2-} bands, which appear at 980 and 1050 cm^{-1}, respectively. The Raman images shown as insets indicate that the Raman scattering emerges from the laser irradiation position and its antipode of the great circle of the oblate-shaped colliding droplets. The observation of SO_4^{2-} shows that the neutralization reaction between HSO_4^- and NH_4^+ proceeds at the colliding interface of the droplets.

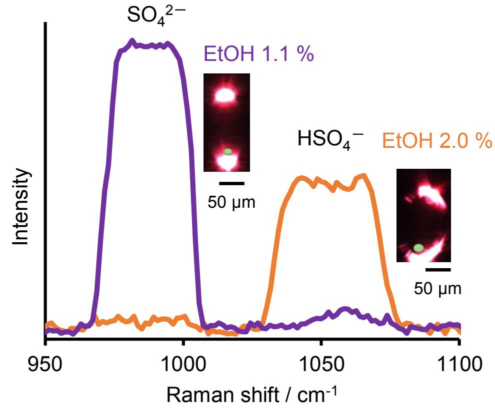

Figure 5 Raman spectra and corresponding images of colliding droplets of 1 M H_2SO_4 and (2 M NH_3 + EtOH) aqueous solutions.

The Raman band intensity represents the composition of the interface of the colliding droplet. Figure 5 shows that the observed sulfate/bisulfate composition depends on the ethanol concentration, which indicates that the interface position is dependent on the ethanol concentration. Figure 6 depicts the interface position and its dependence on the ethanol concentration. Addition of NH_3 and ethanol decreases the surface tension of water, whereas addition of H_2SO_4 increases it. Then, addition of particular concentration of EtOH to the H_2SO_4 droplet equals the surface tension of the colliding two droplets, where the interface locates in the middle of the merged droplet. Otherwise one droplet spreads on the other. Experimental results on the EtOH concentration dependence support this conjecture. This study is particularly important to extend the research to the rapid dynamics between two droplets.

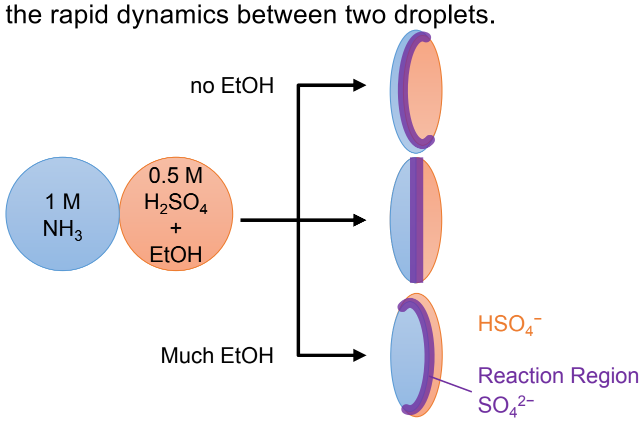

Figure 6 Interface position and its dependence on the ethanol concentration.

References

[1] J. Kohno, M. Kobayashi, T. Suzuki. *Chem. Phys. Lett.*, (2013) **578**, 15-20.
[2] T. Suzuki, J. Kohno. *J. Phys. Chem. B*, (2014), **118**, 5781-5786.
[3] Y. Takano, S. Kikkawa, T. Suzuki, J. Kohno. *J. Phys. Chem. B*, (2015), **119**, 7062-7067.
[4] M. Hoshino-Nagasaka, T. Isoda, T. Takeshima, J. Kohno. *Chem. Phys. Lett.*, (2012), **539-540**, 229-233.
[5] T. Suzuki, J. Kohno. *Chem. Lett.*, (2015), **44**, 1575-1577.

Entropic, Electrostatic, and Interfacial Model of Concentrated Disordered Droplets

Ha Seong Kim[1*], Frank Scheffold[2], Thomas G. Mason[1,3]

[1]Department of Chemistry and Biochemistry, UCLA, Los Angeles, CA, USA
[2] Physics Department, University of Fribourg, Chemin de Musée 3,1700 Fribourg, Switzerland
[3] Department of Physics and Astronomy, UCLA, Los Angeles, CA, USA

*presenting. correspondence e-mail: mason@chem.ucla.edu

We present a near-equilibrium free energy minimization model which describes two thermodynamic properties, the osmotic pressure Π and the linear elastic plateau shear modulus G'_p of concentrated disordered charge-stabilized monodisperse droplets experiencing electrostatic repulsions [1]. This model incorporates entropic, electrostatic, and interfacial (EEI) free energies of repulsive droplets in the glassy and jamming regime over a wide range of droplet volume fractions ϕ. The expressions of the free energy F incorporate concepts of random close packing or critical jamming volume fraction $\phi_c \approx 0.646$ for monodisperse spheres, allow for droplet deformation through a deformation parameter, and account for effects of shear strain γ. The EEI model is validated by comparing the EEI model to measured $\Pi(\phi)$ and the mechanical measurements of $G'_p(\phi)$ of disordered microscale and nanoscale ionic surfactant stabilized oil-in-water (O/W) emulsions. The EEI model is also found to describe $G'_p(\phi)$ of similar nanoemulsions containing dissolved monovalent non-amphiphilic salt.

Introduction and Model:

Emulsions, which have wide applications in industry and consumer products, are soft materials which consist of dispersed droplets of a liquid in another immiscible liquid [2]. The droplets are thermodynamically metastable due to the work done against the interfacial tension σ in creating additional interfaces between the two immiscible liquids. Ionic surfactants such as sodium dodecyl sulfate (SDS), are added to provide interfacial stability against coalescence via short-range electrostatic repulsions. These repulsions can even stabilize droplets experiencing high Π, which allows the droplets to be concentrated, in a disorderly manner, to high ϕ beyond the critical jamming point ϕ_c. For emulsions having $\phi > \phi_c$, the interfaces begin to deform and give rise to a solid-like elasticity for concentrated disordered emulsions [2].

Elastic properties of concentrated micro- and nano-scale monodisperse emulsions have been well measured [3-5]. Mason *et al.* measured $\Pi(\phi)$ and $G'_p(\phi)$ of macro-scale monodisperse SDS-stabilized polydimethylsiloxane (PDMS) O/W emulsions [3, 4]. By adjusting the ϕ into an effective volume fraction ϕ_{eff} in an *ad hoc* manner to account for excluded volume contribution by electrostatic repulsions, Mason *et al.* found that $\Pi(\phi_{eff})$ and $G'_p(\phi_{eff})$ vary quasi-linearly as a function of (ϕ_{eff}-ϕ_c) and the Laplace pressure scale (σ/a). This associated features of $\Pi(\phi_{eff})$ and $G'_p(\phi_{eff})$ to the jamming point of spheres at which the interfaces begin to deform [3, 4]. Mason *et al.* further showed G'_p slightly below ϕ_c resembled that of a hard-sphere colloidal glass transition, further highlighting entropic excitations are important in describing colloidal emulsions [3, 4]. In a later work by Wilking and Mason, measurements of $G'_p(\phi)$ of SDS-stabilized PDMS O/W nanoemulsions, which have average radius a < 100 nm, showed nanoemulsions can display high G'_p for ϕ well below ϕ_c [5]. This result highlighted the importance of electrostatic repulsions as the droplet radius closely approaches the Debye length λ_D, which is the characteristic length scale governing electrostatic repulsions. These measurements highlighted the importance of describing EEI terms to accurately describe electrostatically repulsive emulsion systems.

Many models [3-9] have been proposed to describe the measured $\Pi(\phi)$ and $G'_p(\phi)$, but two models most pertinent to our model are presented. To describe the measurements of microscale emulsions, Mason [3] proposed a near-equilibrium free-energy minimization method, which later appeared in a journal article by Mason and Scheffold [8]. In the model, Mason assumed statistical averaged structure of disordered concentrated emulsions, in which a droplet is surrounded by a cubic arrangement of 6 neighboring droplets, to obtain expressions for the entropic and the interfacial free energy per droplet, F_{ent}/N and F_{int}/N respectively. The expressions are:

$$F_{ent}/N = -3k_B T \ln(\phi_c+\phi_d - \phi - \alpha\gamma^2) \quad (1)$$

$$F_{int}/N = 4\pi\xi\sigma a^2 \phi_d^2 \quad (2)$$

where k_B is Boltzmann's constant, T is the temperature, ϕ_d is a deformation volume fraction arising from weak deformations of the droplet interfaces, N is the number of droplets in the emulsion system, γ is the shear strain amplitude, and α and ξ are dimensionless parameters related to shear and configurational effects, respectively. The total free energy per droplet F/N was minimized with respect to the deformation volume fraction ϕ_d to obtain the minimized total free energy per droplet F^*/N. Afterwards, appropriate thermodynamic derivatives, given below, were taken to determine $\Pi(\phi)$ and $G'_p(\phi)$:

$$\Pi = \left[\phi^2/\left(NV_{drop}\right)\right]\left[\partial F_{tot}/\partial\phi\right]_{\phi_d=\phi_d^*,\gamma=0} \quad (3)$$

$$G'_p = \left[\phi/NV_{drop}\right]\left[\partial^2 F_{tot}/\partial\gamma^2\right]_{\phi_d=\phi_d^*,\gamma=0} \quad (4).$$

The free energy minimization approach described $G'_p(\phi_{eff})$ of microscale emulsions well. However, to describe $G'_p(\phi)$ of nanoscale emulsions well, Scheffold *et al.* [9] showed the inclusion of the electrostatic energy along with the consideration of interfacial interactions leads to a good prediction of $G'_p(\phi)$ for both microscale and nanoscale emulsions. However, the exclusion of entropic considerations prevented $G'_p(\phi)$ of the glassy regime below ϕ_c from being described.

Our approach expands on the two prior approaches by combining all three energetic contributions together [1]. Using the empirical scaling relation deduced by Wilking and Mason [5] for SDS stabilized PDMS O/W nanoemulsions which is very similar to the exponential electrostatic energy of Scheffold *et al.* [9], we model the electrostatic free energy per droplet F_{elec}/N as:

$$F_{elec}/N = 2\pi a^2 \psi_0^2 \varepsilon_0 \varepsilon_r \exp(-h/\lambda_D) \quad (5),$$

where ψ_0 is the surface electric potential, ε_0 is the permittivity of vacuum, ε_r is the relative dielectric constant of the continuous phase, and h is separation distance between two droplet interfaces at regions of closest approach. From geometrical considerations, separation h was found to be:

$$h = 2\phi_c^{1/3} a[\phi^{-1/3} - (\phi_c + \phi_d - \alpha\gamma^2)^{-1/3}] \quad (6).$$

Following the free-energy minimization approach by Mason, $\Pi(\phi)$ and $G'_p(\phi)$ were obtained using equations (3) and (4). The calculation was performed numerically using the FindRoot function in Mathematica.

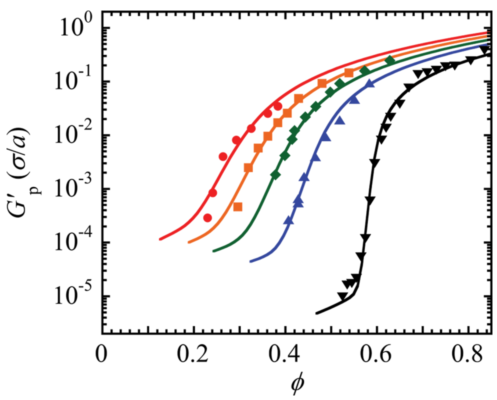

Figure 1. ϕ-dependent plateau elastic shear moduli G'_p, in units of Laplace pressure scale σ/a, at T = 298 K for uniform microscale and nanoscale 10 cSt PDMS O/W emulsions stabilized by 10 mM SDS. From left to right, radius a in nm are: 28 (33), 47 (47), 73 (67), 104 (108), 530 (530) where the values listed inside parenthesis are used in the calculation. Data for a < 100 nm came from [5], a = 530 nm came from [3, 4], and a = 104 nm were measured [1] following procedures consistent to those outlined in [3-5]. Figure from [1].

Results:

Good agreement between the calculated values using the EEI model and the measured values of $\Pi(\phi)$ and $G'_p(\phi)$ was found. As shown in Fig. 1, $G'_p(\phi)$ data, in terms of Laplace pressure scale, for 10 mM SDS stabilized PDMS O/W emulsions agreed well with the model. To obtain agreement, only three parameters (α = 0.85, ξ = 0.15, and ψ_0 = 270 mV) were optimized while other parameters used exactly or closely matched measured or theoretical values (a within 10% of DLS measurement, T = 298 K, σ = 9.8 mN/m, λ_D = 3.4 nm, ε_0 = 8.85 x 10^{-12} F/m, ε_r = 80.1) were used.

This set of parameters successfully fit through experimental $G'_p(\phi)$ data for 5 different radii, ranging from nanoscale to microscale emulsions, and G'_p which spans 4 decades.

Using the same set of parameters, a good fit through $\Pi(\phi)$ for a = 480 nm emulsions stabilized by 10 mM SDS was also obtained. Furthermore, the EEI model describes the $G'_p(\phi)$ of SDS-stabilized PDMS O/W nanoemulsions which contain modest concentrations of NaCl salt. An agreement with the data can be obtained by adjusting the value of the surface potential ψ_0. Lastly, the EEI model can predict dominant regimes of entropy, electrostatic repulsions, and interfacial contributions to $\Pi(\phi)$ and $G'_p(\phi)$, which can serve as a guide in designing emulsions having desired macroscopic rheological properties.

Conclusion:

The EEI model is the first model, to our knowledge, which connects all three principle energetic terms, entropic, electrostatic, and interfacial, that govern rheolgical properties of ionic colloidal emulsions. The model successfully describes $\Pi(\phi)$ and $G'_p(\phi)$ over a wide range of droplet radii, ranging from nano-scale to micro-scale in size using universal set of parameters. The model is also capable of describing $G'_p(\phi)$ of salted emulsions, but comparisons to additional experimental data are needed to further validate the EEI model over a wider range of salt concentrations. The EEI model, nevertheless, serves as a useful predictive tool for researchers studying ionic disordered emulsions.

Acknowledgements. The authors thank UCLA for financial support.

References

[1] H. S. Kim, F. Scheffold and T. G. Mason. *Rheologica Acta*. (2016); **55**, 683-697.
[2] T. G. Mason. *Current Opinion in Colloid & Interface Science*. (1999); **4**, 231-238.
[3] T. G. Mason. Rheology of Monodisperse Emulsions [Ph. D. Dissertation]. Princeton: Princeton University; 1995.
[4] T. G. Mason, M. D. Lacasse, G. S. Grest, D. Levine, J. Bibette and D. A. Weitz. *Physical Review E*. (1997); **56**, 3150-3166.
[5] J. N. Wilking and T. G. Mason. *Physical Review E*. (2007); **75**, 041407.
[6] A. Ikeda, L. Berthier and P. Sollich. *Soft Matter*. (2013); **9**, 7669-7683.
[7] M. D. Lacasse, G. S. Grest, D. Levine, T. G. Mason and D. A. Weitz. *Physical Review Letters*. (1996); **76**, 3448-3451.
[8] T. G. Mason and F. Scheffold. *Soft Matter*. (2014); **10**, 7109-7116.
[9] F. Scheffold, J. N. Wilking, J. Haberko, F. Cardinaux and T. G. Mason. *Soft Matter*. (2014); **10**, 5040-5044.

An organizing framework for sessile drop motions

Joshua B. Bostwick[1], Paul H. Steen[2]

[1]Department of Mechanical Engineering, Clemson University, Clemson, SC, USA
[2] School of Chemical and Biomolecular Engineering and Center for Applied Mathematics, Cornell University, Ithaca, NY, USA

E-mail: jbostwi@clemson.edu

Symmetries are known to produce degeneracies via Noether's theorem, as with the spectrum of the free oscillating Rayleigh drop. We study the spectrum of the `symmetry-broken' sessile droplet, as it depends upon the wetting conditions through the static contact-angle α and the contact-line mobility Λ [2]. Corresponding motions are distinguished by a polar k and azimuthal ℓ wavenumber pair $[k, \ell]$, which is a classification scheme inherited from the associated problem for the free drop. For the hemispherical $(\alpha = 90°)$ base-state with fully mobile contact-line $\Lambda = 0$, the spectrum is degenerate with respect to azimuthal wavenumber, consistent with Noether's theorem and the fully-symmetric Rayleigh drop. We show that varying either α or Λ lifts this degeneracy. For certain values of these symmetry-breaking parameters, two modes may share the same characteristic frequency or the classical ordering of modes can be altered [3]. To organize and explain the hierarchy of frequencies, we construct a corresponding `periodic table of mode shapes' from the spectral data using an *aufbau* principle, whereby modes are filled in order of increasing frequency.

Many physical systems exhibit a degree of inherent symmetry. Noether's theorem, perhaps one of the most significant mathematical ideas of the 20^{th} century, states that symmetries of a characteristic energy functional, the Lagrangian or Hamiltonian, lead to conserved quantities and equivalently degeneracies of the associated spectrum. Only in hindsight have the degeneracies of many, now, classical problems in physics been attributed to underlying symmetries.

Droplets are fundamental to fluid transport on solids in the same manner in which the spectra of the hydrogen atom is fundamental to the fields of chemistry and solid-state physics. The *sessile drop is the canonical problem* upon which many modern fluid transport applications are based. Typical examples include 3D printing with relevance to rapid prototyping, self-cleansing surfaces for enhanced solar cell efficiency, microfluidics, spray cooling for high heat flux applications, drop atomization for drug delivery (aerosol) methods, and energy harvesting technologies, all of which involve the motion of droplets on scales where surface tension dominates. By organizing the fundamental sessile drop motions, we hope to bring a greater understanding to the field and a vision set forth by prediction.

Systems with `broken' symmetry need a framework around which to organize associated spectra. The periodic table of elements is the best example of such a structure. Here, all known chemical elements are organized into a table by the Madelung rule, an aufbau principle that specifies the filling order of atomic orbitals by increasing energy level. The structure of the periodic table lies at the very foundation of the field of chemistry with many modern scientific discoveries attributed to its existence. For our problem, we are interested in organizing the `broken' states describing the characteristic motions of the sessile drop around an `aufbau' principle for the frequency spectrum by constructing a `periodic table of mode shapes'; a classical mechanics analogue to a principal more familiar to quantum mechanics. The perspective is meant to clarify and elucidate the organizational structure. By recasting the governing equations in linear operator form, a number of new predictions follow immediately, some of which have been subsequently observed experimentally [3].

Our results are conveniently framed against those for the free Rayleigh drop [1], which has frequencies ordered in a discrete spectrum,

$$\omega_{k,1}^2 = \frac{k(k-1)(k+1)(k+2)}{(k+1)\varrho_i + k\varrho_e}\frac{\sigma}{R^3} \qquad (1)$$

where k is the polar wavenumber, ℓ the azimuthal wavenumber, σ the liquid/gas surface tension and ϱ_i and ϱ_e are the densities of the interior and exterior fluids, respectively. Corresponding mode shapes are given by the spherical harmonics Y_k^ℓ. These theoretical results have been verified experimentally for immiscible drops [4] and for free drops in microgravity [5]. Note that the Rayleigh frequencies (1) are degenerate with respect to the azimuthal wavenumber ℓ. We recover the Rayleigh frequencies, and the azimuthal degeneracy, for hemispherical $(\alpha = 90°)$ base-state with $\Lambda = 0$. This can be attributed to the fact that this sub-case exhibits the same symmetry as the Rayleigh drop and symmetries are known to produce degeneracies via Noether's theorem. We systematically `break' this symmetry by varying either the i) base-state geometry through the static contact-angle $\alpha \neq 90°$ or ii) the boundary terms through the contact-line mobility parameter $\Lambda \neq 0, \infty$.

For certain values of these symmetry-breaking parameters (α, Λ), there is the possibility for modal crossings, where two modes share the same frequency. The hierarchy of frequencies is organized by constructing a `periodic table of mode shapes' from the spectral data using an aufbau principle, whereby modes are filled in order of increasing frequency. We show that the classical ordering of modes can become distorted. A number of striking predictions follow from the perspective, such as the discovery of a new fundamental fluid instability, the `walking instability', which can be viewed as a natural result of the symmetry-breaking of the Rayleigh drop.

Acknowledgements. PHS acknowledges support by NASA Grant NNX09AI83G and NSF Grant CBET-1236582.

References

[1] L. Rayleigh. 'On the capillary phenomenon of jets.' *Proc. R. Soc. Lond*. **29**, 71 (1879).
[2] J.B. Bostwick & P.H. Steen. 'Sessile drop dynamics. Part 1. Inviscid theory.' *J Fluid. Mech.* **760**, 5-38, (2014).
[3] C.T. Chang, J.B. Bostwick, S. Daniel and P.H. Steen. 'Dynamics of sessile drops. Part 2. Experiment'. *J. Fluid Mech*. **768**, 442-467, (2015).
[4] Trinh, E. & Wang, T.G. 1982 Large-amplitude free and driven drop-shape oscillation: experimental results. *J. Fluid Mech.* **122**, 315–338.
[5] Wang, T.G., Anilkumar, A.V. & Lee, C.P. 1996 Oscillations of liquid drops : results from usml-1 experiments in space. *J. Fluid Mech*. **308**, 1–14.

Dewetting from a Liquid Film into a Single Droplet

Glen McHale[1], Rodrigo Ledesma-Aguilar[1],
Andrew M. J. Edwards[2], Michael I. Newton[2] and Carl V. Brown[2]

[1]Smart Materials & Surfaces Laboratory, Faculty of Engineering & Environment, Northumbria University, Newcastle upon Tyne, NE1 8ST, UK
[2]School of Science and Technology, Nottingham Trent University, Nottingham NG11 8NS, UK

E-mail: glen.mchale@northumbria.ac.uk

Studying the dynamic evolution of an out-of-equilibrium droplet into a liquid film on a wetting surface has enabled significant progress in understanding droplet dynamics. However, because of the difficulty of initiating and controlling film formation on a non-wetting surface, the reverse model situation of a film evolving into a single macroscopic equilibrium droplet has rarely been studied. More usually, the study of dewetting has involved the break-up of a film into multiple droplets or the nucleation and growth of a hole [1-3].

Recently, we have developed the use of liquid dielectrophoresis into an interface-localized liquid form, which can induce and control droplet equilibrium shapes using a voltage (also called dielectrowetting) [4,5]. In the extreme case of an applied voltage beyond the threshold needed to initiate complete spreading of a droplet, we have shown it is possible to study the dynamics of surfactant-free superspreading from a droplet into a film [6].

Here we consider how interface-localized liquid dielectrophoresis can also be used to initiate a circular shaped liquid film on a non-wetting surface. By suddenly removing the applied voltage, the film is left in a non-equilibrium shape which then evolves back to its equilibrium droplet shape on the surface [7]. We find the trajectory of shapes experimentally observed during axisymmetric dewetting of the film includes two distinct types. In the first phase of dewetting the film forms a rim with a central dimple, and the rim retreats at a constant speed determined by the final equilibrium droplet contact angle. In the second phase of dewetting, the rim joins up across the film rapidly leading to an out-of-equilibrium spherical cap shape. This spherical cap chape then relaxes back to the droplet equilibrium shape following exponential laws in time for both contact radius and contact angle.

To support our experimental observations we have performed Lattice-Boltzmann simulations of the dewetting process. These confirm that the formation of a rim with a dimple is independent of the precise initial starting side-profile shape of the film. We also developed a hydrodynamic theory (following ref [8]) explaining the dewetting dynamics of the rim and dimple. Hydrodynamic theory was also developed to explain the long time exponential approach to equilibrium of the spherical cap. The simulations and theory reveal a local dewetting mechanism driven by the equilibrium contact angle, where contact-line slip dominates the dewetting dynamics.

Our studies show that the dewetting process sharply contrasts with the process of wetting from a small macroscopic droplet into a liquid film, which proceeds by a sequence of spherical cap droplet shapes.Our results are relevant to a wide variety of dewetting situations, such as drop rebound, condensation and evaporation. Finally, we discuss how our experimental work can be extended to consider the dewetting process for a liquid film displacing a second immiscible liquid phase, and to induce and study the dewetting of films of prescribed initial shapes.

Acknowledgements. We would like to thank Dr Ian Sage for advice on TMPTGE and the financial support of the UK Engineering & Physical Sciences Research Council (EPSRC grants EP/K014803/1, EP/E063489/1 and EP/E063489/1).

References

[1] A. Sharma, E. Ruckenstein. *Journal of Colloid & Interface Science*, (1989) **133**, 358–368.
[2] C. Redon, F. Brochard-Wyart, F. Rondelez. *Physical Review Letters*, (1991) **66**, 715–718.
[3] R. Seeman, S. Herminghaus, K. Jacobs. *Physical Review Letters*, (2001) **87**, 196101.
[4] G. McHale, C.V. Brown, M.I. Newton, G.G. Wells, N. Sampara. *Physical Review Letters,* (2011) **107**, 186101.
[5] G. McHale, C.V. Brown, N. Sampara. *Nature Communications*, (2013) **4**, 1605.
[6] C.V. Brown, G. McHale, C.L. Trabi. *Langmuir*, (2015) **31**, 1011–1016.
[7] A.M.J. Edwards, R. Ledesma-Aguilar, M.I. Newton, C.V. Brown, G. McHale. *Science Advances*. (2016), **2**, e1600183–e1600183.
[8] J. H. Snoeijer, B. Andreotti. *Annual Review of Fluid Mechanics*, (2013) **45**, 269–292.

Droplet Transportation Using a Selective Leidenfrost Effect

Glen McHale[1], Ben B. Xu[1], Nicasio Geraldi[1], Gary G. Wells[1], Linzi E. Dodd[2], David Wood[2], Simone Stuart-Cole[3], James Martin[3] and Michael I. Newton[4]

[1]Smart Materials & Surfaces Laboratory, Faculty of Engineering & Environment, Northumbria University, Newcastle upon Tyne, NE1 8ST, UK
[2]Microsystems Technology Group, School of Engineering & Computing Sciences, Durham University, Durham DH1 3LE, UK
[3]Reece Innovation, Newcastle upon Tyne NE15 6UX, U.K.
[4]School of Science and Technology, Nottingham Trent University, Nottingham NG11 8NS, UK

E-mail: glen.mchale@northumbria.ac.uk

Transporting droplets in a controllable and energy efficient manner is important for a range of applications including flow, water collection and microfluidics. The Leidenfrost effect has received renewed interest for its ability to levitate and directionally transport droplets with low friction [1,2]. In our previous work, we have shown how this can be used to create a heat engine, which also acts as a mechanical engine [3]. However, the substrates are usually uniformly heated to a constant and high temperature. This requirement for a significant input of energy is a serious limitation on the application of the Leidenfrost effect to low friction droplet transport.

In this work we report an approach to activating the Leidenfrost effect in both a spatially and temporally localized manner thereby significantly reducing the energy input required [4]. In our approach we selectively trigger Leidenfrost levitation of a droplet by the application of a voltage to micrometer-scaled serpentine shaped heating units, which have been microfabricated on the substrate in groups to create voltage addressable heating arrays. We demonstrate that the heating arrays are able to generate a Leidenfrost effect transition for droplets of isopropanol (γ_{LV}~20 mN/m), acetone (γ_{LV}~28 mN/m), and deionized water (γ_{LV} ~72 mN/m).

To support the experimental investigation, we performed surface thermal analysis using the COMSOL Multiphysics software package to model the distribution of thermal energy across the substrate. Experimental data were compared with the COMSOL simulation results for the phase diagrams describing metastable levitation of droplets as a function of device designs involving a range of heating ratios. Various substrates (borosilicate glass and silicon) covering three orders of magnitude of thermal conductivity were used to determine the effect of the substrate's thermal conductivity on the power needed for the Leidenfrost effect to occur.

To provide a proof-of-concept for low friction droplet transport and microfluidics, we conducted experiments on droplet transport down a tilted substrate with voltage addressable heating arrays. In these experiments, four heating arrays were used with typically three activated and one inactive. In each case, low friction high speed droplet transportation (~65 mm/s) across the activated heating arrays on a substrate tilted by ~7° was observed. Droplet motion ceased when the inactive electrothermal heating array was encountered.

This proof-of-concept work could be extended to include active control of the Leidenfrost effect in the specific location and at the specific time required to sustain droplet levitation. The microengineering approach with a voltage triggered actuation also has the potential to be integrated into Lab-on-chip designs. The work therefore is relevant to energy efficient applications of the Leidenfrost effect, *via* the spatial and temporal localization of heating, and as the basis for new approach to droplet microfluidics.

Acknowledgements. The work was supported by the Engineering & Physical Sciences Research Council (EPSRC grants EP/L026899/1, EP/L026619/1, and EP/L026341/1). We also acknowledge funding from the EU-COST MP1106 network.

References

[1] D. Quéré. *Annual Review of Fluid Mechancs*, (2013) **45**, 197−215.
[2] H. Linke, B.J. Alemán, L.D. Melling, M.J. Taormina, M.J. Francis, C.C. Dow-Hygelund, V. Narayanan, R.P. Taylor, A. Stout. *Physical Review Letters*, (2006) **96**, 154502.
[3] G.G. Wells, R. Ledesma-Aguilar, G. McHale, K.A. Sefiane, K. A. *Nature Communications*, (2015) **6**, 6390.
[4] L.E. Dodd, D. Wood, N.R. Geraldi, G.G. Wells, G. McHale, B.B. Xu, S. Stuart-Cole, J.Martin, M.I. Newton. ACS *Applied & Materials Interfaces*, (2016) **8**, 22658–22663.

Electrowetting and Dielectrowetting on Lubricant Impregnated Surfaces

Glen McHale[1], Zuzana Brabcova[2], Gary G. Wells[1],
Michael I. Newton[2] and Carl V. Brown[2]

[1]Smart Materials & Surfaces Laboratory, Faculty of Engineering & Environment,
Northumbria University, Newcastle upon Tyne, NE1 8ST, UK
[2]School of Science and Technology, Nottingham Trent University,
Nottingham NG11 8NS, UK

E-mail: glen.mchale@northumbria.ac.uk

Electrowetting is an effective technique to induce a droplet to spread on a hydrophobic substrate [1]. However, there is a limit to the extent of spreading that can be achieved and films cannot be induced. Moreover, significant hysteresis usually occurs associated with pinning forces at the contact line. Recently, it has been shown in the literature that completely mobile droplets can be achieved by using a lubricant impregnated substrate (or equivalently a slippery liquid infused porous substrate) [2,3].This idea was recently applied to create a completely reversible and tuneable liquid lens with improved transient response due to reduced droplet oscillations [4]. Limited information on the agreement with theory between contact angle and applied voltage was provided, and the persistence of a saturation contact angle precluded film formation.

In recent work, we have shown that liquid dielectrophoresis can be localized to the solid-liquid interface to create an analogous effect to electrowetting, but based on the force acting on the dipoles of a dielectric liquid [5, 6]. This forced spreading, which we have called dielectrowetting, can achieve partial or complete spreading of a dielectric liquid droplet on a non-wetting substrate, including into a film state [7]. Here we present data for the forced spreading and subsequent retraction of axisymmetric droplets into liquid films in air on lubricant impregnated surfaces using both electrowetting and dielectrowetting [8].

In the case of electrowetting we observe a complete removal of hysteresis for voltages above the saturation contact angle voltage. In the case of dielectrowetting, the contact angle hysteresis is reduced to less than 4° whilst retaining the ability to fully spread a droplet into a liquid film. In both cases, the cosine of the contact angle retains a quadratic dependence on applied voltage, consistent with previous theoretical expectations. We show that data for both electrowetting and dielectrowetting can be scaled onto a universal curve by choice of an initial contact angle at zero applied voltage and a threshold voltage for film formation extrapolated from each data set.

Our studies show that fully reversible spreading encompassing a wide range of partial wetting droplet states and a film state can be achieved in air in a controllable manner with very low levels of hysteresis by the use of lubricant impregnated substrates. Since the dielectrowetting approach can achieve reversible low hysteresis control between a droplet and a film state in air without mechanical parts and in a scalable manner, it may be significant for a range of applications, including liquid-based optics and droplet-based microfluidics.

.

Acknowledgements. We would like to thank Dr Michael Cooke, Dr Pietro Maiello, Dr Edward Bentley, Dr Ben Xu and Andrew Edwards for valuable advice and technical support. This work was financially supported by the UK Engineering & Physical Sciences Research Council (EPSRC grants EP/K014803/1 and EP/K015192/1).

References

[1] F. Mugele and J. Baret. *Journal of Physics: Condensed Matter*, (2005) **17**, R705-R774.
[2] T. Wong, S.H. Kang, S.K.Y. Tang, E.J. Smythe, B.D. Hatton, A. Grinthal, and J. Aizenberg. *Nature*, (2011) **477**, 443-447.
[3] J.D. Smith, R. Dhiman, S. Anand, E. Reza-Garduno, R.E. Cohen, G.H. McKinley, and K.K. Varanasi. *Soft Matter*, (2013) **9**, 1772-1780.
[4] C. Hao, Y. Liu, X. Chen, Y. He, Q. Li, K.Y. Li, and Z. Wang. *Scientific Reports*, (2014) **4**, 6846.
[5] G. McHale, C. V Brown, M.I. Newton, G.G. Wells, and N. Sampara. *Physical Review Letters*, (2011) **107**, 186101.
[6] Z. Brabcova, G. McHale, G.G. Wells, C. V. Brown, M.I. Newton, and A.M.J. Edwards. *Langmuir*, (2016) **32**, 10844-10850.
[7] G. McHale, C.V. Brown, N. Sampara. *Nature Communications*, (2013) **4**, 1605.
[8] Z. Brabcova, G. McHale, G.G. Wells, C.V. Brown, M. I. Newton. *Applied Physics Letters*, (2017) accepted.

Colloidal Particles at Fluid Interfaces: Adsorption, Assembly, and Mechanics

Nivi Samudrala[1], Eric R. Dufresne[2]

[1]School of Engineering and Applied Sciences, Yale University, New Haven CT 06511
[2] Department of Materials Science, ETH Zurich, Switzerland

E-mail: nivi.samudrala@yale.edu

Mechanics of emulsion droplets is crucial in applications where the encapsulated payload needs to be released under mechanical stimulus. This work explores the use of dumbbell nanoparticles as emulsifiers with focus on the emergent mechanical stability of particle-assembly at interfaces. Using a combination of freeze fracture shadow casting cryo-scanning electron microscopy and analytical modelling, we first investigate the complex adsorption behavior of individual dumbbells and the corresponding implications for particle-assembly at the interface. Using micropipette aspiration, we then investigate the onset of mechanical instabilities in droplets stabilized by dumbbells. We compare our findings to the control experiments of bare droplets and droplets stabilized with molecular surfactants under aspiration. In all three cases, the magnitude of the critical pressure for the onset of instabilities is set by the fluid surface tension. While dumbbells have a dramatic impact on the mechanism of failure, the mechanical strength of the droplets is only modestly increased. This work provides experimental handles that can be tuned to aid the mechanical stability of emulsion droplets. Our findings also inform advances in the mechanics of highly bendable sheets.

Acknowledgements. NSF and AmorePacific Co.

References

[1] L. Isa, N. Samudrala, and E. R. Dufresne, Adsorption of sub-micron amphiphilic dumbbells to fluid interfaces. *Langmuir*, *30*(18), pp.5057-5063. (2014)
[2] N. Samudrala, J. Nam, R. Sarfati, R. Style, and E. R. Dufresne, Mechanical stability of particle-stabilized droplets under micropipette aspiration*, Physical Review E* (95), 012805 (2017)

DROP IMPACT DYNAMICS ON LIQUID-INFUSED SUPERHYDROPHOBIC SURFACES

Jeong-Hyun Kim[1] and Jonathan P. Rothstein[1]

[1]Department of Mechanical and Industrial Engineering, University of Massachusetts, Amherst, MA, USA

E-mail: Rothstein@ecs.umass.edu

Superhydrophobic surfaces are engineered by taking materials with micron or nanoscale surfaces roughness and chemically treating them to make them hydrophobic. Because of the hydrophobicity of these microscale and nanoscale protrusions, when water is brought in contact with a superhydrophobic surface, it does not fully wet the surface. Instead, it remains in contact with only the peaks of the surface topology resulting in a shear-free air-water interface. The presence of this air-water interface trapped within superhydrophobic surfaces are known to mobilize drops by reducing contact angle hysteresis and reducing drag [1-7]. However, under high static pressures, the air-water interface can fail leading to transition from the Cassie to the Wenzel stand and a loss of drag reduction. One approach to achieving drag reduction at large static pressures is to replace the air that fills the gaps of the superhydrophobic surface with a low-viscosity, immiscible, incompressible liquid. These liquid-infused micro and nanostructured surfaces have become very popular recently because they have been shown to demonstrate very low contact angle hysteresis in droplet dynamic studies and have been shown to suppress the ice formation [8].

In this talk, we present a series of experiments investigating the drop impact dynamics on hydrophobic, air-infused and lubricant-infused superhydrophobic surfaces. To create the superhydrophobic surfaces, smooth Teflon (PTFE) surfaces were roughened by a 240-grit sandpaper. The spreading and retraction dynamics on lubricant-infused superhydrophobic sanded PTFE surfaces were next investigated through high speed imaging. The viscosity of infused silicone oil was varied to investigate the effect of the viscosity ratio between the impinging droplet and the infused lubricant layer. The evolution of the droplet diameter, droplet spreading and retraction velocities and the dynamic contact angles were measured as a function of time after impact. A time series of droplet impact dynamics are shown in Figure 1. A complete set of data can be found in our recent publication, Kim et al. [9, 10].

The maximum spreading diameter of the droplet on lubricant-infused surfaces was found to increase with decreasing viscosity of the infused silicone oil. Furthermore, the droplet spreading velocities became larger as the oil viscosity was reduced. These increases in the maximum droplet diameter and the droplet spreading velocities resulted from the presence of a finite slip length and the reduction in shear stress at the oil-water interface on lubricant-infused surfaces. The results for the largest oil viscosity tested were indistinguishable from experiments performed on a smooth PTFE surface, showing the importance of increasing the viscosity ratio between the droplet and the infused oil phase to a value as large as possible. These differences with oil viscosity were not observed in previous studies because the oil viscosity was large and the resulting viscosity ratio between the water and oil phases was much less one, $\mu_w / \mu_o \ll 1$, in all cases [11, 12]. This point is reinforced by a scaling analysis we derived which was able to collapse the maximum diameter data onto a master curve when it was replotted as $D_{max} / D_0 = \left[1 + (t/h)(\mu_w / \mu_o)\right]^{1/2} We^{1/4}$ where We is the Weber number defined as $We = \rho_w U_0^2 D_0 / \sigma_w$ Here, ρ_w is the density of the droplet, U_0 is the drop impact velocity, D_0 is the initial diameter of the droplet before impact, and σ_w is the surface tension of the droplet.

Interestingly, significant and perhaps non-intuitive differences were observed in the maximum droplet diameter between the least viscous silicone oil case,

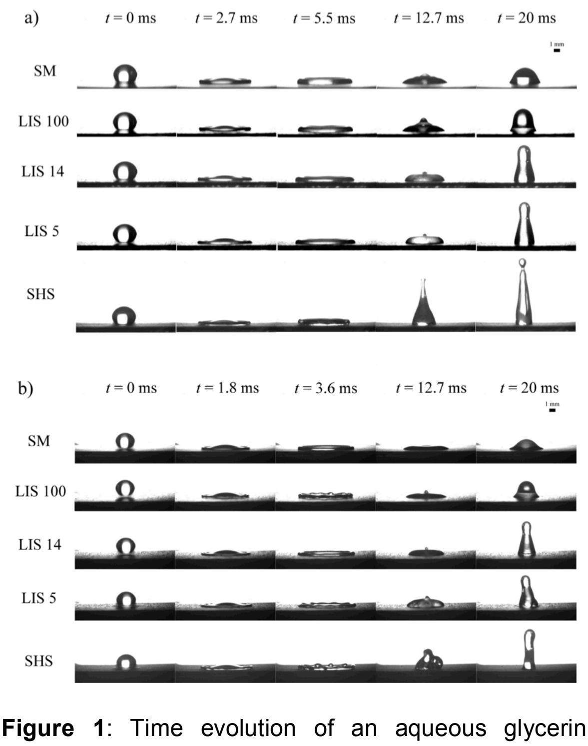

Figure 1: Time evolution of an aqueous glycerin drop (μ=6cP) impacting on a series of test surfaces at Weber numbers of (a) *We*=52 and (b) *We*=132. The surfaces include: SM-smooth, SHS-superhydrophobic air-infused, LIS-lubricant-infused. For the lubricant-infused surface, the viscosity of the silicone oil in cP is included following LIS.

LIS 5, and the air-infused superhydrophobic surface, SHS. At the lower Weber numbers tested, the maximum droplet diameter on the LIS 5 was found to be larger than that of the SHS even though the viscosity of the oil infused into the surface features of the LIS 5 was 250 times larger than the air infused into the surface features of the SHS case. This was shown to be due, in part, to the larger advancing contact angle on the superhydrophobic surface. However, it was also shown that a significant amount of energy was dissipated during the impact of a droplet on the SHS due to a wetting transition from the superhydrophobic Cassie state to the fully-wetted Wenzel state induced by the large pressures produced beneath the drop. The presence of the incompressible oil in the lubricant-infused surface was found to mitigate these losses while still producing slip at the oil-water interface thus resulting in a larger fraction of the initial kinetic energy available to deform the droplet to a greater maximum droplet diameter. As the Weber number was increased, the energy dissipation at impact was found to grow more slowly with Weber number than the energy dissipation during spreading. As a result, at *We*=100, the maximum spreading droplet diameter on the superhydrophobic surface was found to surpass the lubricant-infused surfaces.

The retraction rate of the droplet on lubricant-infused surfaces was also found to increase with decreasing lubricant viscosity. The retraction rate on the LIS 5 approached that of the SHS, however, a significant difference in the time between reaching maximum diameter and beginning of the retraction was observed between the LIS 5 and the SHS. Once the droplet reached the maximum deformation, the motion of the droplet was observed to pause as the contact angles decreased from the dynamic advancing to the dynamic receding contact angle. Because the dynamic contact angle hysteresis on the SHS was extremely low, $\theta_H = 5^{\circ}$, the observed delay time was quite small, t_{delay} < 5ms. However, even though the static contact angle hysteresis on the lubricant-infused surfaces were all similar to the SHS and less than $\theta_H < 4^{\circ}$, the contact angle hysteresis observed during spreading were all found to be much larger than the static case, $\theta_H > 25^{\circ}$. As a result, an increase in contact angle hysteresis and delay time was observed with increasing oil viscosity. Variation in contact angle with spreading velocity is known to occur due to viscous losses near the moving contact line.

Using the data from the droplet impact experiments, the first ever measurements of the dynamic advancing and dynamic receding contact angle were made for liquids spreading on lubricant-infused surfaces. The advancing contact angles on the smooth surface and both the LIS 14 and LIS 100 surfaces were found to increase with increasing capillary number. Furthermore, the advancing contact angles on the surfaces were all found to follow the expected Cox-Voinov-Tanner laws, $\theta_A^{\,3} \propto Ca$. However, the onset of growth in the contact angle was delayed as the viscosity of the lubricant was decreased. The dynamic advancing contact angle on the LIS 5 surface did not follow the expected scaling laws, but instead showed little to no growth in the contact angle with increasing capillary number. This behavior was similar to our observations for droplet spreading on superhydrophobic surfaces and is known to be a result of the large slip length and reduced shear stress near the moving contact line [13]. Similar observations were made for the dynamic receding contact angle which was found to decrease with an increasingly negative capillary number. Note, however, that the receding angle appeared to be more sensitive to lubricant viscosity than the advancing angle. These differences are the driving force behind the increase in observed dynamic contact angle hysteresis with increasing oil viscosity. Although these measurements are an important beginning, forced wetting experiments over a wider range of capillary numbers are needed to fully understand the dynamic wetting process on lubricant-infused surfaces.

Acknowlegement: This research was supported by the National Science Foundation under grant CBET-1334962.

References:

[1] J. Ou, J.B. Perot, J.P. Rothstein, Laminar drag reduction in microchannels using ultrahydrophobic surfaces, Phys. Fluids, 16 (2004) 4635-4660.
[2] J. Ou, J.P. Rothstein, Direct velocity measurements of the flow past drag-reducing ultrahydrophobic surfaces, Phys. Fluids, 17 (2005) 103606.
[3] J. Ou, G.R. Moss, J.P. Rothstein, Enhanced mixing in laminar flows using ultrahydrophobic surfaces, Phys. Rev. E, 76 (2007) 016304.
[4] J.P. Rothstein, Slip on Superhydrophobic Surfaces, Annu. Rev. Fluid Mech., 42 (2010) 89-109.
[5] M. Nilsson, R. Daniello, J.P. Rothstein, A novel and inexpensive technique for creating superhydrophobic surfaces using Teflon and sandpaper, J. Phys. D: Appl. Phys., 43 (2010) 045301.
[6] M. Nilsson, J.P. Rothstein, The effect of contact angle hysteresis on droplet coalescence and mixing, J. Colloid and Interface Sci., 363 (2011) 646-654.
[7] M. Nilsson, J.P. Rothstein, Using sharp transition in contact angle hysteresis to move and deflect droplets on a superhydrophobic surface, Phys. Fluids, 24 (2012) 062001.
[8] P. Kim, T.-S. Wong, J. Alvarenga, M.J. Kreder, W.E. Adorno-Martinez, J. Aizenberg, Liquid-Infused Nanostructured Surfaces with Extreme Anti-Ice and Anti-Frost Performance, ACS Nano, 6 (2012) 6569 -6577
[9] J.-H. Kim, J.P. Rothstein, Dynamic Contact Angle Measurements of Superhydrophobic Surfaces, Phys. Fluids, 27 (2015) 032107.
[10] J.-H. Kim, J.P. Rothstein, Droplet Impact Dynamics on Lubricant-Infused Superhydrophobic Surfaces: The Role of Viscosity Ratio, Langmuir, 32 (2016) 10166-10176.
[11] C. Lee, H. Kim, Y. Nam, Drop Impact Dynamics on Oil-Infused Nanostructured Surfaces, Langmuir, 30 (2014) 8400-8407.
[12] C. Hao, J. Li, Y. Liu, X. Zhou, Y. Liu, R. Liu, L. Che, W. Zhou, D. Sun, L. Li, L. Xu, Z. Wang, Superhydrophobic-like tunable droplet bouncing on slippery liquid interfaces, Nature Communication, 6 (2015).
[13] J.-H. Kim, H.P. Kavehpour, J.P. Rothstein, Dynamic contact angle measurements on superhydrophobic surfaces, Physics of Fluids, 27 (2015).

Wetting and evaporation of vesicle dispersion droplets on porous substrates

Abhijeet Kumar[1], Jochen Kleinen[2], Joachim Venzmer[2], Victor Starov[3] , Tatiana Gambaryan-Roisman[1]

[1]Institute of Technical Thermodynamics, Technische Universität Darmstadt, 64367 Darmstadt, Germany
[2] Research Interfacial Technology, Evonik Nutrition & Care GmbH, 45127 Essen, Germany
[3] Department of Chemical Engineering, Loughborough University, Loughborough, LE11 3TU Leicestershire, UK

E-mail: kumar@ttd.tu-darmstadt.de

Lipid vesicles have recently found widespread use in applications such as softening of paper and textiles. The mode of treatment in these applications typically involves the spraying of aqueous vesicle dispersions onto dry porous substrates. The wetted porous substrate is subsequently dried via evaporation of the bulk liquid leaving behind the vesicles deposited on the porous substrate. The important factors which determine the effectiveness of such treatments include (i) the rate at which droplets spread and imbibe on the porous substrate, and (ii) the post-drying distribution of softening ingredients on the porous substrate. It is therefore important to have a good understanding of the above processes, and the factors which influence them.

In this work, an experimental investigation of the wetting of vesicle dispersion droplets on cellulose fiber filter papers and the subsequent drying process has been carried out. Two different types of vesicles which are composed of chemically similar lipids but exhibit contrasting bilayer phase behavior have been used. The filter papers used have different porosities and thicknesses. The wetting of liquid droplets on porous substrates which proceeds with simultaneous spreading and imbibition is observed using an experimental setup as shown schematically in Fig. 1. This setup allows simultaneous determination of the imbibed area and the drop shape during the drop spreading, imbibition and liquid evaporation. A sample of images obtained during the spreading and evaporation phases, has been provided in Fig. 2(A) and (B), respectively.

It is found that the droplet wetting behavior is of the "complete wetting" [1] type on Whatman 903, whereas it is of the " partial wetting" [2] type on Sartorius 388. Furthermore, it is observed that the spreading of droplets containing vesicles with liquid-crystalline phase bilayers occurs faster than that of vesicles with solid-gel phase bilayers. An investigation of the subsequent evaporation process reveals that the deposited vesicles are localized near the periphery on the wetted area, which resembles the characteristic "coffee-ring"- like deposition. It is observed that the strength of the obtained coffee-ring is dependent on the porosity of the filter papers, and the bulk electric conductivity of the vesicle dispersion. Larger pores result in the formation of stronger coffee-rings. The strength of the formed coffee ring is enhanced at high bulk electrical conductivity of the liquid.

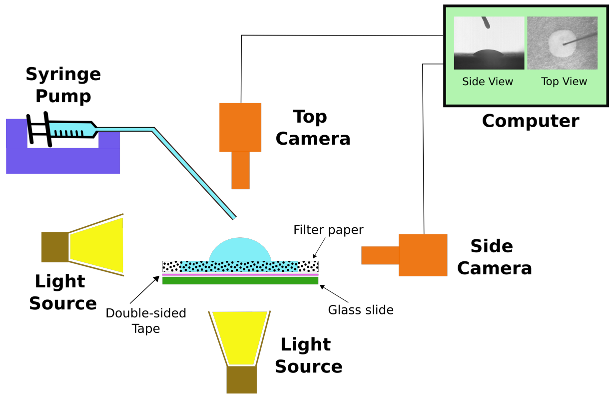

Fig. 1 : Experimental set-up for the investigation of droplet spreading, imbibition and evaporation

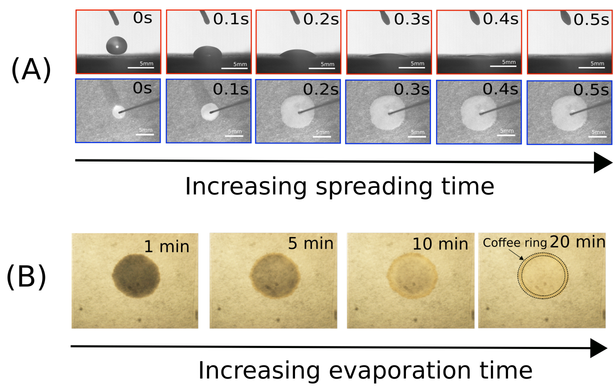

Figure 2 : Images obtained during the spreading and imbibition phase (A), and during the evaporation phase (B) of the process

Acknowledgements. The study has been prepared in the framework of the Marie Curie Initial Training Network Complex Wetting Phenomena (CoWet), Grant Agreement no. 60786.

References

[1] Chao, T.C., Arjmandi-Tash, O., Das, D.B. and Starov, V.M. Journal of Colloid and Interface Science, 446 (2015), 218-225.

[2] Chao, T. C., Arjmandi-Tash, O., Das, D. B., Starov, V. M. Colloids and Surfaces A, 505 (2016), 9-17.

MOTION OF DROPLETS ON SUPERHYDROPHOBIC SURFACES

Alexander F.W. Smith*[1], Shaun C. Hendy[1,2], Rebecca Sutton[1], Keoni Mahelona[3]
[1] MacDiarmid Institute for Advanced Materials and Nanotechnology, Department of Physics, University of Auckland, Auckland 1142, New Zealand
[2] Te Pūnaha Matatini, University of Auckland, Auckland 1142, New Zealand
[3] Te Hiku Media, 1 Melba Street, Level 2, PO Box 458, Kaitaia 0410, New Zealand

E-mail: alex.smith@auckland.ac.nz

The surfaces of many plant leaves are superhydrophobic, a property that may have evolved to help keep the leaves clean by encouraging the beading and rolling of water droplets. While the rolling motion of droplets on superhydrophobic surfaces with conventional slip lengths has been investigated and observed experimentally, the existence of slip-dominated regimes on surfaces with sufficiently high slip-lengths remains relatively unexplored.

In this paper, molecular dynamics simulations are used to investigate the roles of droplet size and surface geometry on the subsequent equilibrium velocity of droplets travelling down super-hydrophobic surfaces. The results are examined using an extension of previous theoretical descriptions[1] of droplet motion on surfaces, where an effective slip condition[2] is applied at the liquid-surface interface. This approach yields three limiting cases for the steady-state velocity of the droplets, where energy losses are dominated by viscous dissipation, surface friction or contact line friction respectively.

We find a distinct droplet size regime where the motion of sufficiently small droplets is determined by the energy dissipated due to friction at the fluid-surface interface, and the subsequent droplet velocity is proportional the droplet radius. As droplet size increases, we retrieve the usual rolling state where droplet motion is dominated by viscous dissipation within the droplets. The transition radius is predicted using the slip length of the surface.

We also consider the movement of droplets across a surface that has controlled wettability. Simulations of droplets on a surface that possessed wettability with sinusoidal variations in time and space showed a maximum droplet velocity for droplets with radii close to a quarter of the wavelength of the wettability gradient. Simulation results are presented along with a supporting mathematical model. We discuss the implications of our results for the design of microfluidic mixers and lab-on-a-ship devices using switchable surfaces.

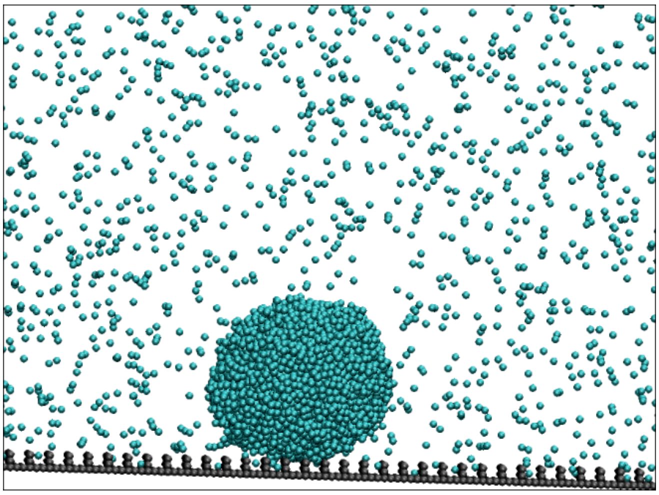

Acknowledgements. We thank the MacDiarmid Institute of Advanced Materials and Nanotechnology for their funding and support of this project.

References

[1] L. Mahadevan and Y. Pomeau, *Phys. Fluids,* **1999**, *11*, 2449-2453.
[2] S. Hendy, M. Jasperse and J. Burnell, *Phys. Rev. E,* **2005**, 72.

Motion of a deformable drop in T-shaped microchannels

Rocio Navarro, Alexander Z. Zinchenko, Robert H. Davis

Department of Chemical and Biological Engineering, University of Colorado Boulder

Email: Rocio.navarro@colorado.edu

An algorithm has been developed to calculate the velocity of a deformable drop moving at small Reynolds number through a microchannel that contains a fluid of different viscosity than the fluid that forms the drop. A similar problem was studied for a deformable drop between two parallel plates by A. J. Griggs, A. Z. Zinchenko, and R. H. Davis [1]. In their case, the drop tended to move to the center of the channel. In our case, the drop is freely suspended in a plane T-junction microchannel with sharp corners. Solid sphere transport through a T-junction has been previously simulated [2]. Similar to their approach (but with a droplet instead of a solid particle in this case), a "moving frame" or computational frame is used to solve the 3D problem inside its boundaries, assuming that the cell is large enough so the flow outside it is not perturbed by the drop. Outside the computational cell, the fluid velocity is provided by the solution of a 2D flow without any particle or droplet. The moving frame is larger than the drop size, and, as it moves with the droplet, it is formed by different geometries or boundaries, including the channel walls (where the no-slip condition is applied) or the main fluid flux.

The main fluid flux is divided into the main branch and the side branch. We study different flow ratios to determine under which conditions the when the drop enters the side channel, whether it will break or not, and if it will become stuck in the microchannel. We expect the drop to deform enough to be able to go around the sharp corners with a sufficient clearance. The drop has an initial spherical shape, but the inlet channel branch is long enough for it to achieve an equilibrium position at the channel center-plane

Besides the flow ratio, other variables studied are the viscosity ratio between the drop and main fluid, the drop capillary number, and the ratio between the drop diameter and the channel height. Results will be presented on drop trajectories and shapes, including conditions for entrance into the side channel and for the drop to become stuck or break.

[1] Griggs, A. J., Zinchenko A. Z. and Davis R. H. 2007 "Low-Reynolds-number motion of a deformable drop between two parallel plane walls". International Journal of Multiphase Flow, vol. 33:182–206.

[2] Zinchenko A.Z., Ashley J.F. and Davis R.H. 2012 "A moving-frame boundary-integral method for particle transport in microchannels of complex shape". Phys. Fluids, vol. 24: 043302.

EFFECT OF SURFACTANTS AND POLYMERS ON DROPLET COALESCENCE

Chinaud, M., Voulgaropoulos, V., Weheliye, W., and Angeli, P.

Department of Chemical Engineering, University College London, London, United Kingdom,

E-mail: p.angeli@ucl.ac.uk

1) Introduction

Liquids with the presence of surface active agents and polymers are ubiquitous in nature, industrial applications (food, cosmetics, enhanced oil recovery; water purification) and emerging technologies (ink jet printing). While the addition of polymers complexifies the rheological behaviour of the fluids, the surfactants alter the interfacial tension properties. Complex fluids and surfactants regularly appear in two-phase dispersions with other immiscible liquids in modern industrial applications. Dispersed flows with non-Newtonian liquids and surfactants pose major challenges because of the interplay of complex flow fields with complex rheology as well as breakage/coalescence phenomena.

The dynamics of coalescence are generally discussed through the study of the neck meniscus evolution and can be divided in two parts. In the first regime, called "viscous regime", there is a linear evolution of the neck in time that results from the local balance between the viscous and the interfacial forces and leads to the development of a scaling law giving the neck velocity $V=\gamma/\mu$ (where γ and μ represent respectively the surface tension and the viscosity) [1]. The purpose of this work is to investigate the effects on the scaling law in the viscous regime when disturbances in the interfacial and viscous forces are introduced from the addition of surfactant and polymeric chains in the fluids. To achieve this purpose, velocity fields within the coalescing bodies need to be acquired.

2) Experimental Setup

The studies focus on the coalescence of an aqueous droplet with an aqueous-organic (Glycerol-Water, 76% v/v- Exxsol D80) flat interface. In the first part of the study, a non-ionic surfactant (Span 80) was added in the organic phase. Four different surfactant concentrations selected below the CMC value were tested and the respective interfacial tension was measured. In the second part of the study, polymers were added into the aqueous phase (Xanthan gum). The corresponding rheological curves were obtained which showed an increase of shear-thinning behaviour with the polymer concentration. Three different Xanthan concentrations in the aqueous phase (500, 1000 and 2000 ppm) have been considered. The surface tension value for surfactant concentrated solutions is presented in Fig. 1.

The coalescence experiments were conducted in a vertical Hele-Shaw cell made from two Plexiglas plates separated by a 1.25 mm gap. Velocity fields were obtained with high speed bright field PIV [2]. 10 µm silver coated particles were seeded into the aqueous phase and the images were acquired by a high speed camera (4000 fps). In order to avoid optical distortion, the Glycerol-Water mixture has been chosen to have the same Refractive index as the organic phase. To distinguish the different phases, blue ink has been added into the aqueous phase.

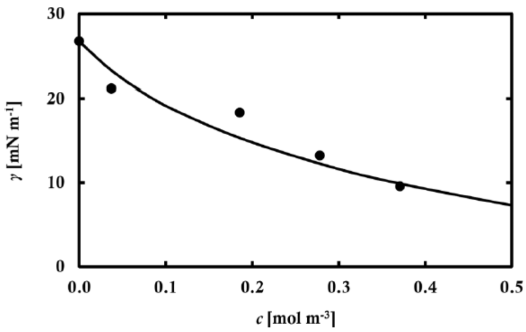

Fig. 1: Interfacial tension values of Exxsol D80 and a water/glycerol mixture for different Span 80 concentrations. The continuous line represents Langmuir isotherm equation.

3) Results

It was found that the time evolution of the neck at the initial stages of coalescence can be described by the linear law developed for pure systems for surfactant concentrated solutions but not for polymeric solutions. Results showed that for surfactant concentrations below the CMC value and for droplet seeding times long enough to assume a uniform spreading of the surface active agent along the interface, the scaling law describing the neck evolution in time [1] did not hold true.

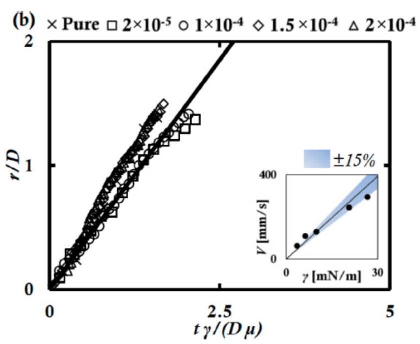

Fig.2: Dimensionless neck evolution in time. The value of surface tension has been as been taken for a double concentration of surfactant.

The interfacial tension value measured for each surfactant concentration has been found too low to fit the models provided by the literature. Recent numerical work [3] suggested that, in the early stage of coalescence, the surfactant concentration were basically doubled at the neck.
Fig. 2 displays the dimensionless neck evolution in time by artificially doubling the concentration of the surfactant from the constitutive equation provided in Fig. 1. Results show clearly the good agreement obtained in this way. To the best of our knowledge, this can be one of the first indirect proofs of the numerical simulation performed in this work [3]. Velocity and vorticity fields, computed inside the coalescing droplet, show that the effect of surfactant significantly changes the interface shape and flow field, while polymers mainly increase mixing due the spatial stratification of the apparent viscosity.
The velocity fields obtained guided us to visualize the complex structure of the flow during the early stage of coalescence.

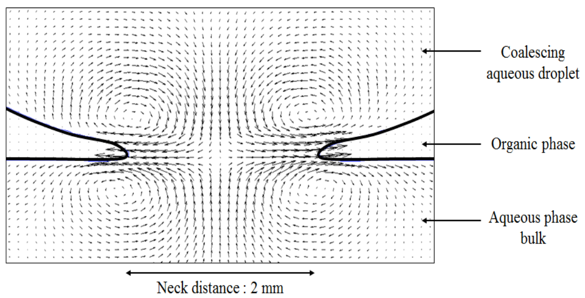

Fig. 3: Velocity field of an aqueous phase droplet coalescing with a flat interface.

Fig. 3 displays the velocity field obtained for a coalescing droplet at 2 mm neck diameter. The pattern shows clearly that in the small volume located at the neck, the flow is a typical extensional flow surrounded by four vortices generating shear flow. This complex flow structure justifies the potential interlink to the complex rheology. Xanthan solutions are known to display shear-thinning properties for concentration bellow 1000 ppm. Above that concentration, extensional viscosity might need to be taken into account. Results show that, for Xanthan concentrated solution, the neck evolutions is fully governed by the high shear rate viscosity value. However the velocity map (Fig. 4) clearly shows a significant stratification of the shear inside the coalescing droplet. Thus stratification displays an effective spatial viscosity stratification which has been computed in time for all Xanthan concentrated solutions. In a similar way, we found that the extensional strain rate computed from the velocity field was high enough to take into account extensional viscosity for the 2000 ppm concentrated solutions.

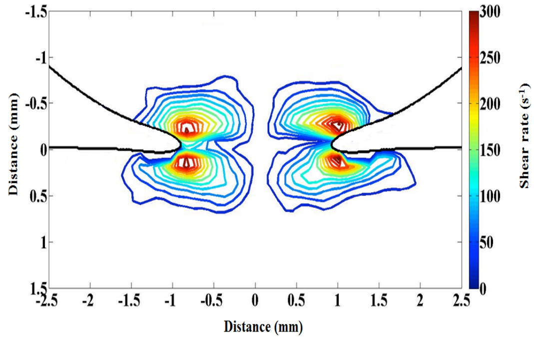

Fig.4: Shear rate measured for a 2mm neck distance

4) Conclusion

The work presented here shows the great interest to investigate velocity field in the coalescence problem. The presence of surfactants showed a huge disturbance in interface resistance which changed the typical geometric assumption commonly considered in modelling efforts. In addition, it has been found that locally at the neck, in the early stages of the coalescence, the concentration of surfactant was doubled. The velocity field measurements allowed us to quantify the spatial stratification of the viscosity inside the coalescing body for Xanthan concentrated solutions. It has been found that locally at the neck the effective viscosity was close the highest shear rate viscosity value.

Acknowledgements. The authors would like to thank EPSRC and Chevron for their support. This work has been part of MEMPHIS multiphase flow program.

References

[1] Yokota, M., & Okumura, K. (2011). Dimensional crossover in the coalescence dynamics of viscous drops confined in between two plates. *Proceedings of the National Academy of Sciences*, *108*(16), 6395-6398.
[2] Chinaud, M., Voulgaropoulos, V., & Angeli, P. (2016). Surfactant effects on the coalescence of a drop in a Hele-Shaw cell. *Physical Review E*, *94*(3), 033101.
[3] Martin, D. W., & Blanchette, F. (2015). Simulations of surfactant effects on the dynamics of coalescing drops and bubbles. *Physics of Fluids*, *27*(1), 012103.

DROPLET SKI-JUMPING ON AN INCLINED MACRO-RIDGED SUPERHYDROPHOBIC SURFACE

Regulagadda Kartik[1], Shamit Bakshi[1], Sarit Kumar Das[1,2]

[1]Department of Mechanical Engineering, Indian Institute of Technology, Madras, Tamil Nadu, India
[2]Current address: Department of Mechanical Engineering, Indian Institute of Technology, Ropar, Punjab, India
E-mail: kartik25192@iitm.ac.in

Superhydrophobic surfaces have become one of the major focuses in the field of anti-ice surface engineering during the past two decades. Conventional surfaces produce complete rebounce when impacted upon by a water droplet where its volume influences the contact time with the surface [1]. It has been showed that the hydrodynamics is significantly altered by the presence of macro-strucutures on the surface with similar wettability which can reduce the contact time [2,3]. The proper design of the surface to produce minimal contact time can be extremely beneficial which increases the anti-icing potential of the surface.

Existing studies deal with droplet impinging on to the surface in the normal direction. However, the droplet can crash on the surface at any inclination in a practical application. Here, we consider the effect of surface inclination (Θ = 15°, 30°, 45° and 60° with the vertical) to study the hydrodynamics of a droplet (radius, R_0 = 1.35 mm) under the influence of a macro-ridge which is an isosceles wedge shaped structure with base width of 1 mm and height of 0.5 mm. We also consider the surfaces which are decorated with multiple parallel ridges with varying peak-to-peak distance (p = 1 mm, 1.5 mm and 3 mm). All the impacts are centered, i.e. the south pole of the droplet impacts on to the peak of a ridge.

During the impact on the surface with multiple ridges and peak-to-peak distance of 3 mm, the droplet performs a ski-jump from the surface without fragmenting (for surface inclinations of 45° and 60° with impact velocity, $U \geq 1$ m/s) and thereby, reducing the contact time as shown in Figure 1. This behavior is not observed on any other substrates considered and indicates the importance of peak-to-peak distance of the ridges to shift the hydrodynamics from fragmentation (during impacts in the normal direction) to ski-jumping (during inclined impacts). In this regard, the probable reasons for the droplet to perform ski-jumping will be discussed.

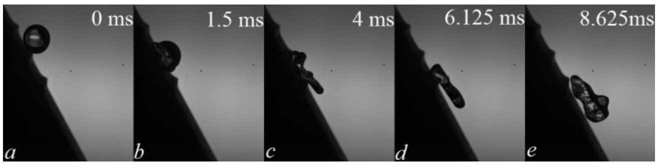

Figure 1: Image sequence showing the impact of a droplet of radius, R_0 = 1.35 mm with velocity, U = 1 m/s on a substrate with multiple ridges (p = 3 mm) and surface inclination, Θ = 60° from the vertical to produce ski-jumping.

Acknowledgements. The authors declare no competing financial interest.

References

[1] Denis Richard, Christophe Clanet, David Quéré. Contact time of a bouncing drop. Nature 417 (2002) 811.

[2] James C. Bird, Rajeev Dhiman, Hyuk-Min Kwon, Kripa K. Varanasi. Reducing the contact time of a bouncing drop. Nature 503 (2013) 385-388.

[3] Anaïs Gauthier, Sean Symon, Christophe Clanet, David Quéré. Water impacting on superhydrophobic macrotextures. Nature Communications (2015) 6:8001.

The effect of particle wettability on the stick-slip behavior of inkjet printed droplets

Dong-Ook Kim, Min Pack, Ying Sun

Department of Mechanical Engineering and Mechanics, Drexel University, Philadelphia, PA, USA

E-mail: ysun@coe.drexel.edu

Despite the myriad of experimental and theoretical work to date,[1–6] the physics governing multi-rings, radial spokes and other patterns formed via colloidal drop evaporation, especially the stick-slip motion of the contact line, is still not well understood.[5] The stick-slip behavior caused by pinning and depinning of the contact line is sometimes attributed to the Marangoni flow induced recirculation of the particles at the vicinity of the contact line.[7] Still others[3] have shown how stagnation flows are created as a result of the concavity shift at the contact line which allows for the particles to accumulate at the contact line to enhance pinning. Nevertheless, the mechanism driving the ring-to-ring spacing of stick-slip-induced evaporation patterns are still not well understood. Frastia et al.[1] have concluded that particle accumulation at the contact line increases the local viscosity or the interparticle friction so that the deposition pattern and ring spacing changes. In time, the local rise in the viscosity at the contact line alone is sufficient for creating a self-organized periodic stick-slip behavior.[1] The effects of particle volume fraction, substrate wettability and particle size have also been studied to better understand the stick-slip motion of the contact line.[5,8]

In this study, we observe the stick-slip behavior of inkjet printed colloidal droplets in-situ via an interferometric technique during the entire evaporation process. Fluorescence microscopy is used to obtain the particle deposition during the stick-slip motion of the contact line. Interferometry is used to calculate the local drop thickness – obtained via a monochromatic interferemetric technique with the fringe-to-fringe spacing representative of a height displacement of half of the wavelength of the light used for each time step. Monodispersed 20 nm polystyrene particles with varying surface wettability – sulfate-modified (relatively hydrophobic at water-air interface) and carboxylate-modified (relatively hydrophilic) – in DI water are printed using a piezoelectric inkjet printhead.

We used droplets 65 μm in diameter at 0.05 – 0.5 v/v% on plasma-treated glass of totally wetting substrates. A Phantom v711 with a high-powered LED 445nm monochromatic light source was coupled to a Zeiss Axiobserver microscope with a 50x objective to obtain highspeed recording of the evaporation dynamics at 5000 fps at a resolution of 1280 × 800. These experiments were carried out in ambient temperature of 22 °C with a relative humidity of 40%.

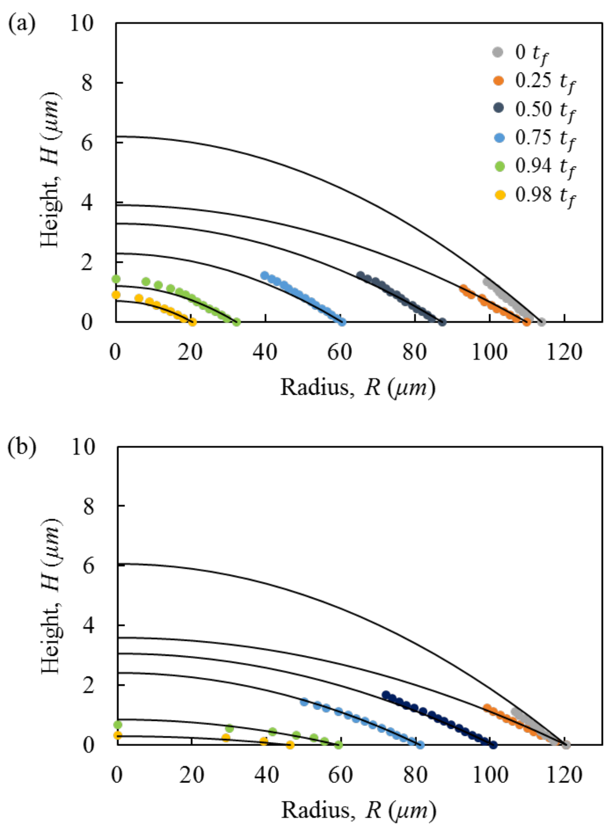

Figure 1: The morphology of the inkjet printed droplets measured in-situ via an interferometry technique for an evaporating aqueous droplet containing (a) 20 nm sulfate-modified polystyrene particles and (b) 20 nm carboxylate-modified polystyrene particles on a plasma treated glass coverslip for in-flight droplet diameters of ≈ 65 μm and 0.25% volume fraction. The time fraction $\Delta t^* \equiv \Delta t/t_f = 0, 0.25, 0.5, 0.75, 0.94$, and 0.98 from right to left lines in (a) and (b).

Figure 1 shows the instantaneous surface profiles of inkjet printed evaporating droplets containing 20nm sulfate-modified (Fig. 1a) and carboxylate-modified (Fig. 1b) particles, respectively, while keeping other parameters identical. The symbols are obtained from interferometry and the lines are obtained from the spherical cap assumpation using the contact angle determined from the interferometry data. For both cases, the drop evaporation undergoes the constant contact area mode (for ~$0.25t_f$), followed by the constant contact angle mode for the sulfate-modified case and by the mixed mode for the carboxylate-modified case. Here, t_f is the time at which evaporation is completed. It is obvious from comparing Figs. 1a and 1b that the contact radius and contact angle for the two cases are very different at the late stage of evaporation, where the contact angle for the case with carboxylate-modified particles decreases more rapidly than that of the sulfate-modified particles, indicating that the droplet ability to pin the contact line increases with an increase in wettability of the particles.

Figure 2 shows the deposition of 20nm sulfate-modified and carboxylate-modified particles with in-flight diameter of 65 μm and 0.25% volume fraction for both particle suspensions. Both cases form an outmost ring. Figure 2a is a multi-ring deposition and Fig. 2b has radial spokes with rings (or the so-called spider web deposit) which stop at a critical radius of R/R_0~0.44.

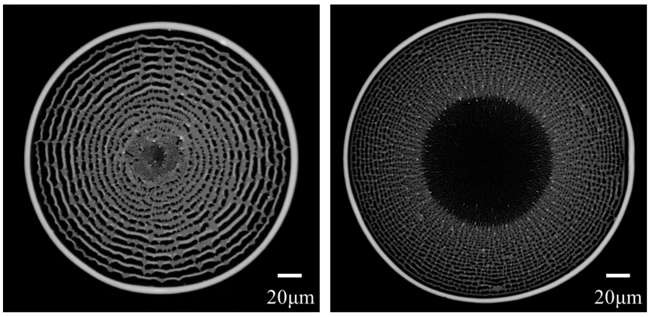

Figure 2: Fluorescent images of the inkjet-printed 20 nm sulfate-modified particles (left) and 20 nm carboxylate-modified particles (right). The in-flight droplet diameters is ≈ 65 μm and 0.25% volume fraction for both particle suspensions.

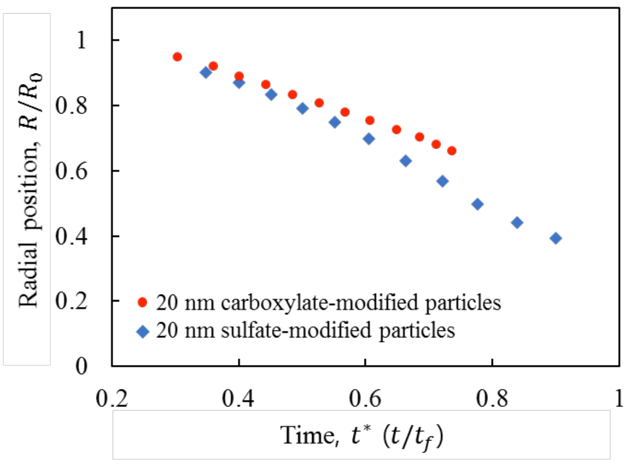

Figure 3: Multi-ring position as a function of evaporation time for 20nm sulfate-modified particles and carboxylate-modified particles. The in-flight droplet diameters is ≈ 65 μm and 0.25% volume fraction for both particle suspensions.

Figure 3 shows multi-ring position as a function of evaporation time for 20nm sulfate-modified particles and carboxylate-modified particles for the same in-flight drop size and volume fraction. We find that while we keep all other conditions the same, the retraction rate of the contact line increases with a decrease in the wettability of the particles and the faster retraction rate increases the ring spacing as shown in both Figures 2 and 3. The change in the retraction rate of the contact line is related to the particle drag as well as the wettability at the contact line. We have also obtained the thickness and spacing of the rings derived from profilometry as correlated to the wettability of the particles.

Acknowledgements. Support for this work was provided by the National Science Foundation under grant No. CMMI-1401438.

References

(1) Frastia, L.; Archer, A. J.; Thiele, U. Dynamical Model for the Formation of Patterned Deposits at Receding Contact Lines. *Phys. Rev. Lett.* **2011**, *106* (77801).
(2) Kaplan, C. N.; Mahadevan, L. Evaporation-Driven Ring and Film Deposition from Colloidal Droplets. *J. Fluid Mech.* **2015**, *781*.
(3) Maheshwari, S.; Zhang, L.; Zhu, Y.; Chang, H. Coupling Between Precipitation and Contact-Line Dynamics : Multiring Stains and Stick-Slip Motion. *Phys. Rev. Lett.* **2008**, *100* (44503).
(4) Orejon, D.; Sefiane, K.; Shanahan, M. E. R. Stick-Slip of Evaporating Droplets : Substrate Hydrophobicity and Nanoparticle Concentration. *Langmuir* **2011**, *27*.
(5) Yang, X.; Li, Y.; Sun, Y. Soft Matter Competition between the Receding Contact Line and. *Langmuir* **2014**, *10*.
(6) Matter, S.; Chhasatia, V. H.; Sun, Y. Interaction of Bi-Dispersed Particles with Contact Line in an Evaporating Colloidal Drop. *Soft Matter* **2011**, *7*, 10135–10143.
(7) Veronica L. Morales; Parlange, J.-Y.; Wu, M.; Perez-Reche, F. J.; Zhang, W.; Sang, W.; Steenhuis, T. S. Surfactant-Mediated Control of Colloid Pattern Assembly and Attachment Strength in Evaporating Droplets. *Langmuir* **2013**, *29*.
(8) Patil, N. D.; Bange, P. G.; Bhardwaj, R.; Sharma, A. Effects of Substrate Heating and Wettability on Evaporation Dynamics and Deposition Patterns for a Sessile Water Droplet Containing Colloidal Particles. *Langmuir* **2016**, *32*.

Post-air entrainment interfacial instability during drop impact on lubricated surfaces

Min Pack[1], Diyuan Zong[1,2], Dong-Ook Kim[1], Hyoungsoo Kim[3], Ying Sun[1]

[1]Department of Mechanical Engineering and Mechanics, Drexel University, Philadelphia, PA, USA
[2]Department of Thermal Engineering, Tsinghua University, Beijing, China
[3]Department of Mechanical and Aerospace Engineering, Princeton University, Princeton, NJ, USA

E-mail: ysun@coe.drexel.edu

The omnipresence of drop impact in both natural and industrial processes has led to an abundance of studies in various conditions and configurations[1-3]. The macroscopic scale of impacting droplets contains complex micro-nanoscale effects at finite times prior to contact due to the entrained air film between the droplet and the substrate. The air entrainment effects of droplets approaching planar surfaces have been observed utilizing a number of techniques including interferometry and total internal reflection-based techniques with recent advances in high speed imaging, to produce elegant traces of the entrained gas in the micro-nano scale[4-7].

Upon contact, the wetting front in drop impact studies is stable until the splash threshold is reached for high inertia drop impacts[8-10](i.e., We≡$\rho U_0^2 R_0/\sigma$ > O(10^2), where ρ is the density of the droplet, U_0 the impact velocity, R_0 the drop radius and σ the surface tension of the droplet). In this study, we examine the post-air film rupture liquid-liquid contact dynamics upon drop impact on a thin liquid film well below the splash thresholds. The wetting front of the droplet containing a mixture of water and glycerine at 10 ≲We≲ 50 displays hydrodynamic instabilities on thin silicone oil films 5 µm thick. As the wetting front moves radially outwards, an air rim is formed between the droplet and the substrate as depicted schematically below in Fig. 1.

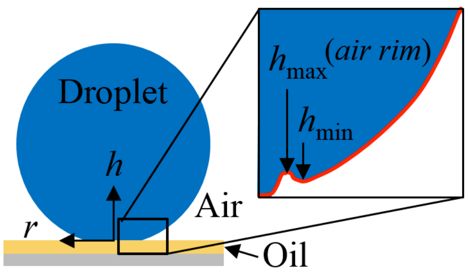

Figure 1: Schematic of the air rim formed by the impacting droplet.

On solid surfaces (besides atomically smooth mica surfaces), minute asperities cause random collapse of the air film, but on atomically smooth oil films, the air film ruptures at the lowest air film thickness, or the kink[7], provided that the droplet has enough inertia. Upon impact, the annular failure at the kink of the air film necessitates that the wetting front pushes against a column of air which forms an air rim which subsequently grows unstable and forms fingers that propagates through time, t (Figure 2). The radius of the wetting front normalized by the drop radius is plotted against time in Figure 3 showing $r_r \sim t^{1/2}$ scaling up to 1.8 ms when the wetting stops. The t = 0 is the instant when the droplet comes into the field of view of the total internal reflection microscopy (TIRM) setup where air film thicknesses down to a single nanometer may be resolved. This technique allows for a stark contrast between the wetted area (black) compared to the ambient air. To study the post-air entrainment interfacial instability, we have varied the viscosity of the droplet and the impacting thin oil film, as well as the impact velocity of the droplets, where the parameters are tabulated in Table 1.

Table 1: Experimental parameters.

	Droplet (water+glycerine, w%)				Oil Film
	0	60	80	85	δ_{oil} = 5µm
μ [mPa s]	1.14	11	49	100	9.30 , 970
σ [mN/m]	72.1	67.0	65.2	63.9	19.7, 21.2
ρ [kg/m^3]	1000	1142	1198	1213	930, 970
iR_0 [mm]	1.05	0.94	0.92	0.91	
U_0 [m/s]	0.9 – 1.4				

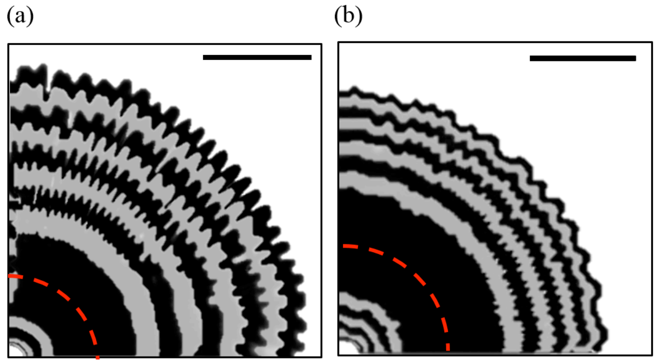

Figure 2: The interfacial instability development for (a) droplet viscosity of 11 mPas with a starting time frame t ≈ 88 µs and time step of Δt ≈ 44 µs (b) droplet viscosity of 100 mPas with a starting time frame t ≈ 440 µs and time step of Δt ≈ 120 µs. Droplet We ≈ 13 and the oil film thickness ≈ 5 µm with viscosity of 970 cP. Scale bars are 1 mm and the red dashed lines represent the annular liquid-liquid contact.

The instability was directly imaged via the TIRM technique. The growing wetted area in time increments of 44 µs for droplet viscosity of 11 mPas and 120 µs for droplet viscosity of 100 mPas are shown in Figure 2. Snapshots at each time steps were superimposed in alternating black and gray images to delineate the propagation of the wetting front and the instability development.

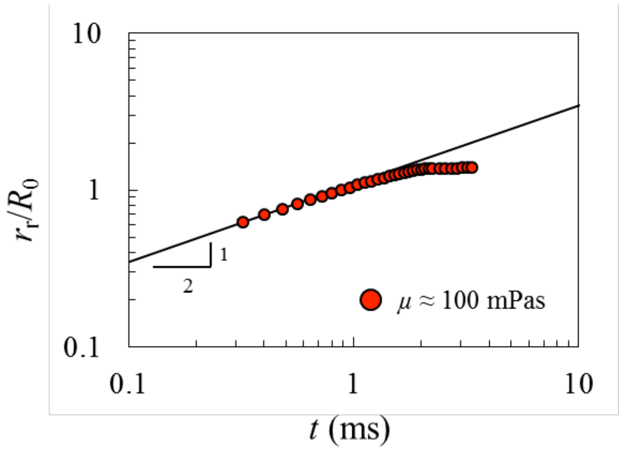

Figure 3: Normalized radius r_r/R_0 with respect to t. Using the same parameters as in Figure 2(b). Data points average of three experiments.

As the instability propagates, the rim thickness h_{max} grows between ≈10 – 160 nm until it exits the spatial resolution of the TIRM setup beyond ≈160 nm at $t \approx 0.88$ ms. A plot depicting the growth of h_{max} with respect to the rim location relative to the wetting radius, i.e., $r^*=r-r_r$, is shown in Figure 4. We find that in order for the fingers to propagate, an air rim is always present where h_{max} grows in nanometers in Figure 4 whereas the wavelength grows in microns (10 – 200 μm) in Figure 2b.

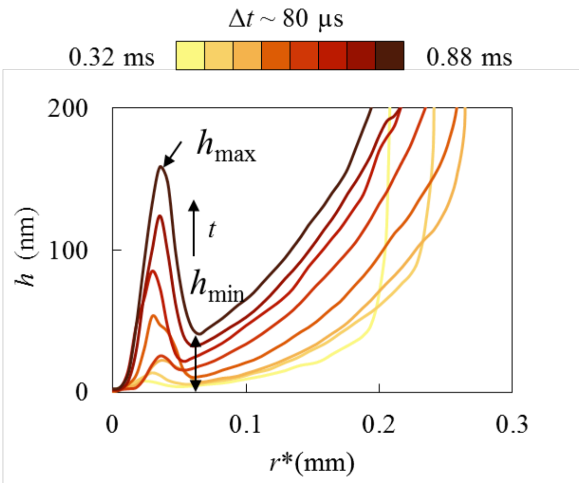

Figure 4: The air film profile h at the wetting front with respect to the scaled radius r^* with $\Delta t \approx 80$ μs for μ= 100 mPas.

Figure 2 shows how an increase in viscosity from 11 mPas in Fig. 2a to 100 mPas in Fig. 2b results in a smaller wavelength of the interfacial instability. An increase in velocity has shown to have a similar effect of decreasing the wavelength. We have also found that decreasing the oil film viscosity from 970 to 9.3 mPas suppressed the fingering instability, probably due to the increased mobility of the air film.

Several instability mechanisms have been investigated to describe the finger-like interfacial instability where the Rayleigh-Taylor[9] and the Kelvin Helmholtz[7] instabilities have been ruled out by an order of magnitude argument. However, we find that the decrease in the fingering wavelengths with an increase the viscosity or velocity qualitatively follows a Saffman-Taylor instability where the wavelength decreases with an increase in the viscosity difference between the air and droplet. We suspect that it is the air rim that moves with the wetting front that is unstable due to the air pushing against the liquid. The role of intermolecular interactions between the drop and the oil film in causing instabilities has also been explored.

Acknowledgements. Support for this work was provided by the National Science Foundation under grant No. CMMI-1401438 to Y.S.

References

1. Martin, R. Phenomena of liquid drop impact on solid and liquid surfaces. *Fluid Dynamics Research* **1993,** *12* (2), 61.
2. Yarin, A. L. Drop Impact Dynamics: Splashing, Spreading, Receding, Bouncing…. *Annual Review of Fluid Mechanics* **2006,** *38* (1), 159-192.
3. Josserand, C.; Thoroddsen, S. T. Drop Impact on a Solid Surface. *Annual Review of Fluid Mechanics* **2016,** *48* (1), 365-391.
4. Bouwhuis, W.; van der Veen, R. C. A.; Tran, T.; Keij, D. L.; Winkels, K. G.; Peters, I. R.; van der Meer, D.; Sun, C.; Snoeijer, J. H.; Lohse, D. Maximal Air Bubble Entrainment at Liquid-Drop Impact. *Physical Review Letters* **2012,** *109* (26), 264501.
5. de Ruiter, J.; Oh, J. M.; van den Ende, D.; Mugele, F. Dynamics of Collapse of Air Films in Drop Impact. *Physical Review Letters* **2012,** *108* (7), 074505.
6. Kolinski, J. M.; Mahadevan, L.; Rubinstein, S. M. Lift-Off Instability During the Impact of a Drop on a Solid Surface. *Physical Review Letters* **2014,** *112* (13), 134501.
7. Pack, M.,; Hu H.; Kim D.; Zheng Z.; Stone H.A.; Sun Y.; Failure mechanisms of air entrainment in drop impact on lubricated surfaces. *Soft Matter* **2017,** DOI: 10.1039/C7SM00117G**.**
8. Liu, Y.; Tan, P.; Xu, L. Kelvin–Helmholtz instability in an ultrathin air film causes drop splashing on smooth surfaces. *Proceedings of the National Academy of Sciences* **2015,** *112* (11), 3280-3284.
9. Lee, C.; Kim, H.; Nam, Y. Drop Impact Dynamics on Oil-Infused Nanostructured Surfaces. *Langmuir* **2014,** *30* (28), 8400-8407.
10. Allen, R. F. The role of surface tension in splashing. *Journal of colloid and interface science* **1975,** *51* (2), 350-351.

Evaporation control of acoustically levitated liquid droplets

Akira Shinoda, Takashi Tomizaki, Soichiro Tsujino

Department of Synchrotron Radiation and Nanotechnology, Paul Scherrer Institute, 5232 Villigen, Switzerland

E-mail: akira.shinoda@psi.ch

In this work, we investigate the evaporation of levitating water-solution droplets in acoustic standing wave with the purpose extending the lifetime of the acoustically levitated droplets. Handling of liquid droplets by ultrasonic fields such as the levitation of liquid droplets in air [1-4] has been studied as a mean to investigate physical and chemical properties of solutions or pure liquid in container-less environment. The present work is motivated by our recent experiment in which we demonstrated for the first time by the use of the acoustic levitation X-ray diffractometer to solve the atomic structure of a standard protein sample to 1.8 Å resolution at room temperature and at high efficiency [5].

In the acoustic levitation diffractometer, we combine the acoustic levitation of single protein crystal in liquid droplet, see Figure 1, with a high-frame-rate X-ray image detector. Due to the acoustic streaming, the crystal in the levitating droplet spins and orbits within but can be maintained within the X-ray beam path. Owing to the spinning of the crystal, an efficient and dense sampling of the reciprocal space is possible with a simple setup. The use of the high-frame-rate X-ray image detector (in the order of 0.1-1 kHz) allowed us to capture Bragg reflection points as if still images were captured. This way, we are able to analyze protein crystals at room temperature, that opens up a possibility to study the structural conformation dynamics of proteins at work, when they are in physiological condition

For the protein crystallography, it is however crucial to maintain the chemical consistency and the temperature of the surrounding liquid before finishing the diffraction dataset collection. In a typical lab condition (e.g. 20-40 % humidity at the temperature of 24 ˚C), a levitating pure water droplet dries out in about 20 min. For the collection of the single dataset for a pristine crystal in the order of 1000-3000 diffraction images, the experiment can be completed well within 1 min, thus the water evaporation does not critically influence the quality of the protein. However, to observe the structural dynamics of proteins triggered by adding chemical agent or illumination, in the order of 1 hour scale for the ligand-combination reaction for example, the control of the water evaporation is crucial for the integrity of experiments.

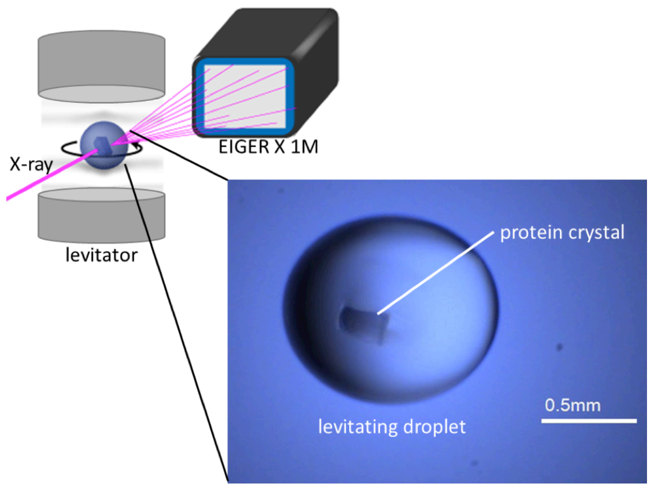

Fig.1 Levitation diffractometer for X-ray crystallography

Accordingly, we report here the methods to control the consistency of levitating droplets. In particular, using an acoustic levitator operating at ultrasonic frequency (39 kHz with the corresponding wavelength in air equal to ~8 mm) enclosed in a compact chamber, that is compatible with the X-ray diffraction experiments at synchrotron beamlines, we investigated the time-evolution of the size and the position of a series of droplets in the order of a few µl volume. We used glycerol-water solution with the concentration of typical protein crystallization liquid.

Figure 2 shows the observed relative volume change of the levitating droplets with the initial volume in the range of 2-7 μl. When the air humidity was 30 % (flow off), the pure water droplet dry out in ~20 min. The droplet with the glycerol content 20-40 % did not dry but the water content appeared to be evaporated in ~20 min. When we turn on the 100 % humidity air flow into the chamber, the volume reduction of the 100 % water droplet was significantly slower, but still decreasing. This appears to be due to the influence of the rapid convective air flow around the levitating droplet by the acoustic streaming [1, 6], albeit its spatial stability. Interestingly, under the 100 % humidity air flow, the volume of the levitating droplet of the 60 % glycerol solution increased in time, and gradually saturated at ~30% additional volume. This manifests the facts that the initial fractional water vapor pressure was lower than that of the supplied humid air flow, hence the droplet absorbed the water molecules instead of evaporating those. Similar but opposite phenomena was observed for the 20 % glycerol concentration solution: the droplet slowly decreased and reached a stable condition with the volume decrease of approximately 30-40 %. Both results indicate that a droplet with the initial concentration of ~40% should be stable, as observed in the experiment (blue filled squares in Fig 2) for 2 hours.

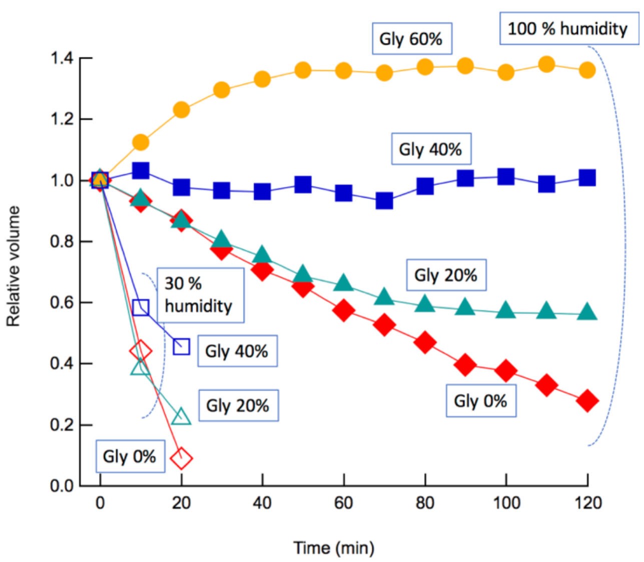

Fig. 2 Volume change of the acoustically levitated glycerol-solution-droplet with (filled symbols) and without (empty symbols).

We will report in addition the experimental results for the levitating droplet size and concentration by environmental humidity control, as well as the influence of the humidity control and the levitation power on the crystal spinning and orbiting within the levitating droplets.

Acknowledgements. The project is partially supported by Swiss Federal Commission for Technology and Innovation (CTI).

References

[1] A. Yarin, G. Brenn, O. Kastner, D. Rensink, C. Tropea, *Evaporation of acoustically levitated droplets*, Journal of Fluid Mechanics 399, 151 (1999).

[2] H. Tanaka, Y. Wada, Y. Mizuno, and K. Nakamura, *Behavior of ultrasonically levitated object above reflector hole*, Jap. J. Appl. Phys. 52, 100201 (2013).

[3] D. Foresti, M. Nabavi, M. Klingauf, A. Ferrari, and D. Poulikakos, *Acoustophoretic contactless transport and handling of matter in air*, PNAS, vol. 110 no. 31 12549–12554 (2013)l

[4] Delißen, F., Leiterer, J., Bienert, R., Emmerling, F. & Thünemann, A. F. *Agglomeration of proteins in acoustically levitated droplets*, Anal Bioanal Chem 392, 161 (2008).

[5] S. Tsujino & T. Tomizaki, *Ultrasonic acoustic levitation for fast frame rate X-ray protein crystallography at room temperature*, Sci. Rep. 6, 25550 (2016).

[6] Abe, Y., Hyuga, D., Yamada, S. & Aoki, K. *Study on Internal Flow and Surface Deformation of Large Droplet Levitated by Ultrasonic Wave*, Annals of the New York Academy of Sciences, Interdisciplinary Transport Phenomena in The Space Sciences **1077**, 49 (2006)

Sessile droplet evaporation: Ultra-high resolution two-phase DNS, Geometry-control and curvature-driven phase segregation in binary mixtures

P. Sáenz[1], A. Wray[2], Z. Che[3], O. K. Matar[3], K. Sefiane[4], J. Kim[5] and P. Valluri[4]

[1] Department of Mathematics, MIT, USA
[2] Department of Mathematics, University of Strathclyde, UK
[3] Department of Chemical Engineering, Imperial College London UK
[4] School of Engineering, The University of Edinburgh, UK
[5] Department of Mechanical Engineering, University of Maryland, USA

E-mail: prashant.valluri@ed.ac.uk

The evaporation of a liquid drop on a solid substrate is a remarkably common phenomenon. Yet, the complexity of the underlying mechanisms has constrained previous studies to spherically-symmetric configurations. We recently demonstrated [1] detailed evolution of thermocapillary instabilities during evaporation of hemispherical and non-hemispherical sessile droplets and iii) non-hemispherical sessile droplets. Rigorous DNS (using our in house TPLS2 solver [2]) showed for the first time, breakage of symmetry and the consequent development of a preferential direction for thermocapillary convection. This results in counter-rotating whirling currents in the drop playing a critical role in regulating the interface thermal and fluid dynamics.

We will also present our recent-most investigations of well-defined, non-spherical evaporating drops of pure liquids and binary mixtures. We deduce a new universal scaling law for the evaporation rate valid for any shape and demonstrate that more curved regions lead to preferential localized depositions in particle-laden drops [3]. Furthermore, geometry induces well-defined flow structures within the drop that change according to the driving mechanism and spatially-dependent thresholds for thermocapillary instabilities. In the case of binary mixtures, geometry dictates the spatial segregation of the more volatile component as it is depleted. In the light of our results, we believe that the drop geometry can be exploited to facilitate precise local control over the particle deposition and evaporative dynamics of pure drops and the mixing characteristics of multicomponent drops.

Acknowledgements. EPSRC EP/K00963X/1, EPSRC EP/K003976/1, EPSRC ARCHER e174 project, EC ThermaPOWER project IRSES GA-2011-294905, EPSRC EP/P50550X/1

References

[1] P. Sáenz, K. Sefiane, J. Kim, O. K. Matar, P. Valluri (2015) *Journal of Fluid Mechanics* 772, 705-739.
[2] D. Scott, A. Collis, L Ó Náraigh, P. Spelt, I Bethune, P. Valluri (2015), TPLS2 Solver – Two-phase flows at unprecedented resolution, speed and accuracy http://sourceforge.net/projects/tpls/
[3] P. J.Sáenz, A.W. Wray, Z. Che, O. K. Matar, P. Valluri, J. Kim, K. Sefiane (2017) *Nature Communications*, 8, 14783.

DROPLET SPREADING ON REACTIVE PATTERENED SUBSTRATES IN ROOM TEMPERATURE

Haim Taitelbaum

Department of Physics, Bar-Ilan University, Ramat-Gan, ISRAEL

E-mail: haimt@mail.biu.ac.il

We introduce a reactive-wetting system in room temperature, in which small mercury droplets (150 micron in diameter) spread on thin silver films (thickness 4000 A). Top-view images of the process are obtained using an optical microscope. The kinetic roughening of the advancing triple line is analyzed using scaling concepts and self–affine fractal geometry.

Previous studies showed that the roughness of the silver surface has an effect on the kinetic roughening of the triple line. In order to study this effect systematically, we use lithography to produce silver films with 'holes' or 'channels' patterns in various sizes (order of a few microns) and a given depth (500 A). These patterns represent isotropic and anisotropic surface patterns, respectively. We found that the scaling exponent which describes the lateral roughening of the triple line contour, does not depend on the substrate roughness, and its value is about 0.8 for all silver substrates (smooth surfaces, isotropic and anisotropic rough surfaces). However, the bulk behavior was different for the anisotropic roughness case. The shape of the droplet at the end of the spreading process was mostly round for the smooth and isotropic rough surfaces while for the anisotropic surfaces it was elliptic (the major axis aligned with the channel's direction).

The spreading velocity on the smooth surfaces was about 4 microns/sec, while on the isotropic rough surfaces it was much slower (about 2.3 microns/sec). Interestingly, in the anisotropic rough surfaces, the reaction front moves faster 'inside' the channels than 'outside' them. For spreading in the channel's direction, this behavior produces 'fingers' shape. For spreading perpendicular to the channel's direction, the velocity jumps between two values. These two phenomena were not observed for the 2 micron channel width – which was found to be the lateral correlation length of the triple line at our previous studies. The macroscopic behavior is explained by the different mechanisms that govern the process in various time regimes: at early stages, the diffusion and wetting are affected by the roughness of the surfaces, while at the final stages, the chemical reaction overcomes the roughness patterns, resulting in the same scaling exponent for all systems.

References:

[1] A. Be'er, Y. Lereah, H. Taitelbaum, Physica A 285, 156 (2000)
[2] A. Be'er, Y. Lereah, I. Hecht, H. Taitelbaum, Physica A 302, 297 (2001)
[3] A. Be'er, Y. Lereah, A. Frydman, H. Taitelbaum, Physica A 314, 325 (2002)
[4] A. Be'er, Y. Lereah, J. of Microscopy, 208, 148 (2002)
[5] I. Hecht, H. Taitelbaum, Phys. Rev. E 70, 046307 (2004)
[6] A. Be'er, I. Hecht, H. Taitelbaum, Phys. Rev. E 72, 031606 (2005)
[7] I. Hecht, A. Be'er, H. Taitelbaum, FNL, 5, L319 (2005)
[8] A. Be'er, Y. Lereah, A. Frydman, H. Taitelbaum, Phys. Rev. E 75, 051601 (2007)
[9] A. Be'er, Y. Lereah, H. Taitelbaum, Mater. Sci. Eng. A 495, 102 (2008)
[10] Y. Efraim, H. Taitelbaum, Cent. Eur. J. Phys. 7, 503 (2009)
[11] L. Lin, B.T. Murray, S. Su, Y. Sun, Y. Efraim, H. Taitelbaum, T. J. Singler, J. Phys. Cond. Mat. 21, 464130 (2009)
[12] Y. Efraim, H. Taitelbaum, Phys. Rev. E, 84, 050602(R) (2011)
[13] T. Ya'akov, H. Taitelbaum (preprint)

Figure 1: "Fingers" spreading in patterened channels

Evaporating pure, binary & ternary droplets: thermal effects & axial symmetry breaking

Christian Diddens[1,2], Huanshu Tan[1], Pengyu Lv[1], Michel Versluis[1], J.G.M. Kuerten[2,3], Xuehua Zhang[4,1], Detlef Lohse[1,5]

[1] Physics of Fluids group, Department of Science and Technology, Mesa+ Institute, and J. M. Burgers Centre for Fluid Dynamics, University of Twente, P.O. Box 217, 7500 AE Enschede, The Netherlands
[2] Department of Mechanical Engineering, Eindhoven University of Technology, P.O. Box 513, 5600 MB Eindhoven, The Netherlands
[3] Faculty EEMCS, University of Twente, P.O. Box 217, 7500 AE Enschede, The Netherlands
[4] Soft Matter & Interfaces Group, School of Engineering, RMIT University, Melbourne, VIC 3001, Australia
[5] Max Planck Institute for Dynamics and Self-Organization, 37077 Göttingen, Germany

E-mail: C.Diddens@tue.nl

While the evaporation process of droplets consisting of a pure liquid is mainly understood, multi-component droplets show in general far more complex evolutions during evaporation. This is due to the complicated coupling of multi-component evaporation, flow of the mixture and possibly also thermal effects.
Even for binary mixtures, the presence of the second component can result in non-monotonic contact angle evolutions [1], initial condensation of the less volatile component [2] or entrapped residuals of the more volatile component at later times [2,3]. Furthermore, the flow in the droplet is primarily driven by the solutal Marangoni effect. In particular, it has been shown that water-ethanol droplets exhibit initially chaotic and highly non-axisymmetric flows, followed by a fast transition to nearly axisymmetric flow and outward radial flow towards the end of the lifetime [4,5].
Recently, it has been shown that ternary mixture droplets, as the next more general liquid, can show an even richer evolution process: By investigating the evaporation of an Ouzo drop (ethanol, water and anise oil), we have revealed multiple phase transitions, where the drop temporarily changes its appearance from an initially transparent liquid to a milky-white colored emulsion [6,7]. The reason lies in the so-called Ouzo effect, i.e. the spontaneous emulsification of oil microdroplets once the local ethanol concentration has reduced by preferential evaporation below a specific threshold.

In our work, we subsequently generalize the complexity of the droplet composition from a pure water droplet over a binary water-ethanol droplet to a ternary Ouzo droplet [5].
To investigate the evaporation of these droplets in detail, we have developed an elaborate numerical model based on the finite element method that is able to account for all relevant processes [2,5]. The model determines the evaporation rates of the components by solving the vapor diffusion equations in the gas phase combined with the vapor-liquid equilibrium based on Raoult's law. Since the liquid properties, i.e. the mass density, the viscosity, the surface tension and the diffusivity strongly depend on the composition and the temperature, experimental data for these quantities has been fitted to accurately incorporate the composition- and temperature-dependence into the model. Thereby, the flow in the multi-component droplet is strongy coupled with the spatio-temporally evolving nonhomogeneous liquid composition. Furthermore, thermal effects caused by the latent heat of evaporation are taken into account by considering the coupling of flow and the evaporation with the temperature field.
The numerical results are compared with good agreement with experimental data obtained by image analysis techniques, confocal microscopy and particle image velocimetry (micro-PIV).

We begin our study by discussing the volume evolution and the flow inside the droplet with the aid of an axisymmetric version of the model. While it is shown that convection in the gas phase can be safely neglected, we point out the importance of the substrate thickness on the evaporative cooling and hence on the volume evolution.
As long as ethanol is present in the binary and ternary droplet, the flow in these droplets is chaotic and almost entirely driven by the solutal Marangoni effect. Once ethanol has evaporated, the flow changes to regular thermal Marangoni flow.
The model can also successfully predict the onset of oil nucleation in Ouzo droplets. This is achieved by testing whether the local liquid composition is in the phase separation region, which has been determined by titration experiments. As in the experiments, the nucleation sets in at the rim for Ouzo droplets with contact angles below 90° [6] and at the apex for droplets with contact angles above 90° [7].

To account for the highly non-axisymmetric flow in the binary and ternary droplet, the model is generalized to a full three-dimensionl version. With the framework of this model, we are able to investigate the transition from non-axisymmetric chaotic flow to regular axisymmetric flow by numerical means. Thereby, we are able to directly compare the results of micro-PIV measurements with the numerically obtained flow.

Interestingly, the chaotic regime driven by solutal Marangoni flow is in good agreement, whereas the thermal Marangoni flow of the remaining water droplet is overpredicted by the model. We substantiate that this effect can presumably attributed to contaminations.

Acknowledgements. This work is part of an Industrial Partnership Programme (IPP) of the Foundation for Fundamental Research on Matter (FOM), which is financially supported by the Netherlands Organization for Scientific Research (NWO). This research programme is co-financed by Océ-Technologies B.V., Twente University and Eindhoven University. We also acknowledge the Dutch Organization for Research (NWO) and the Netherlands Center for Multiscale Catalytic Energy Conversion (MCEC) and the Max Planck Center Twente for Complex Fluid Dynamics for financial support. We kindly acknowledge financial support from the China Scholarship Council (CSC, file No. 201406890017).

References

[1] K. Sefiane, L. Tadrist, M. Douglas. Experimental study of evaporating water-ethanol mixture sessile drop: influence of concentration, Int. J. Heat Mass Trans. 46 (23), (2003) 4527–4534.
[2] C. Diddens, Detailed finite element method modeling of evaporating multi-component droplets, (2017), submitted to J. Comp. Phys.
[3] C. Diddens, J. G. M. Kuerten, C. W. M. van der Geld, H. M. A. Wijshoff, Modeling the evaporation of sessile multi-component droplets, J. Colloid Interf. Sci. 487, (2017) 426–436.
[4] J. R. E. Christy, Y. Hamamoto, K. Sefiane, Flow transition within an evaporating binary mixture sessile drop, Phys. Rev. Lett. 106, (2011), 205701.
[5] C. Diddens, H. Tan, P. Lv, M. Versluis, J.G.M. Kuerten, X. Zhang, D. Lohse, (2017), submitted to J. Fluid Mech.
[6] H. Tan, C. Diddens, P. Lv, J. G. M. Kuerten, X. Zhang, D. Lohse, Evaporation-triggered microdroplet nucleation and the four life phases of an evaporating Ouzo drop, Proc. Natl. Acad. Sci. USA 113 (31), (2016), 8642–8647.
[7] H. Tan, C. Diddens, M. Versluis, H.-J. Butt, D. Lohse, X. Zhang, Self-wrapping of an Ouzo drop induced by evaporation on a superamphiphobic surface, (2017), doi:10.1039/c6sm02860h

3rd International Conference on Droplets
University of California Los Angeles, USA, July 24th to 26th, 2017

DROP BOUNCING ON LIQUID FILM: GAS LAYER DYNAMICS

Xiaoyu Tang*[1], Abhishek Saha[1], Chung K. Law[1,2], Chao Sun[2]

[1]Department of Mechanical and Aerospace Engineering, Princeton University, Princeton, NJ, USA
[2]Center for Combustion Energy, Tsinghua University, Beijing, China

*E-mail: xiaoyut@princeton.edu

Drop impact on a wet surface is critical for IC engines where the fuel spray deposition on the engine wall is highly undesirable as it would lead to incomplete combustion and soot. If the impacting surfaces cannot come into close proximity during the impact to activate the surface van der Waals force, and consequently cannot break the thin interfacial gas layer trapped between them, bouncing of the drop results [1-5]. To assess the controlling mechanisms of the transition, it is thus necessary to understand the dynamics of the gas layer. Recently optical techniques [3-7] have been developed to indirectly interpret the microscopic gas layer thickness for drop impact on solid surfaces. Such studies have mostly been concerned with merging outcomes [7-8], while corresponding studies on the morphology of the gas layer for the bouncing outcomes have been few.

Apart from the fluid properties, the critical system parameters that control the impact response are the impact inertia of the drop and the resistance offered by the impacted surface, with the latter depending on the film thickness. Previous studies have been mostly concerned in the limiting situations of either solid surface [2-4, 6] or liquid pool [5, 7]. Less study, however, has been directed to the intermediate situation [8, 9] for which the film thickness is comparable to the drop radius such that the resistance of the restraining surface is closely felt, while the fluid flow within the drop and film, as well as their respective morphologies, are strongly coupled through the interfacial gas layer. As was shown for tetradecane in [9], globally such strong coupling gives rise to non-monotonic bouncing-vs.-merging transitions as the film thickness increases from zero.

The work of [9] is global in nature, mapping out the merging-vs-bouncing boundaries. In this work, we report, a complete temporal characterization of the gas layer dynamics for drop bouncing on liquid surface (same material as the drop) with thickness comparable to the drop radius ($0 < H^* < 3$), using high-speed imaging and color interferometry. Consequently we have succeeded in identifying the roles of the film thickness and the Weber number in controlling the gas layer morphology in different regimes. In particular, we shall show that the presence of a deformable impacted (liquid) surface drastically modifies the shape and evolution of this thin gas layer in that the central "bell" shaped dimple is no longer the only morphological response, as observed previously for the head-on impact on solid surfaces.

The axisymmetric gas layer dynamics will now be discussed in terms of the evolution of center thickness, h_c, and radial profile, $h(r)$, (schematic in Fig. 1a), both of which evolve with time.

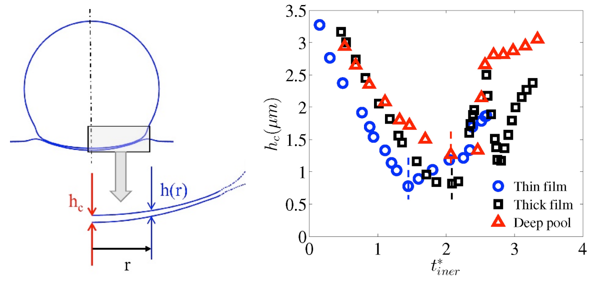

(a) (b)

Figure 1. (a) Schematic of the gas (b) Gas layer center thickness evolution for three different film thicknesses with similar We numbers. The dashed lines indicate the end of approaching stage.

First, we consider the behavior of h_c versus time, normalized by the inertial timescale, 2R/U, in Fig. 1b, which shows two distinct stages of the evolution, namely the approaching stage, when the gap at the center continuously diminishes to reach a minimum point; and the rebounding stage, when the gap increases; here "t=0" represents the instant when the bottom of the drop reaches the location of the unperturbed liquid surface. It is seen that during the approaching stage, for all H^*, h_c decreases linearly with time with almost the same slope, while it decreases with a slower rate for the deep pool. During the rebounding stage, however, the response is dramatically different in that while the rate of increase of h_c is rather steady for the thin film, for the deep pool it first increases rapidly and then slows down substantially. For the thick film, h_c responds non-monotonically by first sharply jumps to a value of 2.5 μm, then immediately reduces to 1 μm, and then increases again within a very short t^*_{iner} increment of about 0.5.

Next we show the instantaneous spatial variation of the gas layer thicknesses (schematic in Fig. 1a) along the normalized radial distance and their evolution for all three conditions in Fig. 2, where the left and right panels respectively indicate the approaching and rebounding stages. It is seen that as the drop approaches close to the liquid surface, it squeezes the interfacial gas layer and hence creates a high-pressure zone, which in turn deforms both the drop and film surfaces and forms a "high-center/low-rim" or a "bell" shaped interfacial gap for the thin film (Fig. 2a). This is analogous to the well-known "dimple" created at the center when a drop impacts a solid surface, although now the interfacial gap for the thin film is formed from the deformation of both the drop and liquid surfaces. Subsequently, the trapped gas layer is gradually squeezed out as the drop further moves down. This is evident from the flattened and even reversed “low-center/high-rim” gas layer profile, with a minimum thickness reaching below 1μm before the rebounding stage begins, recognizing that a typical interfacial gas layer thickness just before merging is about 200 nm. For the deep pool (Fig. 2e), although the shape of the center dimple is maintained, the gas layer profiles are flatter and shorter. Due to the large pool thickness and the diminished constraint from the bottom solid surface, the deformable liquid surface here is more “adaptive” to drop impact, thereby reduces the radial variation in the gap thickness and hence the pressure gradient. The un-restrained deformation in the liquid surface also results in a steeper interface around the drop center (see side-view image of the inset), deflecting the incident light from the bottom away from the camera, making the window of the observable interference pattern smaller. This progressively reduces the extent of the measured profile as the drop penetrates the liquid pool. For the thick film, the gas layer profiles (Fig. 2c) show mixed influence of the deep pool and thin film conditions, in that the profile is flatter due to the “adaptive” nature of the liquid surface and its radial extent increases with time due to spreading against the bottom surface.

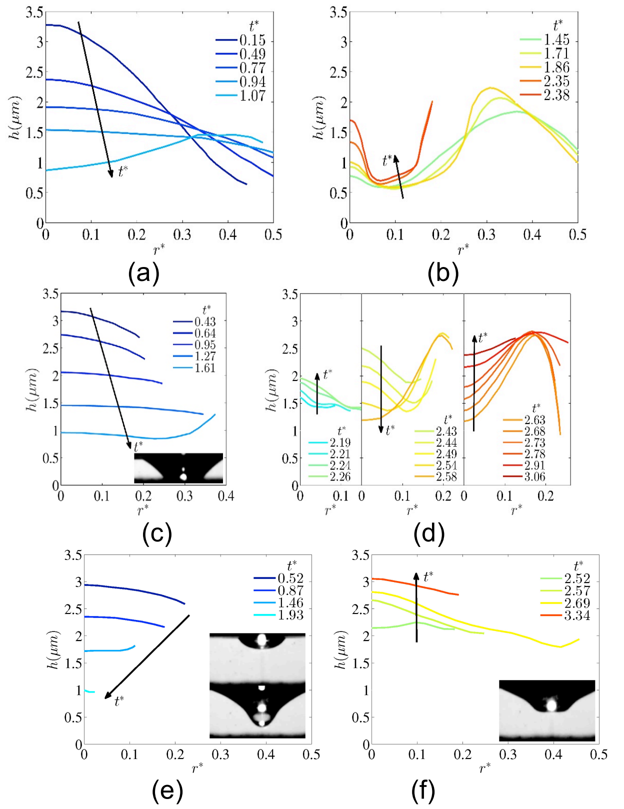

Figure 2. Gas layer profiles at approaching and rebounding stages for three conditions shown in Fig. 2. The profiles are color coded with time. $r^*=r/R$. (a) (b) We=9.91, $H^*=0.12$. (c) (d) We=8.04, $H^*=1.19$. (e) (f) We=9.26, $H^*=2.72$.

During the rebounding stage for the thin film, when the drop as a whole rises upward (Fig. 2b), the center of the gas layer gradually thickens, forming another, albeit much narrower, “bell” shaped profile. At the same time, the rim also thickens forming an “annular dimple”, and is connected to the center dimple with a thin neck (~0.5 μm). Both the dimples at the center and the rim become thicker as the drop moves upward during the rest of the rebounding stage, with the neck moving inward and becoming thicker. Note that the radial extent of the visible interference pattern and thus, measured gas layer thickness, reaches $r^*=0.5$ and hence exceeds those with larger film thicknesses. Mechanistically, deformation of the liquid surface is now largely constrained by the bottom solid surface such that spreading of the drop over the surface closely resembles drop impact on the dry surface. Similarly, for the deep pool (Fig. 2f), the center thickens first but with a flatter profile. The gas layer becomes thicker as the drop leaves the liquid surface without changing its shape. The observable extension is now larger, up to $r^*=0.5$, as compared to the approaching stage because the liquid surface retracts and forms a flat bottom, as shown in the side-view of the inset.

For the thick film, however, evolution of the profiles is markedly different (Fig. 2d). At the beginning of the rebounding stage, the center of the gas layer thickens with the familiar “bell” shaped dimple. It then changes immediately, within 0.28 ms ($t^*=0.7$), as the profile becomes flatter and thinner at the center with a thick rim forming a “reverse bell” shape with the rim being thicker than the center. Finally, with the rim remaining the same, the center starts to become thicker and approaches the thickness of the rim until the drop leaves the liquid surface. The unaltered rim thickness during the latter part of the rebounding stage indicates that shape oscillation of the drop, and relaxation of the stretched/deformed film surface, are perhaps phase matched, and as such they move together near the rim. Such a complex behavior of the gas layer dynamics rises from the interplay of the deformation and relaxation of the drop and film surfaces along with resistance from the solid wall, which is unique for the thick film and absent from drop impact on dry surface.

This work is supported by the Army Research Office and by the Xerox Corporation.

References

[1] A. L. Yarin, Annu. Rev. Fluid Mech. 38 (2016) 159–192.
[2] C. Josserand, S. Thoroddsen, Annu. Rev. Fluid Mech. 48 (2016) 365–391.
[3] J. M. Kolinski, S. M. Rubinstein, S. Mandre, M. P. Brenner, D. A. Weitz, L. Mahadevan, Phys. Rev. Lett. 108 (2012) 0745031-4.
[4] J. de Ruiter, R. Lagraauw, D. van den Ende, & F. Mugele, Nat. Phys. 11 (2015) 48-53.
[5] Y. Couder, E. Fort, C.-H. Gautier, & A. Boudaoud, Phys. Rev. Lett. 94 (2005) 177801.
[6] R. C. van der Veen, T. Tran, D. Lohse, & C. Sun, Phys. Rev. E 85 (2012) 026315.
[7] T. Tran, H. de Maleprade, C. Sun, & D. Lohse, J. Fluids Mech. 726 (2013) R3.
[8] K. L. Pan, C. K. Law, J. Fluids Mech. 587 (2007) 1-22.
[9] X. Tang, A. Saha, C. K. Law, & C. Sun, Soft Matter 12 (2016) 4521-4529.

INVESTIGATING DROPLET INTERNAL FLOW IN CONCENTRATED EMULSION WHEN FLOWING IN MICROFLUIDICS CHANNEL USING MICRO-PIV

Chia Min Leong[*], Ya Gai[**], and Sindy K. Y. Tang[*]
[*]*Department of Mechanical Engineering, Stanford University, CA*
[**]*Department of Aeronautics and Astronautics, Stanford University, CA*

E-mail: ygai@stanford.edu

Droplet microfluidics has enabled a wide variety of high throughput applications through the use of monodisperse droplets.[1,2] Previous fluid studies of droplet microfluidics have focused on single drops or emulsions at low volume fractions.[3,4] The study of concentrated emulsions at high volume fractions is important for increasing the throughput, but the fluid dynamics of such emulsions in confined channels is not well understood.

Here we describe two-dimensional, mid-height measurements of the flow inside individual drops within a concentrated emulsion using micro-PIV. To our best knowledge, no work has probed the flow field inside droplets of concentrated emulsions at high volume fractions in confined channels.

We generated droplets using a flow-focusing device fabricated in poly(dimethylsiloxane) (PDMS). In all our experiments, the droplet volume was 90 pL with a volume dispersity of < 3%.The emulsion has 85% volume fraction and flows as a monolayer in a straight microfluidic channel. We built an in-house μPIV system[5] to probe the flow by combining a green laser, a Phantom fast camera, and an inverted microscope.

The effects of confinement and viscosity ratio on the internal flow patterns inside the drops were studied. The results show rotational structures inside the drops always exist, and are independent of viscosity ratio for the conditions tested. The structures depend on droplet mobility which in turn, depends on the confinement of the emulsion and the location of the drops in the channel. Our results imply that the degree of mixing could differ in droplets within a concentrated emulsion depending on the size of the drops relative to the size of the channel, as well as the position of the drops in the channel.

Current work is in progress to measure the three-dimensional flow field in such system, as well as the effects of other parameters including capillary number, the volume fraction of the emulsion and the choice of the surfactant.

Acknowledgements. We acknowledge support from the National Science Foundation through the NSF CAREER Award No. 1454542. S. T. acknowledges additional support from the 3M Untenured Faculty Award and the Stanford Woods Institute for the Environment.

Reference

1 Rosenfeld, L., Lin, T., Derda, R. & Tang, S. K. Review and analysis of performance metrics of droplet microfluidics systems. *Microfluid Nanofluidics* **16**, 921-939 (2014).

2 Guo, M. T., Rotem, A., Heyman, J. A. & Weitz, D. A. Droplet microfluidics for high-throughput biological assays. *Lab Chip* **12**, 2146-2155 (2012).

3 Oishi, M., Kinoshita, H., Fujii, T. & Oshima, M. Simultaneous measurement of internal and surrounding flows of a moving droplet using multicolour confocal micro-particle image velocimetry (micro-PIV). *Meas. Sci. Technol.* **22**, 105401 (2011).

4 Ma, S., Sherwood, J. M., Huck, W. T. & Balabani, S. On the flow topology inside droplets moving in rectangular microchannels. *Lab Chip* **14**, 3611-3620 (2014).

5 Santiago, J. G., Wereley, S. T., Meinhart, C. D., Beebe, D. & Adrian, R. J. A particle image velocimetry system for microfluidics. *Exp. Fluids* **25**, 316-319 (1998).

PERIODIC DISLOCATION DYNAMICS IN TWO-DIMENSIONAL CONCENTRATED EMULSION FLOWING IN A TAPERED MICROCHANNEL

Ya Gai[*], Chia Min Leong[**], Wei Cai[**], and Sindy K. Y. Tang[**]
[*]*Department of Aeronautics and Astronautics, Stanford University, CA*
[**]*Department of Mechanical Engineering, Stanford University, CA*

E-mail: ygai@stanford.edu

Droplet microfluidics has been shown as a strong candidate for high-throughput applications.[1-3] Tapered microchannel was often integrated in many high-throughput on-chip devices to enforce droplets passing through interrogation region in a serial manner.[4,5] Despite the wide use of tapered microchannel, the dynamics of how drops flow and rearrange in such geometry has not yet been characterized.

In this work, we report a surprising order in concentrated emulsion when flowing as a monolayer in a tapered microfluidic channel. Our results could find practical use in the design of flow control systems for effective on-chip droplet manipulations such as mixing and incubation.[6] In addition, our results are helpful in understanding shaping and material forming of confined low-dimensional crystal materials.

We used a flow-focusing nozzle to generate monodisperse 50-pL droplets which were concentrated to form an emulsion with a volume fraction ~85%. We reinjected the emulsion into a microchannel using a pressure pump. The channel height was less than one droplet diameter. Droplets thus flowed as a 2D monolayer. We recorded movies of the drops flowing in the microchannel using an inverted optical microscope and a high-speed camera (Phantom v7.3). We used custom Matlab scripts to track the position and the shape of all drops in each frame.

At sufficiently slow flow rates, the drops arrange into a hexagonal lattice. At a given x-position, the time-averaged droplet velocities are uniform. The instantaneous drop velocities, however, reveal a different, wave-like pattern. Within the rearrangement zone where the number of rows of drops decreases from N to N-1, there is always a drop moved faster than the others. Close examination reveals the anomalous velocity profile arises from a series of dislocations that are both spatial and temporal periodic. To our knowledge, such reproducible dislocation motion has not been reported before.

Our results are useful in novel flow control and mixing strategies in droplet microfluidics as well as modeling crystal plasticity in low-dimensional nanomaterials.

Acknowledgements. We acknowledge support from the National Science Foundation through the NSF CAREER Award No. 1454542. We also acknowledge additional support from the 3M Untenured Faculty Award, the Stanford Woods Institute for the Environment, Office of Science, Office of Basic Energy Sciences, of the U.S. Department of Energy under contract No. DE-SC0010412.

Reference

1 Rosenfeld, L., Lin, T., Derda, R. & Tang, S. K. Review and analysis of performance metrics of droplet microfluidics systems. *Microfluid Nanofluidics* **16**, 921-939 (2014).

2 Agresti, J. J. *et al.* Ultrahigh-throughput screening in drop-based microfluidics for directed evolution. *Proc. Natl. Acad. Sci. USA* **107**, 4004-4009 (2010).

3 Brouzes, E. *et al.* Droplet microfluidic technology for single-cell high-throughput screening. *Proc. Natl. Acad. Sci. USA* **106**, 14195-14200 (2009).

4 Guo, M. T., Rotem, A., Heyman, J. A. & Weitz, D. A. Droplet microfluidics for high-throughput biological assays. *Lab Chip* **12**, 2146-2155 (2012).

5 Gai, Y., Khor, J. W. & Tang, S. K. Confinement and viscosity ratio effect on droplet break-up in a concentrated emulsion flowing through a narrow constriction. *Lab Chip* (2016).

6 Mary, P., Abate, A. R., Agresti, J. J. & Weitz, D. A. Controlling droplet incubation using close-packed plug flow. *Biomicrofluidics* **5**, 024101 (2011).

Dynamics of the evaporation of completely wetting drops on geometrically textured surfaces

Loucine Mekhitarian, Benjamin Sobac, Sam Dehaeck, Benoit Haut, Pierre Colinet

TIPs – Fluid Physics, Université libre de Bruxelles, Brussels, Belgium

E-mail: bsobac@ulb.ac.be

Introduction. Evaporation of sessile drops remains a topic of active research nowadays, not only due to its widespread occurrence both in nature and technology, but also because it raises a number of interesting fundamental questions. Among these, the influence of the substrate topography is far from being understood. While the wetting dynamics of drops on textured substrates has already been studied [1] (in particular it is known that the drop shape typically tends to adopt the symmetry of the pattern it lies upon [2] and that in some cases, a central drop could appear on the top of a liquid film remaining between pillars [3]), the influence the texture has on the evaporation dynamics (including the influence of pinning) has not yet received much attention. In this presentation, we focus on the evaporation dynamics of completely wetting and highly volatile drops on substrates with controlled geometrical heterogeneities and analyze the influence of geometrical parameters of the textured surface on the shape and the dynamics of evaporation of the drop.

Methods. The experiment consists in gently depositing a millimetric drop on a geometrically textured but chemically homogeneous surface and characterizing its evaporation with a standard Mach–Zehnder interferometer.

The geometrically textured surfaces considered are composed of a square array of circular micropillars of SU-8 resin erected by photolithography on sapphire wafers (previously covered by a thin layer of SU-8 resin). Such an array of micropillars is illustrated in fig.1(a). A parametric study is realized by varying the height h_p and the radius r_p of the micropillars such that 0 µm < h_p < 40 µm and 20 µm < r_p < 100 µm, respectively. The pitch distance d between the micropillars is kept constant at 320 µm in all the experiments. The liquid used is HFE-7100, which has the properties to be highly volatile and completely wetting.

The images obtained (see fig.1(b-c)) are analyzed thanks to a wavelets-based image analysis method, detailed in [4], which allows measuring the evolution of the contact angle (local slope), the volume and the wetting surface (and so the equivalent wetting radius R_T) of the drop during the evaporation. For some values of the geometrical parameters, the drop adopts a shape composed of a film invading the surface texture with a central spherical cap sitting upon this liquid film (see fig.1(c)). In this situation, the image processing is also able to provide the radius (R) and the inflection angle of the central spherical cap.

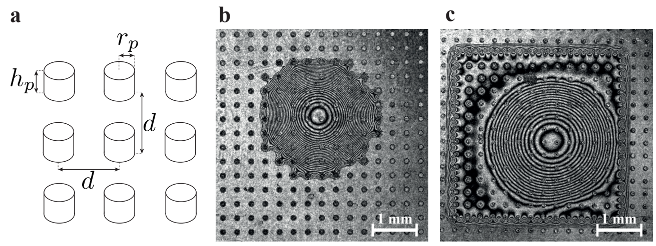

Figure 1 (a) Schematic representation of a square array of circular pillars. (b-c) Images obtained by interferometry for two HFE-7100 drops evaporating on geometrically textured surfaces whose dimensions of the pillars (d, h_p and r_p) are (b) 320 µm, 15 µm, 60 µm and (c) 320 µm, 30 µm, 60 µm, respectively.

In parallel, a mathematical 2D modelling of the evaporation of a liquid drop deposited on a geometrically textured surface was developed. The drop is assumed to be axisymmetric and to evaporate quasi-steadily. In this system, the transport of the liquid is induced by two mechanisms: the evaporation of the liquid and the imbibition of the liquid inside the surface texture by capillary pumping. This problem highlights a dimensionless number F, revealing the competition between the receding of the drop resulting from the evaporation rate and the spreading of the drop resulting from the capillary forces. The order of magnitude of the value of F allows to predict the behavior of the triple line during the evaporation.

Results and discussion. Figure 2 represents the dimensionless evolutions of the characteristic radii (R and R_T) of drops evaporating on geometrically textured surfaces characterized by various dimensions of the pillars. The experimental results show two evaporation regimes, depending on the dimensions of the pillars. These two regimes are also found thanks to the theoretical simulations.

When deposited on a geometrically textured surface with small (in our experiments) pillars, the drop adopts an almost central spherical cap shape (see fig.1(b)), similarly to the one on a flat surface. Classically, R_T decreases over time until the complete disappearance of the drop (see fig.2(a)), following an evaporation law similar to the one of a drop evaporating on a flat surface (R^2-law). This regime is well simulated by the model for small values of F, highlighting that the receding of the triple line due to evaporation seems to widely dominate the spreading of the drop due to capillary forces. This regime is thus called the evaporation-dominated regime.

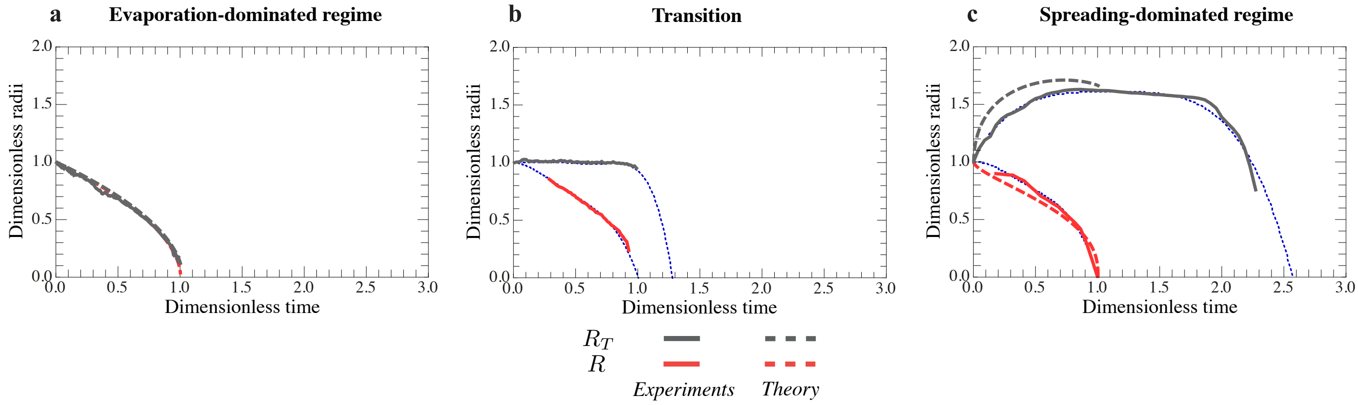

Figure 2 Experimental and theoretical evolutions, as a function of the dimensionless time, of the dimensionless radii of a HFE-7100 drop evaporating at room temperature on a geometrically textured surface (a) in an evaporation-dominated regime, (c) in a spreading-dominated regime and (b) at the transition. For the experimental results, the dimensions of the pillars (d, hp and rp) are (a) 320 µm, 5 µm and 30 µm, (b) 320 µm, 20 µm and 50 µm and (c) 320 µm, 30 µm and 70 µm, respectively. Note that the theoretical model, here fitted to the experiments, allows simulating the evolutions of the characteristic radii R and R_T in the two regimes as long as $R > 0$. The blue dotted lines (b,c) show the expected total experimental radii evolutions and indicate the lifetime of the drops.

When deposited on a geometrically textured surface with large (in our experiments) pillars, the drop adopts a more complex shape composed of a central spherical cap sitting upon a liquid film invading the surface texture (see fig.1(c)). The triple line follows the direction of the rows of pillars, leading to a wetting area faceted as a square, as already shown by [2]. The typical evolutions of R and R_T during the evaporation of a drop deposited on an array of such pillars is shown in fig.2(c). At the beginning, this regime is characterized by the continuous spreading of the drop while R decreases. Then, the drop becomes a film evaporating with a pinned triple line before depinning and completely disappearing. This regime is well simulated by the model for large values of F, highlighting that the spreading of the drop due to capillary forces seems to widely dominate the receding of the triple line due to evaporation. Hence, this regime is called the spreading-dominated regime.

When deposited on a geometrically textured surface with pillars of intermediate size (in our experiments), the shape of the drop is identical to the previous situation (see fig.1(c)). The difference with the spreading-dominated regime lies in the fact that, in this case, the triple line is pinned even during the disappearance of the central spherical cap (i.e. R_T is constant while R decreases, see fig.2(b)). The pinning effect is not included in the model. Therefore, this behavior could only be simulated by the model by artificially taking R_T as constant during the decrease of R. Experimentally, pinning turns out to occur when the spreading of the drop due to capillary forces roughly balances the receding of the triple line due to evaporation. This behavior is thus obtained at the transition between the two regimes, corresponding to a certain critical value of F.

Several scaling laws on R and R_T are obtained according to these regimes, in agreement with the mathematical model.

A phase diagram representation of the two regimes of evaporation of a drop deposited on a textured surface, according to the dimensionless radius of the pillars texturing the surface (r_p/d) and their dimensionless height (h_p/d) is proposed. It highlights that the height of the pillars has a bigger influence on the regime of evaporation than their radius.

Acknowledgements. We acknowledge the master students M. Flandroy and V. Schmidt for their preliminary works on this topic, and BELSPO (IAP 7/38 Micro-MAST project), ESA-BELSPO (PRODEX Evaporation Project) and the Fonds de la Recherche Scientifique - FNRS for their financial support.

References

[1] D. Quéré. Wetting and roughness. Annual Review of Materials Research 38(1) (2008) 71—99.
[2] L. Courbin, E. Denieul, E. Dressaire, M. Roper, A. Ajdari, H.A. Stone. Imbibition by polygonal spreading on microdecorated surfaces. Nature Materials 6(9) (2007) 661—664.
[3] J. Bico, U. Thiele, D. Quéré. Wetting of textured surfaces. Colloids and Surfaces A: Physicochemical and Engineering Aspects 206(13) (2002) 41—46.
[4] S. Dehaeck, Y. Tsoumpas, P. Colinet. Analyzing closed-fringe images using two-dimensional Fan wavelets. Applied Optics 54(10) (2015) 2939—2952.

ELECTRODEPOSITION OF SUPERHYDROPHOBIC AND SUPEROLEOPHOBIC THICK LAYERS

Barbora Pijáková[1], Milan Alberti[1], Vilma Buršíková[1], Miloš Klíma[1]

[1]Department of Physical Electronics, Masaryk University, 267/2 Kotlářská, Brno CZ-61137, Czech Republic

E-mail: barbora.pijakova@mail.muni.cz

Problematics of liquid repellent surface production is widely spread in recent research projects. Numerous aspects, such structure in micro and nano scale, chemical composition and environmental conditions are crucial for preservation of lyophobic property state [1].
Main ways to produce such a surface is to create the suitable structure, followed by chemical modification to enhance the lyophobic properties. For production of superhydrophobic and superoleophobic surfaces, immersion in fluorinated reagent is frequently used [2]. This approach has typical use for metals [3]. Another possibility is reaction of fluorinated precursor directly with metal [4].

Our main goal was to incorporate production of superhydrophobic and superoleophobic surface in time-saving one-step modification of stainless steel substrate. In comparison with published modifications, we chose aqueous solution of fluorinated precursor as an electrolyte. No additional agents were necessary to produce the surface with contact angle ≥150° for water and olive oil.

Optimization of electrolysis by variation of applied voltage, deposition time and solution concentration lead to operative parameters U = 5V; t = 20 min and 0.045 M perfluorooctanoic acid (PFOA) aqeous solution (deionized water).

Surface energy evaluation (SEE) System (Advex Instruments) enabled easy calculation of contact angles (CAs) for various liquids. Implementation of six liquid Owens-Wendt model was used for surface free energy determination. The droplet volume was 2.5 μl. Resulting layer exhibited water CA 159±2°, olive oil CA 153±3° and surface free energy 0.60 mJ/m^2 respectively (Fig. 1). The values were averaged from 10 measurements. Combination of Peltieri element, IR thermometer and SEE System allowed to record the change of CA during varying temperature and observe the freezing procedure.

Confocal microscope Olympus LEXT OLS4000 and scanning electron microscope Tescan MIRA3 imaged macroscopic and microscopic topography of surface.

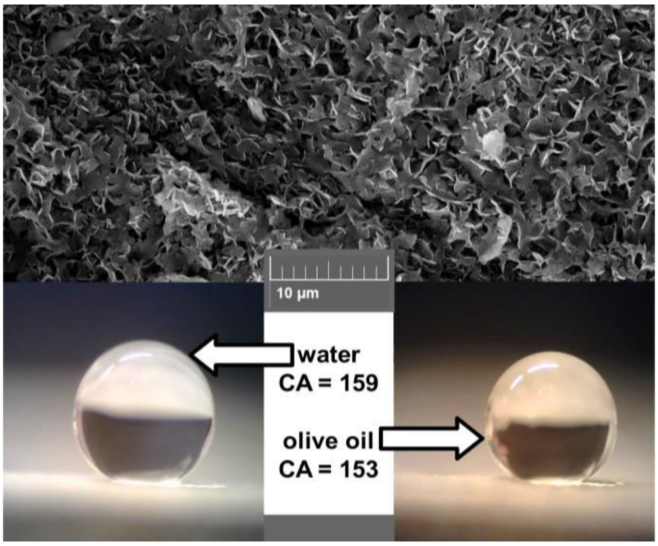

Fig. 1: Topography (SEM; SE detector, mag. 5kx) and CA values for deionized water and olive oil droplets (2.5 μl)

Produced layer consisted of plate-shaped formation analogous to products prepared on zinc [4] (Fig.1). Optimized working conditions eliminated the appearance of macroscopic crackles in layer.

Tribological testing realized by Hysitron TI950 and Fisherscope H100 nanoindenters provided data for hardness up to 3 MPa and elastic modulus up 1 GPa. Revetest Xpress plus scratch tester confirmed dominant plastic deformation for penetration depths exceeding the film thickness. Indicated friction coefficient was ranging from 0.1 to 0.25.

Chemical composition estimated by SEM-EDX mapping confirmed reasonable amount of fluorine from PFOA, inducing the oil repellency [2]. FTIR spectrometer Bruker vertex 80v with ATR plate measured reflectance spectra. Indicated bands at 1681 and 1448 cm^{-1} reffered to carboxylate groups (COO^-) whereas bands at 1201 and 1143 cm^{-1} allocated to fluorine content ($-CF_2$). Presence of COO^- and $-CF_2$ groups can be interpreted as production of PFOA salt during the deposition, similarly as in [4].

For corrosion resistance or propagation observation, norm-referenced neutral salt spray corrosion test was carried out for 1000 hours according CSN EN ISO 9227 NSS with no evidence for corrosion product generation.

To summarize the experiment, preparation of water and oil repellent layer on stainless steel substrate was demonstrated by short electrodeposition. Averaged values for water and olive oil contact angle were 159±2° and 153±3° with calculated surface free energy 0.60 mJ/m^2. Electrolyte consisted of dissolved perfluorooctanoic acid in deionized water. Applying of 5V for 20 min resulted in production of soft plate-shaped formations with hardness up to 3 MPa, elastic modulus up to 1 GPa and friction coefficient ranging from 0.1 to 0.25. Chemical analysis of layer confirmed the production of carboxylate and significant amount of fluorine.

Acknowledgements.
This work was supported by Masaryk University, project number TACR TE02000011 funded by Technology Agency of Czech Republic, project number CZ.1.05/2.1.00/03.0086 funded by European Regional Development Fund and project LO1411(NPU I) funded by Ministry of Education Youth and Sports of Czech Republic. Authors would like to thank Synpo, a.s. for corrosion testing.

References

[1] E. Boromashenko, Progress in understanding wetting transitions on rough surfaces, Advances in Colloid and Interface Science 222 (2015) 92–103, http://dx.doi.org/10.1016/j.cis.2014.02.009

[2] T. Jiang, Z. Guo, W. Liu, Biomimetic superoleophobic surfaces: focusing on their fabrication and applications, J. Mater. Chem. A 3 (2015) 1811–1827, http://dx.doi.org/10.1039/C4TA05582A.

[3] N. Valipour Motlagh, J. Sargolzaei, N. Shahtahmassebi, Super-liquid-repellent coating on the carbon steel surface, Surf. Coat. Technol. 235 (2013) 241–249,
http://dx.doi.org/10.1016/j.surfcoat.2013.07.039.

[4] H. Meng, S. Wang, J. Xi, Z. Tang, L. Jiang, Facile means of preparing super-amphiphobic surfaces on common engineering metals, J. Phys. Chem. C. 112 (2008)11454–11458,
http://dx.doi.org/10.1021/jp803027w.

MAGNETOPHORETIC INTERACTION OF A PAIR OF FERROFLUID DROPLETS IN A ROTATING MAGNETIC FIELD

Mingfeng Qiu[1], Shahriar Afkhami[2], Ching-Yao Chen[3], James J. Feng[1,4]

[1]Department of Mathematics, University of British Columbia, Vancouver, BC, Canada
[2]Department of Mathematical Sciences, New Jersey Institute of Technology, Newark, NJ, USA
[3]Department of Mechanical Engineering, National Chiao Tung University, Hsinchu, Taiwan, ROC
[4] Department of Chemical and Biological Engineering, University of British Columbia, Vancouver, BC, Canada

E-mail: mqiu@math.ubc.ca

INTRODUCTION

A ferrofluid is a stable suspension of magnetic nano-particles in a suitable carrier fluid. The ultra-fine particles and the colloidal stability make the ferrofluid behave as a homogeneous medium, while displaying a variety of novel phenomena under an external magnetic field. In the past decades, thorough knowledge on a single droplet under the influence of a rotating field has been obtained, e.g. [1-2]. It is well known that when the driving frequency is low, a droplet is going to elongate and rotate with the field with or without a phase lag depending on the driving frequency and other parameters. In a high-frequency field, the droplet will display starfish-like patterns. However, the interaction of multiple droplets has received much less attention. Recent experiments have discovered several modes of pairwise interaction in a rotating magnetic field of low frequency [3], the most intriguing of which is the so-called planetary motion. It consists of the self-spin of individual droplets in phase with the driving field, and the global revolution of the droplet pair around each other with a phase lag from the rotating field. In this study, we explore such droplet interactions using direct numerical simulations.

METHODOLOGY

The computational setup is such that a pair of ferrofluid droplets are suspended in a viscous medium in a large square container. The flow field is governed by the Navier-Stokes equations for incompressible two-phase flow:

$$\partial_i v_i = 0,$$

$$\rho(\partial_t v_i + v_j \partial_j v_i) = -\partial_i p + \partial_j(2\eta D_{ji}) + \sigma\kappa n_i \delta_s + \partial_j \tau_{ji},$$

where η is the viscosity and D_{ji} is the rate of deformation tensor. σ is the surface tension coefficient between ferrofluid and the surrounding medium. κ represents the curvature, n_j the outer normal vector to the interface, and δ_s the Dirac delta function that is concentrated on the interface. τ_{ji} is the Maxwell stress tensor, which is determined by the local magnetic field strength vector H_i through

$$\tau_{ji} = \mu HjHi - (\mu/2)H^2 I_{ji}.$$

μ is the magnetic permeability of the material. For simplicity we only consider linear magnetization of the ferrofluid. As a magnetostatic problem, the field strength $H_i = -\partial_i \varphi$ for some magnetic potential φ, and φ is governed by a Laplace equation. Boundary conditions are of the standard type on the interface between the ferrofluid and the medium. Here we note two crucial dimensionless parameters: the magnetic Bond number Bo_m which represents the ratio of magnetic forces and surface tension, and the dimensionless driving field frequency *f*.

A Volume-Of-Fluid (VOF) formalism is used to compute the interfacial dynamics. An open source software Gerris is employed [4]. The package features adaptive mesh refinement on a structured quad-/oct-tree grid and an accurate computation of the surface tension. The calculation is done in 2D due to the high computational cost for 3D problems.

RESULTS

Direct simulations have reproduced the key features of the experiments. Overall, there are four modes of motion depending on the initial droplet separation D_0: i) negligible interaction for very large D_0; ii) planetary motion for intermediate D_0; iii) locked rotation for closer D_0; iv) coalescence for even smaller D_0.

In the planetary motion regime, the center of mass of droplets oscillates in both the radial and azimuthal directions. The frequency of the oscillations is approximately double the driving frequency *f*. This is because the driving field rotates much faster than the droplet pair, and the phase lag between the pair and the rotating field changes with a period of about half that of the field. This agrees well with the experimental observations. Eventually the drop separation settles into an oscillation around a “terminal separation” *D*, which depends on the driving frequency *f* but not the initial separation D_0.

When the magnetic Bond number Bo_m is reduced, indicating an increase in surface tension and thus a more rounded shape of the droplets, the radial motion of the droplets is hardly affected, which suggests little change in the magnetic force. However, the angular velocity of the pair’s revolution drastically decreases. This implies that the viscous sweeping induced by the deformed droplets accounts significantly for the angular velocity of the pair. The hydrodynamic interaction is also more dominant at higher driving frequency *f*, leading to higher angular velocity. This phenomenon forms a contrast to the situation of rigid magnetized circular particles in a rotating field. In the latter case, the angular velocity of the pair is purely due to the magnetic torque, and decreases with increasing driving frequency *f* [5].

Besides planetary motion, a droplet-locking regime is discovered under certain operating parameters. When the droplets start with a small initial separation D_0 and aligned with the external field, the viscous drag on the droplets are not strong enough to prevent them from being attracted together by the magnetic force. In the locking regime, individual droplets stick together and rotate in phase with the driving field, while maintaining a thin film between them. Typically this leads to coalescence in time. If the initial separation is even smaller, coalescence occurs outright without going through the locked rotation episode.

Acknowledgements. This study has been supported by the University of British Columbia Four-Year Doctoral Fellowship and the Texas Advanced Computing Center under the XSEDE program.

References

[1] J.-C. Bacri, A. Cebers, R. Perzynski. *Physical Review Letters*, (1994) **72** (17), 2705-2708.
[2] S. Afkhami, A.J. Tyler, Y. Renardy, M. Renardy, T.G. St. Pierre, R.C. Woodward, J.S. Riffle. *Journal of Fluid Mechanics,* (2010) **663**, 358-384.
[3] C.-Y. Chen, H.-C. Hsueh, S.-Y. Wang, Y.-H. Li. *Microfluidics and Nanofluidics*, (2015) **18**, 795-806.
[4] http://gfs.sourceforge.net/wiki/index.php/Main_Page.
[5] G. Helgesen, P. Pieranski, A.T. Skjeltorp. *Physical Review A*, (1990) **42** (12), 7271-7280.

Resolving the Viscosity and Surface Tension of Droplets using Aerosol Optical Tweezers

Jim S. Walker, Bryan R. Bzdek, Young C. Song, Jonathan P. Reid

School of Chemistry, University of Bristol, UK

E-mail: jim.walker@bris.ac.uk

Aerosol optical tweezers (AOT) can be used to isolate individual picolitre volume droplets (3-10µm radius) and study important physicochemical properties in a controlled environment and over a wide range of timescales. Radius, refractive index and chemical composition can be routinely monitored using cavity enhanced Raman spectroscopy (CERS) as the trapped droplet is subjected to environmental and chemical changes. Previous work has shown that this capability enables accurate measurements of vapour pressure, mixing state and hygroscopicity. This contribution will discuss recent advances to directly measure the droplet surface tension and viscosity through coalescence of two optically trapped droplets. Knowledge of both surface tension and viscosity are of key relevance to a range of industrial and atmospheric processes such as spray drying, inkjet printing, cloud droplet activation, semivolatile partitioning, and chemical aging, and also are required to understand droplet dynamics more generally.

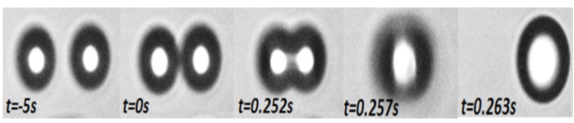

Figure 1. Example binary coalescence process for 2 glucose droplets at 55% RH.

In a coalescence experiment, two droplets are captured in neighbouring optical traps, equilibrated to a desired relative humidity (RH), and coalesced through manipulation of the relative trap positions (Figure 1). The moment of coalescence is captured using high frame-rate imaging as well as elastically backscattered laser light recorded with a photodiode (Figure 2).

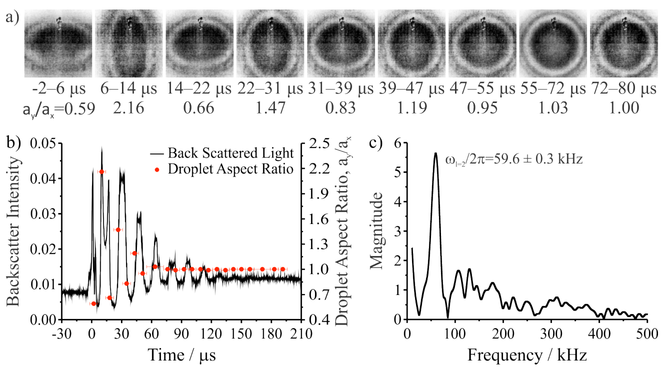

Figure 2. Morphology analysis of the composite droplet following the coalescence of two low-viscosity surfactant coated aqueous droplets. a) is imaging with a camera, b) elastically backscattered light from a photodiode and c) frequency of oscillatory modes in the backscattered light signal.

Viscosity is determined by measuring the characteristic relaxation time (µs to days) as the final composite droplet returns to a spherical morphology under the influence of capillary forces. The fast relaxation dynamics of low viscosity droplets are probed using the elastically scattered light signal whilst the aspect ratio of the droplet image is used for slow coalescence / high viscosity systems. In cases where coalescence is very slow, the relaxation time is monitored through the disappearance (loss of sphericity) and subsequent reappearance (return of sphericity) of whispering gallery modes in a Raman spectrum.

Using this approach we report viscosity measurements from a wide range of binary (organic + water) systems containing alcohols, saccharides and carboxylic acids and with measured viscosities covering 13 orders of magnitude (10^{-3} to 10^{10} Pa s). Example viscosity measurements are shown in Figure 3. These data compare well with bulk-phase studies, where bulk measurements are possible, and are used to test various viscosity prediction models.

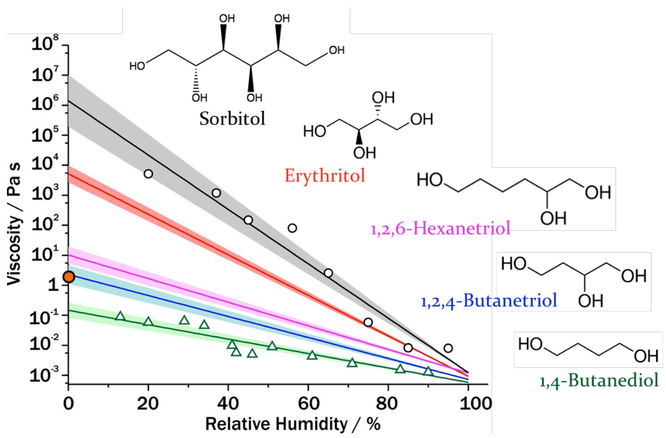

Figure 3. Viscosity measurements for droplets containing a range of water + organic combinations and covering the full range in RH.

In addition, for low viscosity droplets, the surface tension can be measured from the frequency of damped surface oscillations following coalescence, which are observed as fluctuations in the time-resolved elastic scattering signal (Figure 2b & 2c).

The surface tensions of mixed component droplets (e.g. mixtures of NaCl and glutaric acid in differing mass ratios) were measured across the entire range of RH (including beyond the solubility limit) and compared to a model of surface tension. Experimental values agree well with bulk values where possible and validate existing models that predict the surface tension of supersaturated droplets. Moreover, trapped droplets were exposed to air, and the time-dependent changes to surface tension was monitored. Surface tension was observed to rapidly decrease to a value consistent with surfactant coated droplets regardless of the initial bulk composition. This observation suggests that the surface tension of atmospheric aerosol, a key parameter that defines the number of cloud droplets in climate models, is likely consistent with a surfactant coated surface rather than pure water, which is currently assumed in models. More recent work has provided the first measurements of surfactant coated picolitre droplets. These experiments indicate that due to the high surface/volume ratio and very small volumes in aerosols, partitioning of surfactant to the surface results in depletion of that surfactant from the bulk. This disagreement with bulk measurements can be quantified and modelled.

Acknowledgements
We acknowledge EPSRC and NERC for funding.

References

[1] R.M. Power, S.H. Simpson, J.P. Reid, A.J. Hudson, 'The Transition from Liquid to Solid-Like Behaviour in Ultrahigh Viscosity Aerosol Particles', Chemical Science 4 (2013) (6) 2597-2604.
[2] Y.C. Song, A.E. Haddrell, B.R. Bzdek, J.P. Reid, T. Bannan, D.O. Topping, C. Percival and C. Cai, 'Measurements and Predictions of Binary Component Aerosol Particle Viscosity', J. Phys. Chem. A 120 (2016) 8123-8137.
[3] B.R. Bzdek, R.M. Power, S.H. Simpson, J.P. Reid and C.P. Royall, 'Precise, contactless measurements of the surface tension of picolitre aerosol droplets', Chemical Science 7 (2016) 274-285

TESTING THE PERFORMANCE OF ALUMINIUM SUPERHYDROPHOBIC SURFACES

Miguel Cabrerizo-Vilchez, F.J. Montes Ruiz-Cabello, P. Ibáñez-Ibáñez, Miguel Ángel Rodríguez-Valverde

Biocolloid and Fluid Physics Group, Applied Physics Department, Faculty of Sciences, University of Granada, Campus de Fuentenueva s/n, 18071, Granada, Spain

E-mail: mcabre@ugr.es

Superhydrophobic (SH) are surfaces with the apparent ability to repeal liquids. Appart from the evident utilities attributed to SH surfaces (water-proofing or self-cleaning), SH surfaces may have other interesting applications: drag reduction, anti-biofouling, anti-icing, condensation delay, etc. However it is not clear and it is a source of discussion and controversy which factors influence the better or worse performance of SH surfaces when thay are used for the above mentioned purposes [1, 2]. Potential differences between SH surfaces are not easily captured by the conventional methods used to characterize the wetting properties. The main reason is that contact angle of SH is hardly measurable with accuracy [3]. For this reason, it is currently demanded a tool for validating SH surfaces further than the analysis of water contact angles.

In this work, we show a new strategy to validate the performance of different superhydrophobic (SH) surfaces fabricated on aluminium substrates. These surfaces were produced using acid etching and a further hydrophobization using hydrophobic films of fluropolymer, siliconation by PDMS, or silanization.

The validation of the produced SH surfaces was carried out using a combination of standard goniometry methods, that served to identify a surface as SH, and a novel methodology focused on the analysis of bouncing drop dynamics using a high speed camera [4].
The aim was to show that the standard methods for testing the wetting properties of SH surfaces are hardly able to differenciate between different SH surfaces. In contrast, the analysis performed with bouncing drops reported differences more pronounced than the one obtained by contact angle measurements. We connected these differences in the wetting properties with the efficiency of the surfaces in delaying condensation. This property was characterized by the interpretation of ESEM images acquired under saturating conditions. Since all the created surfaces were textured in the same way, the reported differences were attributed to the different surface energy of the hydrophobizating agent and a different degree of coverage, estimated from elemental chemical analysis using XPS.

Acknowledgements. This research was supported by the projects: MAT2014-60615R funded by MINECO, and P12-FQM-1443 funded by “Junta de Andalucía”,

References

[1] S. Jung, M. Dorrestijn, D. Raps, A. Das, C.M. Megaridis, D. Poulikakos, Are Superhydrophobic Surfaces Best for Icephobicity?, Langmuir, 27 (2011) 3059-3066.
[2] R. Enright, N. Miljkovic, A. Al-Obeidi, C.V. Thompson, E.N. Wang, Condensation on Superhydrophobic Surfaces: The Role of Local Energy Barriers and Structure Length Scale, Langmuir, 28 (2012) 14424-14432.
[3] Y.-L. Hung, Y.-Y. Chang, M.-J. Wang, S.-Y. Lin, A simple method for measuring the superhydrophobic contact angle with high accuracy, Review of Scientific Instruments, 81 (2010) 065105.
[4] Y.C. Jung, B. Bhushan, Dynamic Effects of Bouncing Water Droplets on Superhydrophobic Surfaces, Langmuir, 24 (2008) 6262-6269.

Three-dimensional simulations in droplet-based microfluidics: Investigation of drop generation, breakup and flow resistance

Mehdi Nekouei, Siva Vanapalli*

Department of Chemical Engineering, Texas Tech University, Lubbock, TX, USA

*E-mail: siva.vanapalli@ttu.edu

Interest in droplet-based microfluidics has grown significantly due to applications in biochemical analysis and material synthesis [1]. For these applications, understanding and controlling different unit operations such as drop generation, breakup and coalescence is necessary. In this work, we focus on implementing volume-of-fluid (VOF) numerical simulations to investigate different aspects of drop manipulation in microchannels. VOF is categorized as an Eulerian method of multiphase flow simulations where fluid properties such as viscosity and density are smoothed and the surface tension force is distributed over a thin layer near the interface as a body force. The details of this method and its implementation can be found in references [2,3].
We report results on three different systems that have relevance for droplet-based fluidics. First, we study droplet production from a T-junction device, and focus on the effect of viscosity ratio on droplet size. Second, we investigate breakup of droplets in a confined channel containing pillar obstacle. Here we focus on the system dynamics and discuss the conditions necessary for droplet breakup. Third, we determine the flow resistance of trapped drops and its dependence on system parameters. In all three systems, we compare the simulation results with experimental data.
Effect of viscosity on drop size in a T-junction geometry. In a microfluidic T-junction geometry, two immiscible fluids, dispersed and continuous phases, meet at the junction, followed by breakup of the dispersed phases (see Figure 1). Motivated by the lack of adequate studies investigating the influence of viscosity ratio (λ) on the generated droplet size, we mapped the dependence of drop volume on capillary number ($0.001 < Ca < 0.5$) and viscosity ratio ($0.01 < \lambda < 15$). We have shown the results in figure 1d. We find that for all viscosity ratios investigated, droplet size decreases with increase in capillary number. However, the reduction in droplet size with capillary number is stronger for $\lambda < 1$ than for $\lambda > 1$. In addition, we find that at a given capillary number, the size of droplets does not vary appreciably when $\lambda < 1$, while it increases when $\lambda > 1$.

Drop breakup at a linear obstacle. As a confined droplet approaches a linear obstacle in a microchannel, the pressure drop in the system increases. This rise in pressure drop leads to droplet break-up, if it gets sufficiently high. We investigated the influence of different system parameters such as droplet size, viscosity and confinement on pressure drop and break-up of the droplet.
We observed that, highly viscous droplets break-up at smaller imposed flow rates, see figure 2. To understand this counter-intuitive observation, we evaluated the dynamics of the system as the droplet approaches the constriction. We found that, the induced hydraulic resistance of the droplet in the system plays a crucial role in break-up of the droplet.
Flow resistance of trapped drops. When a droplet sits at a microfluidic constriction, it induces a hydraulic resistance to the microchannel. Using volume-of-fluid method and PTV experiments we investigated the effect of presence of droplet on pressure drop at a microfluidic constriction. We studied the effect of droplet confinement and viscosity ratio over a range of capillary number ($10^{-4}<Ca<10^{-2}$), on induced pressure drop in the channel. The results are shown in figure 3.
We found that when a droplet is not fully confined, the system experiences two different induced resistances at low and high Ca. By increasing the Ca, there is a jump in hydraulic resistance, which is due to degree of occupancy of the constriction at low and high Ca. On the other hand, for fully confined droplet system experiences only one resistance since the constriction is always occupied, even at small Ca.

Acknowledgements. We thank the National Science Foundation (CAREER Grant No. 1150836 and AIR-TT Grant No.1445070) for supporting this work.

References

[1] Teh SY, Lin R, Hung LH, Lee AP. Droplet microfluidics. *Lab on a Chip*. 2008:**8**(2):198-220.
[2] Nekouei M, Vanapalli SA. Volume-of-fluid simulations in microfluidic T-junction devices: Influence of viscosity ratio on droplet size. *Physics of Fluids*. 2017, **29**(3):032007.
[3] Deshpande SS, Anumolu L, Trujillo MF. Evaluating the performance of the two-phase flow solver interFoam. *Computational science & discovery*. 2012, **9:**5(1):014016.
[4] Anna SL. Droplets and bubbles in microfluidic devices. Annual Review of Fluid Mechanics. 2016, **3**;48:285-309.
[5] Sun, M., S.S. Bithi, and S.A. Vanapalli, Microfluidic static droplet arrays with tuneable gradients in material composition. *Lab on a chip*, 2011. **11**(23): p. 3949-3952.
[6] Salkin L, Schmit A, Courbin L, Panizza P. Passive breakups of isolated drops and one-dimensional assemblies of drops in microfluidic geometries: experiments and models. *Lab on a Chip*. 2013;**13**(15):3022-32.

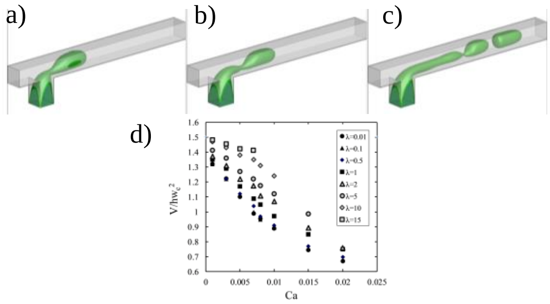

Figure 1. Drop generation at microfluidic T-junction. a)The scematic of T-junction geometry. a) squeezing b) dripping and c) jetting regimes. d)This figure is taken from our paper in Physics of Fluids (reference 2).

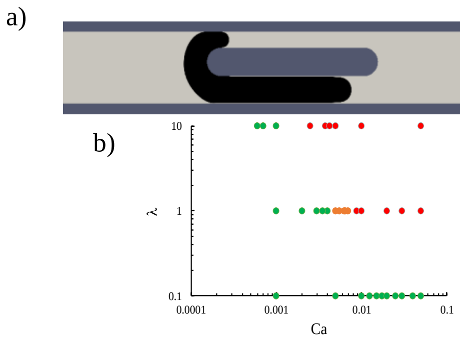

Figure2. Droplet break-up at a linear obstacle. a) 2D view of droplet break-up against the linear obstacle in the microchannel. b) Plot showing the effect of viscosity ratio on droplet break-up. Green, orange and red are showing no-break up, break-up with and without retraction, respectively.

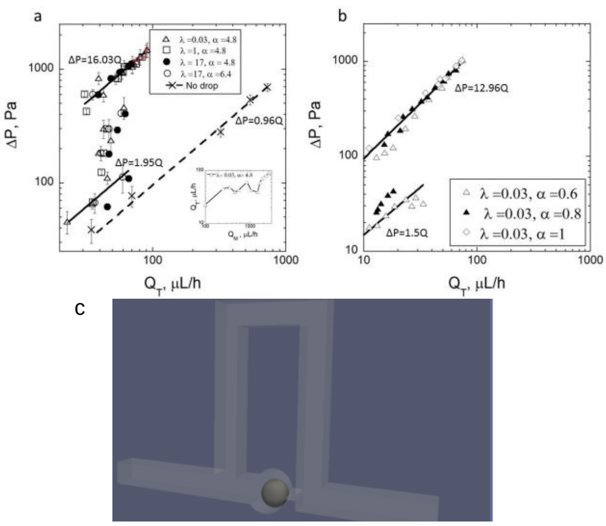

Figure 3. Trapped drop resistance. a) Experimental measurements of pressure drop b) simulation results of pressure drop c) the volume of fluid simulation of trapped drop (3D view)

Dynamics of droplet trapping and squeezing at a microfluidic constriction

Mehdi Nekouei, Siva Vanapalli*

Department of Chemical Engineering, Texas Tech University, Lubbock, TX, USA

*E-mail: siva.vanapalli@ttu.edu

Droplet transport and clogging in confined geometries is a problem of fundamental importance in oil recovery and droplet-based microfluidics. A confined droplet flowing through a conduit can either be trapped at the constriction or squeeze through it. The dynamics of the trapped and squeezed states are expected to depend on the fluid properties of droplet and continuous phase flow, as well as the channel geometry.

The literature on droplet transport through a constricted channel dates back to pioneering work by Olbricht and Leal [1]. They measured the extra pressure drop upon droplet's passage through a converging-diverging cylindrical tube. Their experiments showed that for systems with small flow rates, the size of the droplet plays a crucial role in determining the pressure drop. Additionally, they showed that as the droplet moves toward the narrowest part of the channel, a maximum in pressure drop occurs. Martinez et al. [2] investigated the same problem numerically and confirmed the strong dependency of pressure drop on location of the drop in the constricted tube.

With advances in microfluidics, there is significant interest in understanding the transport of drops in microchannels. In rectangular microfluidic channels, where the dimensions of the channels can get as small as microns, droplet entrapment is very common [2,3]. In order to trap the droplets passively, small constrictions are designed in the microfluidic channels. The presence of these constrictions, resists the pushing force of the continuous phase. There have been several studies, where the passive traps are used to trap the droplets [3-5]. On the other hand, there have been very few studies which investigate the physics of the droplet entrapment in constricted microchannels. In a recent study by Xu et al., they showed that by increasing the size of droplet and surfactant concentration the flow rate needed to trap the droplet decreases [6].

Although there have been a number of studies on the dynamics of droplets passing through a cylindrical constriction, investigations of dynamics of trapped droplets in constricted microchannels is lacking. Unlike cylindrical tubes, where the lubrication film thickness is uniform [7], the presence of angular corners, i.e. gutters in microchannels makes the film thickness non-uniform. As a result, gutters are expected to play an important role in dictating drop dynamics in microfluidics, however, its role has not been fully elucidated.

In this work, we performed three-dimensional volume-of-fluid (VOF) simulations of droplet transport in a constricted microchannel. This work builds on our previous study, where we have benchmarked VOF method for applications in droplet microfluidics [8]. We also conducted microfluidic experiments to validate the key results of the simulations. The geometry of the system is shown in Fig. (1). We investigated the impact of different system parameters: drop size, confinement and viscosity on the onset of droplet trapping at a constriction.

In simulations, we found that when constant inlet flow rate is used, as the droplet reaches to the constriction, the pressure drop increases due to limited space available for the continuous phase to flow around the drop. The magnitude of pressure rise depends on the continuous phase flow rate and dimensions of the channel. When this pressure rise exceeds the Laplace pressure at the back-end of the droplet, the droplet gets trapped.

We found that gutter flows play an important role in determining the onset of droplet trapping. Therefore, we evaluated the effect of different system parameters on gutter flows. We found that the hydraulic resistance of gutters depends on the viscosity, size and confinement of the droplet. In figure 2, the effect of droplet size on critical capillary number is shown. As we can see in this plot, by increasing the size of the droplet critical capillary number decreases significantly. Finally, we observe that high-viscosity drops even though less deformable than low-viscosity drops, squeeze through at a lower capillary number in both square and circular geometries. We verified this observation experimentally as well. The mechanism underlying this counter-intuitive phenomenon will be discussed.

Acknowledgements. We thank the National Science Foundation (CAREER Grant No. 1150836 and AIR-TT Grant No.1445070) for supporting this work.

References

[1] Olbricht, W. and L. Leal, The creeping motion of immiscible drops through a converging/diverging tube. *Journal of fluid mechanics*, 1983. **134**: p. 329-355.

[2] Martinez MJ, Udell KS. Axisymmetric creeping motion of drops through circular tubes. *Journal of fluid mechanics*. 1990;**210**:565-91.

[3] Sun, M., S.S. Bithi, and S.A. Vanapalli, Microfluidic static droplet arrays with tuneable gradients in material composition. *Lab on a chip*, 2011. **11**(23): p. 3949-3952

[4] Huebner, A., et al., Static microdroplet arrays: a microfluidic device for droplet trapping, incubation and release for enzymatic and cell-based assays. *Lab on a Chip*, 2009. **9**(5): p. 692-698.

[5] Bai, Y., et al., A double droplet trap system for studying

mass transport across a droplet-droplet interface. *Lab on a chip*, 2010. **10**(10): p. 1281-1285.
[6] Xu, K., et al., Microfluidic Investigation of Nanoparticles' Role in Mobilizing Trapped Oil Droplets in Porous Media. *Langmuir*, 2015. **31**(51): p. 13673-13679.
[7] Bretherton FP. The motion of long bubbles in tubes. *Journal of Fluid Mechanics*. 1961 Mar 1;**10**(02):166-88.
[8] Nekouei, M., & Vanapalli, S. A., Volume-of-fluid simulations in microfluidic T-junction devices: Influence of viscosity ratio on droplet size. *Physics of Fluids*, 2017, **29**(3), 032007.

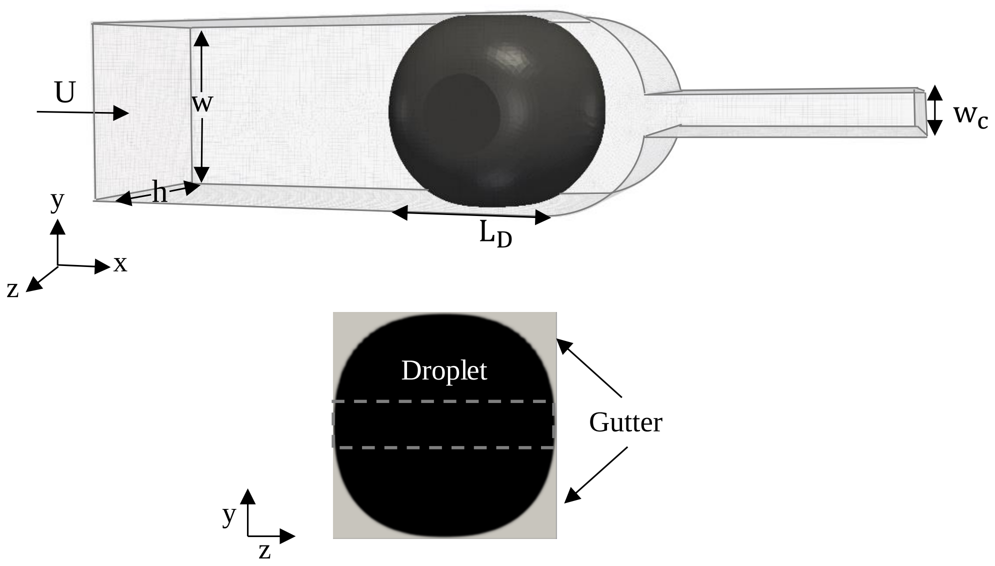

Figure 1. Geometry of the problem and cross section view of the channel with the droplet.

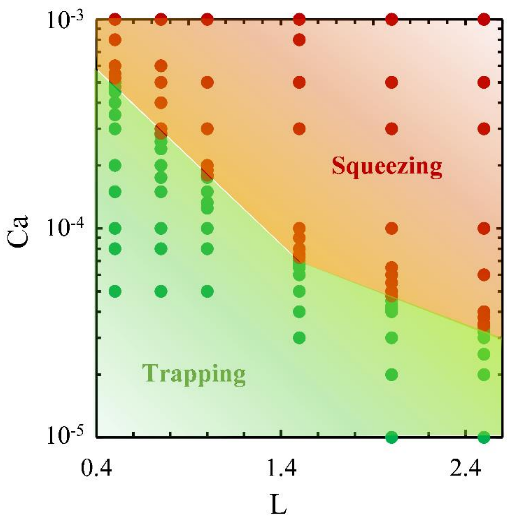

Figure 2. Critical capillary number against droplet size phase diagram

Impact of Inter-Droplet Interactions on Pickering Emulsion Rheology

Max Kaganyuk[1], Ali Mohraz[1]

[1]Department of Chemical Engineering and Materials Science, UCI, Irvine, CA, USA

E-mail: mkaganyu@uci.edu

Pickering emulsions are multiphase mixtures in which solid particles, typically in the colloidal range, reside at the interface between two immiscible fluids such as oil and water, kinetically stabilizing droplets against coalescence to form an emulsion. Since their introduction in the early 20th century [1,2], Pickering emulsions have been commonly used in a variety of consumer products, ranging from cosmetics to food items. More recently, the technological application of solid-stabilized emulsions in composite materials [3], pharmaceuticals, and the oil industry, has motivated the need to understand the salient microstructural and mechanical characteristics of these complex materials, particularly their rheology, at a more detailed level. Depending on the processing and physicochemical conditions, these multiphase mixtures can exhibit rich rheological behavior including liquid-like viscoelasticity, creep deformation, gelation, and yielding. Specific interest in the rheology of solid-stabilized emulsions is twofold: from a technological standpoint, the rheology of Pickering emulsions directly mediates their mechanical stability, shelf life, and processability, which are crucial aspects of their use in any of the applications mentioned earlier. From an academic perspective, many fundamental questions are present in regards to understanding how the multiphase nature of solid-stabilized emulsions, and the rich interfacial phenomena at play in these systems give rise to their complex mechanical properties.

The purpose of this study is to investigate how inter-droplet interactions impact the rheology of solid-stabilized emulsions. We utilize two fluid systems and particles with different surface chemistries to create Pickering emulsions with three types of interactions. The stabilizing particles employed in each emulsion mediate the interactions between droplets, resulting in the following multi-phase mixtures examined in this study: a system of repulsive droplets, a system of attractive droplets and a system in which droplets interact through monolayer particle bridges. Characterization of each system's microstructure and mechanical behavior is done by confocal microscopy imaging and small amplitude oscillatory rheology. Comparing between the different emulsions examined, we first observe different routes to gelation. In the case of either repulsive or attractive droplets, arrested dynamics arise when droplets jam at volume fractions near the random close packing limit of spheres. Bridging interactions between droplets result in a percolating network of droplets stitched together by colloidal particles, and gel-like rheology is observed far below random close packing limits. Nontrivial dependence of mechanical behavior on sample composition, for all three emulsion systems, is also observed. This includes the non-monotonic growth in gel strength, and subsequent loss, with increasing particle volume fraction in the bridging system [4]. Our observations are analyzed and discussed in the context of the microstructure exhibited in each emulsion system.

The results of this investigation have important implications for a wide range of industrial applications where solid-stabilized emulsions are utilized, and specific rheological properties must be engineered in their formulation. Fundamental knowledge is also gained by this study, in regards to the role particles play in the complex mechanical behavior of multi-phase solid-stabilized emulsions.

Acknowledgements

Financial support for this study was provided by the NASA Research Opportunities in Complex Fluids and Macromolecular Biophysics Program (NNX13AQ69G), and a GAANN fellowship to M.K. from the Department of Education.

References

[1] W. Ramsden, *Proc. R. Soc. London,* 1903, **72**, 156–164.
[2] S.U. Pickering, *J. Chem. Soc.*, 1907, **91**, 2001–2021.
[3] K. Kim et al., *Nat. Comm.*, 2017, **8**, 14305
[4] M. Kaganyuk, A. Mohraz. *Soft Matter*, 2017, DOI:10.1039/c6sm02858f

Fluidisation of a drop of molten chocolate under vibration

Nico Bergemann[1], Anne Juel[1], Matthias Heil[1], Beccy Smith[2]

[1] Manchester Centre for Nonlinear Dynamics, The University of Manchester, Manchester, UK
[2] Mondelēz International, Birmingham, UK

E-mail: nico.bergemann@manchester.ac.uk

The fluidising effect of vibrations on tempered chocolate is widely utilised on production lines to distribute chocolate in moulds. However, a description of the physics of fluidisation is lacking. We address the mechanism of fluidisation by studying the axisymmetric spreading of a sessile drop of molten chocolate on a pre-existing layer of the same fluid due to vertical vibrations.

In experiments with 5 ml drops, the drop remains static under gravity and spreading only occurs when the acceleration of the substrate exceeds approximately 2 *g*. This onset of spreading is followed by a well-defined reduction in spreading time scales with increasing acceleration. Informed by our rheological measurements, we model the molten chocolate as a generalised Newtonian fluid with a yield stress.

Numerical simulations, based on the axisymmetric free-surface Navier-Stokes equations, accurately capture the overall spreading dynamics observed in the experiments. During the upward motion of the substrate the acceleration is enhanced relative to gravity. When it exceeds a critical value, a large part of the drop fluidises almost instantaneously, which results in spreading. For the rest of the cycle, the acceleration is below the critical value and the drop remains static.

However, the numerical simulations predict an earlier onset of spreading than the experiments once the vibration is imposed. This discrepancy is thought to be related to the viscoelastic behaviour of chocolate around the yield point, which is not captured by the generalised Newtonian constitutive model. Although the elasticity of tempered chocolate is insignificant once the chocolate is fluidised, it affects how the chocolate yields and therefore impacts the fluidisation and the onset of spreading.

Acknowledgements. NB is grateful to Mondelēz International and the School of Mathematics (The University of Manchester) for the financial support of this work.

Dynamics of drops and bubbles in a confined space

Ko Okumura[1]

[1]Department of Physics, Ochanimizu University, Tokyo, JAPAN

E-mail: okumura.ko@ocha.ac.jp

Recently, the dynamics of fluid drops has acquired considerable attention. We have been working on the dynamics, in particular, in a space confined in between two parallel plates, to find scaling laws, which is the focus of this presentation. In such a "Hele-Shaw cell" geometry, dimensional crossovers, self-similarity and role of liquid thin films appear as important issues, which are the key concepts of the presentation.

Introduction

This presentation is divided into a few parts. In each part, we introduce our previous studies and discuss the recent developments of the studies. Depending on the time of the presentation, we may focus on selected topics. Figures are collected at the end.

Drop Coalescence and Self Similarity

In the coalescence of drops in the Hele-Shaw cell, we have found dimensional crossovers in the dynamics, together with a self-similar dynamics under an uncontrolled influence electric field [1] (Fig.1 left), and the effect of symmetry breaking in bursting of a thin film has been revealed [2] (Fig.1 right). Recently, we have performed experiments under a controlled electric field and have found non-coalescence above a critical field, for which the self-similar dynamics is also discussed. We also introduce another type of self-similar dynamics that we found in the Hele-Shaw cell geometry. We may also discuss the control of the modes of coalescence, the contact type and film-formation type (Fig. 1), by electric field.

Viscous Dissipation in Thin Films

Studies on rising and sinking motion of fluid drops [3] and on the lifetime of bubbles [4] in the Hele-Shaw cell have unveiled various boundary conditions realized in thin films. In Ref. [3], we found two different scaling regimes for viscous drag friction associated with liquid thin films (Fig. 2). Recently, we have found another scaling regime and provided a phase diagram for scaling regimes [5]. We may briefly discuss the granular drag friction in a Hele-Shaw cell that diverges towards the jamming point [6].

Imbibition of Textured Surfaces

It has been found that, in the dynamics of imbibition of a certain textured surface, the dynamics is governed by balance of three effects of capillarity, gravity and viscous dissipation [7]. Recently, we have found an interesting non-slowing down imbibition dynamics on the leg of a strange animal [8]. We also discuss devices for mixing small amounts of liquids by using capillary force [7].

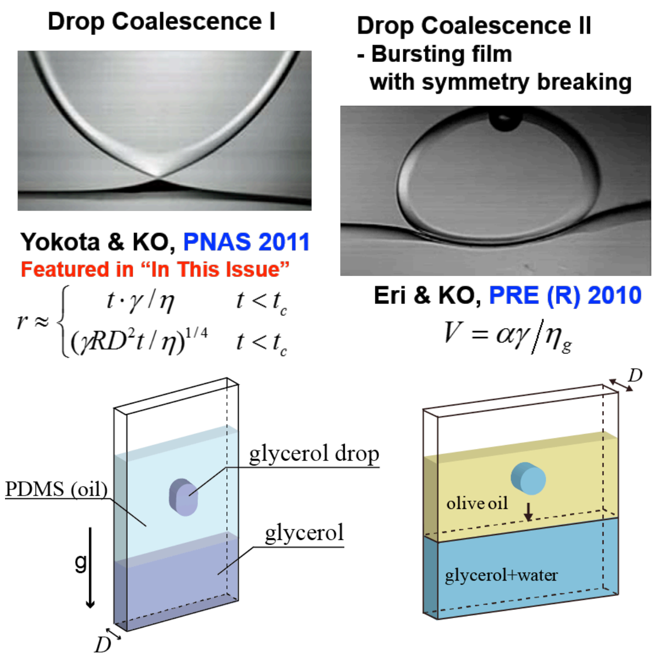

Fig. 1: Drop coalescences in Hele-Shaw cells. (left) Contact-type coalescence [1]. The two scaling laws describe two regimes of the neck dynamics. (right) film-formation-type coalescence [2]. The neck expands at the constant velocity V. The illustrations placed at the bottom indicate experimental setups and conditions for the corresponding experiments (left for the contact-type and right for the film-formation type, respectively).

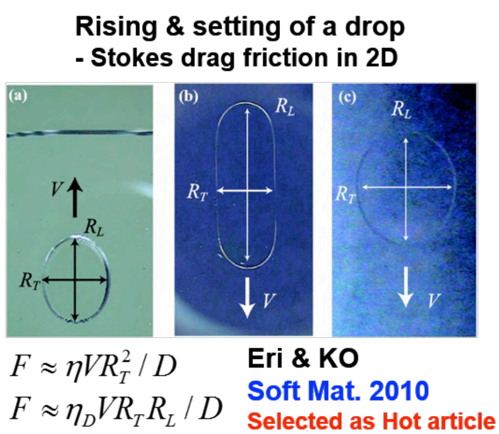

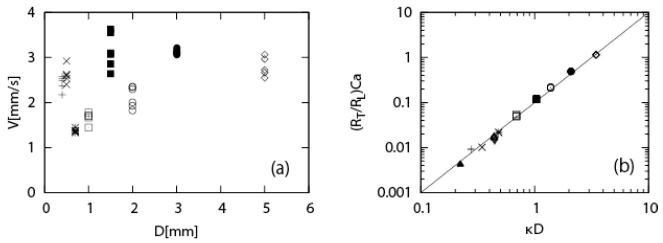

Fig. 2: Rising and sinking fluid drops in Hele-Shaw cells. From velocity measurements, the drag force F can be derived. The two scaling regimes for F indicated in the panel are confirmed in two limiting cases [3]. The bottom two plots demonstrate that how the first scaling law in the panel explains the experimental data through data collapse.

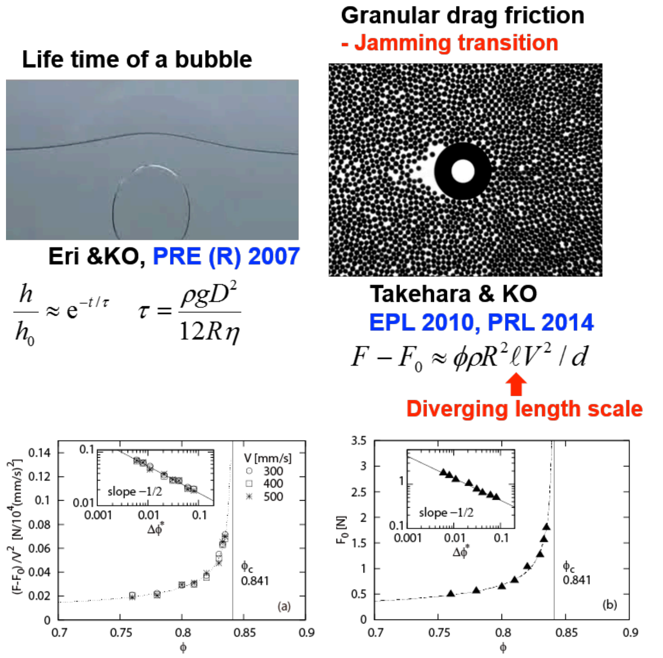

Fig. 3: Air bubble in a Hele-Shaw cell and an obstacle in a two-dimensional granular layer. (top left) Thickness of film encapsulating the bubble, h, follows the expression shown beneath the photograph [4]. (top right) Drag force acting on the obstacle form the granular medium, F, is found to diverge towards the jamming point [5]. The bottom plots show the divergence of the drag force towards the jamming point.

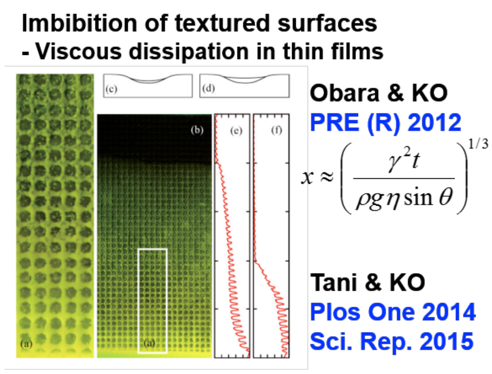

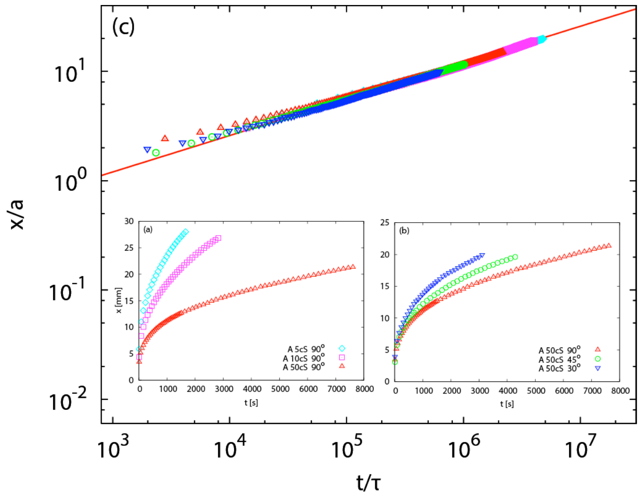

Fig. 4: Imbibition of a textured surface formed by short pillars with rounded edges [7]. (Top) The imbibition height x is given by the scaling law. Surprisingly, this law is independent of the geometrical parameters of pillars. (Bottom) The main plot shows that the six series of data shown in the inset plots collapse well on a master curve in a time range well over four orders of magnitude.

Acknowledgements. This work is supported by the ImPACT program.

References

[1] Maria Yokota and Ko Okumura. Dimensional crossover in the coalescence dynamics of viscous drops confined in between two plates. Proc. Nat. Acad. Sci. (U.S.A.), 108:6395, 2011.
[2] Ayako Eri and Ko Okumura. Bursting of a thin film in a confined geometry: Rimless and constant-velocity dewetting. Phys. Rev. E, 82(3):030601(R), 2010.
[3] Ayako Eri and Ko Okumura. Viscous drag friction acting on a fluid drop confined in between two plates confined in between two plates. Soft Matter, 7:5648, 2011.
[4] Ayako Eri and Ko Okumura. Lifetime of a two-dimensional air bubble. Phys. Rev. E, 76(6):060601(R), 2007.
[5] Misato Yahashi, Natsuki Kimoto, and Ko Okumura, Scaling crossover in thin-film drag dynamics of fluid drops in the Hele-Shaw cell, Sci. Rep. 6, 31395 (2016).
[6] Yuka Takehara and Ko Okumura. High-velocity drag friction in granular media near the jamming point. Phys. Rev. Lett., 112:148001, 2014.
[7] Noriko Obara and Ko Okumura. Imbibition of a textured surface decorated by short pillars with rounded edges. Phys. Rev. E, 86(2):020601(R), 2012.
[8] Marie Tani, Daisuke Ishii, Shuto Ito, Takahiko Hariyama, Masatsugu Shimomura, and Ko Okumura. Capillary rise on legs of a small animal and on artificially textured surfaces mimicking them. Plos One, 9(5):e96813, 2014.
[9] Marie Tani, Ryuji Kawano, Koki Kamiya, and Ko Okumura. Towards combinatorial mixing devices without any pumps by open-capillary channels: fundamentals and applications. Sci. Rep., 2015.

Pinch-off Dynamics, Dripping-onto-Substrate (DoS) Rheometry and Printability of Complex Fluids

Jelena Dinic, Leidy Nallely Jimenez, Madeleine Biagoli and Vivek Sharma
Chemical Engineering, University of Illinois at Chicago, IL.

Liquid transfer and drop formation/deposition processes involve complex free-surface flows including the formation of columnar necks that undergo spontaneous capillary-driven instability, thinning and pinch-off. For simple (Newtonian and inelastic) fluids, a complex interplay of capillary, inertial and viscous stresses determines the nonlinear dynamics underlying finite-time singularity as well as self-similar capillary thinning and pinch-off dynamics. In rheologically complex fluids, extra elastic stresses as well as non-Newtonian shear and extensional viscosities dramatically alter the nonlinear dynamics. Stream-wise velocity gradients that arise within the thinning columnar neck create an extensional flow field, and many complex fluids exhibit a much larger resistance to elongational flows than Newtonian fluids with similar shear viscosity. Characterization of pinch-off dynamics and the response to both shear and extensional flows that influence drop formation/ deposition in microfluidic and printing applications requires bespoke instrumentation not available, or easily replicated, in most laboratories. Here we show that dripping-onto-substrate (DoS) rheometry protocols that involve visualization and analysis of capillary-driven thinning and pinch-off dynamics of a columnar neck formed between a nozzle and a sessile drop can be used for measuring shear viscosity, power law index, extensional viscosity, relaxation time and the most relevant processing timescale for printing. We showcase the versatility of DoS rheometry by characterizing and contrasting the pinch-off dynamics of a wide spectrum of simple and complex fluids: water, printing inks, semi-dilute polymer solutions, yield stress fluids, food materials and cosmetics. We show that DoS rheometry enables characterization of low viscosity printing inks and polymer solutions that are beyond the measurable range of commercially-available capillary break-up extensional rheometer (CaBER). We show that for high viscosity fluids, DoS rheometry can be implemented relatively inexpensively using an off-the-shelf digital camera, and for many complex fluids, similar power law scaling exponent describes both neck thinning dynamics and the shear thinning response. Using a particular example of aqueous polymer solutions, we show the measurement of both the extensional relaxation time and extensional viscosity of weakly elastic, polymeric complex fluids with low shear viscosity $\eta < 20$ mPa· s and relatively short relaxation time, $\lambda < 1$ ms. Lastly, we will elucidate how polymer composition, flexibility and molecular weight determine the kinetics of capillary-driven thinning and pinch-off in our experiments.

ANALYSIS OF CONTACT ANGLES FOR A PERFECTLY WETTING SESSILE DROPLET EVAPORATING INTO AIR AT THE EVAPORATION STAGE

Alexey Rednikov[1], Yannis Tsoumpas[1,2], Sam Dehaeck[1], Pierre Colinet[1]

[1]TIPs Laboratory, Université Libre de Bruxelles, C.P. 165/67, Brussels, Belgium
[2]Atomic Energy and Alternative Energies Commission, Gif-sur-Yvette, France

E-mail: aredniko@ulb.ac.be

When a droplet of a volatile liquid is deposited on a flat solid substrate, it first undergoes either a fast spreading or a fast retraction, depending on the initial conditions. The droplet volume remains practically constant at this stage, the mass loss due to evaporation being a slow process relative to the mentioned 'fast' ones. Eventually, the sessile droplet reaches a kind of quasi-steady state, whose further evolution is governed by a 'slow' evaporative volume reduction. It is this latter stage that is in the focus of the present study. The volume loss gives rise to a slowly receding contact line (slower than it could be at the initial fast-retraction stage). We note beforehand that no essential pinning is observed in the present series of experiments, and the contact line is therefore treated as freely receding.

Here we deal with droplets of perfectly wetting liquids such as various HFEs (7100, 7200 and 7500), the volatility decreasing with the number. Finite contact angles observed at the evaporation stage are principally evaporation-induced by their nature (e.g. [1-5]). In the present series of experiments, the droplets are deposited on a horizontal polycarbonate plate of thickness 3 mm. The initial contact radius of the sessile droplet is typically between 1 mm and 2 mm. The contact angles are of the order of 10° or below.

The polycarbonate plate and the liquids being transparent, the droplet thickness profiles are measured by means of Mach-Zehnder interferometry [6]. A local wavelet analysis technique [6] also allows to extract the local slope profiles. A typical result for the slope profile is shown in Fig.1. A remarkable feature observed in Fig.1 is a drastic decrease of the slope in the vicinity of the contact line. This is a result of the Marangoni effect on the shape of the droplet pointed out in [5]. The liquid being pure (one-component) here, the Marangoni effect is of thermal nature and comes from evaporative cooling at the droplet free surface. Overall, a significant deviation from the classical steady shape (as determined by gravity and capillarity) is observed for a droplet of a given contact radius and contact angle (cf. Fig 1). In contrast, a theory appropriately taking into account the Marangoni effect succeeds in reproducing the experimental profile (see Fig. 1).

On the other hand, such a Marangoni-induced drastic decrease of the slope near the contact line makes it more difficult to precisely measure the actual contact angle (the slope at the rightmost point of the profile): the high curvature renders the wavelet analysis method not sufficiently accurate near the contact line [6]. In the present study, unlike [5], we shall not rely upon such a direct measurement of the contact angle and proceed in a different way. This is partly motivated by the fact that we shall here be interested in finer effects like the dependence of the contact angle on the contact radius of the droplet, hence a need to exclude such potential sources of imprecision.

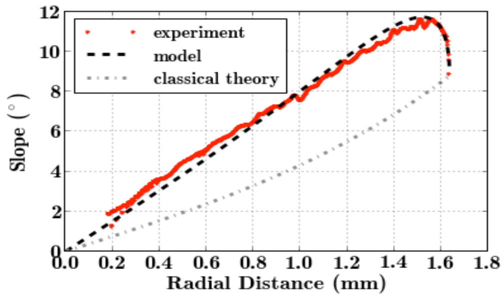

Figure 1: Slope profile of an HFE-7100 droplet, with the radial distance counted from the symmetry axis and the end of the profile corresponding to the contact line.

Namely, we proceed as follows. At first, with the help of a theoretical processing, we shall measure the so-called *apparent contact angle* of the sessile droplet. It is quite commonly defined as the angle required in the (theoretical) quasi-stationary droplet profile in order to have given values of the droplet's volume and contact radius. In experiment, the volume and the radius are measured from the droplet profile at each moment of the observed evolution of an evaporating droplet. Then, at each moment, the apparent contact angle is thereby inferred.

As it follows from what was already mentioned, the theoretical quasi-stationary profile, used to define the apparent contact angle, is here not merely the classical one, shaped just by gravity and capillarity, but rather the Marangoni-modified one [5]. The theoretical consideration is based upon the radial distribution of the *local* evaporation rate as derived in the framework of a diffusion-limited theory [7]. Yet, the measured *global* evaporation rate (obtained by taking the time derivative of the measured droplet volume) generally turns out to somewhat deviate from the predictions of the diffusion-limited theory. On the one hand, this is attributed to neglected convective effects. On the other hand, a possible evaporative cooling of the polycarbonate plate itself is not accounted for either. To make allowance for these effects, we modify the theory by heuristically correcting the diffusion-limited local evaporation rates in proportion to the mentioned discrepancy between the measured and diffusion-limited global evaporation rates. Such an approach has proved to work well in [5]. Another confirmation thereof, now unlike [5] not hinging upon a direct measurement of the contact angle, comes from a good agreement observed in Fig.2 in terms of the maximum slope (reliably measurable quantity within a slope profile as the one in Fig.1).

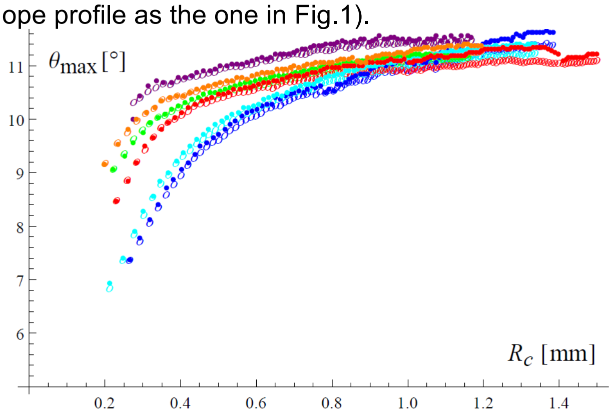

Figure 2: The measured (circles) and computed (points) maximum slopes of the droplet profile (cf. Fig.1) versus the droplet contact radius for HFE-7100. Different colors hereafter correspond to different experimental runs (the same in all subsequent figures).

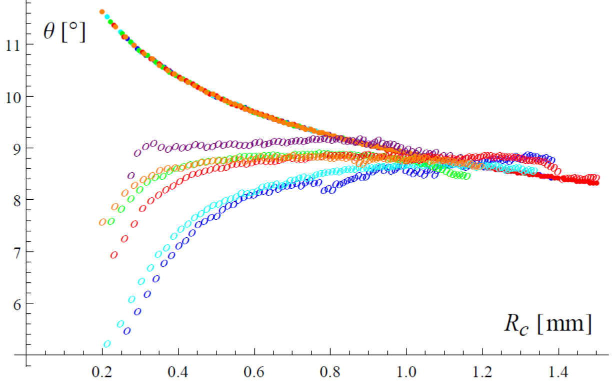

Figure 3: The measured apparent contact angles (circles) obtained by theoretical processing of the experimental data as described in the text, and the theoretical evaporation-induced contact angles (points, here coinciding for all runs) obtained from the de-Gennes-based contact-line microregion model described in [2]. Results for HFE-7100. The molecular scale value used in the model [2] is a*=1 nm.

Coming back to the apparent contact angles, the results are shown in Fig.3. Normally, for slowly receding contact lines as at the evaporation stage in question, one expects the apparent contact angles to largely coincide with the evaporation-induced ones [3,4]. Yet the comparison drawn in Fig.3 puts into evidence quite diverging tendencies for these two angles as functions of the contact radius. This compelled us to recur to asymptotic developments similar to [3,4], looking for the velocity and other related corrections into the contact angle. However, unlike [3,4], these developments are here applied explicitly to the evaporation stage and also take the Marangoni effect into account. The goal is to more precisely deduce the evaporation-induced angles from the apparent ones at the evaporation stage, rather than to merely assume them equal. On the other hand, an appropriate modification of the results coming from [2] is also applied (see Fig.4 caption). All this turns out to work in the right sense indeed, by bringing the circles and points closer together in Fig.4 as compared to Fig.3 (a disparity of ~20% now *versus* ~60% before), albeit no perfect agreement is still achieved. Curiously enough, the ~20% dispersion of the evaporation-induced contact angles observed in Fig.4 turns out to be roughly the same as the one obtained from the microregion model [2] as the spreading coefficient (whose value is not really known here) is varied in the range of small positive values. It is perhaps in the realm of this sensitivity to the spreading coefficient that the explanation for the remaining discrepancy and for the fact that different experimental runs result in different curves could be searched.

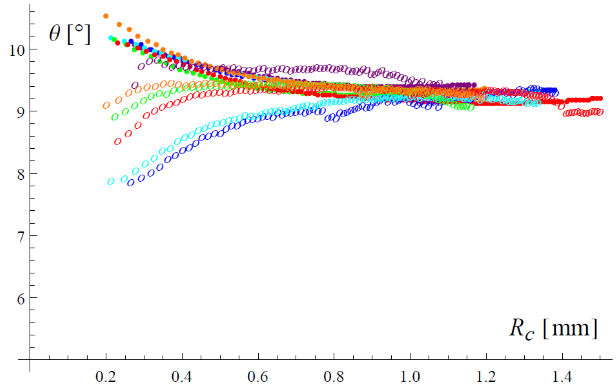

Figure 4: Evaporation-induced contact angles deduced from i) further theoretical processing of the measured apparent contact angles of Fig.3 as described in the text (circles), and ii) the microregion model [2] by applying the same heuristic evaporation rate modification as the one used in the context of the Marangoni effect (points). HFE-7100 with a*=1 nm.

To recapitulate, a straightforward naïve comparison between experiment and theory yields worryingly disparate tendencies for the evaporation-induced contact angle as a function of the droplet radius. However, an appropriate account for contributions and corrections due to the Marangoni effect and contact-line velocity as well as heuristic modifications, based on experiment, of diffusion-limited evaporation rates are shown to drastically reduce such a disparity. The results for other HFE liquids will also be presented.

Acknowledgements. We are grateful to the support from BELSPO & ESA PRODEX and F.N.S.-FNRS.

References

[1] G. Guéna, P. Allançon, A.Cazabat. *Colloids Surf. A* **300** (2007) 307-314.
[2] P. Colinet, A. Rednikov. *Eur. Phys. J. Special Topics* **197** (2011) 89-113.
[3] M.A. Saxton, J.P. Whiteley, D. Vella, J.M. Oliver. *J. Fluid Mech.* **792** (2016) 134-167.
[4] N. Savva, A. Rednikov, P. Colinet. *J. Fluid Mech.* (2017), submitted.
[5] Y. Tsoumpas, S. Dehaeck, A. Rednikov, P. Colinet. *Langmuir* **31** (2015) 13334-13340.
[6] S. Dehaeck, Y. Tsoumpas, P. Colinet. *Applied Optics* **54** (2015) 2939-2952.

[7] Y.O. Popov. *Phys. Rev. E* **71** (2005) 036313.

Dynamics of thin films under the influence of thermal fluctuations

Maulik SHAH, Volkert VAN STEIJN, Chris R. KLEIJN, Michiel T. KREUTZER

Department of Chemical Engineering, Faculty of Applied Sciences, Delft University of Technology
van der Maasweg 9, 2629 BZ, Delft, The Netherlands

E-mail: m.s.shah@tudelft.nl

Controlling the stability of emulsion droplets or foam bubbles is key to food processing industries to prolong the flavor and the texture of food products. This requires understanding how the film between neighboring bubbles or droplets thins and eventually ruptures. In this work, we study the dynamics of thin films between droplets. For dewetting of liquid films on solid substrates, nanometer scale fluctuations at the interface due to thermal molecular motion strongly influence the rupture time [3]. Here, we explore how thermal fluctuations influence the rupture of non-conformal films present in emulsions and foams.

Previous studies on planar thin-film rupture used the deterministic thin-film equation [1-3]

$$\frac{\partial h}{\partial t} = \frac{\partial}{\partial x}\left\{\frac{h^3}{3}\frac{\partial}{\partial x}\left(\phi'(h) - \gamma\frac{\partial^2 h}{\partial x^2}\right)\right\} \tag{1}$$

for the evolution of a thin film under the influence of intermolecular forces that are lumped into disjoining pressure, $\phi'(h)$, and capillary pressure, $\gamma(\partial^2 h/\partial x^2)$. Experimental rupture times are over-predicted with this fluctuation-free theory.

When thermal fluctuations were accounted for by adding a stochastic noise term as shown in equation (2), the rupture time decreases roughly fourfold, in better agreement with experiments [3].

$$\frac{\partial h}{\partial t} = \frac{\partial}{\partial x}\left\{\frac{h^3}{3}\frac{\partial}{\partial x}\left(\phi'(h) - \gamma\frac{\partial^2 h}{\partial x^2}\right) + \sqrt{2\theta}\sqrt{\frac{h^3}{3}}N(x,t)\right\} \tag{2}$$

We implemented this noise-containing model using a semi-implicit solver which we validated using the planar-film case found in the literature [3], see Fig 1. For the deterministic case, the dimensionless rupture time is 15.5, while the mean rupture time for the stochastic simulations is distributed around a mean of 4.6 with a standard deviation of 0.8 (Fig. 1c). This confirms the previously reported factor of four difference in rupture times. We also studied the effect of the spatial correlation in the thermal fluctuations in these films by imposing a correlation length, l_c, as described in literature [3,4], with $l_c = 0$ signifying spatially uncorrelated noise and $l_c = 15$ signifying a high spatial correlation. Fig. 1c and 1d show the distribution of rupture times for both situations. The rupture times increases with increasing spatial correlations in the noise. The mean rupture times for highly spatially correlated noise corresponds to the deterministic rupture times highlighting the importance of spatial correlations in determining accurate rupture times.

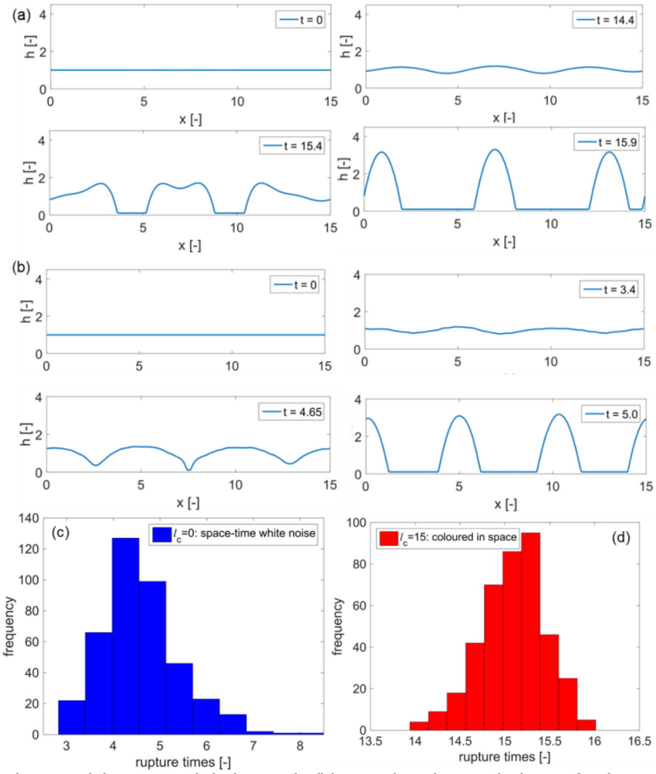

Fig. 1: (a) Deterministic and (b) stochastic evolution of planar thin-films with rupture occurring at 15.5 and 4.6 in dimensionless time. (c,d). Distributions of rupture times for 400 realizations of a stochastic thin-film rupture for a dimensionless temperature, $\theta = 1.25.10^{-3}$. (c) Distribution for l_c=0 (spatially uncorrelated noise) has rupture time statistics of 4.6± 0.8 in dimensionless units. (d) Distribution for l_c=15 (equivalently, l_c /L=1) (highly colored noise) and has rupture time statistics of 15±0.45.

While the influence of thermal fluctuations is now well understood for flat conformal films, their relevance to predicting coalescence time for non-conformal films is largely unexplored. Before presenting the results with thermal fluctuations included, it is instructive to first present the thin film dynamics in the absence of thermal fluctuations. We consider non-conformal emulsion films, where so-called Plateau borders with curvature connect to the planar portion of the film. Figure 2a presents a schematic of the non-conformal thin-film with its initial condition. The curvature causes an accelerated film thinning due to the jump in capillary pressure at the connection to the Plateau border. Fig. 2b shows that a localized dimple is formed at the transition region. The evolution of the film thickness can be divided into two time regimes. The first regime where the drainage due to capillary suction is the

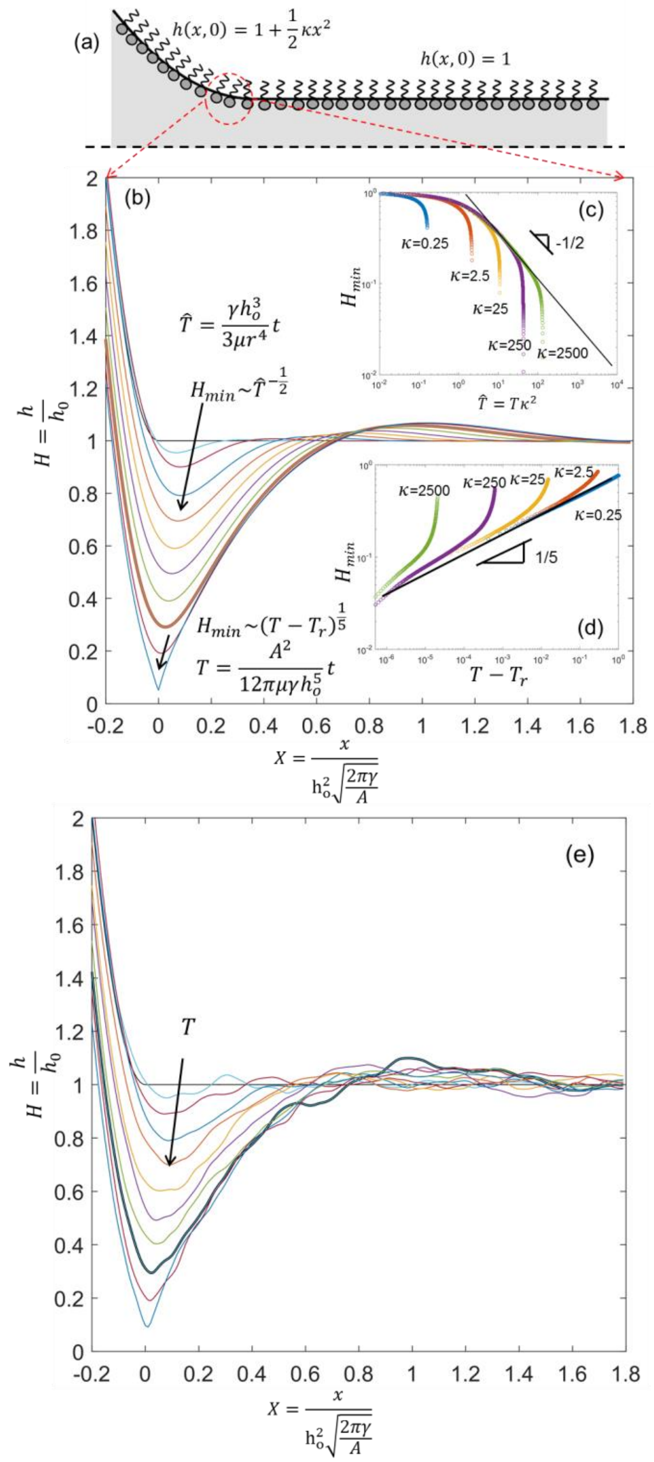

Fig. 2: (a) Schematic of a non-conformal thin-film with its initial and far-field boundary conditions. (b) Deterministic evolution of the non-conformal thin-films for dimensionless curvature, $\kappa = 50$. (c,d) Minimum film height values extracted from the numerical solutions of (b) for different values of κ. The minimum film thickness follows self-similar solution as predicted theoretically by Aradian et al. [5] and Zhang et al. [6] for early and late times of film thinning respectively. Figure adapted from [7]. (e) Stochastic evolution of the non-conformal films for $\kappa = 50$ and dimensionless T=4.10^{-3}.

dominant force for film thinning and the second regime where the long-range van der Waals forces dominate the evolution of the film. We recover the self-similar solution as derived by Aradian et al. [5] with $H_{min} \sim T^{-1/2}$ as shown in Fig. 2(c). Subsequently, long-range van der Waals forces become dominant and the film thins rapidly. As the film approaches rupture at $T = T_r$, the evolution of the film height follows another self-similar solution [6] with $H_{min} \sim (T - T_r)^{1/5}$ as shown in Fig. 2(d).

We extend the deterministic description of these films by adding a stochastic noise term as in equation (2) to account for the presence of thermal fluctuations at the interfaces of these films. The current work focuses on studying how the strength of the fluctuations and the magnitude of the curvature influence the coalescence time. Fig. 2(e) shows a single stochastic evolution of the film profile where we see that the dimple formation is unaffected by the influence of thermal fluctuations. The rupture times for $\kappa =$ 0.001 and 0.01 for deterministic simulations were found to be 26.5 and 13.5 respectively in dimensionless units. When thermal fluctuations are accounted for, with a dimensionless temperature, θ = 4.05.10^{-3} (noise intensity, $\sqrt{2\theta}$ = 0.09), the rupture time decreases to 8.5 $\pm$ 0.8 and 7 $\pm$ 0.9 for 60 realizations of their stochastic evolutions. Thereby, it shows a factor of 3 and 2 decrease in the rupture times for $\kappa =$ 0.001 and 0.01 respectively. This decrement in the rupture times further depends on the strength of the stochastic term used, with higher noise intensity leading to a further decrease in the rupture time of these non-conformal films. For higher values of dimensionless curvature, κ, drainage flow due to high capillary suction stabilizes the perturbations caused by thermal fluctuations leading to rupture times that are close to the deterministic rupture times.

In conclusion, we have numerically confirmed the stochastic thin-film evolution for planar films [3], accounting for thermal fluctuations, and we have extended the analysis to non-conformal films. It was found that for low values of curvature, the rupture times decrease in the presence of thermal fluctuations, with this decrease depending on the strength of the stochastic noise.

Acknowledgements. This research is carried out under the framework of ISPT project COFILM.

References

[1] A. Oron, S. H. Davis, and S.G. Bankoff, Rev. Mod. Phys., 69, 931 (1997)
[2] J. Becker, G. Grun, R. Seemann, H. Mantz, K. Jacobs, K.R. Mecke, and R. Blossey, Nat. Mat, 2, 59-63 (2003).
[3] G. Grun, K. Mecke, M. Rauscher, Jour. Stat. Phys., 122, 6, (2006)
[4] J.A. Diez, A.G. Gonzalez, R. Fernandez, Phys. Rev. E., 93, 013120 (2016)
[5] A. Aradian, E. Raphael, and P.G. de Gennes, Europhys. Lett., 55, 834 (2001)
[6] W.W. Zhang and L.R. Lister, Phys. Fluids, 11, 2454 (1999)
[7] M.T. Kreutzer, P. Parthiban, and S.A. Khan, [in preparation]

MODELING OF MASS TRANSFER INSIDE A COLLOIDAL DROPLET CAUSED BY DRYING UNDER A MASK WITH HOLES

I.V. Vodolazskaya[1], Yu.Yu. Tarasevich[1]

[1]Astrakhan State University, Astrakhan, Russia

E-mail: tarasevich@asu.edu.ru

A method of evaporative lithography has been proposed in [1]. In evaporative lithography, a mask is placed above a drying film to create regions of free and hindered evaporation. Inhomogeneous evaporation induces a fluid convection. This convection carries colloidal particles to regions of highest evaporative flux. The binary colloidal films exhibit pattern formation when subjected to a periodic evaporative landscape during drying.

Recently, some results of modelling for two limiting cases have been published [2,3]. In the present work, we propose the consideration that is more common. We consider a droplet that dries on a solid horizontal surface under a mask with holes. Initially, colloidal particles are homogeneously distributed inside the droplet. The holes in the mask form a flat hexagonal structure. The droplet's radius, R, is supposed to be much larger than a distance between the holes, P. Hence, only one hexagonal cell of the droplet under mask with one central hole can be considered. In our study, both a centre-to-centre separation distance between the holes in the mask, P, and a gap height between the mask, h_g, and the underlying droplet varied as in the experiments [1] (Fig. 1).

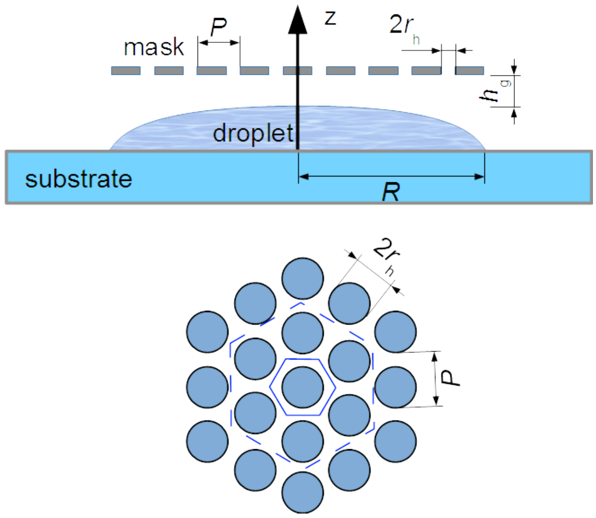

Fig.1. Colloidal droplet on a horizontal flat hydrophilic surface desiccates beneath a mask.

The vapour could escape only across the hole in the mask. To get a density of the vapour flux, a stationary diffusion equation was solved in the atmosphere. Profile of the vapour flux varies from almost flat, when h_g is large, to crater-like which has been reported in [5], when h_g is small (Fig. 2).

The mass conservation and the advection-diffusion equation with sedimentation were solved to find the vertically averaged volume fraction of particles in the solution. In the model, we assume that the droplet surface is flat and the density of the flux of the sedimentation is proportional to the volume fraction of the particles [4]. We examine the effect of mask design, diffusion, sedimentation and initial volume fraction of the particles on the mass transfer when the solvent evaporates.

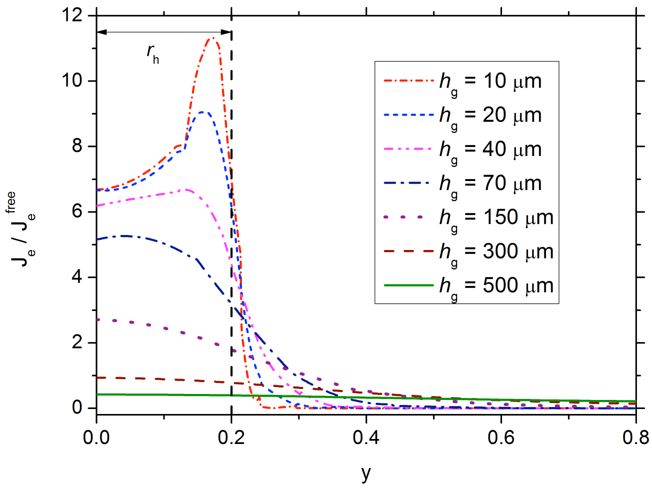

Fig.2. Normalized evaporative flux for r_h = 0.2 and different values of h_g. Distances along the axis y are measured in the units of $P/2$. J_e^{free} is the evaporative flux when the mask is absent.

Our results consistent with the experimental data [1]. Colloidal particles in the solution are carried by advective flow to the holes in the mask. The effect is enhanced when the mask design parameter is reduced. An increase in the size of the holes or a decrease in the distance between the holes in the mask results in a more uniform distribution of the particles in the solution. An increase in the initial volume fraction of particles in the solution leads to an increase in the flux of deposition of particles onto the substrate and, accordingly, to a decrease in the number of particles in the solution.

Fig.3 demonstrates effect of hole's radius on the height averaged volume fraction of colloidal particles inside the droplet at time corresponding to $0.2t_e$, where t_e is the total time of drying. The particle distribution become more homogeneous when the holes increase.

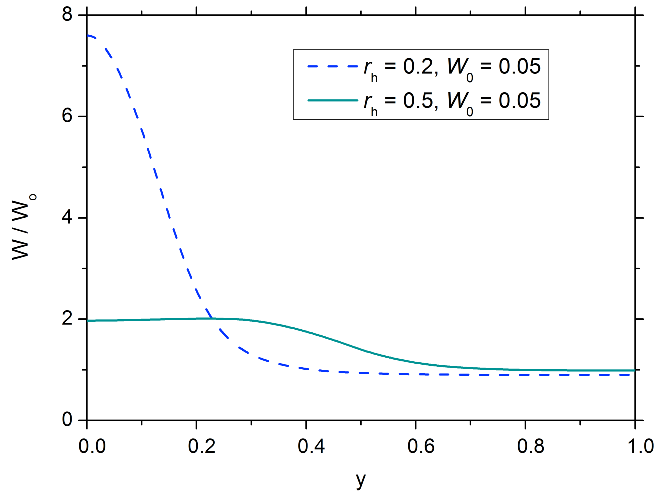

Fig.3. Normalized height averaged volume fraction of colloidal particles, W/W_0, for initial volume fraction W_0 = 0.05 and two different radii of holes, r_h. $t = 0.2t_e$, h_g = 30 μm. Distance along the axis y is measured in the units of $P/2$.

Fig.4 demonstrates effect advection and diffusion on the spatial redistribution of the colloidal particles. When the Péclet number is about 1, i.e., advective transport is approximately equal to diffusive transport, the particles tend to concentrate in the region of higher evaporation. In contrast, diffusion can counteract this concentration, when the Péclet number is small.

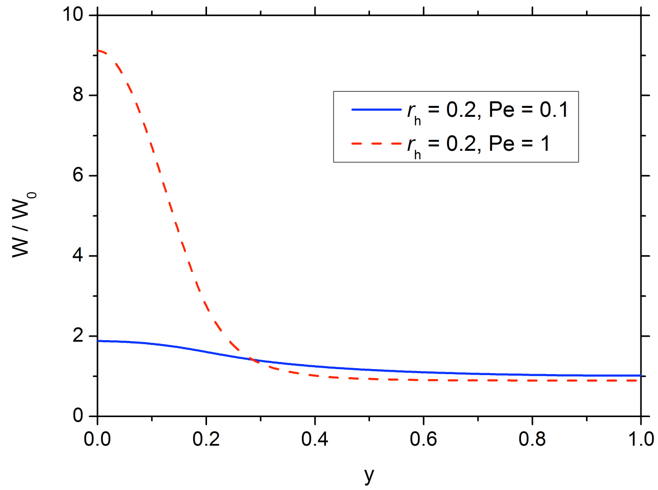

Fig.4. Normalized height averaged volume fraction of colloidal particles, W/W_0, for different values of Péclet number. $t = 0.2t_e$, W_0 = 0.005, h_g = 30 μm, K = 0.5. Distance along the axis y is measured in the units of $P/2$.

Fig.5 shows effect of sedimentation rate on spatial redistribution of the colloidal particles. Naturally, sedimentation reduces concentration of the colloidal particles inside the droplet. Nevertheless, our simulation evidences that sedimentation almost does not modify the spatial distribution of the colloidal particles.

Fig.6. demonstrates how the ratio of the mass of particles deposited directly under the hole to the total deposited mass varies with time.

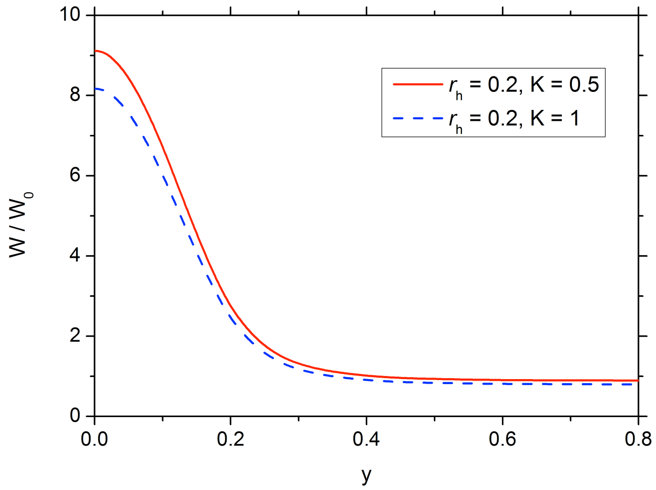

Fig.5. Normalized height averaged volume fraction of colloidal particles, W/W_0, for different values of sedimentation rate, K. $t = 0.2t_e$, W_0 = 0.005, h_g = 30 μm, Pe = 1. Distance along the axis y is measured in the units of $P/2$.

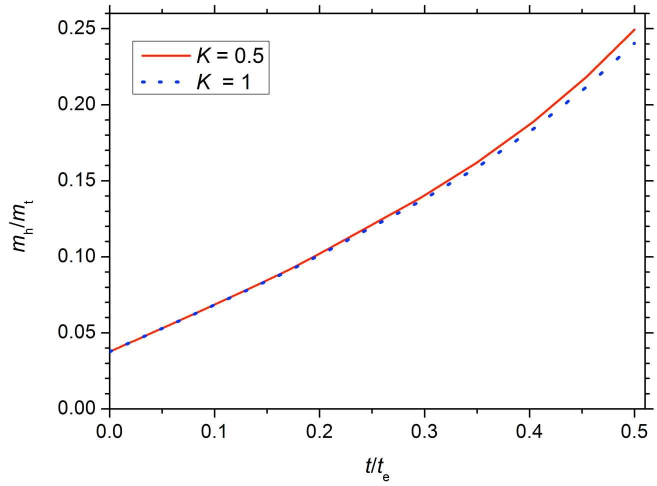

Fig.6. Ratio of the mass of particles deposited directly under the hole to the total deposited mass vs dimensionless time for different values of deposition rate, K. W_0 = 0.005, r_h = 0.2, h_g = 30 μm, Pe = 1.

References

[1] D.J. Harris, H. Hu, J.C. Conrad, J.A. Lewis. *Physical Review Letters*, **98** (2007), 148301.
[2] Yu.Yu. Tarasevich, I.V. Vodolazskaya, L.V. Sakharova. *European Physical Journal E*, **39** (2016), 26.
[3] Yu.Yu. Tarasevich, I.V. Vodolazskaya. *Journal of Physics: Conference Series,* **681** (2016), 012033.
[4] E. Widjaja, M.T. Harris. *AIChE Journal*, **54** (2008), 2250-2260.
[5] M. Cachile, O. Bénichou, A.M. Cazabat. *Langmuir,* **18** (2002), 7985-7990.

CAPILLARY OSCILLATION AND BREAKUP OF DROPLET COALESCENCE: IDENTIFYING REGIME AND TRANSITION

Le Qin PENG, Zheng Yuan LUO, Gang YAN, Bo Feng BAI*

State Key Laboratory of Multiphase Flow in Power Engineering, Xi'an Jiaotong University, Shaanxi, 710049, China

E-mail: bfbai@mail.xjtu.edu.cn

When two identical droplet come into contact with each other, they typically coalesce into a larger one for minimizing the free surface energy. Notably, the hydrodynamic behaviors during the process after coalescence, including rapid expanding of liquid bridge formed between two droplets, are of great scientific interest because of the richness of the underlying physics, such as free surface flow[1-4], Rayleigh-Plateau instability[5-7], and singularity dynamic[8], all of which are also essential to appropriately manipulate droplet coalescence in various application[9-11]. The capillary driven expansion of the neck generates capillary waves from the released surface energy. The wave carry momentum and propagate axisymmetrically along the droplet surfaces, thereby be blocked by the connecting solid surface, e.g. needle, simultaneously, stretch outward from the opposite poles to form protrusions, which are sometimes pinched off to form satellites. Chen et al.[9] observed three regimes after pinched droplet coalescence, with on satellite droplet formation. Thoroddsen et al.[7, 12, 13] provided models for predicting the satellite size generated from the capillary wave induced by drop coalescence, and the pinch-off limitation.

In this work, we have systematically studied the oscillation process of liquid bridge after the coalescence of a pendent and sessile droplet pinched on the needles. As shown in Figure 1(a), the coalescence of the distilled water droplets in atmosphere were controlled inside a stainless steel cell with sight glass. Two droplets were formed at the flat extremities of facing vertical coaxial needles by injecting liquid from corresponding syringe pump. The injection rate of micropump (Harvard PHD ULTRA) was set from 0.01ml/min to 0.2ml/min for obtaining various approaching speed. A sessile droplet was first generated on the lower needle extremity by controlling the volumetric flowrate Q_v and running time of pump. Then a pendent droplet grew on the upper needle extremity. The dynamic process of millimeter-sized droplets after generation, including the process from coalescence to oscillation, and sometimes broken, is directly recorded by a high-speed camera (Photron MINI UX100 with 1280 × 480 resolution) cooperated with long distance microscope lens (KEYENVE VH-Z50) from the side, at the frame rate of 10000 fps. A LED parallel light source (power 3W, spot diameter 20mm) was used to provide back-lit illumination. The side-view image of a pendent and a sessile droplet pinched on the needle before coalescence is shown in Figure 1(b). This allows the study of a liquid bridge of volume V attached to the edges of two facing solid disks of diameter D (corresponding radius R) separated by a distance H. Droplet volume, centroid coordinates (x_c, y_c) and curvature radius r_1, r_2 were determined via image analysis using Matlab software.

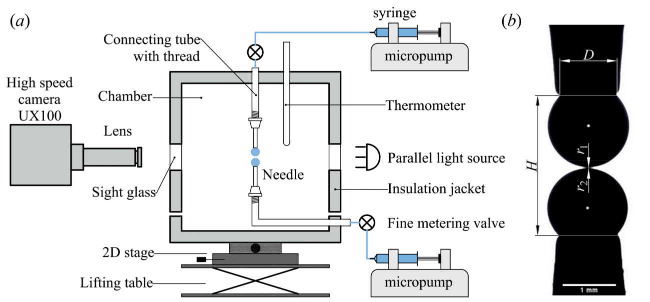

Figure.1 (a) Schematic of the experimental set-up. (b) The side-view of two initial droplets before merging. The distance between needles H, width of droplet contacting with needle D and curvature radius of two droplets r1, r2.

Results and discussion

Three different coalescence regimes are observed during the entire droplet coalescence process, including pinch-off in two necks during first necking stage (*type I*) (Figure 2a), pinch-off in one neck during second necking stage (*type II*) (Figure 2b), and stable liquid bridge with no pinch-off (*type III*) (Figure 2c).

Note that, these results indicate that gravity turns to be increasingly pronounced in morphologies development of coalescences after the initial expansion of the liquid bridge, especially in the final pinch-off process. Therefore, we represent these regimes using the Bond number (Bo=$\rho g R^2 \gamma^{-1}$, which compares gravity to the surface tension forces), and the Weber number (We=$\rho u^2 R \gamma^{-1}$, which compares inertial to surface tension forces).

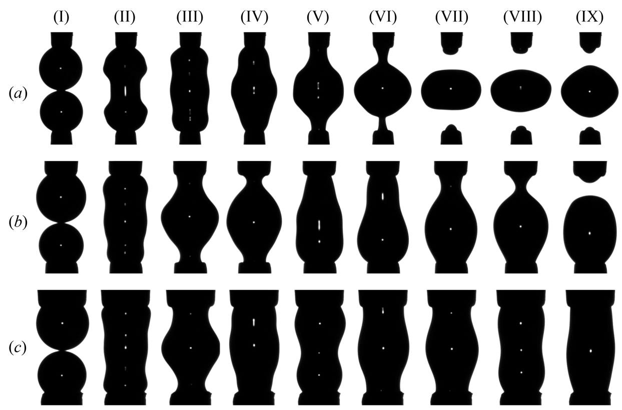

Figure.2 Evolutions of the liquid bridges after coalescence of

the two distilled water droplets. (I) Initial arrangement; (II)-(IX) Oscillation of liquid bridge formed by coalescence of droplets. Three typical regimes: (a) satellite droplet generated from pinch-off in two necks during first necking stage (volumetric flow rate: 0.01ml/min, outer diameter: 0.55mm, time interval: 60ms); (b) pinch-off in one neck during second necking stage (0.05ml/min, 0.9mm, 150ms); (c) stable liquid bridge with on pinch-off (0.01ml/min, 1.34mm, 150ms).

We use Matlab software to obtain the contour of the gas-liquid interface on each image, and plot *W*, normalized by W_{max}, as a function of time in Figure 3(b). This damping behavior of nondimensional W is clearly illustrated by the blue dotted line and exhibits a single dominant period intuitively. Using the damped oscillation sine function to fit. Then, the dependence of the oscillation parameters (A, γ, T) on the pinned needle and approaching speed.

$$w(t) = w_0 + Ae^{-\delta t}\sin\left(2\pi\frac{t}{T}+\phi\right) \qquad (1)$$

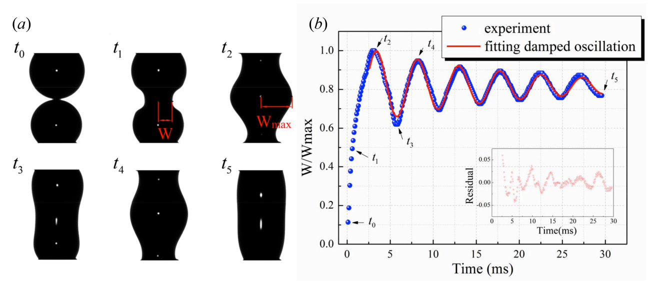

Figure.3 (a) Typical moments of coalescence process of DI water droplets pinched on the needles, corresponding to the marked time in (b). At t_0 = 0 ms, the droplets are just contact; At t_1 = 0.5 ms, the liquid bridge expanding, corresponding half of width is marked as *W*; At t_2 = 2.9 ms, *W* reaches its maximum value W_{max} for the first time; Then it decreases until t_3 = 6.3 ms; At t_4 = 8.1 ms, *W* reaches the peak once again. After several damped oscillation periods, the liquid bridge closes to a static state at the final recording time t_5= 29.6 ms. (b) Normalized width in the middle of the bridge W/W_{max} versus time; blue dotted line represents the experimental results obtain from sequence images; red line is the fitting curve by damped sine function. Inset: the residual of W/W_{max} with fitting.

Furthermore, we analyze the oscillation behavior of liquid bridge in the middle position at various volumetric flowrates and needle diameters. The damped behaviors are significantly influenced by the contact condition with the needle tips, conversely, less influenced by the approaching speed.

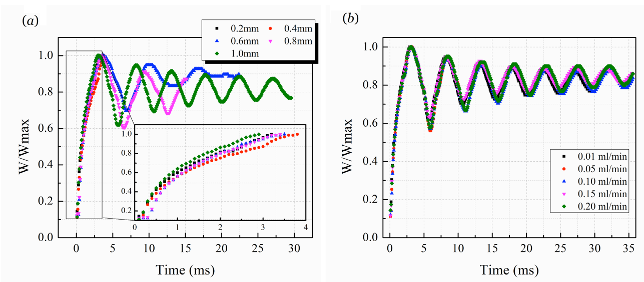

Figure.4 Normalized width in the middle of the bridge W/W_{max} versus time *t*. (a) width oscillation of liquid bridge pinned on inner diameters 0.2, 0.4, 0.6, 0.8, 1.0 mm (using inner diameter for convenience; outer diameters used as analytical size) at the same approaching speed; (b) oscillation of bridge at 0.01, 0.05, 0.1, 0.15 and 0.2 ml/min volumetric flowrate and 0.2 mm diameter needle.

We will further study these three regimes and transition, especially the pinch-off and damped oscillation from aspect of wave instability.

Acknowledgements. This work was supported by the China National Funds for Distinguished Young Scientists (Grant No. 51425603).

References

[1] J. Billingham and A. C. King, *J Fluid Mech*, (2005) 533.
[2] J. Billingham, *SIAM Journal on Applied Mathematics*, (2006) **66**(6), 1949-1977.
[3] H. N. Oguz and A. Prosperetti, *J Fluid Mech*, (2006) **203**, 149.
[4] J. Lu, S. Fang, and C. M. Corvalan, *Phys Rev E*, (2016) **93**(2), 023111.
[5] F. Blanchette and T. P. Bigioni, *J Fluid Mech*, (2009) **620**, 333.
[6] H. Aryafar and H. P. Kavehpour, *Physical Review E*, (2008) **78**(3).
[7] F. H. Zhang, M. J. Thoraval, S. T. Thoroddsen, and P. Taborek, *J Fluid Mech*, (2015) **782**, 209-239.
[8] B. W. Zeff, B. Kleber, J. Fineberg, and D. P. Lathrop, *Nature*, (2000) **403**(6768), 401-404.
[9] Y. Chen, C. Shen, and G. P. Peterson, *Industrial & Engineering Chemistry Research*, (2015) **54**(37), 9257-9262.
[10] X. Li, H. Ren, W. Wu, H. Li, L. Wang, Y. He, J. Wang, and Y. Zhou, *Scientific reports*, (2015) **5**, 15190.
[11] T. Li, W. Wu, and H. Li, Phys. Chem. Chem. Phys., (2016) **18**(39), 27500-27506.
[12] F. H. Zhang, E. Q. Li, and S. T. Thoroddsen, *Phys Rev Lett*, (2009) **102**(10), 104502.
[13] H. Ding, E. Q. Li, F. H. Zhang, Y. Sui, P. D. M. Spelt, and S. T. Thoroddsen, *J Fluid Mech*, (2012) **697**, 92-114.

Impact, Spreading and Splashing of Superfluid Drops

Matthew Wallace[1], David Mallin[1], Andres Aguirre [2], Kenneth Langley [2]
Sigurdur Thoroddsen[2], and Peter Taborek[1]

[1]Department of Physics and Astronomy, UC Irvine, Irvine, CA, USA
[2] Division of Physical Sciences and Engineering and Clean Combustion Research Center, King Abdullah University of Science and Technology (KAUST). Thuval 23955-6900, Saudi Arabia

E-mail: ptaborek@uci.edu

We have used high speed video to investigate the impact of superfluid and normal liquid helium drops onto glass plates and into bulk liquid in the temperature range from 1.2-2.5K. The unusual properties of liquid helium allow us to explore ranges of parameters that are difficult to obtain in conventional systems.

Even in the normal state with T>2.17K, the viscosity and surface tension of liquid helium are unusually low, so it is easy to prepare drops with Reynolds numbers>30,000 or Ohnesorge numbers<0.0005. Our experiments with helium drops take place in an atmosphere of helium gas whose pressure is determined by the vapor pressure curve. Near the lambda point, the pressure is approximately 40 Torr. Many of the phenomena observed in conventional impact and splashing experiments are due to the dynamics of the (incondensable) air that is trapped by the impinging drop[1]. Experiments with helium do not involve an incondensable exterior phase, so the dynamics can be expected to be quite different.

Below the lambda point, helium has an inviscid superfluid fraction that grows as the temperature is lowered. Conventional viscous drops in free fall assume a near spherical shape because the initial perturbations of pinch-off are damped by viscosity. In contrast, falling superfluid drops can have rough surfaces and complex, distinctly non-spherical shapes[2]. Superfluids are also superconductors of heat, which means that removable of latent heat from an interface that is evaporating or condensing can be very rapid.

We have constructed an optical cryostat with a superconducting bellows pump which can deliver liquid helium drops in either the superfluid or normal state. Impacts of normal phase droplets onto smooth glass plates generate splashing and breakup even at very low Weber numbers. Superfluid droplets spread without splashing. The radius of the fluid rim grows as a power law in time with an exponent of approximately 0.4. The velocity of the fluid rim can exceed 4 m/s, which is significantly higher than the superfluid critical velocity.

Impact of drops into bulk liquid shows a Rayleigh breakup structure with a cascade of satellite drops. The details of the breakup is dependent on state (normal or super) of the liquid. Impact of superfluid drops into bulk liquid show unusually sharp structures in the vapor crater, and extremely fast dynamics in the collapse of vapor bubbles.

Acknowledgements This research was supported by funding from King Abdullah University of Science and Technology (KAUST).

References

[1] E.Q. Li and S.T. Thoroddsen, J. Fluid Mech. (2015), **780**, 636-648
[2] J.C. Burton, J.E. Rutledge, and P. Taborek, *Phys. Rev. E*, (2007) **75**, 036311

THEORETICAL AND EXPERIMENTAL ANALYSES OF MOLTEN DROPLET IMPACT ON COLD SUBSTRATES

Elaheh Alizadeh-Birjandi and H.Pirouz Kavehpour

Department of Mechanical Engineering, UCLA, Los Angeles, CA, USA

E-mail: ealizadeh@ucla.edu

The molten dynamic contact line problem is inherently different from isothermal spreading process as solidification plays a crucial role in controlling the molten contact line arrest and the value of contact angle during solidification. In non-isothermal spreading followed by phase change, at some point, spreading stops due to solidification.

Many researchers are trying to obtain the final shape of the droplet, contact angle and radius of the drop after the solidification is complete [1-5] since understanding the physics behind the non-isothermal spreading of droplet is of utmost importance due to its broad applications in diverse areas of industry.

This work mainly focuses on obtaining important physical parameters involved in the process of spreading of molten droplets as well as controlling the post-solidification geometry of droplets. Here, we will examine the solidification in inviscid and impact driven region and explain the process both analytically and experimentally.

A complete set of experimental study is performed that shows the final radius in the case of free fall of droplet under high impact velocity is independent of the initial conditions of the impact including the impact velocity and temperature gradient at the substrate. The analytical modeling of the problem also verifies the accuracy of these results.

References

[1] R. Bhola and S. Chandra, "Parameters controlling solidification of molten wax droplets falling on a solid surface," *Journal of Materials Science,* vol. 34, pp. 4883-4894, 1999 1999.

[2] S. Chandra and C. T. Avedisian, "On the Collision of a Droplet with a Solid Surface," *Proceedings of the Royal Society of London Series a-Mathematical Physical and Engineering Sciences,* vol. 432, pp. 13-41, Jan 8 1991.

[3] P. Ehrhard, "Experiments on Isothermal and Nonisothermal Spreading," *Journal of Fluid Mechanics,* vol. 257, pp. 463-483, Dec 1993.

[4] T. Watanabe, I. Kuribayashi, T. Honda, and A. Kanzawa, "Deformation And Solidification Of A Droplet On A Cold Substrate," *Chemical Engineering Science,* vol. 47, pp. 3059-3065, Aug 1992.

[5] F. Tavakoli, S. H. Davis, and H. P. Kavehpour, "Spreading and Arrest of a Molten Liquid on Cold Substrates," *Langmuir,* vol. 30, pp. 10151-10155, 2014.

DROPLET SPREADING AND JETTING ON POROUS SURFACES

Jan Carmeliet[1,2], Amir Ashrafi Habibabadi[1], Dominique Derome[2]

[1]Chair of Building Physics, ETH Zürich, 8093 Zürich, Switzerland
[2]Laboratory for Multiscale Studies in Building Physics, Swiss Federal Laboratories for Materials Science and Technology, Empa, 8600 Dübendorf, Switzerland

E-mail: carmeliet@arch.ethz.ch

Introduction

The phenomenon of drop impact on porous media is ubiquitous in nature and is associated with mechanisms found in various industrial applications When a liquid droplet impacts on a porous surface, it spreads on the surface and is afterwards absorbed into the porous material due to capillary action. The spreading behavior of the impinging droplet on the surface is known to depend on the properties of the liquid, i.e. density, viscosity and surface tension, impact conditions such as drop size and impact velocity, and the surface wettability and roughness [1, 2]. In addition, a jetting can occur.

In this study, we aim to capture the maximum spreading and the occurrence of jetting of impinging droplets on natural porous stones.

Methodology

Samples

Three stones with varying porosity, roughness and capillary uptake characteristics are selected, one limestone (Savonnières), two sandstones (Meule, Pietra serena), Figure 1. Their porosity is 26.9, 16.6 and 5.1%, respectively. The arithmetic average roughness Ra for Savonnières, Meule and Pietra serena is respectively 10, 9 and 4 μm while the equivalent pore radius Req, defined from pore size distribution measurement using mercury intrusion porosimetry is respectively 100, 10 and 0.04 μm.

(a) 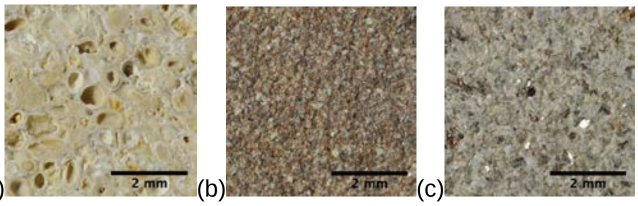 (b) (c)

Figure 1. Microscope images of porous stones: (a) Savonnières, (b) Meule and (c) Pietra serena.

Droplet generation

Water droplets are generated at the flat tip of a needle by pushing a syringe pump. The droplets have an initial diameter of 2 mm, reproducible with a relative error of 1%. Upon release, the droplet accelerates by gravity reaching an impact velocity between 0.5 and 3.0 m/s.

Optical light shadowgraphy

Water drop impact on porous stone is recorded in shadowgraphy using a high-speed camera (10 000 frame per second, 7.38 μm spatial resolution and 5 μs exposure time).

Results

We present here the results for Savonnières. Figure 2 shows the time evolution of spreading and a photo at maximum spreading. Careful investigation yields that, for the porous stones studied, the volume loss of the droplet by liquid penetration into the porous substrates due to inertial effects at impact can be neglected and that mass uptake by the substrate due to capillary absorption only starts after maximum spreading of the droplet. Such behavior is explained by the existence of a partial air layer, which is entrained between the droplet and the porous substrate during the spreading process preventing penetration either due to inertial effects or capillary absorption.

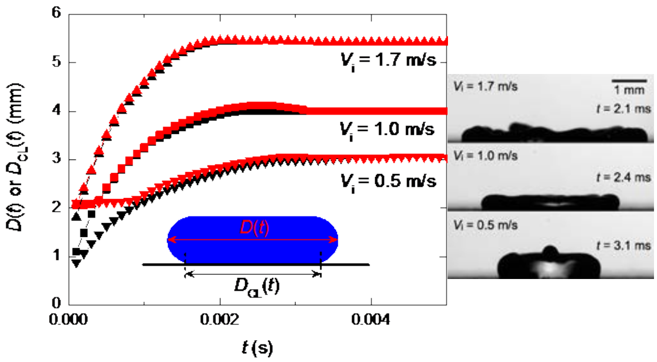

Figure 2: (left) Time evolution of spreading diameter D (red) and contact line D_{CL} (black) and (right) snapshots at maximum spreading for different impact velocities on Savonnières limestone.

Maximum spreading

The maximum spreading is characterized by the maximum spreading ratio $\beta_{max} = D_{max}/D_0$ and is governed by the balance between kinetic energy, capillary or surface tension energy before impact and at maximum spreading in surplus of the viscous dissipation during spreading. Energy balance models are commonly formulated using two dimensionless parameters: the Weber number ($We = \rho D_0 Vi^2/\gamma$) describing the ratio between the kinetic and capillary energy and the Reynolds number ($Re = \rho D_0 Vi/\mu$) describing the ratio between the kinetic and viscous energy. Here, we apply to porous materials the approach of [3] for the corrected maximum spreading ratio, where a smooth transition between the capillary and viscous regimes is described as:

$$\left(\beta_{max}^2-\beta_{Vi=0}^2\right)^{1/2}\cdot \mathrm{Re}^{-1/5}=\mathrm{We}^{1/2}/\left(A+\mathrm{We}^{1/2}\right)$$

which is based on the first order Padé approximation. Figure 3 shows the corrected measured data

$(\beta_{max}^2 - \beta_{Vi=0}^2)^{1/2}$as a function of the Weber number for drop impact on the porous stones and steel surface.

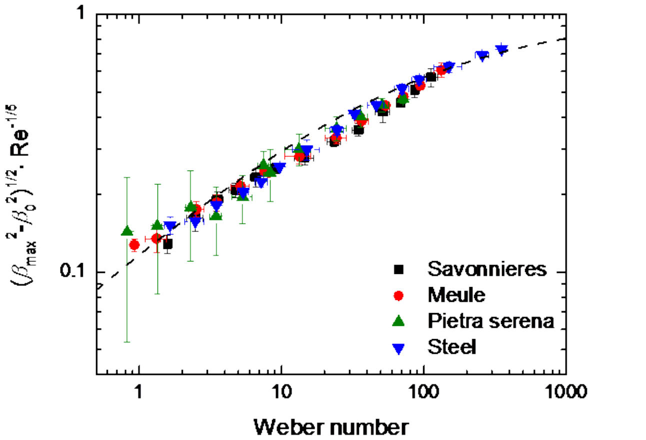

Figure 3: Rescaled maximum spreading ratio as a function of Weber number in log-log plot for the three stones and steel. The dotted line is the first order Padé approximation (see Eq).

We show that the maximum spreading can be rescaled properly for porous and impermeable surfaces by taking the capillary energy at zero impact velocity into account [4].

Jetting

In our experiments on the porous stones, in a specific impact speed range, we see the release of high speed singular jets (Figure 4). The release of this singular jets was previously reported only during impact on superhydrophobic surfaces and proposed to be related to the collapse of the air cavity inside the droplet [5]. In our experiments we see two different regimes for the jetting mechanism on porous surfaces. In the low speed regime (V_i<0.65 m/s) it is seen that similar to the the impermeable superhydrophobic surfaces, jetting is mainly due to the collapse of the cavity during the receding phase of the drople. In this regime normally several droplets with high speed are ejected from the main droplet (Figure 1a). However, by increasing the impact velocity, jetting can be attributed mostly to the pinning of the contact line with the porous surface. In this regime one big droplet with low speed ejects from the main droplet (Figure 1b).

(a) Low impact velocity (Vi=0.46 m/s)

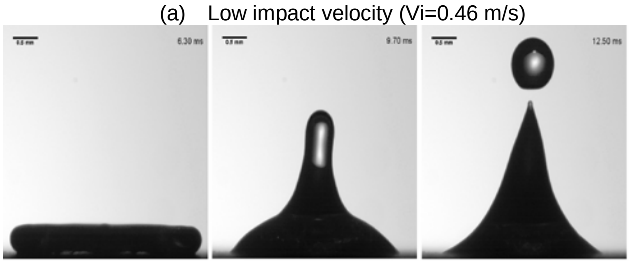

(b) High impact velocity (Vi=1 m/s)

Figure 4. Fast camera snapshots of jetting mechanism at two different regimes, on Pietra Serena.

In Figure 2, the velocity of the ejected jet at different impact velocities for different porous and non-porous surfaces is given. For all the porous surfaces, the highest jet velocity occurs at low impact velocities. The jet velocity decreases with increasing impact velocity.

We observe a difference in the jetting behavior on porous and non-porous surfaces which suggests the effect of the air film formed under the droplet on porous surfaces which results in less energy dissipation during droplet impact.

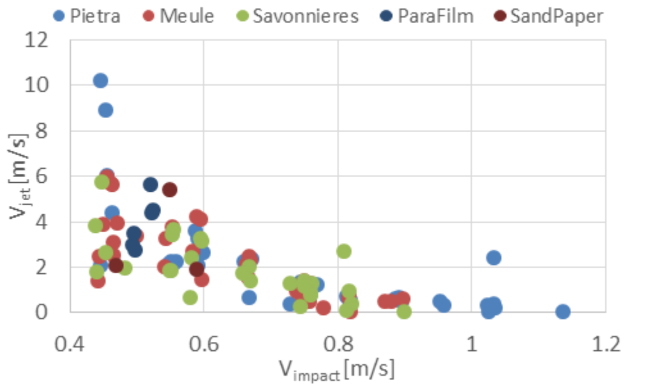

Figure 5. Velocity of the ejected jet at different impact velocities for different porous and non-porous surfaces.

Conclusion

We demonstrate that dynamic wetting plays an important role in the spreading at low velocity and that the dynamic wetting as characterized by the dynamic contact angle has to be taken into account for predicting the maximum spreading. Correcting the maximum spreading ratio for the dynamic wetting behavior, we demonstrate that all data for porous and non-porous substrates collapse onto a single curve. Finally, we observe the occurrence of jetting at low impact velocities.

Acknowledgements

We acknowledge the important contribution of the PhD work of Dr. Jaebong Lee to the spreading discussion in this paper. His PhD was made possible through Swiss National Science Foundation project no. 200021-135510. Swiss National Science Foundation project no. 200021-13551 supports Amir Ashrafi Habibabadi.

References

[1] J.B. Lee, D. Derome, J. Carmeliet. Drop impact on natural porous stones. J. Colloid and Interface Science, 469 (2016)147-156.
[2] J.B. Lee, D. Derome, J. Carmeliet. Absorption of impinging water droplet in porous stones. J. Colloid and Interface Science, 471(2016) 59-70.
[3] N. Laan, K.G. de Bruin, D. Bartolo, C. Josserand, D. Bonn. Maximum Diameter of Impacting Liquid Droplets. Phys. Rev. Applied 2 (2014): 044018.
[4] J.B. Lee, N. Laan,K. de Bruin,G. Skantzaris, N. Shahidzadeh,D. Derome, J. Carmeliet, D. Bonn D. Universal rescaling of drop impact on smooth and rough surfaces. J. Fluid Mechanics, 786 (2016):R4.
[5] Bartolo, Denis, Christophe Josserand, and Daniel Bonn. "Singular jets and bubbles in drop impact." Physical review letters 96.12 (2006): 124501.

Pinned and Sliding Drops -- Bifurcations and Statistics

S. Engelnkemper[1], M. Wilczek[1,2], S.V. Gurevich[1,2,3], U. Thiele[1,2,3]

[1] Institute for Theoretical Physical, WWU, Münster, Germany
[2] Center for Nonlinear Science (CeNoS), WWU, Münster, Germany
[3] Center for Multiscale Theory and Computation (CMTC), WWU, Münster, Germany

E-mail: engelnkemper@wwu.de

The long-wave evolution equation for a liquid film (thin-film equation) describes the dynamics of free surface structures, e.g., drops and ridges on solid substrates. These structures may represent ridges in the 2d case and drops in the 3d case. The main subject of our work is to analyze the behavior of such 3d drops when applying a lateral driving force, e.g., inclining a substrate of spatially homogeneous or heterogeneous wettability.

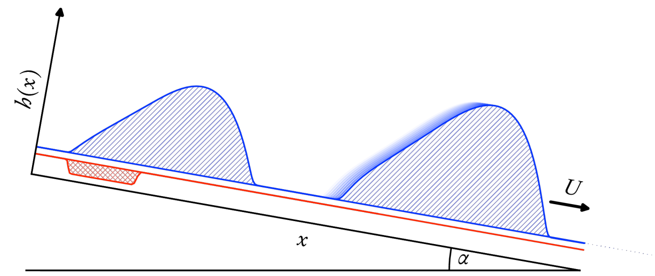

Fig. 1: *Sketch of pinned and sliding drop on an incline*

Given a homogeneous substrate, i.e., wettability is constant in space, any structure slides at any applied driving force. The sliding drops are steady states in a comoving frame and continuation techniques [3,4] may be applied. Continuing in the angle at fixed drop volume, (Fig. 2), small inclinations lead to slight drop deformations and linearly increasing velocity U [5].

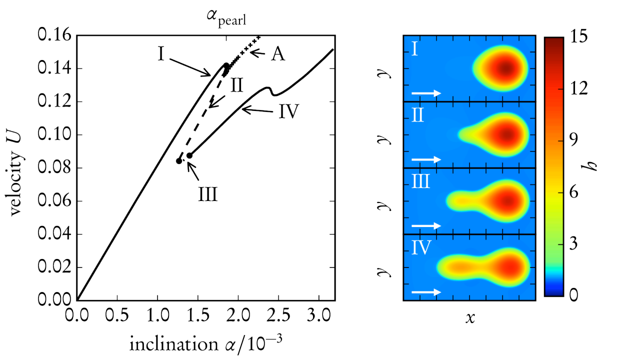

Fig. 2: *Bifurcation diagram (left) and stationary profiles (right) of sliding drops*

Increasing the driving further, the change in shape becomes more significant (solution I). Reaching a critical driving force (α_{pearl}), which manifests itself in a saddle-node bifurcation, drops undergo a pearling instability where large drops emit small satellite drops, as known from experiments [1]. Also, our everyday experience, e.g., drops on a window pane at rainy weather, show these transitions.

As the bifurcation diagram shows, the so-called pearling solutions form another solution branch (A) obtained by direct numerical simulation. Due to the periodic boundary conditions in sliding direction the emitted drop coalesces again with the larger drop, i.e., these solutions represent pearling-coalescence cycles. Following the main branch, the now linearly unstable drop elongates (II). After a second saddle-node bifurcation, a branch of linearly stable non-trivial sliding drops (IV) is found, i.e., a region of multi-stability occurs. Inclining the substrate further the drop undergoes a transition to a ridge state. Related details depend on the domain size and are therefore not discussed here.

From our everyday experience, we know that most of the drops of small volume do not move at all, but rest at certain spots on the window. This is due to small inhomogeneities of the substrate. To cover these effects, we next consider heterogeneous substrates, namely, substrates with wettability patterns. Here, we focus on a case where spots of larger wettability occur, where drops tend to remain pinned. Again, applying continuation techniques, we continue in the drop volume at fixed inclination angle (Fig. 3).

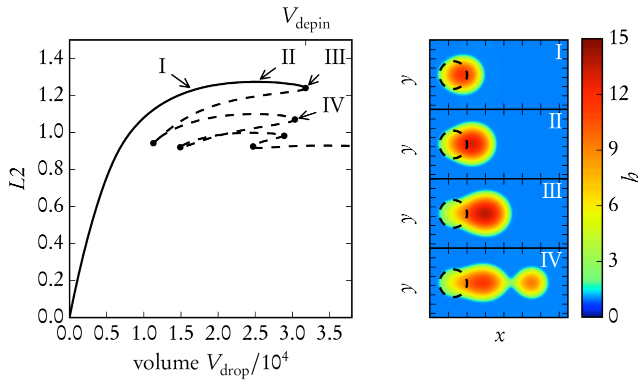

Fig. 3: *Bifurcation diagram (left) and solutions (right) of pinned drops*

Beginning at rather small volumes (I) the drop mainly covers the wettable spot (black dashed circle). Increasing the volume, a primary saddle node bifurcation (V_{depin}) occurs defining the largest stable pinned drop. Drops of larger volume do not pin but undergo a stick-slip motion as analyzed for 2d drops in [2]. Following the main branch, a series of saddle nodes results in non-trivial elongated pinned solutions (IV), which are however unstable. For even larger volumes the solution branch ends on a ridge state in analogy to the case of a homogeneous substrate.

The saddle node bifurcations at α_{pearl} and V_{depin} may be continued in the plane spanned by inclination and drop volume over several orders of magnitude and be represented as power laws (Fig. 4, also see [5]).

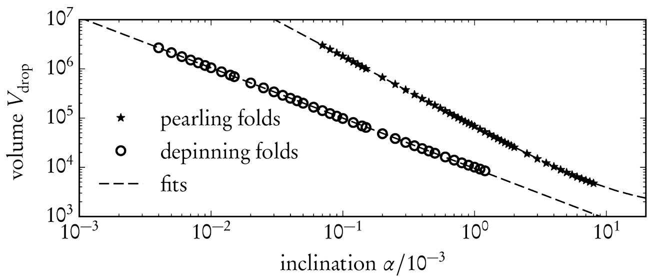

$$V_{pearl} = a \cdot \alpha_{pearl}^{b} + c$$

$$a = 3.25 \pm 0.03 \qquad b = -1.436 \pm 0.001 \qquad c = (1.5 \pm 0.3) \cdot 10^3$$

$$V_{depin} = a_\rho \cdot \alpha_{depin}^{b_\rho}$$

$$a_{1.0} = 8.15 \pm 0.14 \qquad b_{1.0} = -1.02 \pm 0.01$$

Fig. 4: *Power laws of pearling and depinning instabilities*

Direct numerical simulations on large domains, give us the statistics of ensembles with hundreds of individual drops (Fig. 5).

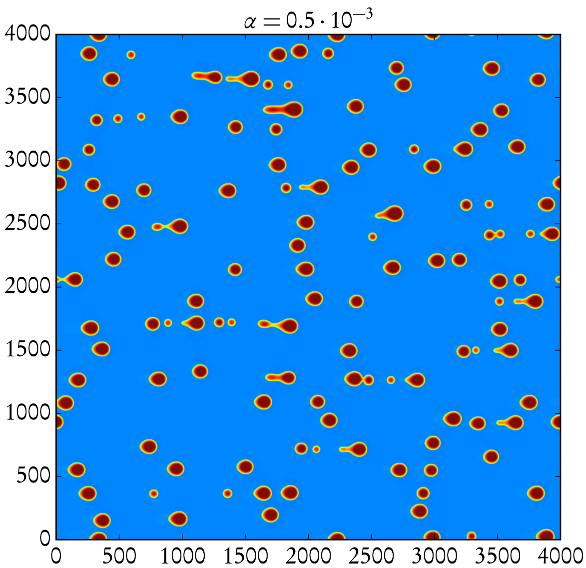

Fig. 5: *Snapshot of a large-scale direct numerical simulation*

Employing kernel density estimates of drop volumes allows us to determine volume distribution functions. These tend to a stationary state. Comparing the latter with the critical volumes for the pearling instability reveals the predictive character of the results obtained by single drop continuations. Here, the threshold volume for pearling at different inclinations is connected to the upper inflection point of the corresponding volume distribution (Fig. 6).

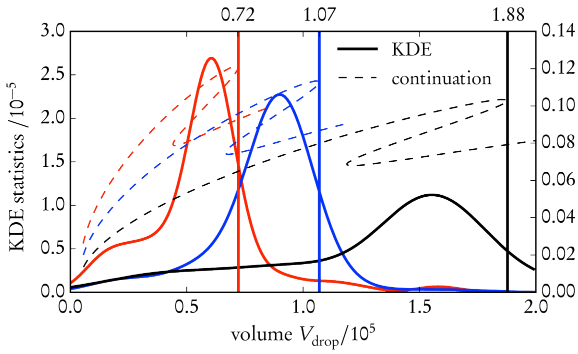

Fig. 6: *Stationary volume distributions and single drop volume continuations for different inclination angles*

All numerical results are obtained by implementation of the thin film equation into the continuation-toolbox PDE2PATH [3,4] and the open source framework DUNE [6].

Acknowledgements.

This work was partly supported by the Deutsche Forschungsgemeinschaft within the Transregional Collaborative Research Center TRR 61.

References.

[1] T. Podgorski, J.M. Flesselles, L. Limat, Phys. Rev. Lett. 87, 036102, (2001).

[2] U. Thiele, E. Knobloch, New J. Phys. 8, 313 (2006).

[3] T. Dohnal, J. D. M. Rademacher, H. Uecker, and D. Wetzel, arXiv:1409.3119, (2014).

[4] H. Uecker and D. Wetzel, SIAM J. Appl. Dyn. Syst., 13:94-128, (2014).

[5] S. Engelnkemper, M. Wilczek, S.V. Gurevich, U. Thiele, Phys. Rev. Fluids 1, 073901, (2016).

[6] P. Bastian, F. Heimann, and S. Marnach, Kybernetika, 46:294–315, (2010).

Curvature Directed Assembly in Soft Matter

Kathleen Stebe

[1]Department of Chemical & Biomolecular Engineering, University of Pennsylvania, Philadelphia, PA, USA

E-mail: kstebe@seas.upenn.edu

Colloidal particles at interfaces between isotropic fluids interact via capillarity. Particles distort the interface around them to satisfy wetting or pinning conditions at the three phase contact line, and migrate to lower the interfacial area. These interactions have aspects that are universal, and others that are remarkably sensitive to particle shape. (1-3)

When the interfaces are curved, the interface shape and area around the particle depends on the curvature. As a result, particles move along curvature gradients. The curvature field acts on the colloids like an external electric field on charge multipoles. Again, universal behavior is observed for particles that are small enough, as leading order modes in the interface distortion dictate particle trajectories. Small particles are attracted to regions of high curvature. (4-6)

For larger particles, however, more complex trajectories occur. Experiments performed for colloids on curved fluid interfaces molded around a micropost are presented for disks, spheres and cylinders are discussed, along with supporting theory.

Such curvature directed motion occurs in other systems. Colloids adhered to giant unilammelar vesicles can also distort the lipid bilayer around them. Considering the deformation field in the context of a Helfrich model, particle sourced distortions impose a curvature cost owing to finite bending moduli, or an area cost owing to finite tensions. On vesicles that are tense, the curvature cost becomes a weak correction. In this limit, there are important analogies between the colloid's behavior of lipid bilayers and on interfaces between isotropic fluids. We discuss theory and experiment in which colloids move along well defined curvature gradients akin to the migration reported on isotropic fluid interfaces. (7)

These are but two examples of assembly driven by geometry and confinement in soft matter. Time permitting, other examples, including lock and key assembly of colloids in confined nematic liquid crystals (8) and directed assembly of nanoparticles in liquid crystalline hosts will be discussed.

Acknowledgements. Acknowledge funding support from NSF CMP 1607878, NSF DMR05-1120901, ARO W911NF-16-1-0288

References

[1] L. Botto, Y. Lu, R. L. Leheny and K. J. Stebe. Capillary bond between rod-like particles and the micromechanics of particle-laden interfaces. Soft Matter 4971-4979 (2012).

[2]L. Yao, L. Botto, M. Cavallaro, V. Garbin, and K.J. Stebe. Near Field Capillary Repulsion. Soft Matter 779–786 (2013).

[3] L. Botto, E. P. Lewandowski, M. Cavallaro, Jr., and K. J. Stebe. Capillary interactions between anisotropic particles. Soft Matter 9957-9971 (2012).

[4] M. Cavallaro Jr., L. Botto, E. P. Lewandowski, M. W ang, K. J. Stebe. Curvature-driven capillary migration and assembly of rod-like particles. Proc Natl Acad Sci U S A. 108 (2011) 20923-20928.

[5] N. Sharifi-Mood, I. Liu and K. J. Stebe. Capillary Curvature Migration of Microspheres. Soft Matter 6768-6779 (2015).

[6] L. Yao, N. Sharif-Mood, I.B. Liu, and K.J. Stebe. Capillary migration of microdisks on curved interfaces. J. Colloid Int. Sci 436-442 (2015) 449.

[7] N. Li, N. Sharifi-Mood, F. Tu, D. Lee, R. Radhakrishnan, T. Baumgart and K. J. Stebe, Curvature-Driven Migration of Colloids on Tense Lipid Bilayers. Langmuir 33 (2016) 600 – 610.

[8] Y. Luo, F. Serra, and K. J. Stebe, Experimental realization of the "lock-and-key" mechanism in liquid crystals. Soft Matter 12 (2016) 6027-6032.